Development of conjunctival and retinal models for improved eye disease treatments

Rachel Victoria Ann Gater

Institute for Science and Technology in Medicine

Keele University

Thesis submitted for the degree of

Doctor of Philosophy

December 2019

Abstract

Eye diseases such as glaucoma, macular degeneration and retinitis pigmentosa can lead to significant sight problems and blindness if left untreated. Current treatments are invasive, have a low success rate and lack the ability to regenerate damaged ocular tissue. The requirement for more effective treatments is therefore high. The development of tissue engineering strategies to treat ocular disease has advanced significantly over recent years with promising results. Therefore, the establishment of improved conjunctival and retinal tissue models for investigation of ocular disease mechanisms and testing of new treatments is required. The overall aim of this project was to develop and apply improved conjunctival and retinal models using tissue engineering approaches for eye disease treatments.

2D and 3D Tenon's capsule and conjunctival tissue (TCCT) models were constructed by seeding porcine TCCT fibroblasts into collagen hydrogel. These were used to investigate key stimulatory factors (growth factors, cytokines, aqueous humour and shear stress) believed to influence tissue fibrosis response after glaucoma surgery. In addition to cellular metabolic assessment, a new non-destructive assay using added azido-L-proline to quantify neocollagen synthesis in response to these factors, was applied for up to 14 days of culture. Results found that 3D TCCT fibroblast metabolism, actin expression and neocollagen synthesis increased by up to 60% by day 7 of culture with the addition of TGF-β, VEGF, TNF-α (50 ng/mL) or 50% aqueous humour. Furthermore, shear stress-induced mechanotransduction was found to promote metabolic activity across *in vitro* experimental conditions, with shear stress in combination with aqueous humour triggering the strongest fibrotic response, followed by TGF-β, TNF-α and VEGF. Shear stress therefore appeared to enhance the influence of growth factors and further promoted fibrotic responses within the TCCT model. These novel findings offer a useful contribution to the understanding of wound healing response triggered by aqueous fluid outflow after glaucoma surgery.

The established TCCT models were also used for evaluation of glaucoma treatment efficacy and *in vitro* medical device assessment. Key growth factor inhibitors, decorin proteoglycan and the novel application of calcium signalling channel blocker nifedipine were each tested. Furthermore, the Xen Gel Stent glaucoma medical device was tested *in vitro* for the first time using the established 3D TCCT model. Key results found that TCCT fibroblast metabolism decreased by up to 281.9% by day 3 of culture with the addition of TNF-α and TGF-β inhibitors (10μM) or nifedipine (100μM). Furthermore, fibroblast activity surrounding the stent lumen was evident when implanting the Xen Gel Stent glaucoma medical device into the 3D TCCT tissue model, altogether offering convenient new methods to assess new glaucoma treatment drugs/devices.

In the final results chapter, a 3D *in vitro* organotypic retinal tissue model was developed for improved retinal disease study and treatment. A compressed collagen gel was tested for the first time as an (artificial vitreous) substrate for the culture of organotypic retinal explants. Non-destructive imaging modality, OCT, was applied to monitor the full culture period, with cross-validation by conventional histological examinations. Findings confirmed that compressed collagen was beneficial in providing the biochemicals and mechanical strength required to preserve retinal tissue *in vitro* in the absence of intraocular pressure, whilst still being biocompatible. All layers of porcine retinal tissue were preserved intact and with minimal distortion for up to 2 weeks. The study also demonstrated the novel use of OCT to monitor live *in vitro* retinal explants during culture. Following establishment of a laser injury method for the retinal tissue, added stem cells were found to aggregate towards the retinal injury site, with differentiation evident.

Overall, the ocular models developed in this thesis offer useful tools for the study of ocular disease mechanisms and testing of potential drug interventions, new medical devices and stem cell therapies, whilst also reducing the requirement for live animal experiments.

Table of contents

List of figures

List of tables

Acknowledgements

First and foremost, I would like to give special thanks to my lead supervisor Professor Ying Yang, for believing in me from the start and supporting me throughout my PhD journey. Her continued encouragement, patience and advice has been imperative in my personal development as a scientific researcher. I would also like to thank my secondary supervisors, Dr Dan Nguyen and Professor Alicia El Haj, for their insightful suggestions throughout, which have contributed to such an interesting and productive research project.

Another special thank you to all of my colleagues associated with Professor Ying's research group, the Guy Hilton Research Centre, Keele University and the EPSRC Centre for Doctoral Training. Your friendship, support and assistance throughout this time has been invaluable. Notably, thank you to Jess and Nicky for being such great housemates during the year at Loughborough University. Also, a big thank you to each of the mini project students who have worked alongside me during the PhD. In addition, the funding sources that made this PhD work possible are gratefully acknowledged; Keele University ACORN fund and Faculty of Medicine and Health Sciences.

Furthermore, I am grateful to my family for always encouraging me to achieve my best, and to my partner Matthew, for his continued support and understanding throughout the PhD. It has been wonderful to see our relationship develop during this time.

Finally, I would like to thank my friends, both old and new. Alongside the PhD journey, adventures and experiences shared with friends have made the past few years a truly enriching and memorable part of my life, to which I am grateful. Even if you couldn't help me with the PhD work directly, those times spent having a drink of gin with me on the weekend are much appreciated.

Publications

1. Rachel Gater, Dan Nguyen, Alicia El Haj, Ying Yang. Development of better treatments for retinal disease using stem cell therapies. International Journal of Stem Cell Research & Therapy, (2016): 3(2), 032.

2. Rachel Gater, Tugce Ipek, Salman Sadiq, Dan Nguyen, Lynval Jones, Alicia El Haj, Ying Yang. Investigation of conjunctival fibrosis response using a 3D glaucoma Tenon's capsule + conjunctival model. Investigative Ophthalmology & Visual Science, (2019): 60(2), 605-614.

Proceedings paper

1. Rachel Gater, Nicholas Khoshnaw, Yvonne Reinwald, Dan Nguyen, Alicia El Haj, Ying Yang. Optical coherence tomography as a convenient tool to assess the quality and application of organotypic retinal samples. SPIE Proceedings, Dynamics and Fluctuations in Biomedical Photonics XIII (2016): 9707.

Book chapter

1. Gater R, Njoroge W, Owida HA, Yang Y. Scaffolds mimicking the native structure of tissues. Handbook of Tissue Engineering Scaffolds: Volume One, Chapter 2. Editors: Mozafari M, Sefat F, Atala A. Woodhead Publishing, 2019

Oral presentations

1. **EPSRC CDT (Centre for Doctoral Training) Cross Cadre Conference 2018:** Rachel Gater, Dan Nguyen, Alicia El Haj, Ying Yang. Investigation of fibrosis response within a 3D Tenon's capsule + conjunctival model.

2. **FIRM (Future Investigators of Regenerative Medicine) symposium 2018:** Rachel Gater, Dan Nguyen, Alicia El Haj, Ying Yang. Assessment of metabolic response to biochemicals and shear stress within a 3D tissue engineered Tenon's capsule + conjunctival (TCCT) model.

Poster presentations

1. **SPIE (Society of Photo-Optical Instrumentation Engineers) West Photonics Conference 2016:** Rachel Gater, Nicholas Khoshnaw, Yvonne Reinwald, Dan Nguyen, Alicia El Haj, Ying Yang. Optical coherence tomography as a convenient tool to assess the quality and application of organotypic retinal samples.

2. **TCES (Tissue and Cell Engineering Society) Conference 2016:** Rachel Gater, Tugce Ipek, Sudeshna Bhunia, Dan Nguyen, Alicia El Haj, Ying Yang. Investigation of the effect of growth factors and inhibitors on fibroblasts in a glaucoma conjunctival model.

3. **TCES (Tissue and Cell Engineering Society) Conference 2017:** Rachel Gater, Salman Sadiq, Dan Nguyen, Alicia El Haj, Ying Yang. Assessment of new glaucoma treatment devices- using a tissue engineered conjunctival model.

4. **TCES (Tissue and Cell Engineering Society) Conference 2018:** Rachel Gater, Sara Bodbin, Dan Nguyen, Alicia El Haj, Ying Yang. Assessment of metabolic response to biochemicals and shear stress within a 3D tissue engineered Tenon's capsule + conjunctival model.

Abbreviations

2D	Two dimensional
3D	Three dimensional
ASCs	Adipose stem cells
AMD	Age-related macular degeneration
BSA	Bovine serum albumin
CFSE	5(6)-Carboxyfluorescein N-hydroxysuccinimidyl ester
DAPI	4',6-Diamidino-2-Phenylindole, Dihydrochloride
DMEM	Dulbecco's Modified Eagle's Medium
DMSO	Dimethyl sulfoxide
ECM	Extracellular matrix
ELISA	Enzyme-linked immunosorbent assay
ESCs	Embryonic stem cells
FBS	Fetal bovine serum
FITC	Fluorescein isothiocyanate
GAGs	Glycosaminoglycans
IL8	Interleukin-8
IOP	Intraocular pressure
iPSCs	Induced pluripotent stem cells
LG	L-Glutamine
MIGS	Minimally invasive glaucoma surgery
OCT	Optical coherence tomography
PBS	Phosphate buffer saline
rMSCs	Rat bone marrow mesenchymal stem cells
rpm	Rotations per minute
RPCs	Retinal progenitor cells
RPE	Retinal pigmented epithelium
TCCT	Tenon's capsule and conjunctival tissue
TGF-β	Transforming growth factor beta
TNF-α	Tumour necrosis factor alpha
TRITC	Tetramethylrhodamine
VEGF	Vascular endothelial growth factor

Chapter 1

Literature review

1.1 Human eye anatomy

The human eye is a light reactive, sensory organ which determines vision. Vision is widely considered to be the most important sensory system of the body, providing us with a three dimensional (3D), moving image of the world. As shown in Figure 1.1, the human eye is composed of several tissue structures both internally and externally. Briefly, light enters the eye via the pupil and is focused onto the retinal tissue at the back of the eye to determine vision (Mutti, 2003). Similar to other organs of the body, eye structures are prone to damage by disease and trauma, which can lead to visual impairment. Visual impairment is severely debilitating and can often psychologically close an individual's window to the world, making it an important area for scientific research.

Figure 1.1 Anatomical structure of the human eye

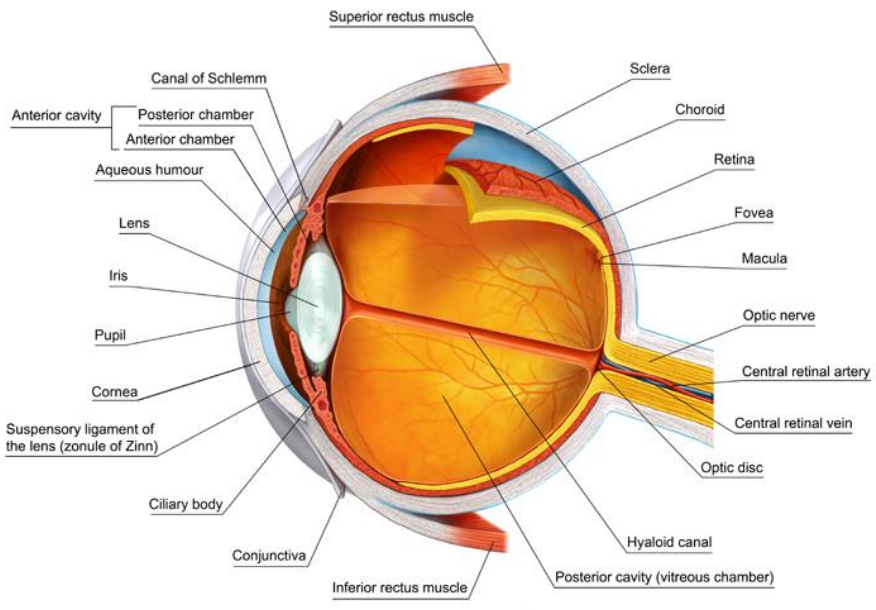

A summary of human eye anatomical structure. Source: Virtual Medical Centre, 2018

1.1.1 The anterior chamber and aqueous humour

The anterior chamber is an internal cavity of the eye situated between the iris and cornea. A transparent fluid known as aqueous humour fills the anterior chamber, which plays a key role in maintaining intraocular pressure (IOP) of the eye and retaining its taut, spherical shape. In healthy eyes, aqueous humour is continually produced by the ciliary body and drained via a pathway known as the trabecular meshwork, leading into the Schlemm's canal (Figure 1.2). The trabecular meshwork allows aqueous humour to filter gradually, maintaining fluid pressure inside the eye (Goel *et al.*, 2010).

Figure 1.2 Aqueous humour production and drainage in the anterior chamber

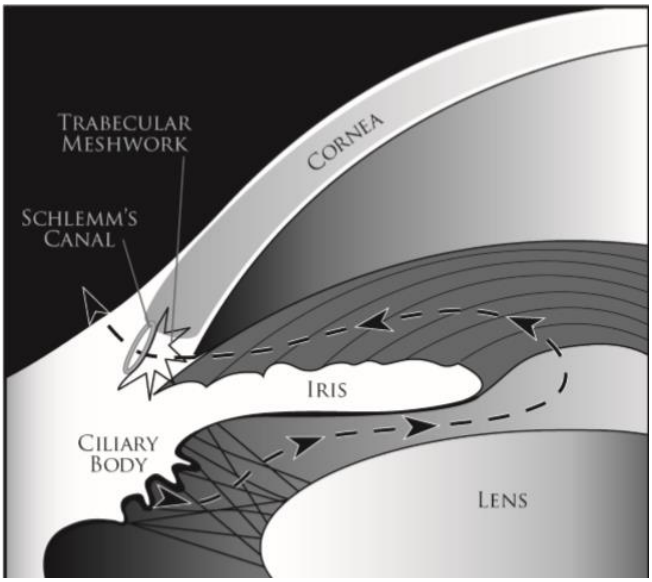

The pathway of continuous aqueous humour fluid production and drainage in the anterior chamber. Source: Goel *et al*., (2010).

After leaving the Schlemm's canal, aqueous humour then enters the aqueous veins and subsequently mixes with blood in the episcleral veins. Approximately 90% of aqueous drainage occurs via this pathway and 10% via a secondary pathway known as uveoscleral drainage. Uveoscleral drainage does not have a distinct pathway and is instead a route

whereby fluid drains gradually through tissues such as the supraciliary space, ciliary muscle, choroidal vessels, emissarial canals, sclera and lymphatic vessels (Toris, 2013).

In addition to the maintenance of IOP, other functions of aqueous humour include the removal of metabolic waste products, supply of nutrients, transport of neurotransmitters and stabilisation of the lens structure. As the name would suggest, aqueous humour is composed of approximately 98% water. In addition, other major components of aqueous humour include amino acids and proteins transported by the ciliary muscles, organic and inorganic ions, carbohydrates, glutathione, urea, oxygen, carbon dioxide, electrolytes and cytokines/growth factors (Goel *et al.*, 2010). According to literature, glucose and urea make up approximately 80% of aqueous humour plasma. Additionally, aqueous humour is thought to contain anti-oxidant substances, such as glutathione (which diffuses in from the blood) and ascorbate, which help protect the internal eye structures from light-induced oxidative damage (Gabelt and Kaufman, 2005). Furthermore, the presence of enzymes such as collagenase are believed to help regulate the extracellular matrix (ECM) of the trabecular meshwork (Vadillo-Ortega *et al.*, 1989). In addition, aqueous humour is thought to contain several growth factors and cytokines such as transforming growth factor beta (TGF-β) and vascular endothelial growth factor (VEGF) (Jampel *et al.*, 1990; Tripathi *et al.*, 1992; Huang *et al*., 2015).

1.1.2 Conjunctival membrane

The conjunctiva is a mucous membrane covering the inside of the eyelids and fore part of the sclera. As shown in Figure 1.3, the bulbar conjunctiva sits loosely on top of the sclera, separated by a thin, fibrous tissue layer known as the Tenon's capsule. The fibrous protein

present within Tenon's capsule and conjunctival tissue (TCCT) is reported to be primarily Type I collagen, with a sparse distribution of elastin (Park *et al.*, 2016).

Figure 1.3 External anterior eye cup structures around the limbus

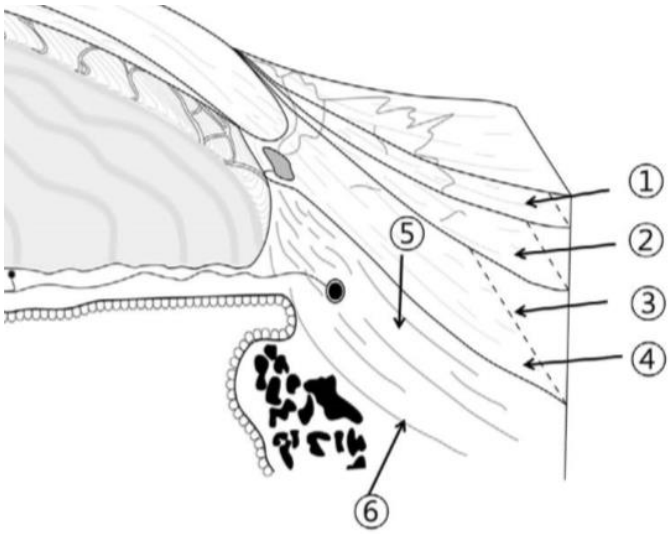

Diagram of anterior eye segment structures around the limbus. Source: Park *et al*., (2016)

Conjunctival membrane consists of three layers; fibrous, adenoid and epithelium. Being a connective tissue, these layers contain several cell types including fibroblasts, goblet cells, melanocytes, Langerhan's cells and epithelial cells. Similar to the cornea, the conjunctival membrane functions to offer a barrier of protection for the ocular surface. Here, the goblet cells secrete mucus to trap and prevent bacteria from entering ocular structures such as the cornea (Read *et al.*, 2016). In cases of conjunctival membrane disease and wound healing, the proliferation and behaviour of TCCT cell types can often be influenced by stimulatory factors such as cytokines and shear stress (section 1.4).

1.1.3 The retina

The retina is a complex, light-sensitive tissue layer on the inner surface of the eye, which functions to transduce light stimuli into nerve impulses which travel to the brain via the optic nerve. Retinal tissue lines a pigmented, vascular layer of connective tissue known as the choroid, which makes contact with the retina via the Bruch's membrane. Both of these structures function to support retinal tissue, providing oxygen and nourishment. As shown in Figure 1.4, the retina is made up of several neuronal layers consisting of at least eight different cell types including the retinal pigmented epithelium (RPE) cells, photoreceptors, bipolar cells and ganglion cells (Livesey and Cepko, 2001).

Figure 1.4 The various cellular layers of human retinal tissue

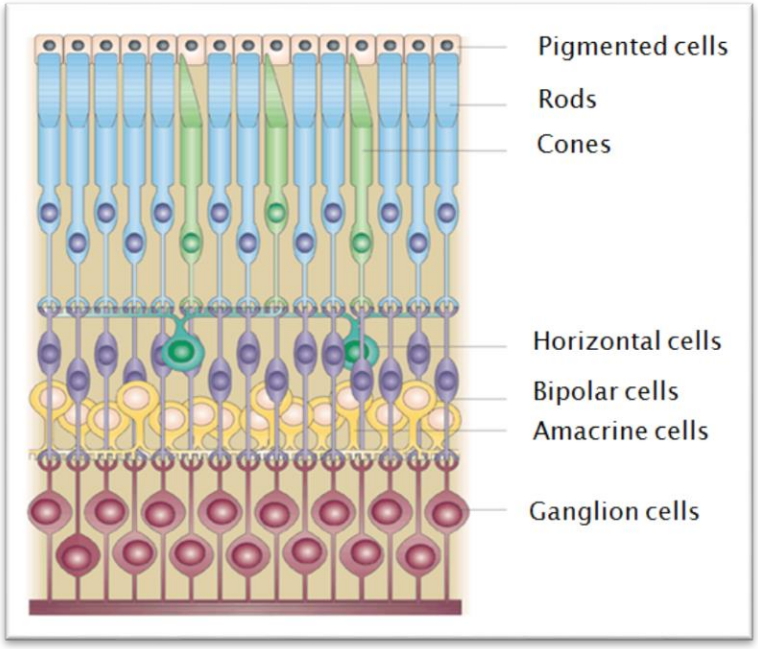

The various cellular layers of human retinal tissue including retinal pigmented epithelial (RPE) cells, photoreceptors (rods and cones), horizontal cells, bipolar cells, amacrine cells and ganglion cells. Source: Livesey and Cepko, (2001).

RPE is a pigmented cell layer situated between the neural retina and Bruch's membrane. RPE is involved in several functions such as the absorption of scattered light, recycling of visual pigments and transport of chemicals between the choroid/Bruch's membrane and

neural retina. In the cellular layer below RPE are two types of photoreceptor; rods and cones. Rods function in scotopic vision (in darkness) and are insensitive to colour with low visual acuity. Cones function in photopic vision (in light) and are sensitive to colour with high visual acuity. Photoreceptors absorb photons, triggering a change in cell membrane potential which passes the signalling onto bipolar cells. The retina has several bipolar cell types that provide channels to encode various visual stimulus properties, such as shape and contrast. Bipolar cells transform the input from photoreceptors and transmit signals onto the ganglion cells. Axons of ganglion cells collectively form the optic nerve, transmitting the information to the brain (Kolb *et al*., 2010).

1.1.4 Vitreous humour

In addition to the choroid and Bruch's membrane, the *in vivo* retina makes contact with vitreous humour; a hydrated, gel-like mass which consists almost entirely of water. Native vitreous is composed of 99% water, a network of collagen fibrils, hyaluronic acid (also known as hyaluronan) and hyalocyte cells, as well as certain salts, sugar and ascorbic acid. The vitreous humour supports retinal metabolism by acting as a reservoir for substances such as oxygen, glucose and ascorbic acid, as well as a removal system for metabolic waste products (Kokavec *et al.*, 2016).

The continued development of intravitreal medical interventions has led to a need for improved vitreous humour substitutes, for use in vitreoretinal surgery (Alovisi *et al.*, 2017) and *in vitro* experiments (Kummer *et al.*, 2007). Current clinically available sources of artificial vitreous include silicone oil, heavy silicone oil and polymeric gels. However, these materials are frequently associated with complications such as emulsification, inflammatory reaction and failure to support the retina adequately in the long term

(Stefánsson *et al.*, 1988). One study tested a physiological balanced solution-filled capsule to fill the vitreous cavity. This method was promising for *in vivo* use to push areas of detached retina back into position, but lacked the biocompatible properties of native vitreous humour (Gao *et al.*, 2008). Ongoing research into the improvement of artificial vitreous bodies aim to use materials which are; transparent, injectable, biocompatible, hydrophilic and able to form a gel within the vitreous cavity (Colthurst *et al.*, 2000). Another study conducted by Schramm et al., (2012) explored cross-linked hyaluronic acid biopolymers as an artificial vitreous body. This material was promising for use *in vivo* or *in vitro*, since the gels were transparent, had a similar refractive index to human vitreous and were highly biocompatible (Schramm *et al.*, 2012). More recently, materials such as low polymeric content hydrogels (Hayashi *et al.*, 2017) and hyaluronic acid based hydrogels (Januschowski *et al.*, 2019) offer other interesting methods to mimic vitreous artificially. Furthermore, self-assembling vitreous-like peptide gels such as PanaceaGel SPG-178 have the advantage of being injectable without risk of damage, whilst still being highly biocompatible (Uesugi *et al.*, 2017).

1.2 Glaucoma

According to the World Health Organisation, an estimated 70 million people worldwide suffer from glaucoma (WHO, 2019). Furthermore, it is estimated to affect approximately 10% of people aged over 75 (NICE, 2018). Glaucoma is caused by an increase in IOP, due to insufficient drainage of aqueous humour through the trabecular meshwork. A patient's IOP can be recorded using air puff tonometry, measured in millimetres of mercury (mmHg). The IOP of a healthy eye should range between 12-22 mmHg. An IOP higher than this could indicate glaucoma or ocular hypertension. As shown in Figure 1.5, the increased IOP applies pressure to the retina and optic nerve regions which, over time, can lead to the deterioration of vision. Symptoms usually begin with deterioration of the

peripheral vision. However, if left untreated, this deterioration spreads more centrally over time and can eventually lead to complete blindness (Quigley, 2011).

Figure 1.5 The aetiology of glaucoma

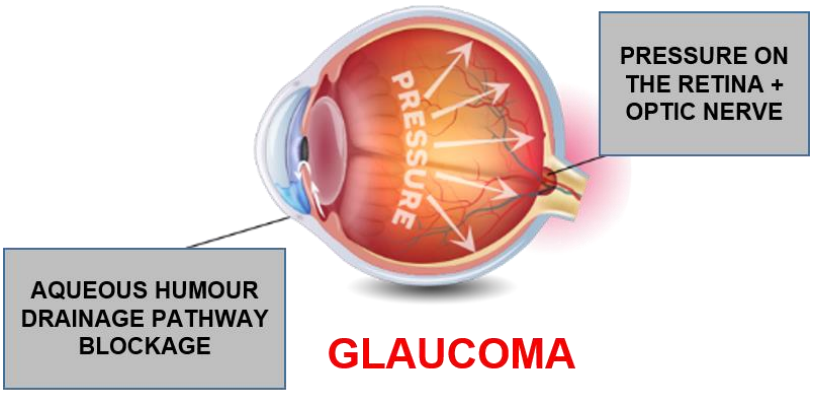

The aetiology of glaucoma. Source: adapted from Laser Eye Surgery Hub, 2019.

Generally, there are two considered types of glaucoma; closed angle and open angle. Closed angle glaucoma is a rare condition which can occur when the pupil is dilated and the lens happens to stick to the back of the iris. This can cause sudden closure of the aqueous humour drainage angle completely, causing a rapid IOP increase. This rare occurrence is a medical emergency requiring rapid treatment (Moorfields Eye Hospital, 2017). Open angle glaucoma, the most common type, is instead caused by a partial blockage of the drainage canal due to insufficient drainage of aqueous humour through the trabecular meshwork. Factors such as mechanical stress, injuries and the aging process can cause death of trabecular meshwork cells and a build of up debris. This leads a gradual blockage of the drainage pathway and a steady IOP increase over time (Hong *et al.*, 2005).

1.2.1 Treatments for early stage glaucoma

For the treatment of early stage glaucoma, medication can be administered to modulate aqueous production or increase aqueous humour outflow, thereby reducing IOP. Eye drops containing prostaglandin analogues function to increase the outflow of aqueous humour from the eye. Eye drops containing beta blockers alternatively function to decrease the production of aqueous humour. Eye drops containing alpha agonists can also be used, which function to both decrease the production of aqueous humour and also increase the drainage. Alternatively, a pill containing carbonic anhydrase inhibitors can be taken which functions to decrease the production of aqueous humour. Laser therapy is another therapeutic option, which reduces IOP by increasing flow through the trabecular meshwork to allow better outflow of aqueous humour (Heijl, 2014).

1.2.2 Glaucoma filtration surgery

For advanced stage glaucoma which can no longer be controlled using medication, the most common surgical treatment is glaucoma filtration surgery (also known as a trabeculectomy). As shown in Figure 1.6, a trabeculectomy involves making an incision into the sclera and carefully placing sutures. This allows aqueous humour to drain into the sub-Tenon's/conjunctival space, forming a bleb. The fluid is then absorbed by capillaries in the sub-conjunctival/episcleral tissue leading to a reduction of IOP.

Figure 1.6 Glaucoma filtration surgery (trabeculectomy) procedure

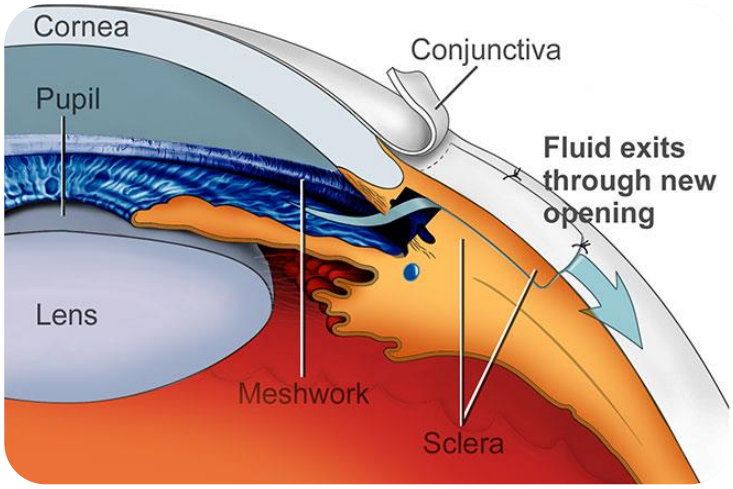

The incision made into conjunctival and scleral tissue during glaucoma filtration surgery (trabeculectomy). Source: All About Vision, 2019.

1.3 Failure in glaucoma filtration surgery

Unfortunately, the trabeculectomy procedure is an invasive operation with potential complications, including a risk of infection and wound/bleb leakage. Furthermore, excessive wound healing of TCCT following glaucoma surgery can cause the opening created to heal up again and become blocked, which significantly reduces the surgery success rate to approximately 55% (Hong *et al.*, 2005). Various factors contribute to this wound healing response, including the TCCT extracellular matrix, glycosaminoglycans, proteoglycans and the stimulation of cytokines, growth factors and shear stress.

1.3.1 The role of extracellular matrix

All native tissue structures contain an intricate microenvironment known as the extracellular matrix (ECM). ECM is a complex mixture of molecules secreted by cells to provide their surrounding structural and biochemical support. ECM characteristics can differ significantly between different tissue types, depending on the requirements of a particular tissue. It is composed of glycosaminoglycans (GAGs) attached to proteoglycans,

adhesive glycoproteins and fibrous proteins (e.g. collagen) which provide structural support (Frantz *et al.*, 2010). The most abundant fibrous protein within tissue ECM, including Tenon's capsule and conjunctival tissue, is collagen (Park *et al.*, 2017). Collagen functions to provide the 'scaffolding' of tissues for the attachment of proteoglycans and other ECM components. The name 'collagen' is used as a generic term for proteins forming a characteristic triple helix of three polypeptide chains. All members of the collagen family form these supramolecular structures in the extracellular matrix, although their size, function and tissue distribution vary considerably. There are 28 different types of collagen identified in vertebrates, with fibrillar collagen being the most abundant accounting for approximately 90% of all collagen in the body. Fibrillar collagen includes types I, II, III, V, XI, XXIV and XXVII, with type I being the most common. Tissue fibrosis is characterised by the disproportionate increase and deposition of ECM, leading to scar tissue formation and abnormalities in tissue function.

1.3.2 The role of glycosaminoglycans

GAG molecules are long unbranched polysaccharides with a repeated disaccharide unit. The major GAG types with physiological significance can be categorised into four groups: chondroitin sulphate/dermatan sulphate, heparin/heparan sulphate, keratan sulphate and hyaluronan. Minimal previous literature reports the precise GAG content of conjunctival ECM, however as a connective tissue with the presence of collagen it can be assumed that chondroitin sulphate/dermatan sulphate GAG chains are present and attached to the proteoglycans decorin and biglycan. One study confirms a content of mainly chondroitin sulphate within conjunctival tissue, with no other GAG molecules reported (Kaneko *et al*., 1986). The GAG content of scleral tissue is reported to contain primarily chondroitin sulphate/dermatan sulphate, with a small quantity of hyaluronan (Brown *et al.*, 1994). The GAG content of the cornea appears to be reported more widely, known to contain

chondroitin sulphate/dermatan sulphate, heparan sulphate and keratan sulphate (Coulson-Thomas *et al.*, 2015). GAGs play a major role in maintaining the equilibrium of healthy tissue by sequestering or 'protecting' ECM proteins and cytokines. In wounded tissue, GAGs such as heparan sulphate are degraded and no longer 'protect' the ECM proteins and cytokines. This causes the proteins and cytokines to be released into surrounding tissue and hinders efficient wound healing. Stimulation of increased fibroblast proliferation and the excessive production/deposition of ECM then follows, leading to scar tissue formation and abnormal tissue structure

1.3.3 The role of cytokines and growth factors

Following glaucoma surgery, the wound created in TCCT can frequently lead to activation of immune cells such as mast cells, neutrophils and macrophages, causing them to release proinflammatory cytokines into the wound (Amin, 2012). The cytokines released often include growth factors such as TGF-β, tumour necrosis factor alpha (TNF-α) and VEGF (Schlunck *et al*., 2016; Cunliffe *et al.*, 1995), which increase the proliferation and activity of TCCT fibroblasts. TGF-β is a secreted protein involved in the activation of several cellular responses such as cell growth, proliferation, differentiation and apoptosis (Massagué, 2000). TNF-α, secreted by macrophages and monocytes, is also involved in the activation of cellular responses such as necrosis and apoptosis (Idriss and Naismith, 2000). Furthermore, VEGF activates inflammatory responses such as vasculogenesis and angiogenesis. Each of these cytokines trigger signalling cascades in cells, which activate the transcription of key genes, such as those that function in proliferation. Each subtype then binds to specific receptors which activate the cellular responses (Shibuya, 2011).

As previously described, activation of fibroblasts by cytokines and growth factors subsequently modulates the formation of collagen. In TCCT, this can lead to an excessive accumulation of ECM and scar tissue, causing the surgically created opening to heal up again and become blocked. Furthermore, it is thought that an increase in fibroblast activity may be further influenced by the flow of aqueous humour across TCCT after glaucoma surgery. Aqueous humour itself has also previously found to contain growth factors such as TGF-β, TNF-α and VEGF (Jampel *et al.*, 1990; Huang *et al*., 2015).

1.3.4 The role of shear stress

The continuous drainage of aqueous fluid via the newly created drainage pathway after glaucoma surgery may also exert shear stress to the TCCT wound, further promoting fibrotic response. Shear stress is a frictional force that is caused by the motion of fluid across a surface. This can subsequently trigger mechanotransduction, where cells convert a mechanical stimulus into electrochemical activity. A few molecular mechanisms have been proposed to explain mechanotransduction previously. The stretching/movement is believed to stimulate several intracellular signalling pathways (Iskratsch *et al*., 2014) and has previously been found to stimulate the overexpression of cytokines such as TGF-β (Dan *et al*., 2010).

As shown in Figure 1.7, many biological constituents have been reported to act as cellular mechanosensors in previous research. Strain caused by shear stress can lead to changes in the intracellular cytoskeleton and stretch open ion channels in cell membrane, causing an influx of ions such as calcium. Calcium signalling is an ubiquitous secondary messenger regulating several cellular activities and can therefore promote processes such as secretion, proliferation, migration and neurotransmission (Ando and Yamamoto, 2013; Turczyńska *et*

al., 2013). Additionally, stretching/movement of cell-cell receptors and ECM-cell focal adhesions (e.g. integrin) can stimulate changes in the cellular environment, triggered by shear stress stain. Furthermore, it is thought that deformations of chromatin in cell nuclei may alter transcription processes and subsequently change gene and protein expression profiles as a consequence of shear stress (Jaalouk and Lammerding, 2009).

Figure 1.7 Pathways of shear stress induced mechanotransduction on cells

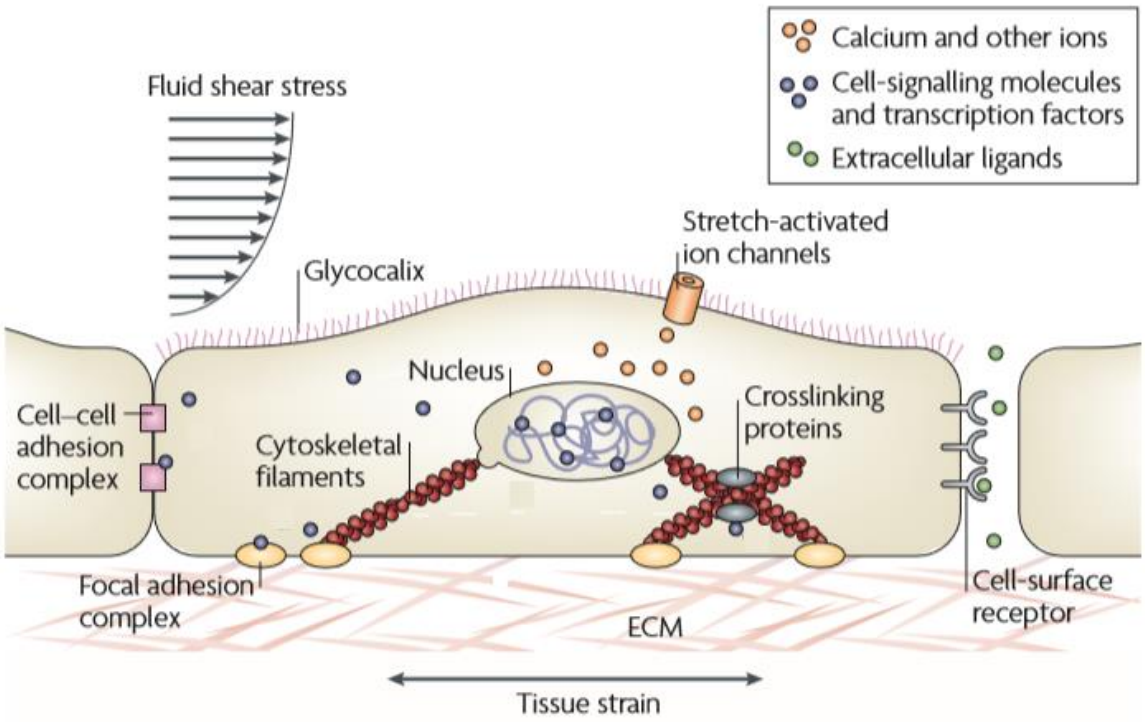

Shear stress induced mechanotransduction. Source: Jaalouk and Lammerding, (2009)

Shear stress force of approximately 0.05 – 25 dye/cm^2 has previously been found to initiate mechanotransduction in fibroblasts (Dan *et al*., 2010; Song *et al.*, 2013). Therefore, due to the apparent influence of shear stress on cellular processes, it could be hypothesised that glaucoma surgery failure is largely due to shear stress stimulation of fibrosis, in addition to growth factors and cytokines. However, more research is required to know the quantitative influence of shear stress on TCCT and how aqueous humour fluid flow may stimulate scar tissue formation.

1.3.5 The role of proteoglycans

As mentioned previously, it can be assumed that chondroitin sulphate/dermatan sulphate GAG chains in TCCT are attached to the proteoglycans decorin and biglycan. Decorin is a proteoglycan found in the extracellular matrix of various tissues, known to interact with several proteins involved with matrix assembly, cell adhesion, migration and proliferation (Chen and Birk, 2012). It is a small, interstitial proteoglycan named after its association with collagen fibrils and the idea that it 'decorates' the fibrils. Decorin is known to regulate collagen fibril formation by binding the d and e_1 bands of fibrils, with its attached GAG chains extending into the interfibrillar space (Orgel *et al.*, 2009). It is therefore known to aid wound healing and certain studies have found decorin deficient mice to exhibit slower wound healing and fragile skin (Jarvelainen *et al.*, 2006). Biglycan is another closely associated proteoglycan which competes for the same fibril binding region as decorin, but with decorin having the higher affinity. Interestingly decorin deficient mice have also been found to present an increase in biglycan expression, suggesting a functional compensation (Zhang *et al.*, 2009).

Decorin and biglycan are also known for their non-structural functions and ability to bind to growth factors such as TGF-β, to either sequester them or present them to cellular receptors (Chen and Birk, 2012). The application of decorin has previously been found to reduce conjunctival fibrosis *in vivo* following glaucoma surgery (Grisanti *et al.*, 2005). Biglycan however, is not reported to reduce fibrotic responses. One study suggests that this may be explained by the tissue localisation of proteoglycans. As decorin is known to bind to collagen it can be assumed that it probably binds sequestered TGF-β to the collagen, preventing its interaction with cellular receptors. However, biglycan is known to be located in the pericellular space/cell surface and may therefore bind with TGFβ but still allow its interaction with cell receptors (Kolb *et al.*, 2001). Consequently, perhaps only in the

absence of decorin would biglycan function as an anti-fibrotic. Decorin therefore has multiple functions both as a structural molecule and matrikine. It can bind to cytokines and either sequester them or present them to cellular receptors. These factors are likely to contribute to tissue function, however the mechanisms underlying these differences remain to be discovered. As decorin is naturally present in cells, it may have the potential to be applied as an anti-fibrotic agent after glaucoma surgery (Grisanti *et al.*, 2005) .

1.3.6 Currently used anti-metabolic drugs

Current anti-metabolic drugs used in an attempt to reduce the fibrotic response after glaucoma filtration surgery include Mitomycin C and 5-Fluorouracil. These reduce the proliferative ability of fibroblasts in the TCCT via disruption of deoxyribonucleic acid (DNA) synthesis (Tomasz, 1995). However, the mechanism is highly toxic and can lead to further complications such as sub-conjunctival bleb thinning and leakage, cytotoxicity and destruction of other tissues (e.g. cornea) (Wolner *et al.*, 1991; Stamper *et al*., 1992). A better understanding of the fibrotic mechanisms in TCCT after glaucoma surgery would aid in the development of safer and more efficient anti-inflammatory agents.

1.3.7 Xen Gel Stent glaucoma medical device

In an effort to overcome some of the problems associated with trabeculectomy, minimally invasive glaucoma surgery (MIGS) has become a popular alternative treatment option in recent years. MIGS typically involves the use of a glaucoma medical device, such as the Xen Gel Stent manufactured by Allergan. As shown in Figure 1.7, the Xen Gel Stent is inserted into the anterior chamber and subconjunctival space to create an alternative diffuse outflow pathway for aqueous humour. Similar to the trabeculectomy procedure, a subconjunctival bleb remains which is then monitored over time (Allergan, 2017).

Figure 1.8 Xen Gel Stent glaucoma medical device insertion procedure

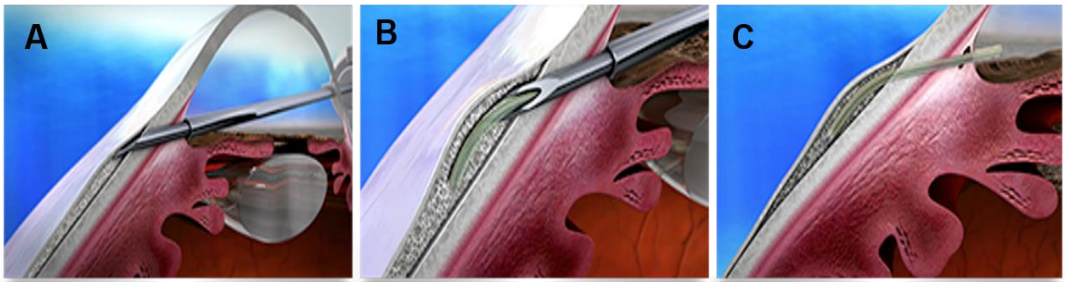

Schematic diagram of the initial incision made using a Xen Injector (A), followed by insertion of the Xen Gel Stent device (B, C) during MIGS. Source: Allergan, (2017).

Manufactured by Allergan, the Xen Gel Stent is a made from gelatin cross-linked with glutaraldehyde, which is claimed to reduce the chance of inflammation and fibrotic response. When hydrated the stent is described to be soft and tissue conforming, making it possible to manipulate the stent into the desired position. However, recent case studies which highlight problems with the Xen Gel Stent raise scepticism regarding its use. These include cases of post-operative stent exposure (Fea *et al.*, 2015), blood clot formation inside the stent lumen (Ferreira *et al*., 2017) and bleb hypertrophy (Fernández-García *et al*., 2015).

1.3.8 Development of conjunctival membrane models

In vivo and *in vitro* models of conjunctiva are advantageous for drug treatment assessment and the study of the wound healing mechanisms after glaucoma surgery. Previously, animal models have been used to study conditions such as conjunctivitis (Groneberg *et al.*, 2003), as well as fluid outflow after glaucoma surgery (Nguyen *et al.*, 2012). However, *ex vivo* and *in vitro* tissue models are preferable in comparison to live animals studies, as the practice is more ethical and the tissue environment can be better controlled and manipulated (Saeidnia *et al*., 2015). One notable *ex vivo* model of conjunctiva includes Tovell *et al.*, (2011), who cultured segments of porcine and rabbit conjunctiva for the study

of conjunctival contraction during tissue scarring. Alongside *ex vivo* modelling, *in vitro* conjunctival membrane models offer the ability to more accurately quantify several experimental parameters (e.g. cell number). To mimic native soft tissue structures such as conjunctiva *in vitro*, scaffolds using hydrogels and fibrous materials are common (Pei *et al.*, 2017). Polymers containing natural ECM components provide particularly enhanced biocompatibility to hydrogels, providing mechanical integrity to tissues, as well as enhanced support and regulation for cellular processes. Whilst synthetic polymers can aim to mimic natural ECM components, naturally occurring polymers such as collagen are thought to provide cells with a more physiologically relevant substrate on which to reside. As the fibrous protein content of native conjunctiva is primarily collagen, collagen hydrogel based scaffolds with seeded conjunctival cells have previously been used for *in vitro* conjunctival membrane modelling (Niiya *et al.*, 1997).

Co-culture *in vitro* model designs have also been popular in more recent conjunctival membrane models, since co-culture modelling methods offer a more realistic mimic of multicellular native tissue structures in comparison to mono cultures. Examples include a model developed by Garcia-Posadas *et al.*, (2017) consisting of conjunctival fibroblasts seeded within a fibrin based scaffold, with epithelial cells seeded on top. Yao *et al.*, (2017) also recently developed a co-culture model consisting of a collagen and poly (L-lactic acid co-ε-caprolactone) derived porous nanofibrous scaffold, seeded with conjunctival epithelial cells to stimulate stratification. Furthermore, a recent ocular surface and tear film model developed by Lu *et al.*, (2017) used a co-culture of rabbit conjunctival epithelium and lacrimal gland cell spheroids, to mimic aqueous and mucin tear film layers within an optimised air-liquid interface. These models have the benefit of including conjunctival epithelium on top of the fibrous layer. It is the cell-cell communication between conjunctival epithelial cells and fibroblasts that allows cells to polarise and help to regulate

fibroblast proliferation and differentiation. Furthermore, both conjunctival fibroblasts and epithelium are thought to be active participants in conjunctival fibrosis, making both cell types valuable in conjunctival membrane modelling (Cavet *et al.*, 2013). According to Izumi *et al.*, (2005), a healthy epithelial cell layer typically protects and suppresses any abnormal proliferation and differentiation of fibroblasts via regulation of TGF-β and basic fibroblast growth factor (bFGF) signalling. However, when epithelium becomes wounded it is thought to release various growth factors triggering events such as fibroblast proliferation, migration and differentiation into myofibroblasts (Kunihiko *et al.*, 2002; He *et al.*, 2017; Richardson, 2017), further promoting fibrotic response.

Previously developed conjunctival membrane models have been beneficial in understanding the influence of growth factors on conjunctival fibroblasts and fibrosis. However, the quantifiable influence of shear stress on conjunctival fibrosis after glaucoma surgery remains unclear. Whilst the influences of shear stress on other fibroblasts have been studied *in vitro,* for example Ng *et al*., (2005) who assessed the influence of shear stress on human dermal fibroblasts, few studies have specifically explored the influence of shear stress on *in vitro* conjunctival fibroblasts. Therefore, development of an *in vitro* model for the investigation of shear stress triggered by aqueous fluid flow on TCCT, both individually and synergistically with growth factors, would be very beneficial.

1.4 Diseases of the retina

1.4.1 Macular degeneration

Age-related macular degeneration (AMD) is characterised by the degeneration of RPE and photoreceptor cells. According to the World Health Organisation, it is ranked the third leading cause of world blindness, after cataract and glaucoma. Furthermore, it is estimated

to affect approximately 1 in 3 people by the age of 75 (WHO, 2019). Generally, there are two considered types of AMD. Both types initially cause damage to central vision, which progresses outwards towards the peripheral vision over time. Dry AMD, the most common type, is caused by a breakdown and thinning of RPE in the macular region of the retina, leading to degenerative lesions and subsequent photoreceptor damage. Wet AMD, the less common type, is instead caused by the growth of unnecessary new blood vessels underneath the macular region of the retina, also leading to RPE and photoreceptor damage (Stone, 2007).

Macular degeneration can be treated to an extent by intravitreal injections containing ocular drug treatments to target the retina. These can be effective in preserving some level of vision. However, the injections are invasive, require repeated treatments and can lead to significant adverse events such as endophthalmitis, a potentially blinding infection (Falavarjani and Nguyen, 2013). Furthermore, these treatments do not function to regenerate already damaged retinal tissue and cannot restore vision once lost.

1.4.2 Retinitis pigmentosa

Retinitis pigmentosa is an autosomal dominant hereditary condition of vision loss. According to the World Health Organisation, approximately 1 in 4000 blind people inherit blindness due to retinitis pigmentosa (WHO, 2019). Due to a mutation of the rhodopsin gene, the condition is characterised by degeneration of the rod photoreceptors, later followed by cone photoreceptors. This causes an initial loss peripheral vision, which gradually progresses towards the central vision over time. Unfortunately, there are currently no commercially available treatments for retinitis pigmentosa (Hartong *et al*, 2006).

1.5 Regenerative therapies for retinal repair

In an effort to repair retinal tissue damage caused by diseases such as glaucoma, macular degeneration and retinitis pigmentosa, regenerative therapies could be a possibility in the future. Research into stem cell based treatments has advanced significantly over recent years with promising results. Potential future treatments for the retina could include endogenous repair processes, cell replacement therapies and other retinal tissue engineering approaches with the use of biomaterials.

1.5.1 Cell replacement therapies

A widely considered approach to improve the treatment of retinal disease is the possibility of retinal repair using cell replacement therapies. Therapies include embryonic stem cells (ESCs), induced pluripotent stem cells (iPSCs), mesenchymal stem cells, adipose stem cells (ASCs) and retinal progenitor cells (RPCs), as well as RPE replacement. Many groups have successfully transplanted these cells into animal models and some therapies are even commencing into Phase I/II clinical trials.

1.5.1.1 Embryonic stem cells

ESCs are capable of self-renewal indefinitely when provided with the correct culture conditions, whilst still maintaining pluripotency (Pera *et al*., 2000). Various research groups have found the potential to guide ESCs toward lineages such as RPE cells and photoreceptors (Klassen *et al.*, 2004; da Cruz *et al.*, 2018; Lu *et al*., 2018; Mehat *et al.*, 2018), as well as ganglion cells (Teotia *et al*., 2015; Gill *et al.*, 2016), for transplantation into the retina. Some research groups have even found transplanted ESC derived photoreceptors to restore some level of visual function in *Crx*-deficient mice (Lamba *et al*., 2009). However, challenges with ESC derived cell transplantation include the ability to obtain stable cell sources that integrate safely into the diseased retina. There is concern that

the plasticity of ESCs may be a problem, raising the risk of inappropriate progeny such as tumours (Stern *et al*., 2010). A second challenge is the ability to develop a realistic up-scaling strategy in order to generate the large number of cells required for transplantation into patients (Reynolds and Lamba, 2014). A third hurdle is the possibility of immune rejection. The extensive remodelling that occurs following retinal degeneration can result in upregulation of inflammatory proteins and alteration of the blood-retinal barrier, which is likely to increase the chance of immune rejection. Therefore, a better understanding of the immune status of a degenerated retinal environment is required (Bongso *et al*., 2008). A fourth major hurdle for the transplantation of stem cell derived retinal cells, such as photoreceptors and ganglion cells, is that very few cells manage to integrate successfully into the retina (Venugopalan *et al*., 2016). This has also been found for photoreceptors and ganglion cells derived from other types of stem cell.

1.5.1.2 Induced pluripotent stem cells

iPSCs are derived from reprogrammed peripheral cells (e.g. fibroblasts and lymphoblasts) into a pluripotent state. These cells can be directly generated from adult cells and therefore carry less ethical concerns than ESCs (Robinton and Daley, 2012). Most cell types in the retina (including RPE and photoreceptors) have been differentiated successfully from iPSCs (Wright *et al*., 2014). Retinal cells derived from patient-specific iPSCs could be used for autologous transplantation, which has a reduced risk of immune rejection as it uses the patient's own cells. However, personalised cell therapy is time-consuming and expensive; furthermore, iPSCs may require gene correction before transplantation. Human leukocyte antigen (HLA) matched allogeneic iPSCs, may also provide an alternative cell therapy in certain cases (Riolobos *et al*., 2013). Although ongoing clinical trials appear promising, previous trials such as an age-related macular degeneration treatment developed by the Masayo Takahashi group in Japan recently had to be halted due to a risk of tumour

development (The Niche, 2015). Therefore, iPSC safety as a cell therapy is unknown until current and ongoing clinical trials have ran successfully and released their results.

1.5.1.3 Mesenchymal stem cells

Mesenchymal stem cells are multipotent stem cells derived from mesenchymal tissues such as bone marrow, adipose tissue, umbilical cord and placenta (Caplan, 1991). Mesenchymal stem cells have been found to differentiate into photoreceptor-like cells, as well as ganglion-like cells, making cell replacement therapy a future possibility using these cells. Mesenchymal stem cells have also been found to provide neuroprotection for degenerating retinal cells via expression of a variety of neurotrophins which are beneficial for retinal cell survival (Xu and Xu, 2011). Whilst retinal cell replacement therapy using mesenchymal stem cells remains problematic at the present time, some studies using mesenchymal stem cells for their neuroprotective mechanism are promising. For example, one study which involved the injection mesenchymal stem cells intravitreally into a mouse model of acute retinal injury, found that transplanted cells survived for at least 3 months and significantly protected damaged retinal cells long term (Machalińska *et al*., 2013).

1.5.1.4 Adipose stem cells

ASCs are mesenchymal stem cells which, like other stem cells, have the capacity to differentiate into multiple cell types. However, these cells are derived from the more easily accessible adipose tissue, rather than bone marrow (Gir *et al*., 2012). The administration of ASCs into animal models of retinal degeneration is currently being investigated for the potential treatment of diseases such as diabetic retinopathy (Yang *et al*., 2010), glaucoma (Vayl *et al*., 2014) and macular degeneration (Lee *et al*., 2015). As autologous transplantation is also possible with ASCs, the risk of immune rejection is reduced. A transplantation study involving injection of human ASCs into a rat vitreous cavity found

that cells survived and integrated with the eye relatively successfully. However, there was concern that some cells appeared to migrate across the blood-retina barrier and towards non-targeted regions, which could be considered a risk for transplantation to patients (Haddad-Mashadrizeh *et al*., 2013). Therefore, more experiments to fully understand ASC cell mechanisms during transplantation will be required before an optimised treatment can be developed.

1.5.1.5 Retinal progenitor cells

RPCs are typically more predisposed towards a cell fate in comparison to stem cells because they are obtained from donated foetal tissue, rather than embryonic tissue (Schmitt *et al*., 2009). Some groups have successfully transplanted this cell type into animal models of retinal degeneration (Klassen *et al.*, 2004) and some have even shown evidence of improved visual acuity in rats, due to photoreceptor preservation via transplanted RPCs (Luo *et al*., 2014). Companies such as 'ReNeuron' are currently commencing this therapy into Phase I/II clinical trials as a potential treatment for patients with retinitis pigmentosa (ReNeuron, 2016; RNS, 2016). If RPCs can be successfully transplanted into patients, one of the most likely challenges for this treatment will be whether cells are able to integrate into the complex human retinal circuitry. Subsequently, if evidence for photoreceptor preservation is observed, the ultimate challenge will then be whether the photoreceptors can function well enough to improve visual acuity. Furthermore, like ESCs donor tissue is used to obtain RPCs, meaning there could be a chance of immune rejection.

1.5.1.6 RPE transplantation

Another possible cell replacement therapy is replacement of the RPE. The ability to generate large amounts of functional RPE from ESCs and iPSCs makes this cell type an ideal candidate for transplantation (Kokkinaki *et al*., 2011). However, RPE transplantation

in suspension and RPE/choroid patch translocation has previously faced several challenges. Allogeneic RPE transplants have shown eventual rejection and/or a lack of functional recovery, plus autologous RPE transplants have also shown problems (Kohen *et al.*, 1997). The aging process and degenerative disease causes the RPE to accumulate lipofuscin, which diminishes cellular structures and causes a slowing of metabolic capacity. The Bruch's membrane also accumulates debris, making nutrient transport less efficient and the survival/function of transplanted RPE challenging on such an altered substrate (Binder *et al*., 2007). The future potential of each cell therapy will be unknown until current clinical study results are reported. One notable clinical study was undertaken in 2012, where ESC derived RPE was transplanted into patients with Stargardt's macular dystrophy and Macular degeneration. Results found transplanted RPE to have no apparent rejection after 4 months. Therefore, with further development this therapy could overcome the challenge of immune rejection and potentially be used for photoreceptor and central visual rescue (Schwartz *et al*., 2012).

1.5.2 Retinal tissue engineering approaches

Whilst cell replacement therapies appear promising, low cell survival and limited integration remain major challenges for this method of retinal repair. Furthermore it can be difficult to retain injected cells at specifically targeted regions of the retina, such as underneath the fovea (Kador and Goldberg, 2013). Current tissue engineering approaches attempt to overcome these hurdles by supporting cell survival, delivery and integration. These include the development of 2D or 3D biomaterial scaffolds, as well as development of improved retinal disease models for the testing of neuroregenerative materials.

1.5.2.1 Scaffolds for retinal progenitor cell grafting

Many biomaterial scaffolds are currently in development for the grafting of RPCs. For example, Neeley *et al*., (2008) developed a microfabricated thin, porous poly(glycerol-sebacate) scaffold for RPC grafting. The reported scaffold possesses improved mechanical properties which are a better replica to those of the native retina in comparison to other scaffolds. Results indicate that RPCs adhered strongly to this scaffold and expressed a combination of immature and mature cell markers, suggesting a tendency towards cell differentiation (Neeley *et al*., 2008). In continuation of this work, the same research group has since transplanted the RPC grafted scaffold into mice. Transplantation proved relatively successful with long term RPC survival and expression of mature markers in the retinal tissue (Redenti *et al.*, 2009). More recently, Yao *et al*., (2015) developed a biodegradable, thin-film polycaprolactone scaffold. Results indicate that the nano-topographies of the scaffold can interact with RPCs and have the potential to direct these cells towards photoreceptor cell fate before transplantation. The therefore scaffold provides an improved biodegradable platform to guide RPC differentiation and allowed for better organisation and delivery of RPCs to retinal tissue (Yao *et al*., 2015). Although polycaprolactone is known to have improved biodegradability and good ability to drive hRPC differentiation into photoreceptors, poor adhesive qualities limit its use. Therefore, another research group has made a surface modification to a polycaprolactone scaffold by incorporating vitronectin-mimicking oligopeptide, forming a hybrid. Results showed improved cell adhesion of human RPCs and, despite no evidence of functional rescue, the RPCs showed improved migration, integration and survival when transplanted into a degenerated mouse retina on the hybrid scaffold (Lawley *et al*., 2015).

1.5.2.2 Scaffolds for RPE transplantation

Many biomaterial scaffolds are also in development for the improvement of RPE transplantation. For example, Liu *et al*., (2014) developed a supporting scaffold on which RPE would be pre-cultured and supported to mature into a functional monolayer. The scaffold was tested *in vitro* using human foetal RPE cells and transplanted sub-retinally into rabbits. Results found that RPE culture was enhanced with the scaffold and showed improved sub-retinal biocompatibility with scaffolds of 200nm fibre topography. Therefore, the use of biomaterial scaffolds can be considered a future direction for improving cell-based therapies to treat retinal disease (Liu *et al*., 2014). However, challenges continue to remain in ensuring that scaffolds do not cause further damage to the retina, whilst still allowing for sufficient interaction between the retina and other cell layers. Therefore, the surface topography, thickness, mechanical properties and degradation characteristics must be considered in scaffold design to ensure that they are suitable and beneficial for the treatment of ocular disease.

1.5.2.3 Biomaterials for potential retinal ganglion cell repair

At the moment, few biomaterial scaffolds have been developed for the treatment of RGC degenerative diseases such as glaucoma and optic nerve stroke. In diseases such as glaucoma RGCs are permanently damaged, leading to cell death and interruption of retinal signalling to the brain (Sernagor *et al.*, 2001). Due to their highly delicate and disparate axonal projection patterns, RGC replacement therapy for diseases such as glaucoma is highly challenging. Many more experiments to fully understand the complex *in vivo* circuitry and how replacement cells could integrate are required before a potential RGC replacement therapy can be developed (Harvey *et al*., 2006). Over the next few years however, we may see the development of biomaterial scaffolds and peripheral nerve bridges which attempt to repair injured endogenous ganglion cell axons, rather than replace

them. Research into smart biodegradable implants aiding axonal regeneration following spinal cord injury has already been reported, which aim to stimulate repair by 'bridging the gap' between damaged axon sites. This approach has the potential to be used in the visual system and appears to be more promising than RGC replacement therapy at the present stage (Joosten, 2012).

1.5.3 Development of *in vitro* and *ex vivo* retinal tissue models

One strategy for improving the therapeutic potential of cell replacement therapies is with the development of improved *in vitro* and *ex vivo* retinal tissue models, for the testing of neuroregenerative materials such as cell replacement therapies or drug intervention. Typically, retinal cell culture models only allow testing on single cell types. Therefore, although the technique is more challenging, multicellular retinal tissue models with preserved cellular interactions are preferable, since most retinal diseases often affect more than one retinal cell type.

Organotypic slice cultures allow *in vitro* growth of complex biological tissues, whilst still replicating a significant amount of normal physiology and function (Gähwiler *et al.*, 1997). Whereas acute slice preparations are often obtained from adult animals and used for experimentation on the same day that they are prepared, organotypic slice cultures can be preserved *in vitro* for several days or weeks (Wray, 1992). Most organotypic slice cultures typically require a stable substrate, suitable culture medium, sufficient oxygenation and incubation at an appropriate temperature for the tissue (usually 37°C) (Wray, 1992). Due to the high energy demands of photoreceptors, mammalian retinal tissue is particularly difficult to culture *in vitro*. Previously developed organotypic retinal tissue culture systems include Johnson & Martin, (2008) who cultured adult rat retinal explants. Although the retinal explants were viable for 17 days, there were some aspects of their methodology

which could be optimised further. For example, the retina was peeled away from the adjacent tissue using a paintbrush, which is likely to have disrupted layers of the retinal tissue and caused disorganisation (Johnson and Martin, 2008). Another study which cultured postnatal rat retina was Viktorov *et al.*, (2004), who maintained the retinal tissue using roller-tube culturing. The roller-tube culture technique is advantageous in that it maintains many organotypic features and thins the tissue substantially, allowing visualisation of individual cells throughout the cultured tissue. However, though some structure of the retinal tissue was preserved using this technique, it was mainly only the ganglion cell layer and the model therefore did not preserve all physiological layers of the retinal tissue (Viktorov *et al*. 2004).

As the neuronal structure of porcine retina is similar to that of the human retina (Guduric-Fuchs *et al.*, 2009), there have been several previous studies exploring organotypic slice culture of the porcine retina, such as Kobuch *et al*., (2008). This study showed perfusion culture of retinal tissue to be advantageous; however, most retinal tissue showed degradation after just 4 days and only the RPE could be maintained for 10 days (Kobuch *et al*., 2008). Another notable organotypic culture system using adult porcine retinal explants was developed by Wang *et al*., (2011), who were able to maintain full-thickness porcine retinal explants for at least seven days. One major advantage of their methodology is that the photoreceptor layer faces upwards, allowing an increased oxygen supply to photoreceptors and therefore overcoming some of the difficulties associated with culturing retinal tissue *in vitro*. However, some aspects of their methodology could be optimised further. As retinal tissue cultured *in vitro* is often in absence of the choroid, there are additional requirements for the selected substrate to compensate for this. Furthermore, the *in vivo* retina makes contact with the vitreous humour which, as described previously, is a gel-like mass consisting almost entirely of water. In the study undertaken by Wang *et al*.,

(2011), retinal explants were cultured on filter paper, which is arguably a basic substrate for such a complex and fragile composition of tissue.

The National Centre for the Replacement Refinement & Reduction of animals in research (NC3Rs) calls for improved *in vitro* retinal models, highlighting the current lack of human relevant, complex 3D *in vitro* retinal models. In their 'Crack IT Challenge 23: Retinal 3D' they suggest that a model which preserves the morphological resemblance of the retina's layered structure would be beneficial, with an amenity to undertake multiple tests in parallel. Furthermore, they suggest it would be beneficial for retinal models to be reproducible, easily transferable, express specific mature cell markers and have basic functional characterisation. Additionally, they suggest that models in development should avoid having a complex and time consuming set up, materials known to have strong compound absorption and a requirement for specific legal work (NC3Rs, 2016). It can be anticipated that the development of improved *in vitro* retinal tissue models over time will advance ocular disease study and treatment significantly.

1.6 Aims of the PhD project

Due to the ongoing challenges associated with ocular disease treatment, both clinical research and the field of regenerative medicine require the development and application of reliable conjunctival and retinal tissue models, for investigation of ocular disease mechanisms and testing of new treatments. Therefore, the aims of this PhD project were:

- To develop and utilise two dimensional (2D) and 3D TCCT models for the investigation of factors influencing fibrotic response after glaucoma surgery.

- To utilise the established 2D and 3D TCCT fibrosis models for evaluation of glaucoma treatment efficacy and medical device assessment.

- To develop an improved, efficient and reproducible 3D *in vitro* organotypic retinal tissue model, which better preserves all physiological layers of the retina with minimal disorganisation.

- To extend the improved organotypic retinal tissue model into an injury model, in order to assess techniques for retinal tissue lesioning and delivery of cell therapies to the retinal injury site.

- To establish reliable and convenient non-destructive imaging techniques to assess the cellular response towards treatment and associated mechanisms.

Chapter 2

Materials and Methods

2.1 Materials

Table 1 List of materials, catalogue numbers and suppliers

Name	Catalogue number	Supplier
Acetic acid	A6283	Sigma-Aldrich, UK
Adenine, suitable for cell culture	A2786	Sigma-Aldrich, UK
AlamarBlue® assay	BUF012	Bio-Rad, US
Alizarin Red S	A5533	Sigma-Aldrich, UK
Alpha Minimum Essential Medium (MEM) Eagle without L-Glutamine	LZBE12-169F	Lonza, UK
Ascorbic acid	A0278	Sigma-Aldrich, UK
Beta glycerophosphate	G9422	Sigma-Aldrich, UK
Biopsy punches (8 mm)	SCH-33-37	Medisave, UK
Bovine serum albumin (BSA)	A2153-50G	Sigma-Aldrich, UK
B-27 supplement (50x)	A3582801	Thermofisher Scientific, UK
Cell strainers (40 µM)	Z742102	Sigma-Aldrich, UK
CFSE cell labelling dye	ab113853	Abcam, UK
Click-IT Alexa Fluor 594 DIBO Alkyne	C10407	Thermofisher Scientific, UK
Collagen Type I, rat tail	11563550	Fisher Scientific, UK
Collagenase I	C9891	Sigma-Aldrich, UK
0.4 µM culture inserts (12 well plate)	665641	Greiner Bio-One, Austria
Cytokeratin-3 goat polyclonal IgG	SC-49179	Santa Cruz Biotechnology, US
Dexamethasone	D4902	Sigma-Aldrich, UK
Decorin proteoglycan	D8428	Sigma-Aldrich, UK
4',6-Diamidino-2-Phenylindole,	D1306	Thermofisher Scientific, UK

Dihydrochloride (DAPI)		
Dimethyl sulfoxide (DMSO)	D2650	Sigma-Aldrich, UK
Dispase II	D4693	Sigma-Aldrich, UK
Donkey anti-goat IgG FITC	SC-2024	Santa Cruz Biotechnology, US
DPX mounting medium	15538321	Fisher Scientific, UK
Dulbecco's Modified Eagle's Medium: F12 (DMEM:F12)	BE04-687Q	Lonza, UK
DMEM powder	521000	Thermofisher Scientific, UK
DMEM with 1g/L glucose	LZBE12-707F	Lonza, UK
DMEM with 4.5g/L glucose	LZBE12-614F	Lonza, UK
Eosin solution	10562614	Thermofisher Scientific, UK
Epidermal growth factor (EGF)	PHG0311	Thermofisher Scientific, UK
Epidermal keratinocyte medium	CnT-07	CELLnTEC, Switzerland
Fluo-4 AM, cell permeant	F14201	Thermofisher Scientific, UK
Foetal bovine serum (FBS)	DE14-801F	Lonza, UK
Gentamicin	G1397	Sigma-Aldrich, UK
Goat anti-mouse IgG TRITC	T5393	Sigma-Aldrich, UK
Haematoxylin solution	12637926	Thermofisher Scientific, UK
Histo-Clear tissue clearing agent	12358637	Fisher Scientific, UK
H-L-Pro(4-N3)-OH*HCl (2S,4S)	HAA2125	Iris Biotech, Germany
Hydrocortisone stock solution	15681235	Fisher Scientific, UK
IL8 mouse monoclonal IgG	ab18672	Abcam, UK
Indomethacin	I7378	Sigma-Aldrich, UK
Insulin	I1507	Sigma-Aldrich, UK
Insulin-Transferrin-Selenium (ITS)	12097549	Fisher Scientific, UK

3-Isobutyl-1-methylxanthine (IBMX)	I5879	Sigma-Aldrich, UK
Isopropanol	12698645	Fisher Scientific, UK
L-Glutamine (LG, 200 mM)	LZBE17-605E	Lonza, UK
Live/Dead viability/cytotoxicity kit	L3224	Thermofisher Scientific, UK
L-Proline	P0380	Sigma-Aldrich, UK
Mouse monoclonal antibody to IL-8	ab18672	Abcam, UK
Mouse/Rat/Porcine/Canine TGF-beta 1 Quantikine ELISA kit	MB100B	R&D Systems, UK
Neurobasal medium	21103049	Thermofisher Scientific, UK
Nifedipine >98% (HPLC) powder	N7634	Sigma-Aldrich, UK
Non-essential amino acids (NEAA)	M7145	Sigma-Aldrich, UK
Oil Red O	O0625	Sigma-Aldrich, UK
Paraffin wax	12617956	Fisher Scientific, UK
Paraformaldehyde	P/0840/53	Fisher Scientific, UK
Penicillin, Streptomycin	BE17-745E	Lonza, UK
Phalloidin-Tetramethylrhodamine B isothiocyanate (Phalloidin TRITC)	P1951	Sigma-Aldrich, UK
Phosphate buffered saline (PBS)	BE17-516F	Lonza, UK
RPE65 mouse monoclonal IgG	SC-390787	Santa Cruz Biotechnology, US
Sodium bicarbonate	S5761	Sigma-Aldrich, UK
Sodium hydroxide	106467	Sigma-Aldrich, UK
SPD304 (TNF-α inhibitor)	S1697	Sigma-Aldrich, UK
Sodium pyruvate	P2256	Sigma-Aldrich, UK
TGF-β1	PHG9204	Thermofisher Scientific, UK
TGF-β3	SRP3171	Sigma-Aldrich, UK

TGF-β RI Kinase Inhibitor VI	616461	Sigma-Aldrich, UK
TNF alpha	PHC3015	Thermofisher Scientific, UK
TNF alpha porcine ELISA kit	KSC3011	Thermofisher Scientific, UK
Toluidine blue	89640	Sigma-Aldrich, UK
Triton X-100	9002-93-1	Sigma-Aldrich, UK
Trypsin/EDTA10X	LZBE02-007E	Lonza, UK
Vascular endothelial growth factor (VEGF)	PHC9394	Thermofisher Scientific, UK
Vimentin goat polyclonal IgG	SC-7557	Santa Cruz Biotechnology, US

2.2 Methods

2.2.1 Cell and tissue culture techniques

All experiments carried out used either porcine Tenon's capsule + conjunctival tissue (TCCT) fibroblasts, porcine conjunctival epithelial cells, porcine aqueous humour, porcine retinal tissue or rat bone marrow mesenchymal stem cells (rMSCs). Tissue, cells and fluid of porcine origin were isolated from adult porcine heads obtained from a local abattoir (A.J Green & Sons, Ravenscliffe House Farm, Ravenscliffe, Stoke-on-Trent, ST6 4QH). Isolation and use of rMSCs was in accordance with the Animals (Scientific Procedures) Act 1986 and the ethical guidelines of Keele University.

2.2.1.1 Porcine eye enucleation

Adult porcine heads were obtained from the abattoir within 3 hours of slaughter and taken into a dissection flow hood upon arrival at the laboratory. Porcine eyes were then enucleated by crude dissection by making incisions into the ocular tissue using a no.20, 4.5cm scalpel blade (Fisher Scientific, UK) and blunt, toothed forceps (Fisher Scientific, UK) to retrieve each eye from its orbit. The porcine eyes were then stored in high glucose Dulbecco's Modified Eagles Medium (DMEM) supplemented with 5% (2.5/50mL) antibiotics (penicillin & streptomycin) and taken into a sterile laminar flow hood in preparation for immediate dissection and tissue isolation.

2.2.1.2 Isolation of primary porcine TCCT fibroblasts

Following porcine eye enucleation, inside a sterile laminar flow hood the Tenon's capsule tissue and bulbar conjunctiva membrane were trimmed back from the sclera (Figure 2.1)

and cut away using micro dissecting scissors (Fisher Scientific, UK) and fine, toothed forceps (Medisave, UK).

Figure 2.1 Tenon's capsule tissue and bulbar conjunctiva membrane isolation

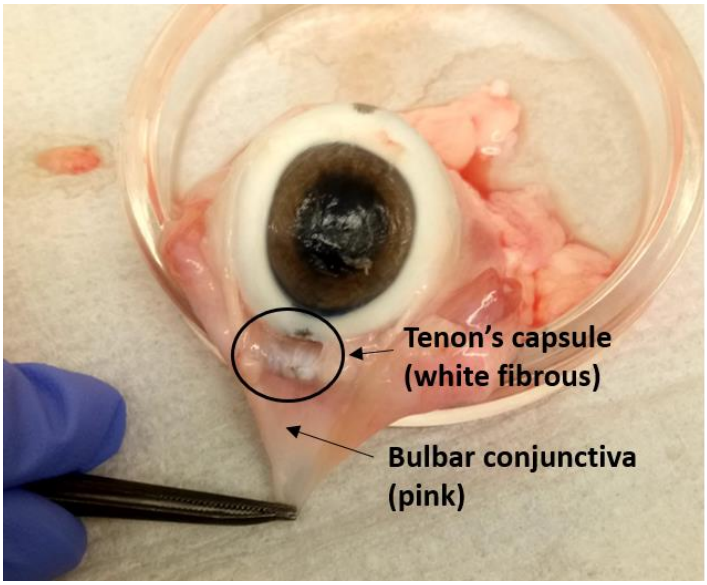

The Tenon's capsule tissue (white fibrous appearance) and bulbar conjunctiva membrane (pink) are trimmed back from the sclera of the porcine eye, before being cut away.

Once isolated from each porcine eye, the TCCT was washed consecutively 3 times in 10x antibiotic solution containing penicillin, streptomycin and gentamicin. The washed tissue was then digested enzymatically by firstly placing the tissue into 3 mg/mL dispase II in PBS and shaking for 1 hour on a 'see saw' motion rocker at 50 rotations per minute (rpm), which was stored in an incubator at 37°C, 5% CO_2 and 95% humidity. After this, the tissue was transferred into 3 mg/mL collagenase I in PBS and shaken for a further 2 hours at 50rpm, stored in an incubator at 37°C, 5% CO_2 and 95% humidity. Following digestion, the resulting solution was passed through a 40 µM cell strainer (Sigma Aldrich, UK) into a falcon tube and centrifuged at 300 x g for 3 minutes. The supernatant was then aspirated and the cell pellet resuspended in 1 mL culture medium. The cells were then counted using a haemocytometer (Counting Chamber; Thomas Scientific, UK) before seeding into flasks.

On average, the TCCT isolated from each porcine eye would provide approximately 2 x 10^4 fibroblasts. The isolated primary TCCT fibroblasts were then cultured in DMEM with 4.5g/L glucose, supplemented with 10% foetal bovine serum (FBS), 1% L-glutamine (LG) and 1% antibiotics (penicillin & streptomycin) at 37°C, 5% CO_2 and 95% humidity.

2.2.1.3 Isolation of primary porcine conjunctival epithelial cells

As described in the previous section, the Tenon's capsule tissue and bulbar conjunctiva membrane was trimmed back from the sclera and cut away using micro dissecting scissors and fine, toothed forceps. The tissue was then placed in a 90 mm petri dish with the orientation maintained to ensure that the conjunctival epithelium remained facing upwards. Fine, toothed forceps and a no. 11, 4cm scalpel blade (Fisher Scientific, UK) were then used to scrape epithelial cells from the conjunctival membrane surface. Once epithelial cells were visible, the scraping residue was mixed with 1 mL PBS and passed through a 40 µm cell strainer into a falcon tube and centrifuged at 300 x g for 3 minutes. The supernatant was then aspirated and the cell pellet was resuspended in 1 mL culture medium and cells counted using a haemocytometer. Cells were then seeded into flasks coated with 10 µg/cm² of type I collagen solution. Three culture medium formulations were tested for the optimised growth of primary porcine conjunctival epithelial cells, as shown in Table 2. Formulations 2 and 3 were adapted from previous literature reporting the culture of epidermal keratinocytes (Simon and Green, 1985). Formulation 2 was selected following its previous efficacy for the growth of corneal epithelial cells in our laboratory. Formulation 3 was selected following its previous efficacy for the growth of lung epithelial cells in our laboratory (unpublished data). Once culture medium had been added, cells were cultured inside an incubator at 37°C and 5% CO_2.

Table 2 Tested culture medium formulations for the optimised growth of primary porcine conjunctival epithelial cells

Formulation 1	Epidermal keratinocyte commercial medium formulation (CELLnTEC, Switzerland)
Formulation 2	1:1 mixture of DMEM and Ham's F12 medium. Prepared by supplementing 44 mL DMEM: F12 (1:1 mixture) with 5 mL FBS, 250 µg Insulin-Transferrin-Selenium (ITS), 20 µg Hydrocortisone, 500 ng Epidermal growth factor (EGF), 1.22 mg Adenine, 500 µL penicillin, streptomycin and 500 µL LG.
Formulation 3	3:1 mixture of DMEM and Ham's F12 medium. Prepared by supplementing 22 mL DMEM (4.5g/L glucose) and 22 mL DMEM: F12 (1:1 mixture) with 5 mL FBS, 250 µg ITS, 20 µg Hydrocortisone, 500 ng EGF, 1.22 mg Adenine, 500 µL penicillin, streptomycin and 500 µL LG.

2.2.1.4 Enzymatic sub-culture with trypsin

All cell types were passaged once they reached approximately 80-90% confluence by firstly discarding the spent culture medium and washing the cells with PBS. Pre-warmed trypsin/EDTA 1X was then added to the flasks/plates (80 µL per cm^2) and incubated at 37°C and 5% CO_2 for 5 minutes. The flasks/plates were then checked using a light microscope for cell detachment. If on occasion cells did not fully detach, a cell scraper (Fisher Scientific, UK) was used to scrape any remaining cells from the flask/plate surface. Once cells had detached, culture medium (160 µL per cm^2) was added to the flasks/plates to inactivate the trypsin. The cell suspension solution was then transferred into a falcon

tube and the tube centrifuged at 300 x g for 3 minutes. The supernatant was then aspirated and the cell pellet resuspended in 1 mL culture medium. The cells were then counted using a haemocytometer before use in experiments. Cells between passage number 1-5 were used in experiments.

2.2.1.5 Isolation of porcine aqueous humour

Following porcine eye enucleation (section 2.2.1.1), inside a sterile laminar flow hood aqueous humour fluid was isolated from each eye by inserting a sterile 23-gauge needle attached to a 1 mL syringe (Medisave, UK) into the anterior chamber at a 90° angle, as shown in Figure 2.3. The fluid was carefully drawn into the syringe and then transferred into an 0.5 mL Eppendorf tube. Approximately 200 µL could be isolated from each eye.

Figure 2.2 Isolation of porcine aqueous humour from the anterior chamber

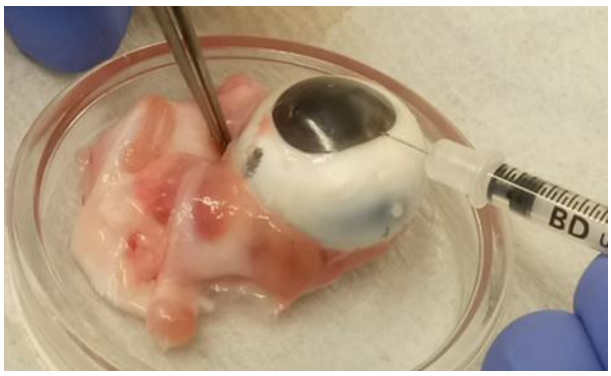

Porcine aqueous humour was isolated from each eye by inserting a 23-gauge needle into the anterior chamber at a 90° angle, before carefully drawing the fluid out.

The fluid was then centrifuged at 200 x g for 1 minute and the supernatant transferred into a new 0.5 mL Eppendorf tube, in order to remove any excess debris/contaminants from the samples. Samples were then stored at -80°C until use in experiments.

2.2.1.6 Collagen hydrogel preparation

In this work, two different types of 3D collagen constructs were prepared; cell seeded collagen hydrogels and acellular compressed collagen gels as substrate for tissue culture. Commercially available rat tail collagen type I was used as the collagen source for both constructs with the same gelation procedure. Sodium hydroxide solution (1M NaOH) was prepared by dissolving 2 g NaOH in 25 mL sterile deionised water (dH_2O). The solution was then filtered inside a laminar flow hood using a syringe and filter (Millipore, USA) to ensure sterility. NaOH neutralises the pH of collagen solution, which is vital for hydrogel formation and cell/tissue viability.

DMEM at 10x concentration was included to provide cells and tissue with a source of nutrients, to promote cell viability. 10x DMEM was prepared by dissolving 10 g DMEM powder into 50 mL dH_2O. The solution was mixed on a magnetic stirrer for several hours until the powder had completely dissolved. 3.7 g sodium bicarbonate was then added to adjust the pH, followed by another 50 mL dH_2O, before being placed back on the magnetic stirrer. Once the solute had fully dissolved, the pH was checked and adjusted if necessary until neutral (approx pH 7). The solution was then filtered inside a laminar flow hood using a syringe and filter to ensure sterility. The volume of reagents required for the collagen solution were calculated as follows, according to manufacturer instructions (ThermoFisher Scientific, 2014):

1. $\text{Volume of 10x DMEM} = \text{Total volume required x } 0.1$
2. $\text{Volume of collagen} = \dfrac{\text{Required concentration}}{\text{Collagen source concentration (on bottle)}} \text{ x Total volume}$
3. $\text{Volume of 1M NaOH} = \text{Volume of collagen x } 0.025$
4. $\text{Volume of } dH_2O = \text{Total volume} - (\text{10x DMEM volume} + \text{collagen volume} + \text{1M NaOH volume} + \text{cell suspension volume if added})$

All ingredients were kept on ice during the mixing procedure to prevent premature gelation. Solution was mixed by pipetting the mixture upwards and downwards, ensuring that no air bubbles were made.

2.2.1.7 Compressed collagen gel formation

To increase collagen concentration in the formed hydrogel, a plastic compression technique has been undertaken, modified from Brown et al., (2005). Following the collagen hydrogel preparation as previously described, 2 x 1 cm^2 filter paper squares were placed inside 2 x 1 x 1 cm metal moulds held inside 9.6 cm^2 petri dishes under sterile conditions (Figure 2.3, A). 2 mL collagen solution was then pipetted into each mould (Figure 2.3, B) and incubated overnight at 37°C and 5% CO_2 to solidify. Once the collagen solution had solidified, each metal mould was flipped out of the petri dish and onto a nylon sheet, with tissue paper underneath. To compress the collagen, a 2 x 1 x 1 cm metal weight (50g) was then quickly placed on top of the collagen hydrogel held inside each mould and left for 5 minutes (Figure 2.3, C). This caused complete compression of the collagen gel onto the filter paper squares placed inside the moulds. After compression, the metal weight was removed and the 2 x compressed collagen gels on filter paper squares held inside each mould were separated using a no. 11, 4cm scalpel blade (Figure 2.3, D).

Figure 2.3 Diagrams of compressed collagen gel formation

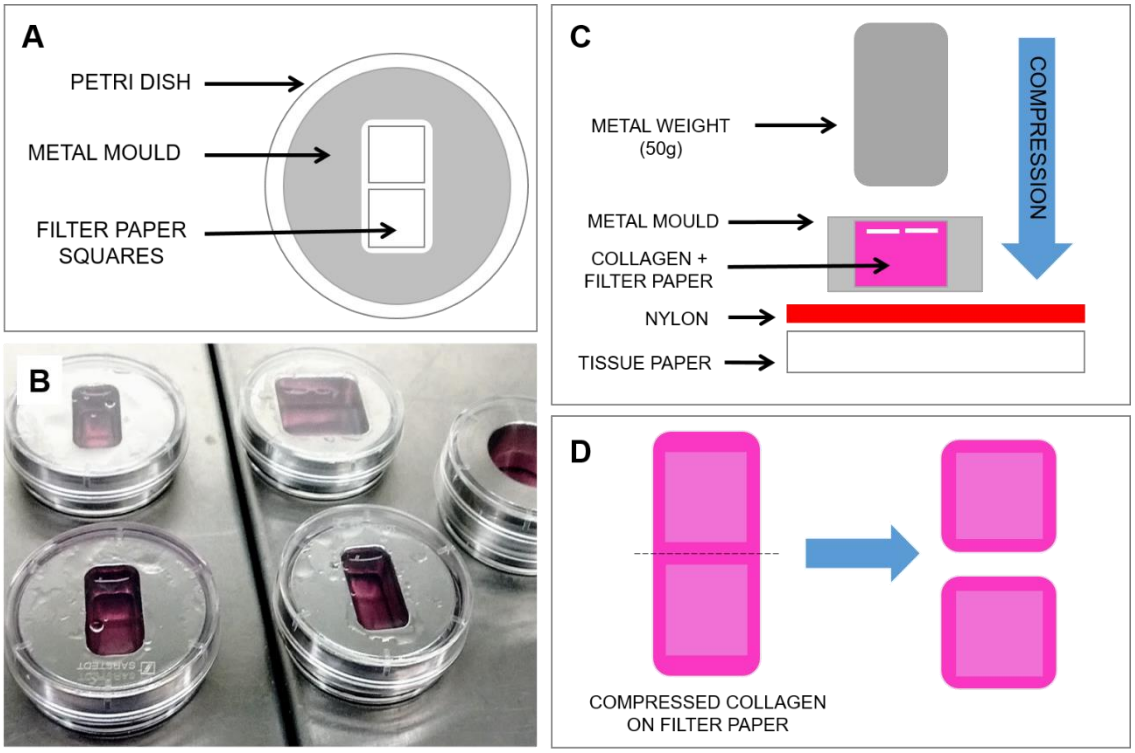

Filter paper squares were placed inside 2 x 1 x 1 cm metal moulds held inside petri dishes (A) and 2 mL collagen solution pipetted into each mould (B). Once solidified, each metal mould was flipped out of the petri dish and onto a nylon sheet, with tissue paper underneath. To compress the collagen, a metal weight (50g) was placed on top of the collagen hydrogel held inside each mould for 5 minutes (C). After compression, the 2 x compressed collagen gels on filter paper squares were separated using a scalpel blade (D).

The compressed collagen gels were then individually stored inside a 48 well plate and covered with 100 µL culture medium until use for retinal tissue culture.

2.2.1.8 Isolation and *in vitro* culture of 3D organotypic retinal tissue explants

Following porcine eye enucleation (section 2.2.1.1), inside a sterile laminar flow hood the extraneous tissue and optic nerve was firstly removed and a small incision made into the side of the eye using a no. 11, 4cm scalpel blade. With the opening created, sharp dissection scissors (Medisave, UK) were used to make a circumferential cut around the eye (Figure 2.4, A). The anterior eye cup and vitreous humour were removed collectively

(Figure 2.4, B), leaving behind the posterior eye cup and fully exposed neural retina (Figure 2.4, C). Circular, full-thickness posterior segments were then punctured and removed (Figure 2.4, D, E) from the eye cup using an 8 mm biopsy punch (Medisave, UK). The retinal tissue was then transferred onto a compressed collagen gel substrate (section 2.2.1.7) and the sclera + choroid peeled away, leaving behind full thickness retina with the photoreceptor and RPE layers facing upwards.

Figure 2.4 Isolation of full thickness 3D organotypic retinal tissue explants

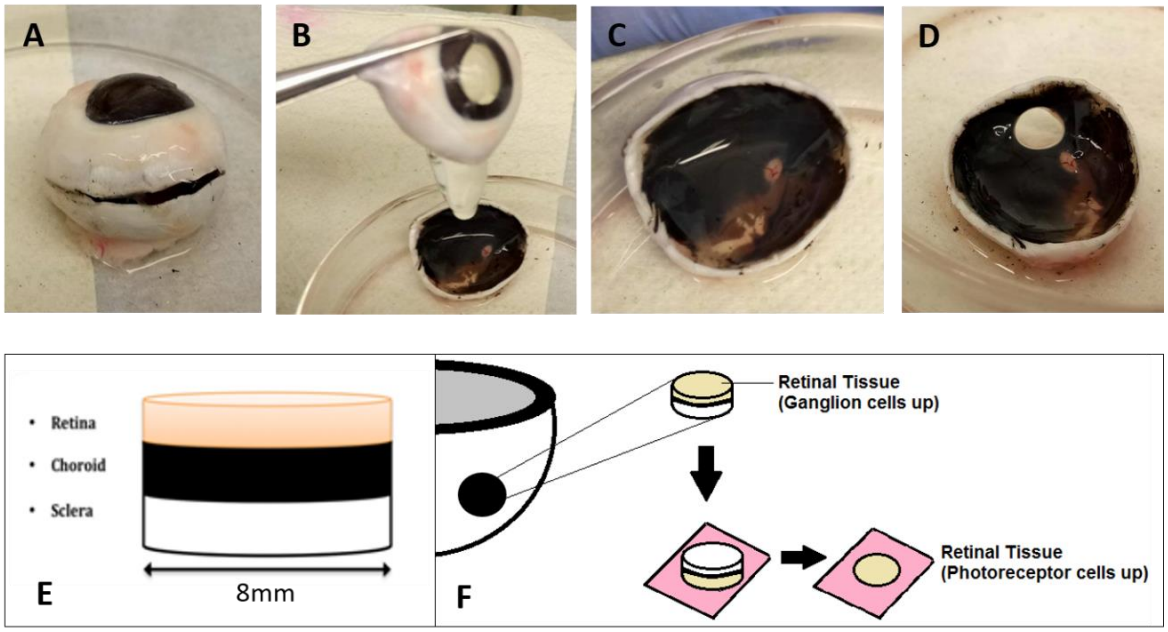

A circumferential cut was made around the porcine eye (A) and the anterior eye cup removed (B), which left behind the posterior eye cup and exposed neural retina (C). Circular, full-thickness posterior segments were punctured using an 8 mm biopsy punch (D, E). Full thickness retinal tissue was then transferred onto a compressed collagen gel substrate (pink) and the sclera (white) + choroid (black) peeled away (F).

During method optimisation additional culture substrates were also tested prior to the use of compressed collagen gel, which are described in detail in Chapter 5. Approximately 2-3 retinal samples could be isolated from each porcine eye, dependent on the success of tissue transfer. Any samples that folded or became distorted during the transfer process were discarded. Once the retinal tissue was transferred to a substrate, samples were maintained

in vitro. The use of 0.4 µm culture inserts (Greiner Bio-One, Austria) were used for the culture of 3D organotypic retinal tissue explants. Samples were transferred into a 12 well plate, positioned on the culture inserts. Isolated 3D organotypic retinal tissue explants were cultured in neurobasal medium supplemented with 2% B-27, 1% L-glutamine and 1% antibiotics (penicillin & streptomycin). 200 µL culture medium was added to each well for samples in a 48 well plate and 1 mL was added for samples in a 12 well plate on an insert. Tissue was cultured inside an incubator at 37°C and 5% CO_2, with culture medium changed every two days.

2.2.1.9 Isolation of primary rat bone marrow mesenchymal stem cells

6 week old Sprague-Dawley rats were obtained from the Keele University animal house and were sacrificed by cervical dislocation (Schedule 1) in accordance with the Animals (Scientific Procedures) Act 1986. The femurs and tibias were removed from the back limbs of each rat by dissection of the skin and muscles using sharp dissection scissors. The removed femurs and tibias were then rinsed in 70% ethanol, followed by PBS, before being transferred to a 90 mm petri dish inside a sterile laminar flow hood. Each bone was held using fine forceps and each end cut open using sharp dissection scissors. Using a sterile 22-gauge needle attached to a 3 mL syringe (Medisave, UK) filled with Alpha Minimum Essential Medium Eagle (α-MEM), the bone marrow was flushed out into a falcon tube by inserting the needle into one open end of the bone. This was repeated 3 times for each bone until all bone marrow had been removed. The bone marrow was then passed through a 40 µm cell strainer to remove excess bone debris and blood aggregates. Cells were then centrifuged at 300 x g for 3 minutes, the supernatant aspirated, cell pellet resuspended in 1 mL culture medium and the cells seeded into flasks. Isolated primary rMSCs were cultured in α-MEM supplemented with 10% FBS, 1% L-glutamine and 1% antibiotics (penicillin & streptomycin) at 37°C, 5% CO_2 and 95% humidity.

2.2.1.9.1 Tri-lineage differentiation

To confirm multipotency of isolated primary rMSCs, a tri-lineage differentiation was carried out for osteogenesis, adipogenesis and chondrogenesis assessment. Cells at passage 1 were cultured in three different culture medium formulations, summarised in Table 3.

Table 3 Culture medium formulations for tri-lineage differentiation of primary rat bone marrow mesenchymal stem cells

Lineage	Reagent	Amount (per 100 mL)
Osteogenesis	DMEM with 1g/L glucose	85.88 mL
	FBS	10 mL
	Antibiotics (Penicillin & streptomycin)	1 mL
	L-Glutamine	1 mL
	Non-essential amino acids (NEAA)	1 mL
	Beta glycerophosphate	1 mL
	Ascorbic acid	100 µL
	Dexamethasone	20 µL
Adipogenesis	DMEM with 1g/L glucose	85.36 mL
	FBS	10 mL
	Antibiotics (Penicillin & streptomycin)	1 mL
	L-Glutamine	1 mL
	NEAA	1 mL
	3-Isobutyl-1-methylxanthine (IBMX)	1.11 mL
	Insulin	250 µL
	Indomethacin	180 µL

	Dexamethasone	100 µL
Chondrogenesis	DMEM with 1g/L glucose	93.76 mL
	FBS	1 mL
	Antibiotics (Penicillin & streptomycin)	1 mL
	L-Glutamine	1 mL
	NEAA	1 mL
	ITS	1 mL
	Sodium pyruvate	1 mL
	Ascorbic acid	100 µL
	L-Proline	100 µL
	Dexamethasone	20 µL
	TGF-β3	20 µL

After 21 days of culture in tri-lineage differentiation medium, the corresponding culture media was removed, and the rMSCs washed with PBS and fixed in 4% paraformaldehyde in PBS for 10 minutes. The cells were then washed again with PBS and samples histologically stained according to the anticipated differentiation lineage (see section 2.2.7.2.4).

2.2.2 TCCT fibroblast model construction

2.2.2.1 2D fibroblast model

For initial assessment of TCCT fibrosis, a 2D TCCT fibroblast model was set up by seeding fibroblasts into a 48 well culture plate at a density of 1 x 10^4 cells per well. 200 µL culture medium was added to each well for culture up to 7 days, with culture medium changed every three days.

2.2.2.2 3D fibroblast model

To more closely replicate the *in vivo* environment of TCCT in experiments, a 3D TCCT fibroblast model was also set up. The 3D fibroblast model was constructed by incorporating fibroblasts into a 3 mg/mL collagen hydrogel (see section 2.2.1.6) at a density of 4 x 10^4 cells per 50 µL volume gel. After mixing cells with the collagen hydrogel, the mixture was pipetted onto 6 mm wide filter paper frames (50 µL each) and incubated for 10 minutes at 37°C and 5% CO_2 until solidified. Once the hydrogels had solidified, each were placed into individual wells of a 48 well culture plate. 200 µL culture medium was added to each well for culture up to 14 days, with medium changed every three days.

2.2.2.3 3D TCCT fibroblast-epithelium co-culture model

To assess the potential influence that conjunctival epithelium may have on TCCT fibrosis, a group of 3D TCCT fibroblast model samples had an additional conjunctival epithelial cell layer seeded on top. The 3D TCCT fibroblast model was firstly constructed as previously described. Once the 3D fibroblast model samples had solidified and been placed into individual wells of a 48 well culture plate, conjunctival epithelial cells were passaged (see section 2.2.1.3). Epithelial cells were then carefully seeded on the top of the 3D fibroblast model samples as 10 µL droplets containing a density of 1 x 10^4 cells per sample. The samples were then incubated for 10 minutes at 37°C and 5% CO_2 to allow the epithelial cells to adhere to the hydrogels. 200 µL culture medium was then added to each sample for culture up to 14 days, with medium changed every three days.

2.2.3 Addition of stimulators and inhibitors to TCCT fibroblast model constructs

2.2.3.1 Growth factors and aqueous humour

Growth factors and aqueous humour were administered at 24 hours after construction of the 2D and 3D models. Growth factors TGF-β, TNF-α and VEGF were administered via addition to the culture medium at concentrations of 20 ng/ml for each well in 2D experiments and 50 ng/ml for each sample in 3D experiments. Porcine aqueous humour fluid was added to culture medium at a 50% concentration. Culture medium was changed every 2 days with fresh growth factor or aqueous humour added at each change.

2.2.3.2 Shear stress

The effect of shear stress on fibrosis was tested using a see-saw motion rocking shaker (mini, 230 VAC) (Cole-Parmer, UK), which rocked samples up to a 7° angle at a speed of 5 rpm whilst stored inside an incubator at 37°C and 5% CO_2. Subjected samples were placed on the rocker for 1 hour per day during experiments.

2.2.3.3 Conditioned media

For the conditioned media study, spent medium samples at the day 7 experimental time point (approximately 80% cell confluency) were collected from the culture plates and frozen (-80°C) for later use. This included spent medium from stationary (control), shear stress treated, TGF-β treated and TGF-β + shear stress treated cultures. The conditioned medium samples were then centrifuged and the supernatant mixed with fresh culture medium at a 50% concentration and administered to a new batch of TCCT fibroblasts.

2.2.3.4 Inhibitors

Mitomycin C used in this study was kindly donated by a local hospital (Leighton Hospital, Middlewich Road, Crewe, CW1 4QJ) and provided at the same dosage as would be used clinically. Mitomycin C was tested on 3D cultured TCCT fibroblasts via topical application to mimic the clinical application process. Following the removal of culture medium from samples, a 10 µL droplet of 0.2 mg/mL mitomycin C solution was added to each sample. During preliminary optimisation work, 10 µL was found to be an ideal droplet size to cover the TCCT samples. After 3 minutes, the mitomycin C solution was removed, the samples washed 3 times with PBS and fresh culture medium returned. Other inhibitors were administered to TCCT fibroblasts via addition to the culture medium. TGF-β RI Kinase Inhibitor VI and TNF-α inhibitor (SPD304) were each administered at a concentration of 10 µM; as recommended by manufacturer instructions. Decorin proteoglycan was administered at concentrations of 0.2 and 100 µg/mL, which were determined during preliminary optimisation work to be the minimum and maximum ranges of response. L-type calcium channel blocker nifedipine was administered at concentrations of 10 and 100 µM; an ideal range determined during preliminary optimisation work.

2.2.4 Assessment of Xen Gel Stent glaucoma medical device in 3D TCCT model

A Xen Gel Stent medical device (Allergan, US) was inserted into the 3D TCCT fibroblast model for the assessment of the fibrosis response surrounding the device. Prior to insertion, each Xen Gel Stent and the included Xen Injector device were washed in 70% ethanol for 15 minutes and subsequently left to dry for 15 minutes inside a laminar flow hood, to ensure sterility. Each 3D TCCT fibroblast model hydrogel was transferred into a 5 mL bijou tube lid for the insertion process, to limit movement of the gels during insertion. Held above a petri dish, the Xen Gel Stent was carefully inserted into the Xen Injector device

using fine forceps (Medisave, UK). Once the Xen Gel Stent was inserted, the Xen Injector was then positioned at a 90° angle to the side of the hydrogel and the injector slowly pressed down to push the Xen Gel Stent into the hydrogel. Once the Xen Gel Stent was inside the hydrogel the Xen Injector could then be slowly removed, leaving the Xen Gel Stent inside the hydrogel. The 3D TCCT fibroblast model hydrogels were then transferred back into 48 well culture plates and covered with 200 µL fresh culture medium.

2.2.5 Characterisation of cellular responses

2.2.5.1 Cell and tissue viability

Viability of cells and tissue was assessed using a commercially available live-dead double staining kit, able to stain both live and dead cells simultaneously. Calcein-AM ester was used to fluorescently label live cells green. Ethidium homodimer-1, which is unable to pass through the membrane of live cells, labelled the nuclear material of dead cells red. Before staining, all culture medium was removed and each sample washed using PBS. Negative control samples were immersed in 70% ethanol for 10 minutes before staining to completely kill the cells/tissue. All samples were then immersed in a staining solution of PBS containing 2 µL per mL of Calcein-AM and 1µL per mL ethidium homodimer-1. Sample plates were wrapped in aluminium foil to protect from light and incubated for 20 minutes at 37°C and 5% CO_2. After another wash using PBS, staining was observed using confocal microscopy (Olympus, UK). Live cell fluorescence (FITC) was imaged at 495/515 nm excitation/emission and dead cell fluorescence (TRITC) was imaged at 557/576 nm excitation/emission, using a 10x objective lens.

2.2.5.2 Tracking cellular location

For certain experiments which involved cell seeding inside gels or on top of tissue, it was of interest for the cellular location to be tracked using a cell labelling dye. For fluorescent labelling, cells were firstly passaged (see section 2.2.1.3) and resuspended in 1 mL culture medium inside a falcon tube. The cell suspension was then mixed with 2 µL CFSE cell labelling dye (Abcam, UK) and incubated for 15 minutes at 37°C and 5% CO_2, whilst protected from light. Following incubation, cells were centrifuged and the supernatant aspirated in order to remove the excess dye. Cells were then resuspended in the required quantity of culture medium for seeding and incubated again for 30 minutes at 37°C and 5% CO_2 for esterification. After incubation, the fluorescently labelled cells were seeded as required and the cellular location observed using either fluorescence microscopy (Leica, Germany) or confocal microscopy (Olympus, UK). Labelled cell fluorescence (FITC) was imaged at 495/515 nm excitation/emission, using a 4x and 10x objective lens.

2.2.5.3 Cellular metabolism

Cellular metabolism was quantified by alamarBlue® (an assay in which the chemical resazurin is reduced by metabolically active cells into the fluorescent molecule resorufin) at days 3, 5 and 7 for 2D experiments and additionally day 14 for 3D experiments. Culture medium was firstly removed and 200 µL of fresh medium containing 10% alamarBlue® reagent was added and incubated with the samples for 2 hours at 37°C. After incubation, the solution was taken from each sample and the fluorescence measured at 530/590 nm excitation/emission using a microplate reader (BioTek Synergy II). Following quantification, samples were washed thoroughly three times in PBS to remove any residual alamarBlue® reagent for continuous culture and measurement. All results were compared

against a control of blank collagen hydrogels without cells, to ensure that any residual alamarBlue® absorbed by the gels did not influence experimental results.

2.2.5.4 Collagen synthesis

Quantification of neocollagen synthesis in TCCT models was conducted using an azide-modified proline in culture medium, with subsequent detection of fluorescent alkyne which corresponded to the newly synthesized collagen, following a protocol previously established in the laboratory (Bardsley *et al*., 2017). Deprotected azido-L-proline (H-L-Pro(4-N3)-OH*HCl) was added to culture medium every two days at a concentration of 36 µg/mL. 3D samples were imaged for neocollagen detection periodically at day 3, 7 and 14. For imaging, all culture medium was removed firstly and each sample washed in PBS to remove any residual culture media before the Click IT reaction. Serum free culture medium was then added to samples before the addition of 10 µM Click IT Alexa Fluor 594 to each sample. Samples were incubated with the agent for 1 hour at 37°C incubator whilst protected from light. Samples were then washed four times in PBS and placed back into the serum containing culture medium. Control samples had no prior deprotected azido-L-proline added to culture medium, but were still stained with 10 µM Click IT Alexa Fluor 594. Confocal microscopy was used to image fluorescently tagged collagen at 594/617 nm excitation/emission, using a 10x objective lens. Individual imaging parameters were kept the same across groups and throughout experiments.

2.2.5.5 Actin expression-cellular morphology

Cellular morphology was observed using phalloidin tetramethylrhodamine-B-isothiocyanate to fluorescently stain F-actin filaments of cells. Each sample was fixed in 4% (4µg/100µL) paraformaldehyde in PBS for 1 hour, before washing 3x in PBS. The

samples were then permeabilised with 0.1% Triton® X100 (in PBS) for 1 hour before washing again 3x in PBS. The staining solution was prepared by dissolving 1 mg of Phalloidin tetramethylrhodamine-B-isothiocyanate in 200 µL DMSO to give a stock solution. The stock solution was protected from light and stored at – 20°C until use. An F-actin staining solution of 2% stock solution, 1% DMSO and 97% PBS was prepared and 100µL of the solution added to each sample. Sample plates were then protected from light and incubated at room temperature for 1 hour. After washing samples a further 3x in PBS, certain samples were then also counterstained with DAPI at a 1:500 dilution in PBS, in order to visualise the nuclei of cells. Following another final wash with PBS, cellular staining was then observed using confocal microscopy. Fluorescently stained F-actin filaments were imaged at 543/573 nm excitation/emission and fluorescently stained nuclei (DAPI) were imaged at 358/461 nm excitation/emission, using a 10x objective lens.

2.2.5.6 Calcium signalling

To assess the calcium signalling response of TCCT fibroblasts, cytosolic calcium was measured using Fluo-4 AM. The staining solution was prepared by dissolving 50 µg Fluo-4 AM in 50 µL DMSO to give a stock solution. The stock solution was protected from light and stored at – 20°C until use. Culture medium was firstly removed from cells and fresh medium containing 10µL per mL Fluo-4 AM stock solution was added and incubated with samples for 20 minutes at room temperature, whilst protected from light. Cells were then washed with indicator free culture medium and incubated for a further 30 minutes at room temperature to allow complete de-esterification of cytosolic AM esters. Confocal microscopy was then used to view the outcome of staining at 494/506 nm excitation/emission, using a 10x objective lens.

2.2.5.7 Immunostaining

Selected protein expression on TCCT and retina was determined with the use of immunohistochemical staining. Each sample was firstly fixed in 4% (4µg/100µL) paraformaldehyde in PBS for 1 hour, as previously described. After washing for 1 minute, 3x in PBS, samples were then permeabilised with 0.1% TritonX-100 in PBS for 1 hour (if required), before washing again 3x with PBS. Samples were then blocked to prevent any non-specific binding using 2% bovine serum albumin (BSA) in PBS for 1 hour. Samples were then washed 3x in PBS and stained with primary antibody (dilutions detailed in Table 4) in 2% BSA in PBS overnight at 4°C. Samples were subsequently washed a further 3x in PBS and stained with secondary antibody in 2% BSA in PBS for 2 hours at room temperature, protected from light. A summary of all primary and secondary antibodies used can be found in Table 4.

Table 4 Summary of the primary and secondary antibodies used for immunohistochemical characterisation

Primary antibody	Secondary antibody	Positive expression:
Vimentin goat polyclonal IgG (1:100)	Donkey anti-goat IgG FITC (1:100)	Fibroblasts
Cytokeratin-3 goat polyclonal IgG (1:100)	Donkey anti-goat IgG FITC (1:100)	Epithelial cells
RPE65 mouse monoclonal IgG (1:100)	Goat anti-mouse IgG TRITC (1:100)	Retinal pigmented epithelium (RPE)
IL8 mouse monoclonal IgG (1:2000)	Goat anti-mouse IgG TRITC (1:1000)	Interleukin 8 (IL8)

After washing the samples a further 3 times in PBS, confocal microscopy was then used to view the outcome of staining. Samples stained with a FITC secondary antibody were imaged at 495/515 nm excitation/emission and samples stained with a TRITC secondary antibody were imaged at 557/576 nm excitation/emission, using a 10x objective lens.

2.2.6 Enzyme linked immunosorbent assay

Commercially available enzyme-linked immunosorbent assay (ELISA) kits were using to quantify TNF-α and TGF-β 1 cytokine levels in porcine aqueous humour. 50 µL of incubation buffer was added to each antibody-coated well, followed by 100 µL of the standards or samples and incubated at room temperature for 3 hours (control blank wells remained empty for this step). The wells were then fully aspirated and washed 4 times with wash buffer, before the addition of 100 µL TNF-α/TGF-β biotin conjugate solution into each well. After a further 1 hour of incubation at room temperature, the wells were then fully aspirated again and washed 4 times with wash buffer, followed by the addition of 100 µL substrate solution to each well. After another 30 minute incubation at room temperature (protected from light), 100 µL Stop Solution was then added to each well. The optical density of each well was then read using a microplate reader at 450 nm wavelength.

2.2.7 Assessment of *in vitro* 3D organotypic retinal tissue explant culture

2.2.7.1 Optical coherence tomography

The preservation of cultured 3D organotypic retinal tissue explants was monitored using optical coherence tomography (OCT), as shown in Figure 2.5. A commercially purchased spectral domain optical coherence tomograph (TELESTO-II; Thorlabs, USA) was used in this study. The OCT utilises a centre wavelength of 1300 nm, providing around 3.5 mm

imaging penetration. Additionally, the lateral resolution of the OCT is 13µm and has an axial resolution of 5.5µm in air when using the LSM03 objective. Both 2D and 3D OCT imaging options were explored. With the standard 2D OCT imaging option, the beam scans in one location and acquires a cross sectional image displayed in real time. These images can be acquired relatively quickly and easily, but may lack detail as they comprise of only a single cross section. With the 3D imaging option, the beam scans across the sample in multiple locations, acquiring several neighbouring 2D-cross sectional images which are constructed into a 3D volumetric image. Although these images can take longer to acquire and have more variable parameters to consider, the denser scan offers more structural information and enhanced detail in comparison to 2D OCT imaging (Gabriele *et al.*, 2010). To maintain a sterile environment inside the culture plate, all samples needed to remain covered by a lid during imaging (Figure 2.5). As the refractive index of the plastic culture plate lid caused image distortion, the plastic lid was exchanged for a manipulated lid with glass windows during imaging. Furthermore, it was found that samples maintained on culture inserts had improved imaging quality due to being elevated above the reflective culture medium liquid.

Figure 2.5 OCT monitoring of cultured 3D organotypic retinal tissue explants

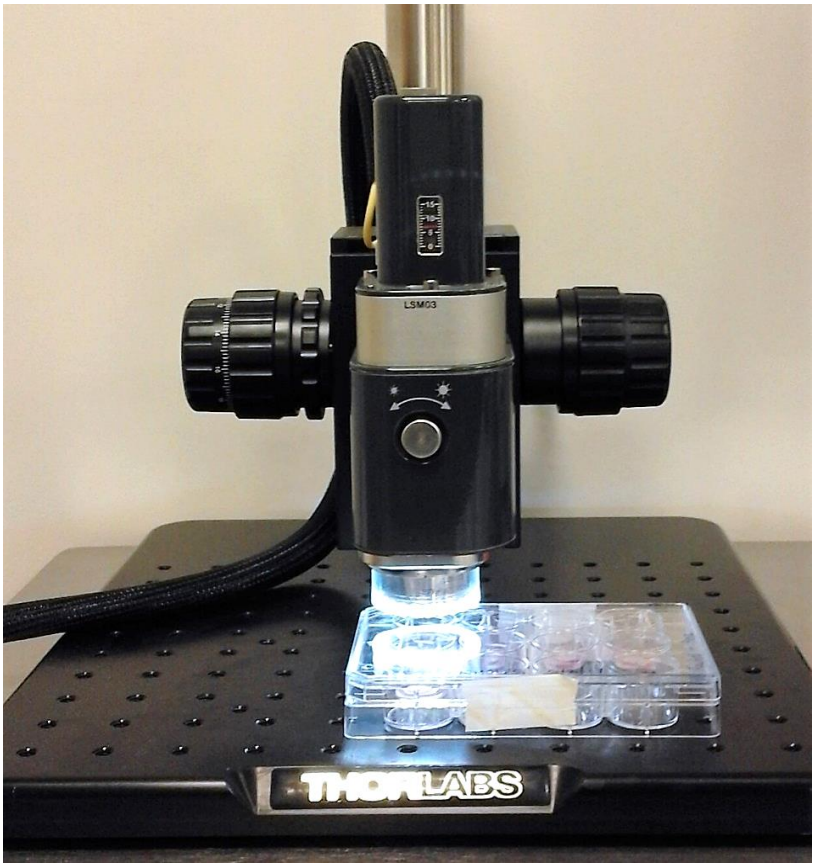

Cultured retinal tissue explants were monitored *in vitro* using OCT (TELESTO-II; Thorlabs). Samples remained inside the culture plate and were imaged from above.

2.2.7.2 Histology

2.2.7.2.1 Paraffin embedding

For histological assessment, all samples were embedded in paraffin wax prior to sample sectioning. Each sample was firstly fixed in 4% (4µg/100µL) paraformaldehyde in PBS for 1 hour, as previously described. Following fixation, samples were washed in PBS and transferred into 50% ethanol in water for 1 hour to begin the dehydration process. Samples were then consecutively transferred into 70%, 90% and 100% ethanol of a multi-step process for 1 hour at each step to fully dehydrate samples. Samples were then transferred into fresh 100% ethanol for another 1 hour to ensure complete sample dehydration. Once

dehydrated, samples were transferred into Histo-Clear for 1 hour and then transferred into fresh Histo-Clear for another 1 hour, to ensure the complete removal of ethanol from the dehydration process. Subsequently, samples were transferred into melted paraffin wax at approximately 60°C (Fisher Scientific, UK) for 2 hours to ensure the complete infiltration of wax into the samples. Once infiltrated with wax, samples were then transferred into tissue embedding cassettes (Fisher Scientific, UK) and topped up with more melted paraffin wax to fill the cassettes. The tissue embedding cassettes were then transferred onto a cooling plate to allow complete solidification of the paraffin wax and embedding of samples.

2.2.7.2.2 Paraffin embedded sample sectioning

Following paraffin embedding, the paraffin block edges surrounding each sample location were trimmed using a razor blade (Fisher Scientific, UK). The sample-containing tissue embedding cassettes were then inserted into a microtome and 5 µm sample sections sliced at a 34° cutting angle using the microtome blade. Using fine forceps, sample sections were then carefully transferred to float in a 40°C water bath. After approximately 1 minute, sample slides ready-coated with polylysine (Thermofisher Scientific, UK) were carefully dipped underneath the floating sample sections in order to transfer onto the slides. Once samples had transferred, slides were then laid out flat and left to dry for 1-2 hours.

2.2.7.2.3 Section de-paraffinisation and rehydration

Prior to the histological staining of sample sections, the removal of paraffin wax and sample rehydration was required. For this process, sample slides were firstly incubated in a 60°C oven 30 minutes to improve the tissue adhesion to the slides. Once the paraffin wax had melted, sample slides were then submerged in Histo-Clear for 10 minutes to ensure the

complete removal paraffin wax from the sample sections. Sample slides were then consecutively transferred into 100%, 90%, 70% and 50% ethanol in water for 3 minutes each time in order to begin the rehydration of sample sections. Sample slides were then submerged in deionised water for 3 minutes to complete the rehydration process, before being laid out flat in preparation for sample section staining.

2.2.7.2.4 Haematoxylin and eosin staining

Once sample slides had been de-paraffinised and rehydrated, samples were stained with haematoxylin solution for 5 minutes. Slides were then submerged in tap water for 1 minute to remove the excess haematoxylin stain. Subsequently, samples were stained with eosin solution for 3 minutes. Slides were then submerged in water again for 1 minute to remove the excess stain, followed by 100% ethanol for 1 minute. Finally, samples were mounted using DPX mounting medium with a glass cover slip and allowed to dry before imaging using a light microscope.

2.2.7.2.5 Tri-lineage differentiation staining

Osteogenic lineage differentiation of rMSCs was identified with a 2% alizarin red S solution in deionised water. Adipogenic lineage differentiation was identified with a 0.5% oil red O solution in isopropanol. Chondrogenic lineage differentiation was identified with 1% toluidine blue solution at pH 2.5. Following fixation in 4% (4µg/100µL) paraformaldehyde as previously described, cells were covered with the stain according to their anticipated differentiation lineage for 15 minutes at room temperature. The cells were then washed twice with deionised water before imaging using a light microscope.

2.2.8 Methods to create injury within the *in vitro* 3D organotypic retinal tissue model

2.2.8.1 Mechanical injury

Retinal tissue samples were temporarily taken out of culture and placed inside a petri dish in preparation for mechanical injury. A section of each sample was then sliced manually using a no. 11, 4cm scalpel blade (Fisher Scientific, UK). To avoid 'dragging' the retinal tissue from its substrate, a full thickness cut of approximately 4 mm was crudely made in a downwards motion going through the retinal tissue and substrate. After injury, the samples were washed with PBS and returned to culture.

2.2.8.2 Acetic acid injury

Retinal tissue samples were temporarily taken out of culture and placed inside a petri dish in preparation for acetic acid injury. Square filter paper pieces of approximately 2 mm^2 size were soaked in 4% acetic acid in PBS. A soaked filter paper piece was then placed on top of each sample for either 5 or 10 minutes and then removed. After injury, the samples were washed with PBS and returned to culture. All tested injury methods were assessed using OCT (section 2.2.7.1) and Live/Dead tissue viability staining (section 2.2.5.1).

2.2.8.3 Laser injury

For laser injury, samples remained inside the culture plate with the plastic lid temporarily exchanged for a manipulated lid with glass windows, to minimise the amount of laser refraction. Lasers were directed onto the centre of each sample for 1 minute. A summary of the lasers tested for retinal model injury can be found in Table 5. Interestingly, the green (532nm) laser tested was of the same wavelength as the frequency-doubled YAG green laser currently used in ophthalmology to create a capsulotomy to treat angle-closure

glaucoma. Furthermore, the red (637nm) laser tested was of a similar wavelength to the Krypton red (647nm) laser currently used to coagulate choriocapillaries for treatment of the subretinal neovascular membrane (Abdulrahman and Marwan, 2019). After subjecting laser injury to the *in vitro* retinal tissue model samples, the plastic culture plate lid was exchanged back and samples were returned to the culture incubator. The laser injury methods were subsequently assessed using OCT (section 2.2.7.1) and Live/Dead tissue viability staining (section 2.2.5.1).

Table 5 Summary of the lasers tested for organotypic retinal model injury

Laser	Colour	Wavelength	Energy (mW)
Vortran	Red	637nm	100
Vortran	Green	532nm	40
Fluoview 1200 confocal DAPI	Blue	405nm	50

2.2.9 Delivery of rat mesenchymal stem cells to retinal tissue explants

To assess rMSC interaction with injured and non-injured *in vitro* 3D organotypic retinal tissue, rMSCs were seeded on top of the cultured explants. rMSCs were firstly passaged and labelled with CFSE cell labelling dye as previously described (section 2.2.5.2). Culture medium was removed from the retinal tissue explants and the labelled rMSCs carefully seeded on the top of each tissue sample as 5 µL droplets containing a density of 1×10^5 cells per sample. The samples were then incubated for 10 minutes at 37°C and 5% CO_2 to allow rMSCs to settle onto the retinal tissue. 200 µL fresh culture medium was then added to each sample for culture up to 14 days, with medium changed every two days. The location of fluorescently labelled rMSCs was observed using an upright fluorescence

dissection microscope (Leica, Germany) during culture and an inverted confocal microscope (Olympus, UK) after sample fixation.

2.2.10 Statistical analysis

ImageJ software version 1.4.3.67 was used for semi-quantification of images. All experiments were run with 3 replicates in each group and values stated are the representative mean and standard error of observations from 3 independent experiments. Analysis of statistical significance was performed using an unpaired, two-tailed Student's *t*-test. Comparisons of different mean values were analysed using GraphPad Prism 6 using *t*-test and one-way or two-way ANOVA with multiple comparisons. Results were considered statistically different at a significance level of 5% ($p < 0.05$). For all graphs, * indicates $p < 0.05$, ** indicates $p < 0.01$ and *** indicates $p < 0.005$.

Chapter 3

Investigation of fibrosis response within a Tenon's capsule and conjunctival tissue (TCCT) model

3.1 Introduction

Glaucoma is a major cause of sight loss globally, estimated to effect approximately 10% of people aged over 75 (NICE, 2019). The disease is characterised by optic nerve damage and retinal ganglion cell apoptosis, caused by an increase in IOP (Quigley, 2011). For advanced stage open angle glaucoma, the most common treatment is trabeculectomy surgery. The conjunctiva is a mucous membrane covering the inside of the eyelids and fore part of the sclera (Park *et al.*, 2017). Trabeculectomy surgery involves making an incision into the sclera and placing sutures into the sub-Tenon's capsule/conjunctival membrane space, forming a drainage cavity for aqueous humour fluid known as a 'bleb'. Drained aqueous fluid is then absorbed by capillaries in the sub-conjunctival/episcleral tissue, leading to IOP reduction. However, trabeculectomy surgery is an invasive operation with potential complications. Excessive fibrosis and scar tissue formation in the Tenon's capsule and conjunctival tissue (TCCT) following surgery can cause the created drainage cavity to heal up again and become blocked. This wound healing response significantly reduces the surgery success rate to just 55% (Hong *et al.*, 2005).

Tissue fibrosis is characterised by the disproportionate increase and deposition of ECM following tissue damage, which can frequently lead to scar tissue formation and abnormalities in tissue function (Frantz *et al.*, 2010). The incision made during glaucoma surgery is likely to trigger the overexpression of growth factors and cytokines such as TGF-β, TNF-α, VEGF and IL-1 (Cunliffe *et al.*, 1995; Schlunck *et al.*, 2016), causing an increase in the proliferation of Tenon's capsule and conjunctival fibroblasts. This activation of fibroblasts subsequently modulates collagen formation, leading to a disproportionate accumulation of ECM and scar tissue that causes the surgically created opening to heal up again and become blocked. It is thought that this increase in fibroblast activity may be further influenced by the flow of aqueous humour fluid, also understood to

contain growth factors such as TGF-β and VEGF (Jampel *et al.*, 1990; Huang *et al.*, 2014). Furthermore, the fluid movement itself via the created drainage pathway is likely to exert shear stress to TCCT, triggering mechanotransduction and the overexpression of growth factors and cytokines such as TGF-β (Dan *et al*., 2010). The quantifiable influence of this shear stress induced mechanotransduction on TCCT fibrosis remains unclear. It would therefore be valuable to assess the synergistic effects of shear stress in the presence of key growth factors, cytokines and aqueous humour.

Anti-metabolite drugs such as mitomycin C and 5-Fluorouracil are frequently used alongside trabeculectomy surgery in an attempt to reduce this TCCT fibroblast proliferation, which trigger apoptosis of the fibroblasts via disruption of DNA synthesis (Tomasz, 1995). However, this mechanism is evidently toxic and can lead to further complications such as sub-conjunctival bleb thinning and leakage, cytotoxicity and damage to other tissues such as the cornea (Wolner *et al.*, 1991; Stamper *et al*., 1992). A better understanding of the fibrotic response after trabeculectomy surgery is therefore required in order to develop safer and more efficient anti-inflammatory agents.

3.2 Aim

This study aimed to utilise 2D and 3D TCCT models for the investigation of factors influencing fibrotic response after glaucoma surgery. The first objective was to screen and assess the effect of growth factors and cytokines in aqueous humour on 2D and 3D cultured TCCT fibroblasts. The secondary objective was to then expose cultured TCCT fibroblasts to shear stress induced mechanotransduction in addition to cytokines, to assess their synergistic effect on TCCT fibrosis. To measure the potential influence that conjunctival epithelium may have on TCCT fibrosis, a 3D TCCT fibroblast-epithelium co-

culture model was also established and tested under some of these conditions. Furthermore, a novel, non-destructive assay using added azido-L-proline was applied to quantify neocollagen synthesis in response to these factors for a prolonged culture period. Following characterisation of how TCCT fibroblasts synergistically respond to growth factors/cytokines and shear stress in this chapter, the reduction of fibrosis response and assessment of a Xen Gel Stent glaucoma medical device would be tested using the TCCT fibrosis model (Chapter 4).

3.3 Results

3.3.1 Tenon's capsule and conjunctival fibroblast characterisation

Primary Tenon's capsule and bulbar conjunctival membrane tissue pieces were isolated from porcine eyes. As shown in Figure 3.1, TCCT fibroblasts stained positively for F-actin (using phalloidin tetramethylrhodamine-B-isothiocyanate; n=3) and vimentin (using vimentin goat polyclonal primary antibody and donkey anti-goat FITC secondary antibody; n=3). Negative control samples were stained with secondary antibody only. The cellular morphology was characteristic of healthy, spindle shaped fibroblasts.

Figure 3.1 Tenon's capsule and bulbar conjunctival fibroblast characterisation

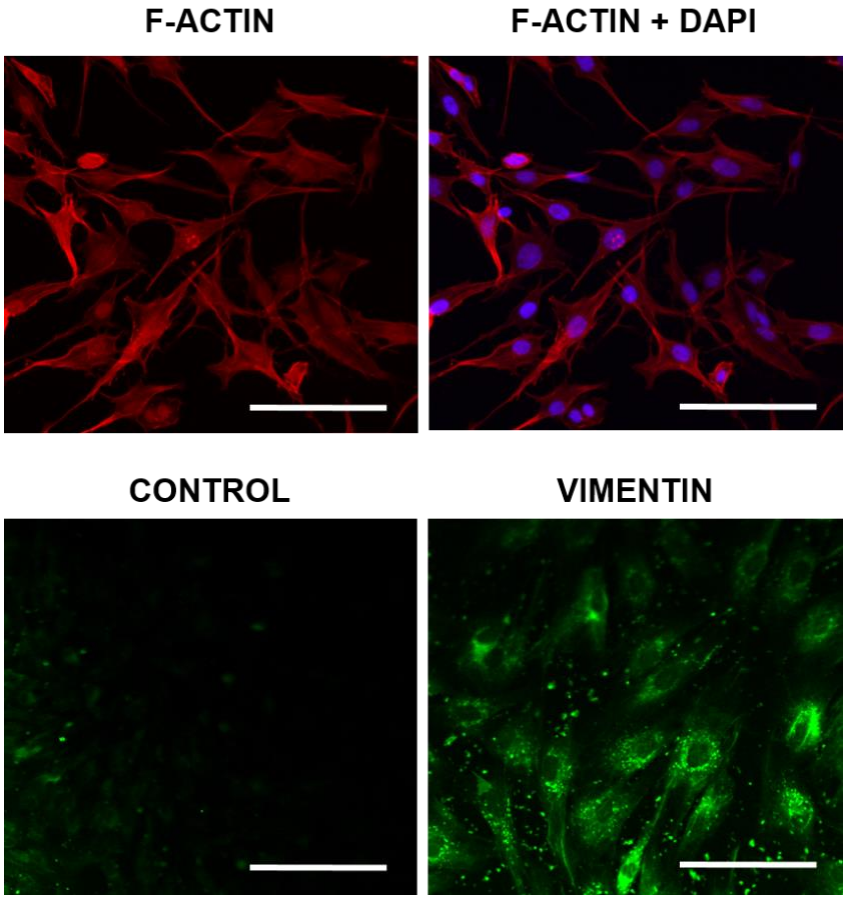

TCCT fibroblasts (n=3) stained with phalloidin (red) to label F-actin and DAPI (blue) to label cell nuclei (top row). Fibroblasts (n=3) immunostained with vimentin goat polyclonal primary antibody and donkey anti-goat FITC secondary antibody (green; bottom row). The control group was stained with secondary antibody only (n=3). Scale bar = 100 µm.

3.3.2 Effect of additives and shear stress on metabolic function in 2D model

Individual growth factors TGF-β, VEGF and TNF-α, conditioned media and porcine aqueous humour were firstly tested on 2D cultured TCCT fibroblasts, via addition to the culture medium. A dosage of 20 ng/mL was used for each growth factor, equating to approximately 0.4 pg/cell based on the 2D seeding density of 1 x 10^4 cells per well. Changes in cellular metabolic function were quantified using alamarBlue® (an assay in which the chemical resazurin is reduced by metabolically active cells into the fluorescent molecule resorufin) at days 3, 5 and 7 for 2D experiments.

As shown in Figure 3.2, 2D TCCT fibroblasts exposed to shear stress (without added growth factors) had a significant (4.6%) increase in metabolic activity at the day 3 time point, in comparison to stationary culture (p= 0.025). Further increases were observed at the day 5 (10.5%) and day 7 (2.5%) time points, though these differences were not significant. In contrast, 2D TCCT fibroblasts treated with 20 ng/ml TGF-β (without shear stress) had an overall significant increase in metabolic activity in comparison to the stationary control groups across all time points (p= 0.0101): a 2% increase at day 3, 4% increase at day 5 and 17% increase at day 7. Interestingly, 2D TCCT fibroblasts exposed to TGF-β in combination with shear stress had further increases in metabolic activity in comparison to TGF-β only: a further 4.85% increase at day 3, 15.9% increase at day 5 and 1.7% increase at day 7. However, this difference was not statistically significant. 2D TCCT fibroblasts treated with TGF-β in combination with shear stress also had increased metabolic activity in comparison to shear stress only, though this difference was not significant.

Figure 3.2 Effect of TGF-β on 2D TCCT fibroblast metabolic function

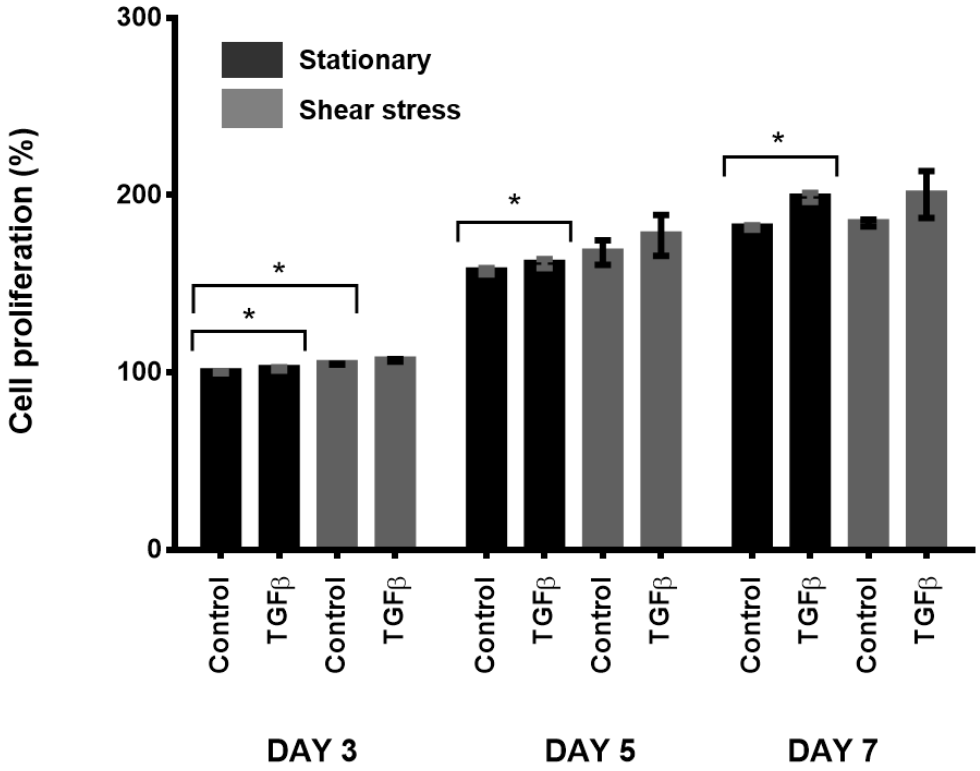

AlamarBlue® assay to assess the effect of TGF-β (20 ng/mL) on TCCT fibroblast metabolic function in the 2D TCCT model, with and without exposure to shear stress. Data are expressed as mean ±SE (n=3). * indicates p <0.05.

As shown in Figure 3.3, 2D TCCT fibroblasts treated with 20 ng/ml TNF-α (without shear stress) had an overall significant increase in metabolic activity in comparison to the stationary control groups (p= 0.0246): notably a 33% increase at day 5 and 13% increase at day 7. In addition, 2D TCCT fibroblasts treated with TNF-α in combination with shear stress had an overall significant increase in metabolic activity in comparison to TNF-α only (p=0.0105): a further 28.5% increase at day 3, 69.3% increase at day 5 and 44.4% increase at day 7. 2D TCCT fibroblasts treated with TNF-α in combination with shear stress also had an overall significant increase in metabolic activity, in comparison to shear stress only (p=0.0043).

Figure 3.3 Effect of TNF-α on 2D TCCT fibroblast metabolic function

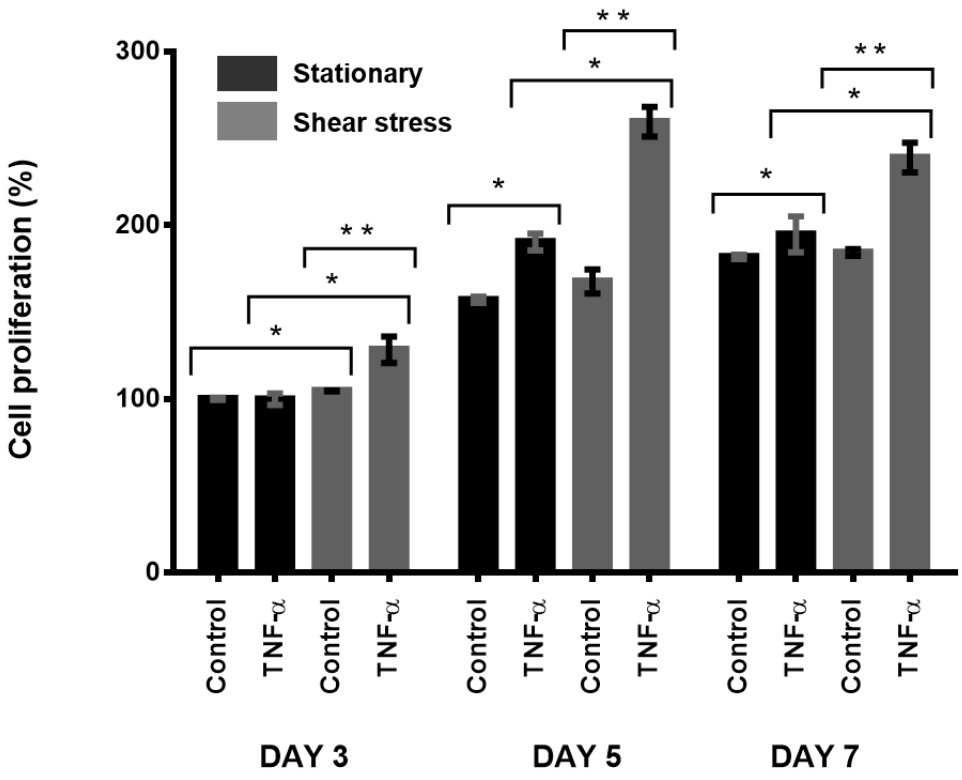

AlamarBlue® assay to assess the effect of TNF-α (20 ng/mL) on TCCT fibroblast metabolic function in the 2D TCCT model, with and without exposure to shear stress. Data are expressed as mean ±SE (n=3). * indicates p <0.05, ** indicates p <0.01.

As shown in Figure 3.4, 2D TCCT fibroblasts treated with 20 ng/ml VEGF (without shear stress) had an overall significant increase in metabolic activity in comparison to the stationary control groups (p= 0.0232): notably a 7% increase at day 5 and 34% increase at day 7. In addition, 2D TCCT fibroblasts treated with VEGF in combination with shear stress had an overall significant increase in metabolic activity in comparison to VEGF only (p=0.0194): a further 13.9% increase at day 3, 19.3% increase at day 5 and 26.2% increase at day 7. 2D TCCT fibroblasts treated with VEGF in combination with shear stress also had an overall significant increase in metabolic activity, in comparison to shear stress only (p=0.0074).

Figure 3.4 Effect of VEGF on 2D TCCT fibroblast metabolic function

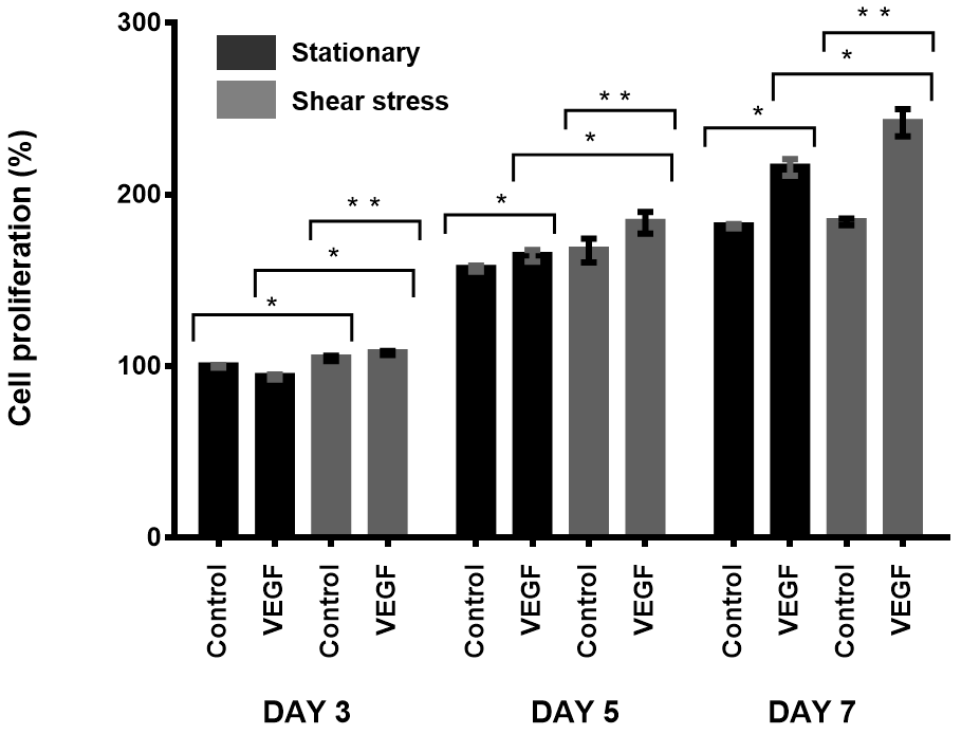

AlamarBlue® assay to assess the effect of VEGF (20 ng/mL) on TCCT fibroblast metabolic function in the 2D TCCT model, with and without exposure to shear stress. Data are expressed as mean ±SE (n=3). * indicates p <0.05, ** indicates p <0.01.

These results were cross validated by the 2D conditioned media study presented in Figure 3.5, where TCCT fibroblasts were treated with 50% conditioned medium containing the secretome of fibroblasts subjected to stationary (control), shear stress treated, TGF-β treated and TGF-β + shear stress treated cultures. Interestingly, TCCT fibroblasts cultured in conditioned medium from the shear stress treated group had a significant (9%) increase in metabolic activity in comparison to the control conditioned medium group (p=0.001). Some increase was also observed in the TGF-β + shear stress conditioned medium group, in comparison to the TGF-β only conditioned medium group, though this difference was not significant.

Figure 3.5 Effect of conditioned media on 2D TCCT metabolic function

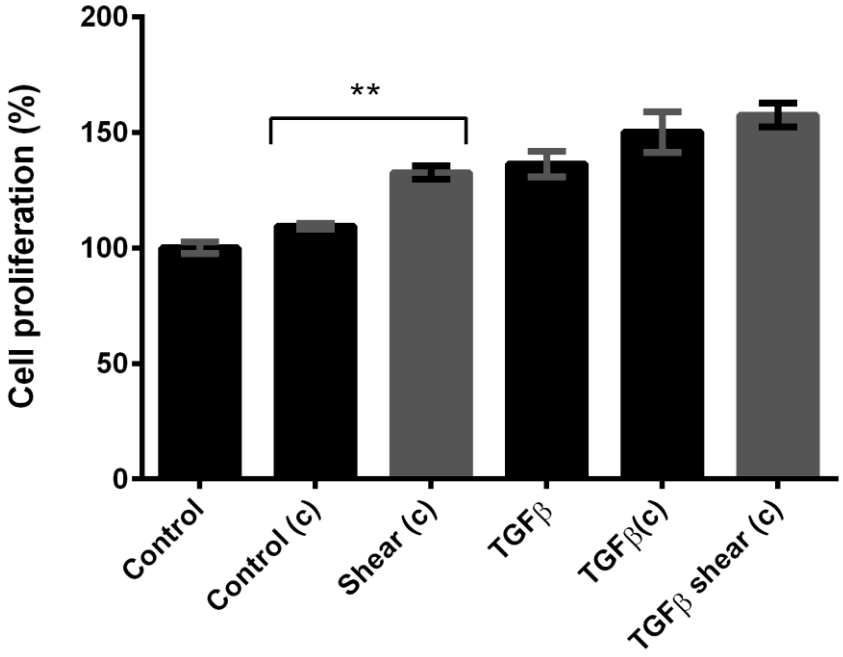

AlamarBlue® assay to assess the effect of conditioned media on TCCT fibroblast metabolic function in the 2D TCCT model. TCCT fibroblasts were treated with the addition of shear stress and TGF-β conditioned (c) medium. Data are expressed as mean ±SE (n=3). * indicates p <0.05, ** indicates p <0.01.

As indicated in Figure 3.6 (A, B), 2D TCCT cultures treated with 50% porcine aqueous humour had an increase in metabolic activity in comparison to the control. Metabolism increased by a further 41% in comparison to the control group at day 3 (p=0.0003), 212.7% at day 5 (p=0.0003) and 144% at day 7 (not significant). Batch to batch variability of the primary cell cultures did present some variation in TCCT fibroblast metabolic rate during experiments. Dependent on this variability, some 2D cultures tended to reach confluency by day 7 and hyper confluency would likely explain for any decline in cell number observed at the final time points.

Figure 3.6 Effect of aqueous humour on 2D TCCT fibroblast metabolic function

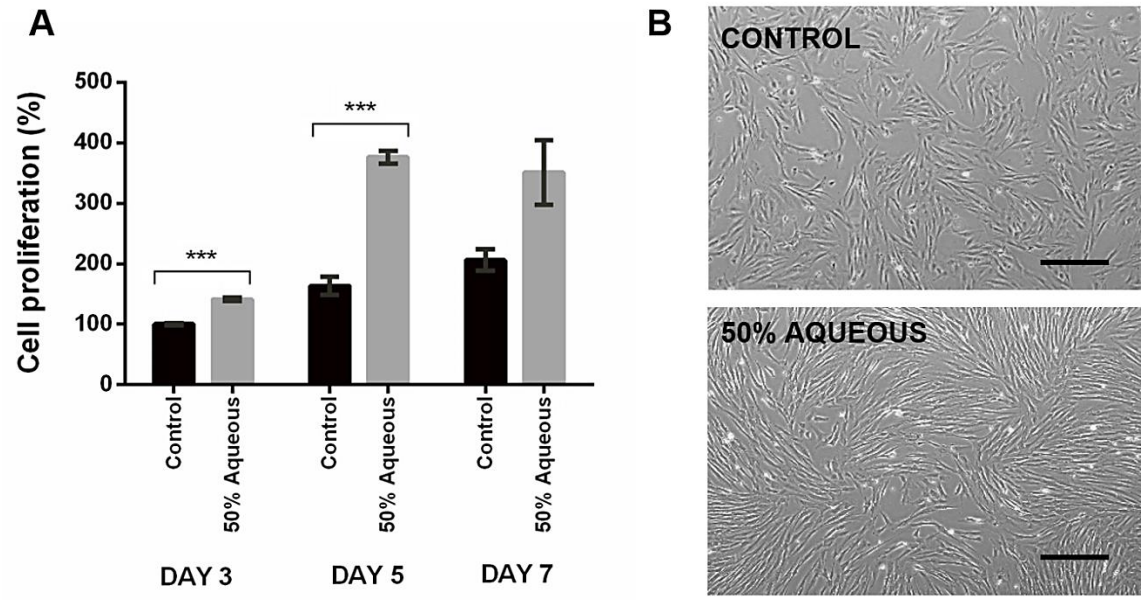

AlamarBlue® assay to assess the effect of 50% aqueous humour on TCCT fibroblast metabolic function in the 2D TCCT model (A). Data are expressed as a mean ±SE (n=3). Differences in morphology between 2D TCCT fibroblasts under control and 50% aqueous humour conditions, imaged at day 3 using light microscopy (B). Scale bar = 400 µm. * indicates p <0.05, ** indicates p <0.01 and *** indicates p <0.005.

3.3.3 TCCT fibroblast morphology and viability within 3D model constructs

As shown in Figure 3.7, TCCT fibroblasts maintained their spindle shaped morphology when seeded from 2D into 3D culture within 3 mg/mL collagen gels at a density of 4 x 10^4 cells per 50 µL volume gel, to form 3D TCCT models. The stretched cell morphology was preserved for the culture duration with a slight reduction in thickness of the collagen hydrogel samples. 3D cultured TCCT fibroblasts maintained viability for up to 2 weeks, with a decline in viability observed at 3 weeks, as indicated by Live/Dead cellular viability staining (Figure 3.7, B).

Figure 3.7 TCCT fibroblast morphology and viability within 3D model constructs

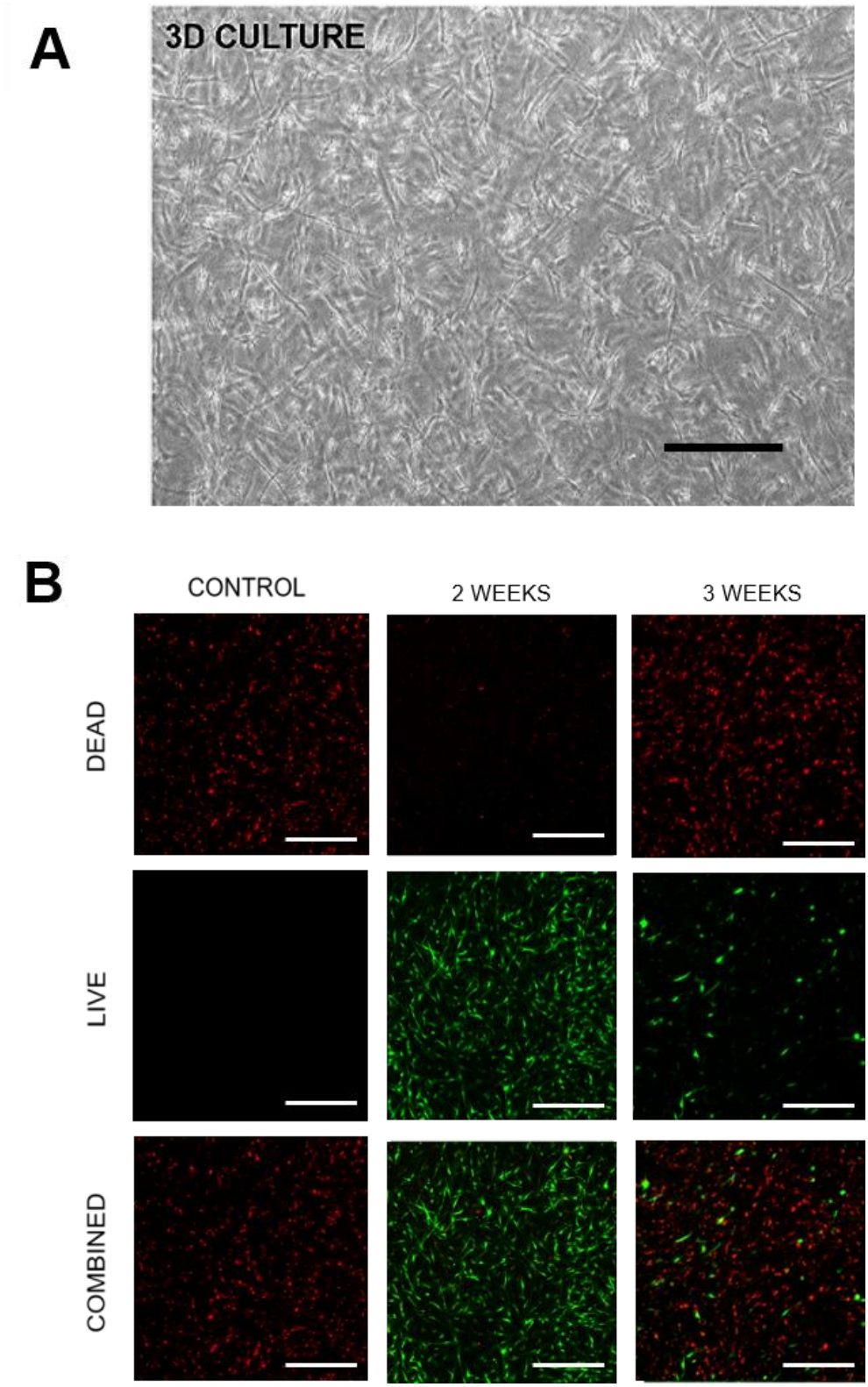

P2 TCCT fibroblasts growing in 3D culture within 3 mg/mL concentrated collagen hydrogel 24 hours after seeding (A). Live/Dead cellular viability staining of 3D cultured TCCT fibroblasts at 2 and 3 weeks. Positive control samples were immersed in 70% ethanol for 10 minutes before staining. Scale bars = 500 µm (B).

3.3.4 Effect of additives and shear stress on metabolic function in 3D model

Due to the increased seeding density for the 3D TCCT model (4 x 10^4 cells/gel), the dosage of growth factors TGF-β, VEGF and cytokine TNF-α was increased to 50 ng/mL, equating to approximately 0.25 pg/cell. Whilst maintaining a dosage of 0.4 pg/cell (as in 2D culture) would have improved consistency, preliminary optimisation work found 0.25 pg/cell to be the maximum dosage suitable for 3D TCCT model culture before a detrimental reduction in collagen gel thickness, due to contraction caused by the fibroblasts.

Changes in cellular metabolism were quantified using alamarBlue® at days 3, 5, 7 and 14 for 3D experiments. As shown in Figure 3.8, 3D TCCT fibroblasts exposed to shear stress (without added growth factors) had a significant (21.1%) increase in metabolic activity at day 3, in comparison to stationary culture (p= 0.011). Further increases were observed at the day 5 (6.91%), day 7 (4.8%) and day 14 (5.7%) time points, though these differences were not significant. In contrast, 3D TCCT fibroblasts treated with TGF-β (without shear stress) had an overall significant increase in metabolic activity in comparison to the stationary control groups (p= 0.0121): notably a 36% increase at day 5 and 60% increase at day 7. In addition, 3D TCCT fibroblasts treated with TGF-β in combination with shear stress had some increase in metabolic activity in comparison to TGF-β only: notably a further 4% increase at day 3 and 5.3% increase at day 5, though this difference was not significant. However, 3D TCCT fibroblasts treated with TGF-β in combination with shear stress did have an overall significant increase in metabolic activity in comparison to shear stress only (p=0.0395). By the day 14 time point, metabolic activity across all groups began to decrease as the cells reached confluency and viability started to decline.

Figure 3.8 Effect of TGF-β on 3D TCCT fibroblast metabolic function

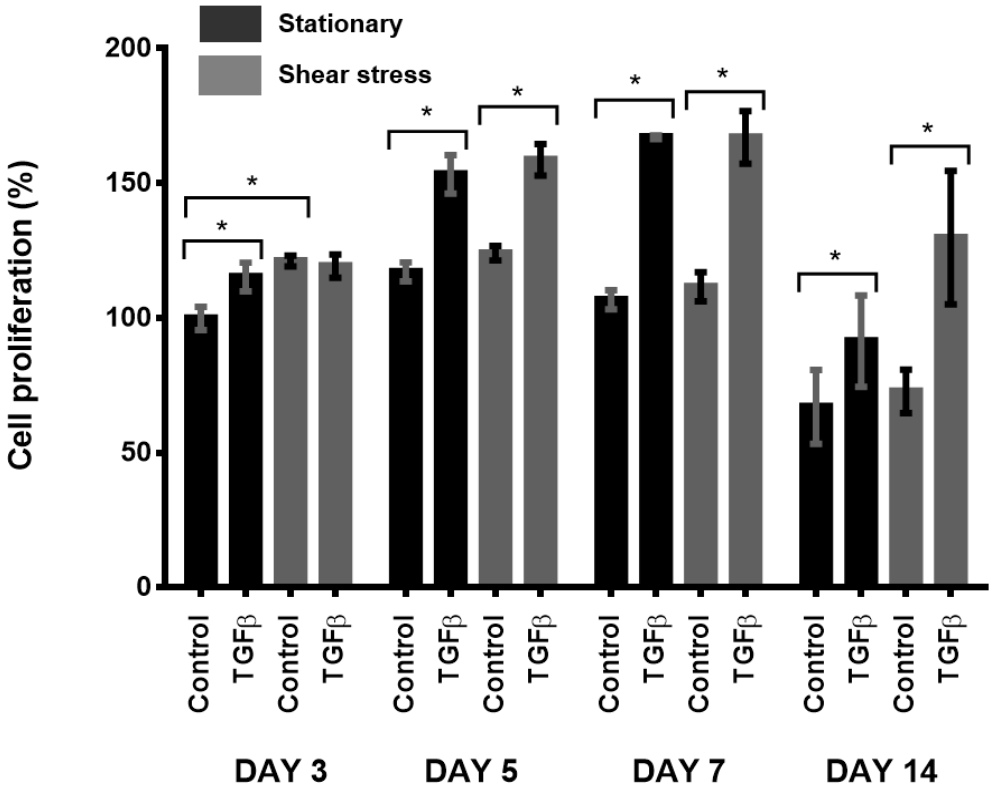

AlamarBlue® assay to assess the effect of growth factor TGF-β (50 ng/mL), under stationary and shear stress conditions, on 3D TCCT model fibroblast metabolic function. Data are expressed as mean ± SE (n=3). * indicates p <0.05.

As shown in Figure 3.9, 3D TCCT fibroblasts treated with TNF-α (without shear stress) had an overall significant increase in metabolic activity in comparison to the stationary control groups (p= 0.0013): notably a 9% increase at day 5 and 58% increase at day 7. In addition, 3D TCCT fibroblasts treated with TNF-α in combination with shear stress had an overall significant increase in metabolic activity in comparison to TNF-α only (p= 0.0146): a further 16.7% increase at day 3, 12.5% increase at day 5, 10.5% increase at day 7 and 20.3% increase at day 14. 3D TCCT fibroblasts treated with TNF-α in combination with shear stress also had an overall significant increase in metabolic activity in comparison to shear stress only (p=0.0007). By the day 14 time point, metabolic activity across all groups began to decrease as the cells reached confluency and viability started to decline.

Figure 3.9 Effect of TNF-α on 3D TCCT fibroblast metabolic function

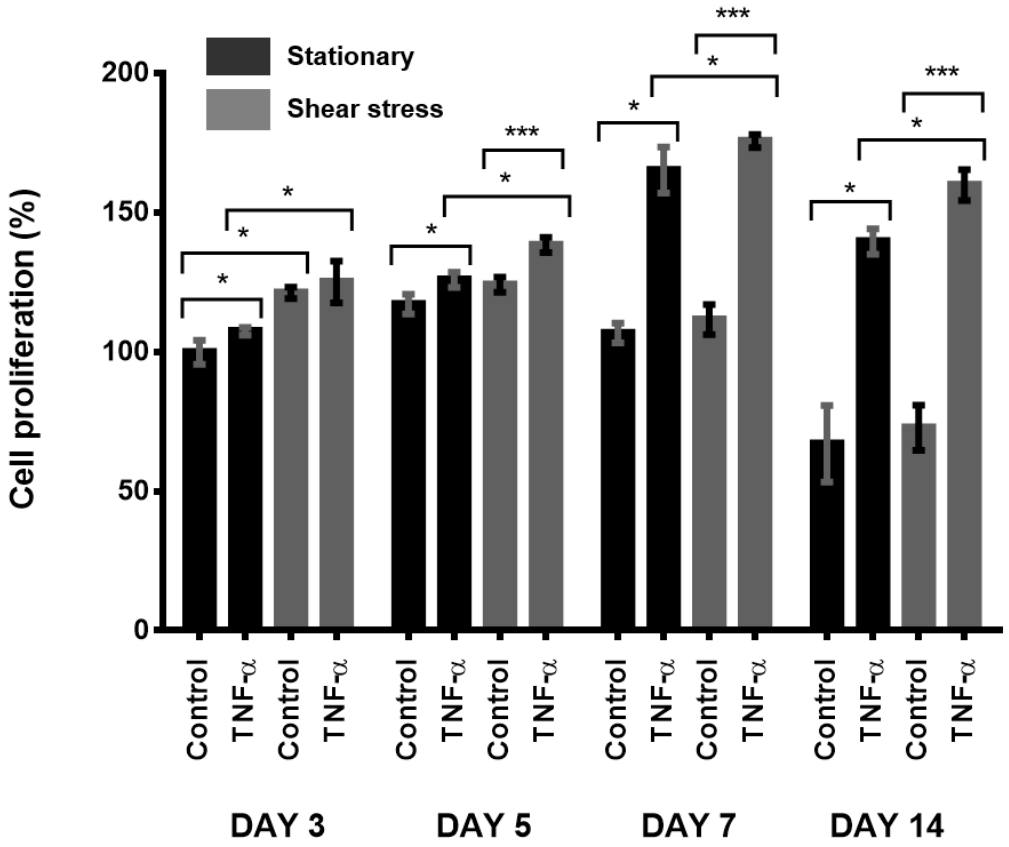

AlamarBlue® assay to assess the effect of growth factor TNF-α (50 ng/mL), under stationary and shear stress conditions, on 3D TCCT model fibroblast metabolic function. Data are expressed as mean ± SE (n=3). * indicates p <0.05, ** indicates p <0.01 and *** indicates p <0.005.

As shown in Figure 3.10, 3D TCCT fibroblasts treated with VEGF (without shear stress) had some increase in metabolic activity in comparison to the stationary control group: notably a 9% increase at day 5 and 4% increase at day 7, though this difference was not significant. However, 3D TCCT fibroblasts treated with VEGF in combination with shear stress had an overall significant increase in metabolic activity in comparison to VEGF only (p=0.01): a further 38.4% increase at day 3, 17.3% increase at day 5, 8.3% increase at day 7 and 21.1% increase at day 14. 3D TCCT fibroblasts treated with VEGF in combination with shear stress also had an overall significant increase in metabolic activity in comparison to shear stress only (p=0.0208). By day 14, metabolic activity across all groups began to decrease as the cells reached confluency and viability started to decline.

Figure 3.10 Effect of VEGF on 3D TCCT fibroblast metabolic function

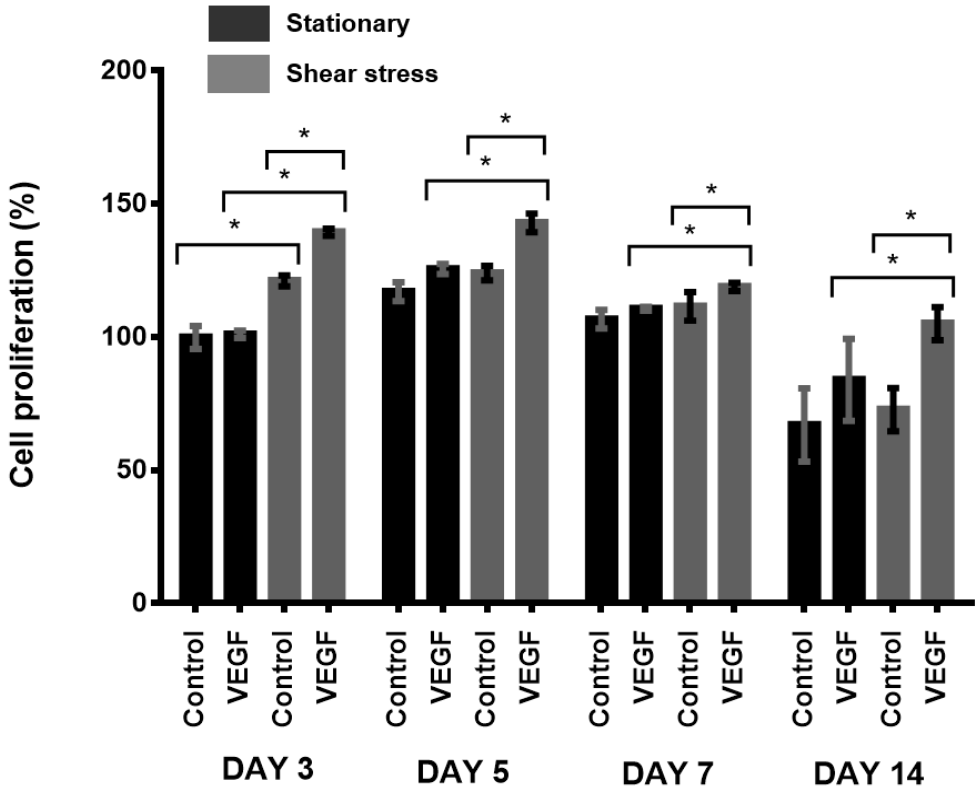

AlamarBlue® assay to assess the effect of growth factor VEGF (50 ng/mL), under stationary and shear stress conditions, on 3D TCCT model fibroblast metabolic function. Data are expressed as mean ± SE (n=3). * indicates p <0.05.

As shown in Figure 3.11, 3D TCCT fibroblasts treated with porcine aqueous humour (without shear stress) had an overall significant increase in metabolic activity in comparison to the stationary control groups (p= 0.0033): notably a 24% increase at day 5 and 45% increase at day 7. In addition, 3D TCCT fibroblasts treated with porcine aqueous humour in combination with shear stress had an overall significant increase in metabolic activity in comparison to aqueous humour only (p= 0.0043): a further 2.6% increase at day 3, 11.5% increase at day 5 and 9.6% increase at day 7. 3D TCCT fibroblasts treated with porcine aqueous humour in combination with shear stress also had an overall significant increase in metabolic activity in comparison to shear stress only (p=0.0084).

Figure 3.11 Effect of aqueous humour on 3D TCCT fibroblast metabolic function

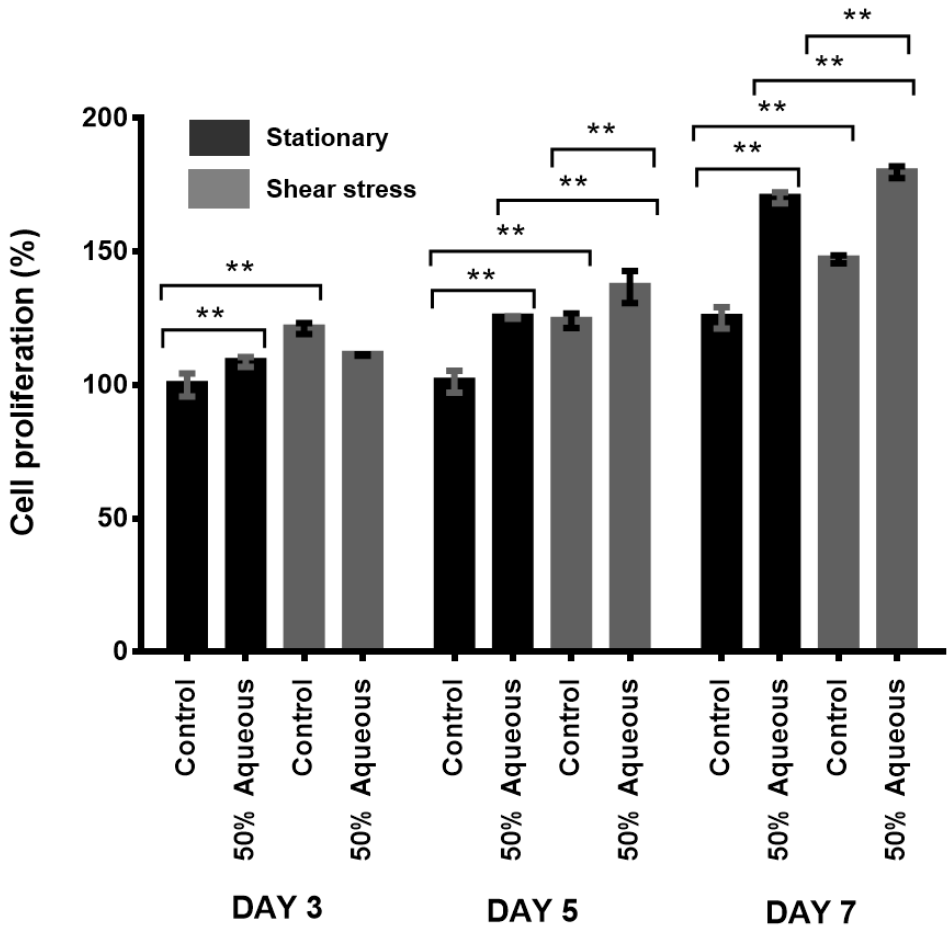

AlamarBlue® assay to assess the effect of aqueous humour (50% in culture medium), under stationary and shear stress conditions, on 3D TCCT model metabolic function. Data are expressed as mean ± SE (n=3). * indicates p <0.05, ** indicates p <0.01.

In comparison of the 2D and 3D model responses, 2D control samples appeared to increase gradually up to day 7. Samples treated with growth factors followed a similar trend, apart from TNF-α which appeared to peak at day 5 and decline somewhat by day 7. The greatest rate of metabolic activity occurred between days 3-5 for samples treated with TNF-α. Interestingly, proliferation rate was slower for 2D samples treated with VEGF. Samples treated with TNF-α had the greatest metabolic rate when combined with the synergistic effect of shear stress, reaching the highest overall metabolic rate (260% at day 5) amongst the 2D samples. In the 3D TCCT model, metabolic activity in control samples appeared to increase steadily up to day 5 before declining. 3D samples treated with the growth factors

TGF-β and TNF-α had increased metabolic activity for longer, with the highest metabolic activity occurring between days 5-7, before a decline after day 7. 3D samples treated with porcine aqueous humour also appeared to show this trend. Interestingly, metabolic activity was slightly faster for 3D samples treated with VEGF, which had the highest metabolic activity between days 3-5. However, these had the lowest overall metabolic activity amongst 3D samples. Similar to the 2D model trend, samples treated with TNF-α metabolised more when combined with shear stress and reached the highest overall metabolic rate (176% at day 7) amongst the 3D samples.

3.3.5 Assessment of neocollagen synthesis in response to additives and shear stress

To assess ECM synthesis by 3D TCCT fibroblasts, deprotected azido-L-proline (H-L-Pro(4-N3)-OH*HCl) was added to the culture medium of experimental samples and subsequently detected after incorporation into the neocollagen using Click-IT Alexa Fluor 594 DIBO Alkyne stain. Figure 3.12 presents the imaged neocollagen of TCCT fibroblasts at culture day 3, 7 and 14. The control (no L-proline) group had no deprotected azido-L-proline added to the medium during culture and evidently had minimal fluorescence when stained using Click-IT Alexa Fluor 594 DIBO Alkyne stain, indicating no false positive outcome. 3D cultured TCCT fibroblasts treated with growth factors TGF-β, TNF-α, VEGF and 50% aqueous humour evidently produced more labelled neocollagen than control samples, with 50% aqueous humour treated samples presenting the most fluorescently labelled neocollagen. Furthermore, samples exposed to shear stress had a slight increase in labelled neocollagen in comparison to stationary conditions.

Figure 3.12 Effect of culture conditions on TCCT fibroblast neocollagen synthesis

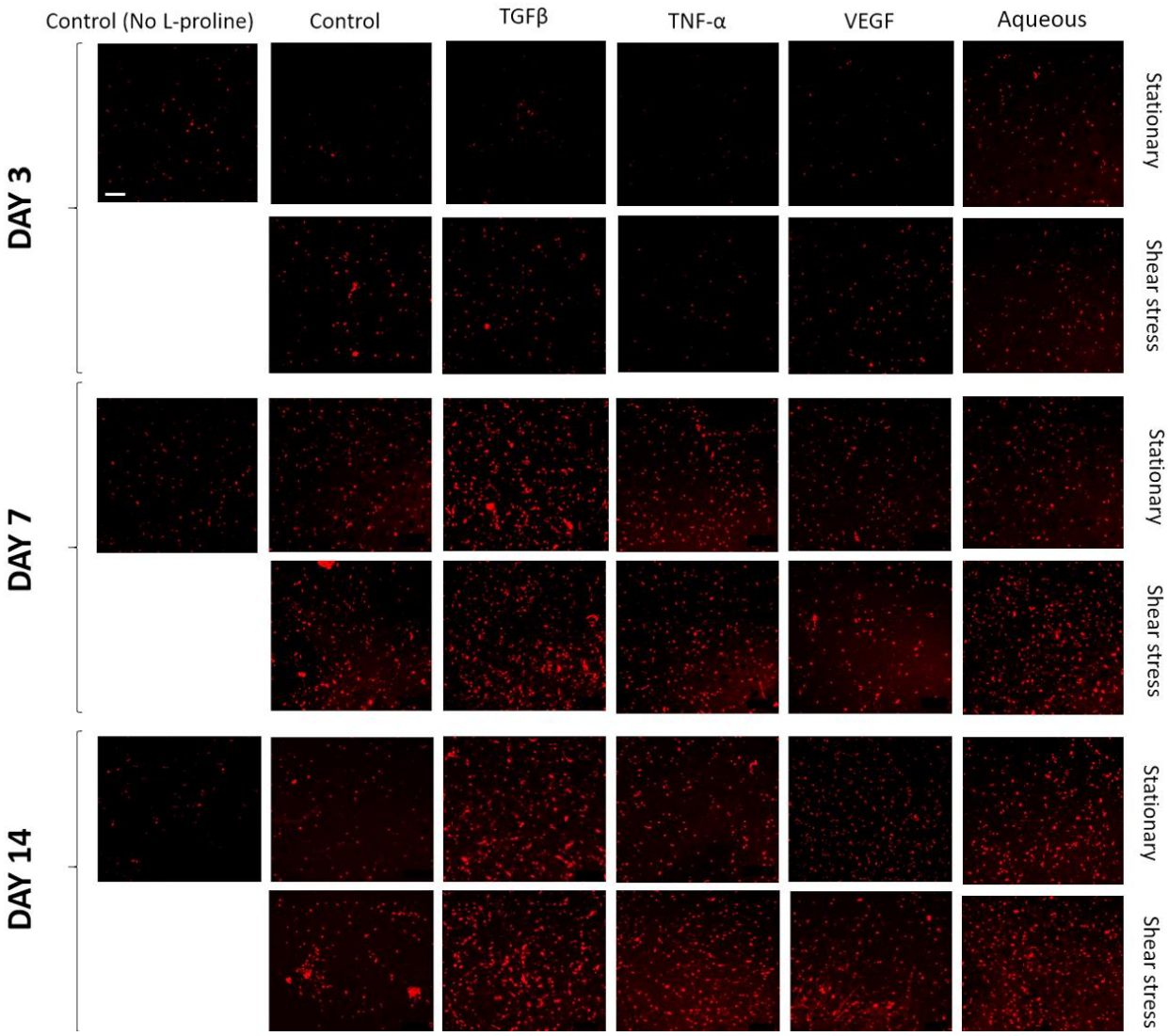

Imaging of neocollagen synthesis (red) monitored by Click-IT Alexa Fluor 594 DIBO Alkyne reaction with azido-L-proline, which was incorporated in the culture of 3D TCCT models with additives TGF-β, TNF-α, VEGF and 50% aqueous humour under stationary and shear stress conditions. The experimental control group had no growth factors or aqueous humour added to the cell culture medium during culture. The control (no L-proline) group also had no deprotected azido-L-proline added to the culture medium. Scale bar = 150 μm.

Figure 3.13 presents the semi-quantified neocollagen labelling fluorescence intensity of 3D TCCT fibroblasts at culture day 14, when labelling was strongest. Complementary to the images presented in Figure 3.12, 3D TCCT fibroblasts treated with growth factors TGF-β, TNF-α, VEGF and 50% aqueous humour appeared to produce more neocollagen than control samples, with aqueous humour treated samples presenting the most fluorescently labelled neocollagen. However, these differences were not statistically significant.

Figure 3.13 Semi-quantification of TCCT fibroblast neocollagen synthesis

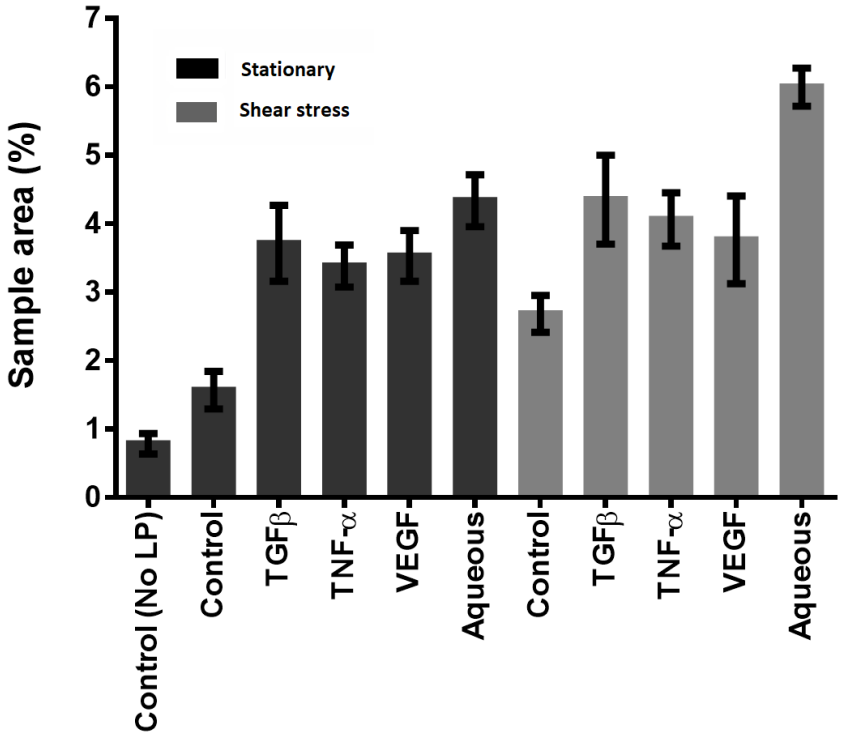

Semi-quantified neocollagen synthesis monitored by Click-IT Alexa Fluor 594 DIBO Alkyne reaction with azido-L-proline incorporated into the culture of 3D TCCT models with additives TGF-β, TNF-α, VEGF and 50% aqueous humour under stationary and shear stress conditions. The experimental control group had no growth factors or aqueous humour added to the cell culture medium during culture. The control (no L-proline) group also had no deprotected azido-L-proline added to the culture medium. Images were semi-quantified using ImageJ software. Data are expressed as mean ± SE (n=3).

3.3.6 Assessment of F-actin expression in response to additives and shear stress

Fibroblast morphology and F-actin expression also appeared to differ in the presence of TGF-β and aqueous humour, as shown in Figure 3.14. 3D TCCT samples cultured with TGF-β and 50% aqueous humour presented an increase in actin expression in comparison to the control group. F-actin expression increased even more dramatically with exposure to shear stress. Cellular morphology also appeared to change, with TCCT fibroblast shape becoming more elongated with exposure to TGF-β and aqueous humour, as well as shear stress. Fibroblasts exposed to shear stress also appeared to have a stretched morphology.

Figure 3.14 Effect of culture conditions on TCCT fibroblast F-actin expression

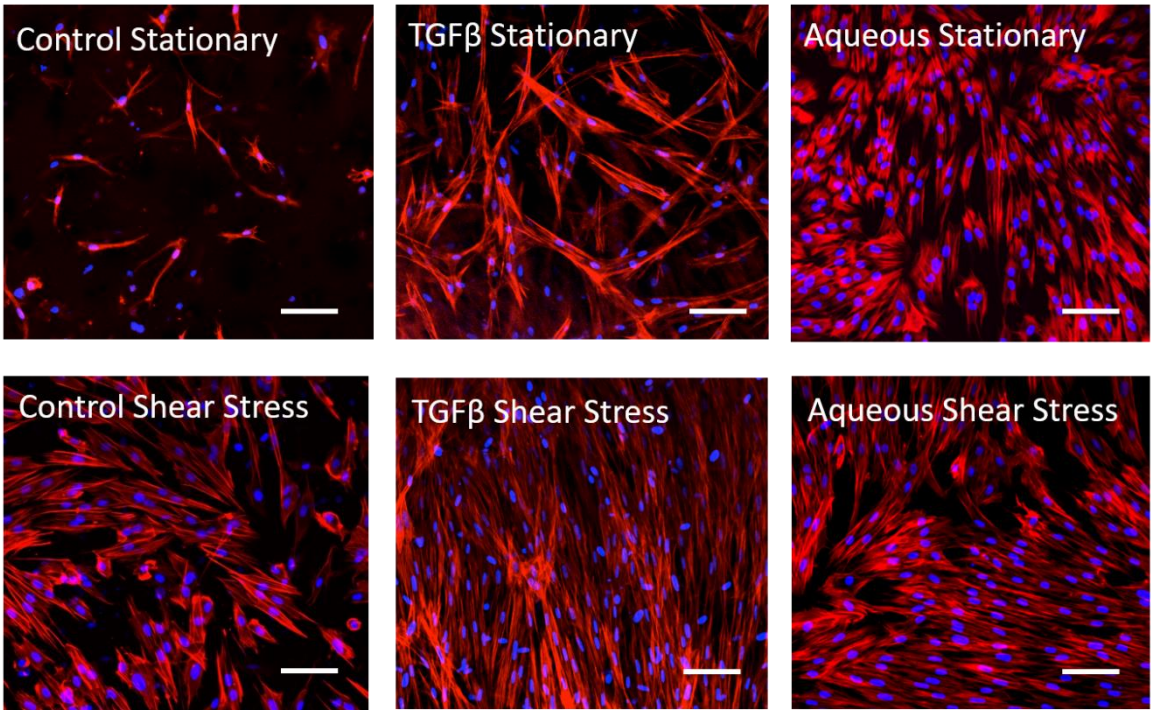

DAPI (blue) and F-actin (red) to indicate differences in cellular morphology and F-actin expression between 3D TCCT model fibroblasts, cultured with the additives TGF-β and 50% aqueous humour under stationary and shear stress conditions. Scale bar = 150 µm.

3.3.7 ELISA quantification of porcine aqueous humour

In consideration of the evident increase in TCCT fibroblast activity stimulated by exposure to porcine aqueous humour, it was of interest to measure the potential quantity of key growth factors present in aqueous humour fluid. The TNF-α and TGF-β cytokine content of aqueous humour obtained from porcine eyes was quantified using ELISA, as shown in Figure 3.15. The average TNF-α content was measured to be approximately 63.88 pg/mL (n=3), with an average upper limit of 97.18 pg/mL and lower limit of 22.59 pg/mL. The average TGF-β content was measured to be approximately 177.46 pg/mL (n=3), with an average upper limit of 192.37 pg/mL and lower limit of 163.54 pg/mL.

Figure 3.15 ELISA quantification of TNF-α and TGF-β in porcine aqueous humour

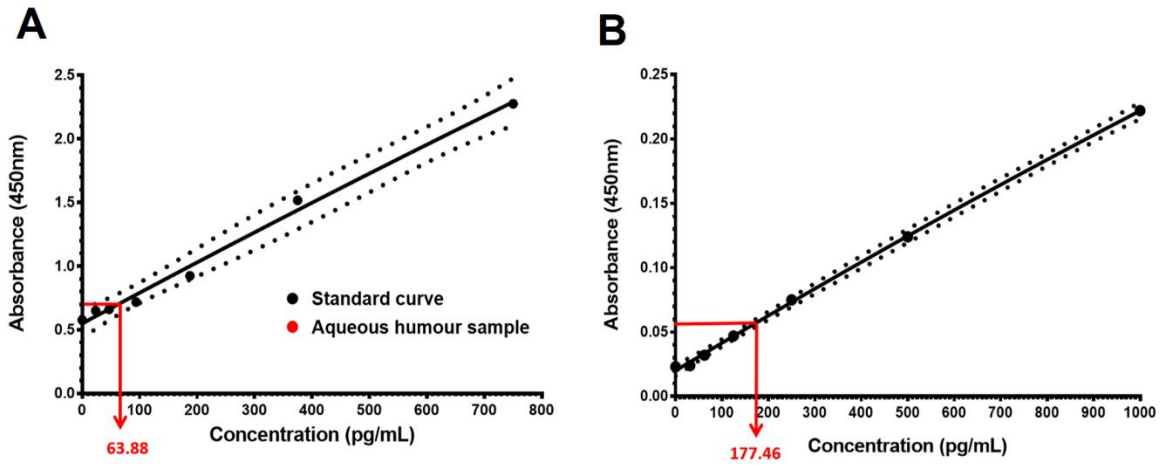

ELISA quantification of TNF-α (A) and TGF-β (B) in porcine aqueous humour against a standard curve (n=3).

3.3.8 Conjunctival epithelial cell growth and characterisation

To determine the potential influence that conjunctival epithelium may have on TCCT fibrosis, a 3D TCCT fibroblast-epithelium co-culture model was also established. Conjunctival epithelial cells were isolated from porcine eyes as previously described

(section 2.2.1.3) and the scraping residue checked for epithelial cells using a light microscope, as shown in Figure 3.16.

Figure 3.16 Isolation of primary porcine conjunctival epithelial cells

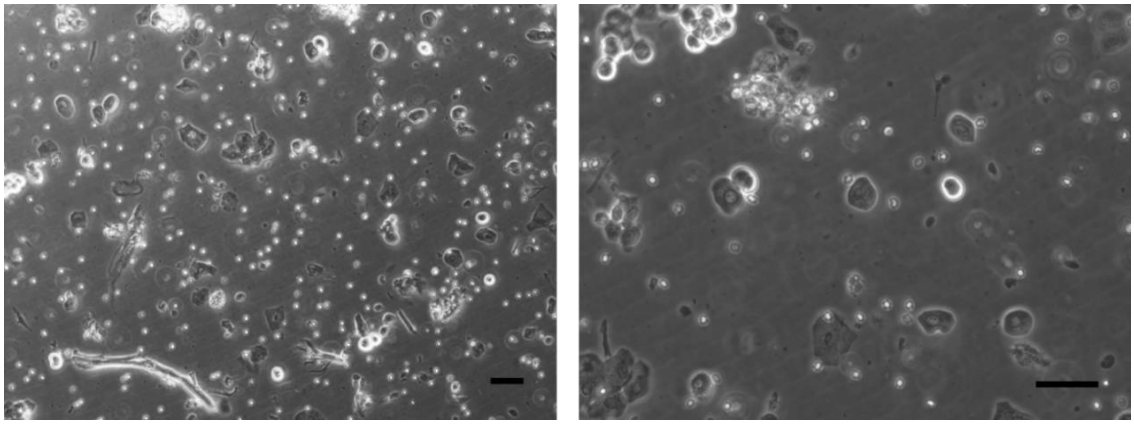

Primary porcine conjunctival epithelial cells (cobblestone morphology) visible amongst debris following conjunctival membrane surface scraping using a scalpel blade and forceps. Scale bar = 100 µm.

Three culture medium formulations were then tested for the optimised growth of epithelial cells, as detailed in Table 2. As shown in Figure 3.17, the epithelial cells cultured with formulation 2 (with 1:1 DMEM and F12) and 3 (with 3:1 DMEM and F12) had evidently improved cell attachment and proliferation at the 24 hour time point, in comparison to cells cultured with formulation 1 (a commercial formulation). Furthermore, cells cultured with formulations 2 and 3 maintained a 'cobblestone' morphology characteristic of healthy epithelial cells. However, by the 48 and 72 hour time point only epithelial cells cultured with formulation 3 appear to maintain this 'cobblestone' morphology, whereas cells cultured with formulation 2 evidently begin to lose this characteristic shape. It was therefore decided that formulation 3, with a 3:1 DMEM and F12 ratio, appeared to be the most suitable for conjunctival epithelial cell growth. Since the TCCT fibroblasts also appeared to grow healthily with this formulation, formulation 3 was used in all co-culture experiments going forwards.

Figure 3.17 Primary porcine conjunctival epithelial cell morphology and growth

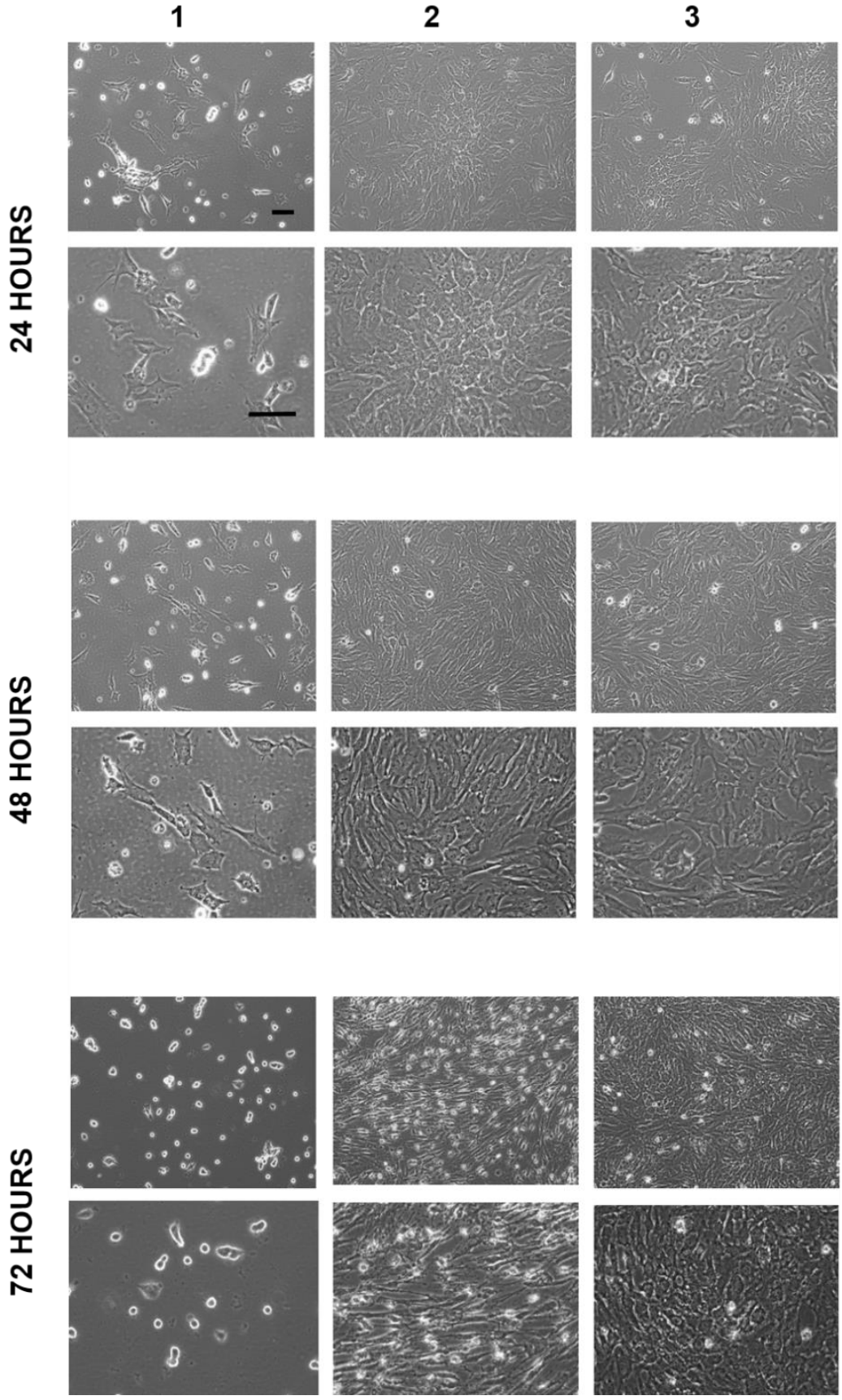

Primary porcine conjunctival epithelial cell growth and morphology observed at 24, 48 and 72 hours in three different culture medium formulations (n=3). Scale bar = 150 µm.

The isolated porcine conjunctival epithelial cells were characterised using cytokeratin 3; a keratin protein found in the cytoplasm of epithelial tissue and one of several markers acknowledged in previous literature for its ability to distinguish conjunctival epithelial cells (Silber *et al.*, 2015). As shown in Figure 3.18, the cells isolated from porcine conjunctival membrane stained positively for cytokeratin 3, using cytokeratin 3 goat polyclonal primary antibody and donkey anti-goat FITC secondary antibody (n=3). The 'cobblestone' morphology was characteristic of healthy epithelial cells.

Figure 3.18 Primary porcine conjunctival epithelial cell characterisation

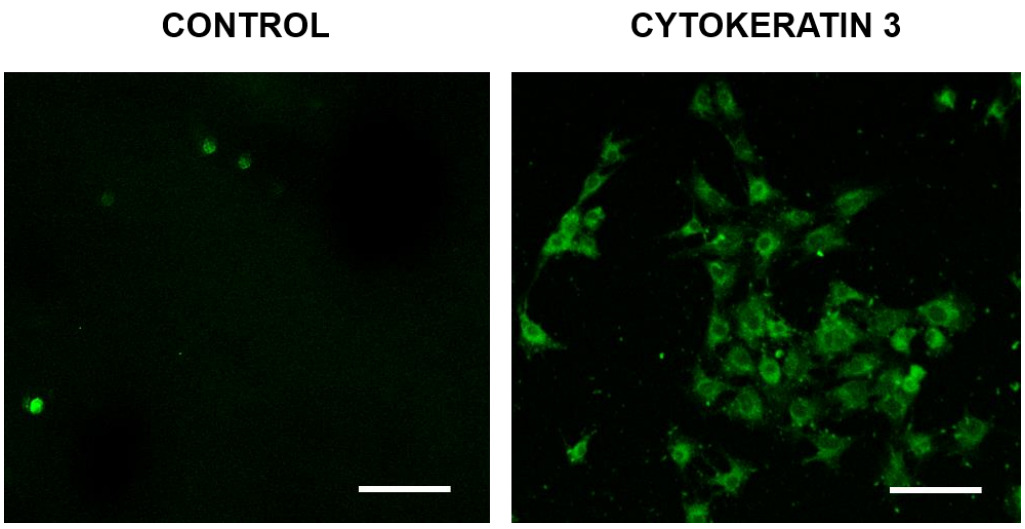

Conjunctival epithelial cells immunostained with cytokeratin 3 goat polyclonal primary antibody and donkey anti-goat FITC (green) secondary antibody (n=3). The control group was stained with secondary antibody only (n=3). Scale bar = 100 µm.

3.3.9 Addition of conjunctival epithelium to 3D fibroblast model construct

3.3.9.1 Culture insert use comparison for co-culture

The 3D TCCT fibroblast models (with a seeding density of 4 x 10^4 cells per 50 µL volume gel) had conjunctival epithelial cells seeded on top of each gel (at a seeding density of 1 x 10^4 cells per sample) as described previously (section 2.2.2.3). Sample co-culture was then

tested with and without the use of culture inserts. 3D TCCT fibroblast-epithelium co-culture samples cultured without culture inserts were placed into a 48 well culture plate covered with 200µL culture medium as normal. Samples cultured with the use of inserts were placed into a 12 well culture plate on top of the inserts, with 200µL culture medium making contact underneath. As shown in Figure 3.19, metabolic rate was greater for all 3D TCCT fibroblast-epithelium co-culture model samples in comparison to the control group (fibroblasts only) due to the additional layer of cells seeded. Interestingly, samples co-cultured without the use of inserts had higher metabolic activity than samples cultured with the use of inserts, by as much as 187.65% at day 14 (p= 0.02). Since co-culture model samples appeared to metabolise better without the use of culture inserts, samples were cultured without the use of inserts for all experiments going forwards.

Figure 3.19 The effect of culture insert use on co-culture model metabolic function

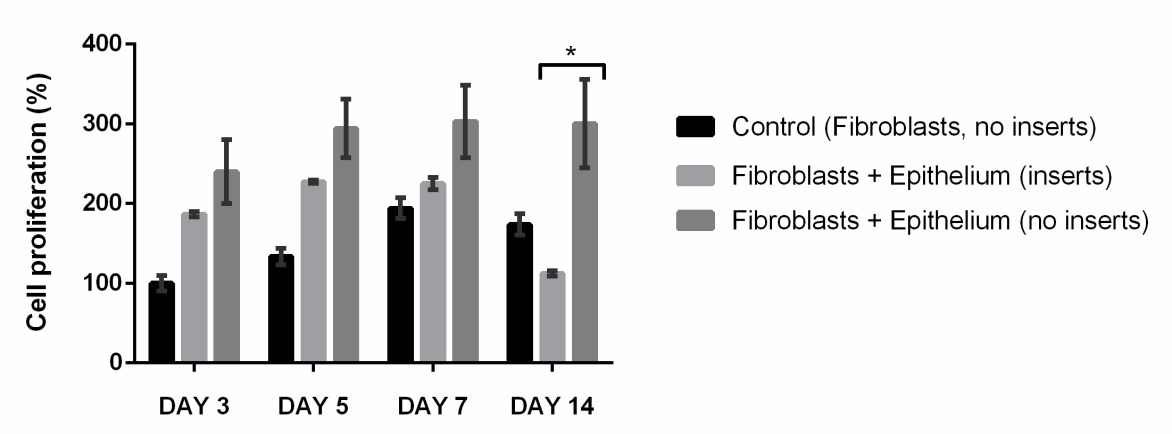

AlamarBlue® assay to assess TCCT fibroblast-epithelium co-culture model metabolic function, with and without the use of culture inserts. Data are expressed as mean ±SE (n=3). * indicates p <0.05.

3.3.9.2 3D TCCT fibroblast and epithelial cell co-culture assessment

As shown in Figure 3.20, conjunctival epithelium seeded on top of collagen hydrogel constructs appeared to have a higher metabolic activity in comparison to TCCT fibroblasts

seeded within collagen hydrogel. Conjunctival epithelium metabolic activity was 120.03% more than fibroblasts at day 3 (p= 0.019) increasing to approximately 363.3% more at day 14 (p= 0.005). Due to there being a greater cell number overall, metabolic rate was again higher for 3D TCCT fibroblast-epithelium co-culture model samples in comparison to fibroblasts and epithelium cultured separately at days 3, 5 and 7, though this was not statistically significant.

Figure 3.20 TCCT fibroblast and epithelial cell metabolic function in co-culture

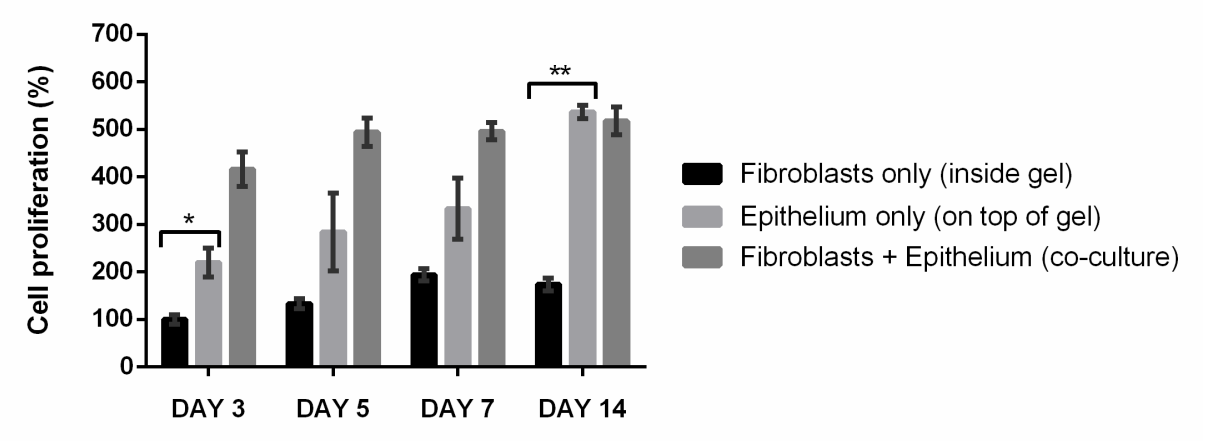

AlamarBlue® assay to assess TCCT fibroblast and epithelial cell metabolic function, cultured separately and in co-culture. Data are expressed as mean ±SE (n=3).
* indicates p <0.05, ** indicates p <0.01.

3.3.10 3D TCCT fibroblast-epithelium co-culture response to shear stress

To determine the potential influence that conjunctival epithelium may have on the TCCT shear stress response, fibroblasts and epithelial cells were exposed to shear stress both separately and in co-culture. As shown in Figure 3.21, TCCT fibroblasts seeded within collagen hydrogel and exposed to shear stress had an increase in metabolic activity, in comparison to the control group. Metabolic rate increased by 21.1% at day 3, 13% at day 5, 13.8% at day 7 and 8.9% at day 14, though this was not statistically significant.

Figure 3.21 The effect of shear stress on TCCT fibroblast metabolism

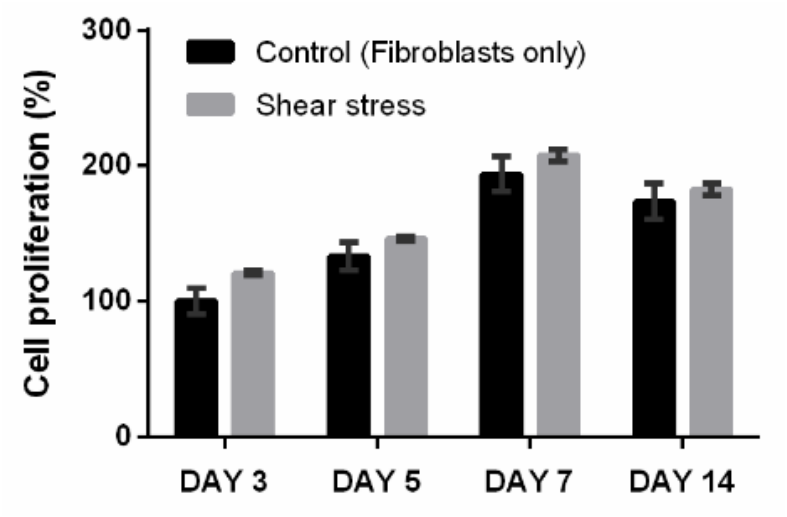

AlamarBlue® assay to assess the effect of shear stress on the metabolic function of TCCT fibroblasts seeded within collagen gel. Data are expressed as mean ±SE (n=3).

As shown in Figure 3.22, epithelial cells seeded on top of collagen hydrogel constructs and exposed to shear stress appeared to have an even greater increase in metabolic rate, in comparison to the control group. Metabolic activity increased by 66.25% at day 3 (p= 0.044), 103.25% at day 5, 80.05% at day 7 and 13.55% at day 14 (not significant).

Figure 3.22 The effect of shear stress on conjunctival epithelium metabolism

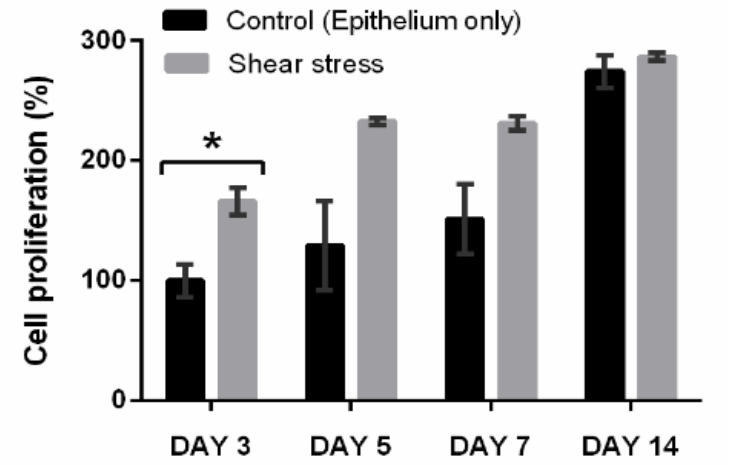

AlamarBlue® assay to assess the effect of shear stress on the metabolic function of conjunctival epithelium seeded on top of collagen. Data are expressed as mean ±SE (n=3). * indicates p <0.05.

As shown in Figure 3.23, in co-culture, combined metabolic activity increased by 31% at day 3, 33.07% at day 5, 32.3% at day 7 and 15.4% at day 14, with the addition of shear stress in comparison to the control group. However, these differences were not significant.

Figure 3.23 Effect of shear stress on fibroblast-epithelium co-culture metabolism

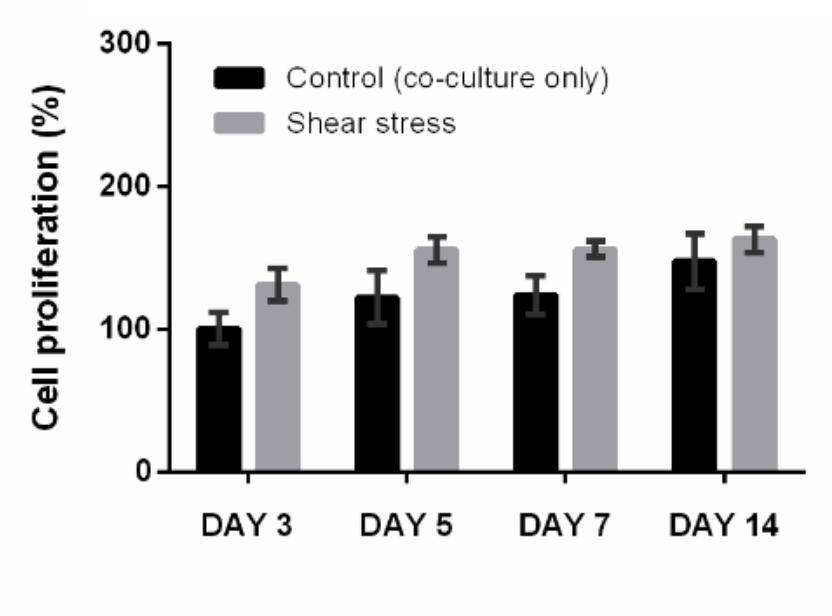

AlamarBlue® assay to assess the effect of shear stress on the metabolic function of TCCT fibroblast-epithelium co-culture. Data are expressed as mean ±SE (n=3).

As summarised in Figure 3.24, the effect of shear stress on cellular metabolism appeared to be greater for conjunctival epithelial cells seeded on top of collagen hydrogel, in comparison to TCCT fibroblasts seeded within collagen hydrogel at day 3 (p= 0.015), day 5 (p= 0.003) and day 7 (p= 0.002). Furthermore, the effect of shear stress on the 3D TCCT fibroblast-epithelium co-culture model appeared to be greater in comparison to the 3D TCCT fibroblast model without epithelium, though this difference was not significant.

Figure 3.24 Comparisons of shear stress effect on TCCT fibroblasts + epithelium

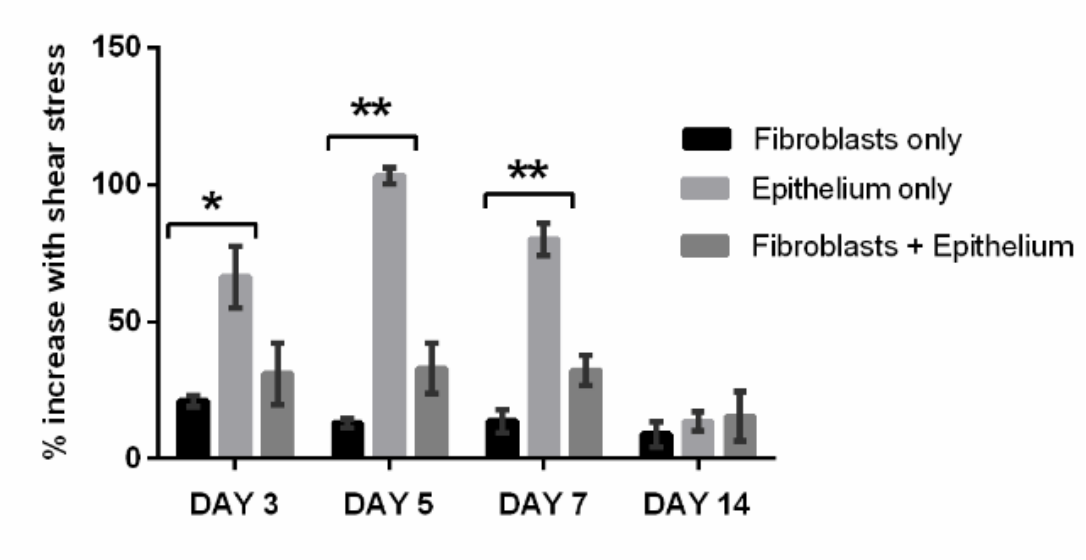

Comparisons of the effect of shear stress on TCCT fibroblast metabolic function seeded within collagen gel and epithelium seeded on top of collagen gel, individually and in co-culture. Data are expressed as mean ±SE (n=3). * indicates p <0.05, ** indicates p <0.01.

3.3.11 3D TCCT fibroblast-epithelium co-culture response to TGF-β and shear stress

To determine the potential influence that conjunctival epithelium may have on the TCCT response to TGF-β and shear stress, the 3D TCCT fibroblast-epithelium co-culture model was treated with 50 ng/mL TGF-β with and without exposure to shear stress. As shown in Figure 3.22, TCCT fibroblast-epithelium co-culture sample metabolism appeared to increase when treated with TGF-β, in comparison to the control group. Metabolic rate increased by 22.9% at day 3, 29.5% at day 5, 31.7% at day 7 and 1.3% at day 14, though this difference was not significant. However, the increase appeared to become significant with additional exposure to shear stress, increasing by 53.1% at day 3 (p= 0.033), 63.9% at day 5 (p= 0.038), 58.8% at day 7 (p= 0.019) and 17.03% at day 14 (not significant).

Figure 3.25 Effect of TGF-β and shear stress on 3D TCCT co-culture metabolism

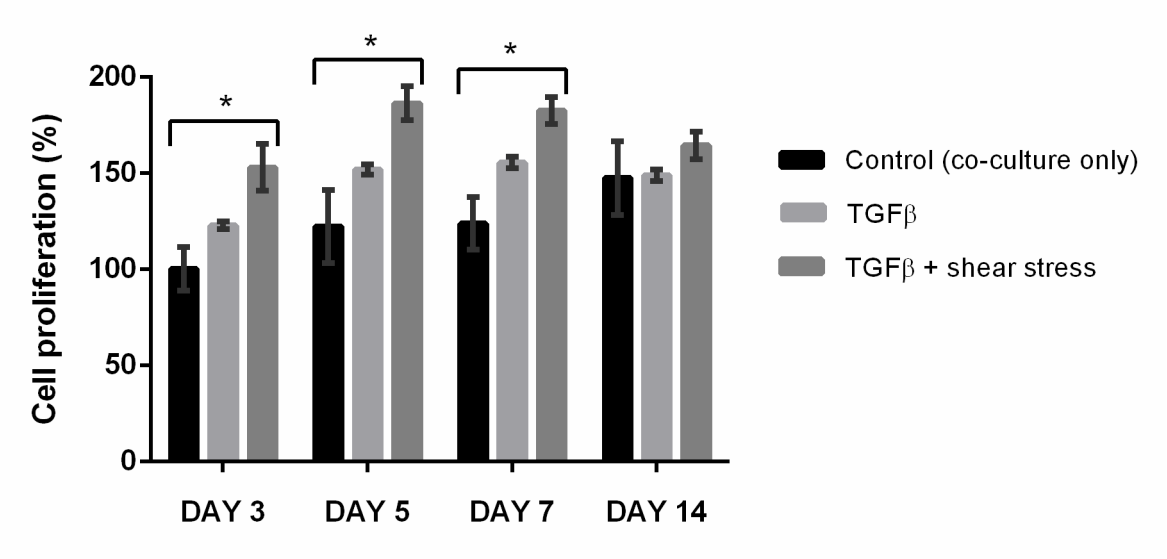

AlamarBlue® assay to assess the effect of TGF-β on 3D TCCT fibroblast-epithelium co-culture metabolic function, with and without exposure to shear stress. Data are expressed as mean ±SE (n=3). * indicates p <0.05.

3.4 Discussion

3.4.1 TCCT model establishment

Conjunctival fibrosis occurring after glaucoma surgery can significantly reduce the treatment success rate to just 55% (Hong *et al.*, 2005). This study used 2D and 3D *in vitro* models to investigate the factors which may influence conjunctival fibrosis after a trabeculectomy. Though size and shape of the conjunctival 'bleb' created during surgery can vary, most post-operative fibrosis is believed to occur in the Tenon's capsule region of the conjunctiva (Sherwood *et al.*, 1987). Cells were therefore specifically isolated from the TCCT anatomical location for use in this study. Isolated primary porcine TCCT fibroblasts were characterised using F-actin and Vimentin expression; markers acknowledged in previous literature to distinguish Tenon's capsule fibroblasts (Przekora *et al.*, 2017).

Initial establishment of the 2D TCCT fibroblast model was a useful starting point for this study, since it enabled assessment of the direct influence that growth factors and shear stress may have on TCCT fibroblasts, without a surrounding ECM. However, subsequent establishment of the 3D TCCT fibroblast model was more valuable, to enable assessment of the additional influence that ECM may have on the fibroblasts and fibrotic response, allowing the simulation of post-operative fibrosis in trabeculectomy. The fibrous protein present within TCCT ECM is thought to be primarily type I collagen (Park *et al.*, 2017). Therefore, the 3D TCCT model construction involved the seeding TCCT fibroblasts within a type I collagen hydrogel. It was anticipated that this would mimic native TCCT more closely, whilst still using a controlled, quantifiable method to study the influence of factors individually or in combination.

3.4.2 The effect of aqueous humour and growth factors on TCCT fibrosis

Aqueous humour is a clear fluid present in the ocular anterior chamber with a range of functions including waste product removal, nutrient supply, the transport of neurotransmitters and stabilisation of eye structure (Goel *et al.*, 2010). The apparent increase in fibroblast activity observed in TCCT after glaucoma filtration surgery may partly be due to the presence of aqueous humour as it drains via the new pathway created during trabeculectomy surgery. It was therefore valuable to test aqueous humour on the *in vitro* TCCT model. TGF-β and VEGF are some of the key growth factors believed to be present in aqueous humour (Jampel *et al.*, 1990; Huang *et al.*, 2015). As presented, the presence of aqueous humour in cell culture medium significantly increased the metabolic rate of TCCT fibroblasts in both 2D and 3D model constructs. This increase was also significantly greater in comparison to fibroblasts cultured in the presence of individual growth factors and cytokines (TGF-β, TNF-α and VEGF) at concentrations of 20 ng/mL and 50 ng/mL respectively. The presence of porcine aqueous humour also appeared to

cause an increase in F-actin expression within TCCT fibroblasts, which further suggests the presence of aqueous humour as a strong contributor to the fibrosis response in TCCT following trabeculectomy surgery.

ELISA quantification confirmed the presence of TNF-α and TGF-β in porcine aqueous humour. Nevertheless, previous studies have quantified levels of numerous different growth factors in human aqueous humour, including hepatocyte growth factor at 12.22 ng/mL and glial cell-line derived neurotrophic factor at 114.42 pg/mL, in addition to TGF-β and TNF-α (Cvenkel *et al.*, 2010). The quantity of TGF-β in human aqueous humour has also been found to vary based on race and age, with healthy African American patients having an average of 165.69 pg/mL and Caucasian American patients having an average of 145.54 pg/mL TGF-β in their aqueous humour, which increased with age (Trivedi *et al.*, 2011). Though higher dosages of TGF-β and TNF-α were used in this study model than the quantities found naturally in aqueous humour, aqueous humour still triggered a far stronger proliferation rate on TCCT fibroblasts. This indicates that there is likely to be many growth factors in aqueous humour with variable quantities, which in combination may synergistically cause the significant increase in TCCT fibroblast proliferation observed in this study, outweighing the influence of individual cytokines TGF-β and TNF-α.

3.4.3 The effect of shear stress induced mechanotransduction on TCCT fibrosis

The continuous flow of aqueous fluid drainage across TCCT after trabeculectomy surgery may further influence the fibrosis response, via shear stress which induced mechanotransduction. Shear stress induced mechanotransduction has previously been identified to promote the overexpression of cytokines such as TGF-β (Dan *et al.*, 2010) and may therefore influence the increase in fibroblast activity seen in TCCT after

trabeculectomy surgery. The quantifiable influence of shear stress induced mechanotransduction on TCCT fibrosis response remains uncertain. It was therefore valuable to assess the synergistic effect of shear stress in the presence of aqueous humour and key growth factors *in vitro.* The 2D and 3D TCCT models were used to test individual growth factors, aqueous humour and conditioned media in stationary and shear stress culture conditions. A 'see-saw' motion rocker was utilised to apply shear stress on samples, since it is an established method used in numerous credible studies to mimic fluid shear stress (Zhou *et al.*, 2010; Tucker *et al.*, 2014), including use with 3D culture (Puwanun *et al.*, 2018). The method enabled a high throughput which was advantageous for this study, allowing shear stress exposure to many samples at once for 1 hour per day during culture in 48 well plates. The method also had a low cost and was easy to establish. The fluid shear stress generated in our 3D model is calculated as previously described (Zhou *et al.*, 2010) to be 0.065 Pa, based on fluid viscosity (10^{-3} Pa.s), a maximum 7° flip angle, 1.6mm fluid depth, 11mm well length and 12 second cycle (5 rpm). There is a possible limitation that fibroblasts at the top of each gel would have been exposed to more shear stress than those at the bottom by using a 'see-saw' motion rocker with 3D cultures. However, it could be argued that this mimics the *in vivo* environment more closely, since fibroblasts located closer to the fluid flow in TCCT after trabeculectomy surgery would have exposure to shear stress stimulus, whereas fibroblasts located more deeply inside the tissue would not.

3.4.4 The synergistic effect of shear stress and growth factors on TCCT fibrosis

Results indicated that exposure to shear stress significantly increased the metabolic rate of 2D and 3D cultured TCCT fibroblasts. Additionally, the stimulatory effect of aqueous humour appeared to be enhanced further by exposure to shear stress. These findings suggest that the combined effect of both aqueous humour and shear stress may

synergistically contribute to the fibrosis response in TCCT after trabeculectomy surgery. Results were cross validated by a 2D conditioned media study where spent culture medium from TCCT fibroblasts previously exposed to shear stress was added to a new sample of TCCT fibroblasts. As presented, TCCT fibroblasts treated with shear stress conditioned medium had significantly increased metabolic activity in comparison to the control group. This result supports the idea that exposure to shear stress may cause an overexpression of growth factors in TCCT via mechanotransduction.

Comparable increases were observed in the presence of individual growth factors (TGF-β, TNF-α and VEGF), where exposure to shear stress appeared to synergistically enhance the metabolic effect of singular cytokines in both 2D and 3D TCCT models. Generally, metabolic rate was higher in 3D samples with most metabolic activity occurring between days 0-7, in comparison to 2D samples where most metabolic activity occurred between days 3-5. This could be explained by the fact that a collagen matrix offered protection to the fibroblasts in 3D culture, making them less prone to initial degradation in comparison to 2D culture where cells were exposed to growth factors more directly. For both 2D and 3D cultures, samples treated with TNF-α appeared to have the greatest metabolic rate when combined with the synergistic effect of shear stress. These findings can be supported by previous literature which mention TNF-α and TGF-β as some of the key growth factors that stimulate fibrosis in conjunctival tissue (Cunliffe *et al.*, 1995; Schlunck *et al.*, 2016).

In addition to metabolic activation, the subsequent formation of neocollagen by fibroblasts is another feature of the fibrosis believed to lead to excessive accumulation of ECM and scar tissue. To determine any influence that growth factors and shear stress may have on the collagen synthesis of TCCT fibroblasts, a non-destructive monitoring technique has

been applied. Since 2D cultures tended to reach confluency by day 7, these would have been too hyper confluent by day 14 for neocollagen assessment. Neocollagen data collection was therefore prioritised for the 3D response, since this was also arguably of most interest for the study. Azido-L-proline was added to the culture medium of experimental 3D samples and subsequently imaged after incorporation into neocollagen through the Click-IT Alex Fluor 594 DIBO Alkyne reaction with the azido-L-proline (Bardsley *et al*., 2017). As presented, cytokines TGF-β, TNF-α and VEGF, plus 50% aqueous humour, all appeared to stimulate an increase in TCCT fibroblast neocollagen synthesis in comparison to the control, with 50% aqueous humour having the greatest effect. Exposure to shear stress also appeared to trigger an increase in neocollagen synthesis, though this difference was subtle. These results therefore confirm the influence that cytokines and shear stress are likely to have on TCCT ECM synthesis, in addition to an increase in metabolic activity. Additionally, neocollagen fluorescent labelling was an advantageous technique for determining the fibrosis response of TCCT fibroblasts over a prolonged culture time period.

3.4.5 The influence of conjunctival epithelium on TCCT fibrosis

To determine the potential influence that conjunctival epithelium may have on TCCT fibrosis, a secondary aim was to establish a 3D TCCT fibroblast-epithelium co-culture model. The isolated porcine conjunctival epithelial cells were characterised using cytokeratin 3; one of several markers acknowledged in previous literature for its ability to distinguish conjunctival epithelial cells (Silber *et al.*, 2015).

Culture insert use was tested for culture of conjunctival epithelium on top of the 3D TCCT fibroblast model, in reference to previous literature reporting an air-liquid interface for

ocular co-culture (Shafaie *et al.*, 2016; He *et al.*, 2018). Interestingly, TCCT samples co-cultured without inserts appeared to metabolise significantly more than samples cultured with the use of inserts. This confirmed that the conjunctival epithelium had likely adhered to the 3D fibroblast model and wasn't 'washed away' by culture medium coverage. Secondly, this indicated that full culture medium coverage may have been more beneficial for conjunctival epithelial cell growth in comparison to an air-liquid interface. Since conjunctiva is a mucous membrane surrounded by the eye lid and eye socket *in vivo*, it may not be exposed to as much of an air-liquid interface *in vivo* in comparison to corneal epithelium.

Interestingly, conjunctival epithelium seeded on top of collagen hydrogel constructs appeared to be significantly more metabolically active in comparison to TCCT fibroblasts seeded within collagen hydrogel. This could have been due to the fact that epithelial cells were seeded on top of the collagen gels rather than inside them, since shear stress is a surface layer effect, plus many cell types proliferate faster in 2D culture than 3D due to reduced resistance for cellular migration (Edmondson *et al.*, 2014). Additionally, the effect of shear stress on the 3D TCCT fibroblast-epithelium co-culture model appeared to be greater in comparison to the 3D TCCT fibroblast model without epithelium. These findings may be supported by previous studies of shear stress on similar ocular surface epithelial cells. For example, Kang *et al.*, (2014) previously reported flow-induced shear stress to increase the proliferation of *in vitro* limbal epithelial stem cells. Furthermore, studies such as Molladavoodi *et al.*, (2017) have reported flow-induced shear stress to influence cytoskeleton reorganisation and increase the proliferation and migration of *in vitro* corneal epithelial cells during wound healing.

TCCT fibroblast-epithelium co-culture metabolic activity also appeared to increase when treated with TGF-β, increasing even further with additional exposure to shear stress. However, some previous studies on healthy skin and ocular surface epithelium would not support this finding (Zheng *et al.*, 2010; Law *et al.*, 2016; Utsunomiya *et al.*, 2016), since TGF-β is thought to inhibit the effect of epidermal growth factor. Therefore, whilst elevated TGF-β levels triggered by ocular surface disease and shear stress can promote the metabolic activity of fibroblasts, it may also inhibit the metabolic activity of epithelial cells. Nevertheless, these findings may be characteristic of what would be expected for injured epithelium. Since conjunctival epithelial cells were seeded on top of the 3D TCCT model gel using a cell culture pipette, any unevenly distributed areas, plus the edges of each gel, would have been 'incomplete' and therefore potentially mimicking injured epithelium. According to Izumi et al., (2005), a healthy/complete corneal epithelial cell layer protects and suppresses any abnormal proliferation and differentiation of fibroblasts via regulation of TGF-β and basic fibroblast growth factor (bFGF) signalling. However, when epithelial layers are injured/disrupted they are thought to release various growth factors triggering events such as fibroblast proliferation, migration and differentiation into myofibroblasts (Kunihiko *et al.*, 2002; He *et al.*, 2017; Richardson, 2017). The increase in metabolic activity observed in the 3D TCCT fibroblast-epithelium co-culture model may therefore be explained by the fact that the model mimicked the activity of injured epithelial cells and therefore further promoted metabolic activity.

Since the epithelial cells in this study were isolated using a 'scraping' method, some fibroblasts may have been mixed with the cultured epithelial cells from tissue underneath the epithelium. This could also explain for any unusual increases observed with exposure to growth factors and shear stress. Though scraping methods have been used successfully in previous literature (Wei *et al.*, 1993; Cook *et al.*, 1998), the use of better tools (e.g.

Jeweler's forceps) and a more specialised dissection protocol to peel away the epithelium might have improved this technique (Geggel and Gipson, 1984; Niiya *et al.*, 1997). Consequently, further experiments would be required in order to draw an accurate conclusion from these results.

3.5 Conclusion

To summarise, this study utilised 2D and 3D TCCT models to investigate the factors which may influence the fibrosis response after trabeculectomy surgery. Initial establishment of the 2D TCCT fibroblast model was a useful starting point for this study, since it enabled assessment of the direct influence that growth factors and shear stress may have on TCCT fibroblasts, without a surrounding ECM. Subsequent establishment of the 3D TCCT fibroblast model added further value, which enabled assessment of the additional influence that ECM may have on the fibroblasts and fibrotic response, and allowed the simulation of post-operative fibrosis in trabeculectomy. Key results confirm that a combination of both the cytokines and growth factors present in aqueous humour, as well as the shear stress induced by aqueous fluid outflow, may synergistically stimulate the metabolic response in TCCT after trabeculectomy surgery. To assess the fibrotic response further, a new fluorescent labelling technique to image the neocollagen produced by TCCT fibroblasts was applied to the 3D model, which allowed for a better determination of the fibrosis response in addition to metabolic activity assessments. Furthermore, the established 3D TCCT fibroblast-epithelium co-culture model potentially mimics injured conjunctival epithelium, which may further stimulate the fibrotic response. These novel findings offer a useful insight for further study into the wound healing response triggered by aqueous fluid outflow after glaucoma surgery.

Chapter 4

Evaluation of glaucoma treatment efficacy and medical device assessment using the established Tenon's capsule and conjunctival tissue (TCCT) models

4.1 Introduction

Anti-metabolic drugs such as mitomycin C and 5-Fluorouracil are commonly used in an attempt to reduce the fibrotic response after glaucoma surgery. These mitigate TCCT fibrosis to an extent by triggering apoptosis of fibroblasts via disruption of DNA synthesis (Tomasz, 1995). However, even with their use intraoperatively the long-term failure rate of glaucoma surgery due to insufficient IOP control is around 46.9% (Suzuki *et al.*, 2002; Jampel *et al.*, 2005; Franz Marie *et al.*, 2009; Gedde *et al.*, 2012). Furthermore, the inhibitory mechanism is highly toxic and can lead to additional complications such as sub-conjunctival bleb thinning and leakage, cytotoxicity and damage to other tissues such as the cornea (Wolner *et al.*, 1991; Stamper *et al*., 1992). Therefore, there is a high demand for more efficient anti-inflammatory agents to target key factors involved in the fibrosis process more specifically. Furthermore, these issues have led to an increased interest in the use of medical devices, such as the Xen Gel Stent, to improve the efficiency of glaucoma filtration surgery and reduce the detrimental effect of fibrosis.

Since growth factor (e.g. TGF-β) upregulation is believed to be one of the major mechanisms stimulating scar tissue formation after glaucoma surgery (Khaw *et al*., 1994, Grisanti *et al*., 2005), the use of growth factor inhibitors is an interesting potential method to reduce the rate of TCCT fibrosis. Proteoglycans such as decorin also have the potential to reduce TCCT fibrotic response rate. Decorin proteoglycan is found in the extracellular matrix of various tissues and is known to interact with several proteins involved with matrix assembly, cell adhesion, migration and proliferation. Decorin is recognised for its role in growth factor interaction, for example, it has the ability to bind to TGF-β and potentially neutralise its activity (Hildebrand *et al.*, 1994). As decorin is naturally already present in cells, it may offer a less toxic and therefore safer method to control fibrosis

response after glaucoma surgery. Decorin has previously been proven as an effective anti-scarring agent for the cornea (Hill *et al.*, 2018; Chouhan *et al.*, 2019) and trabecular meshwork (Hill *et al.*, 2015). Furthermore, the experimental application of decorin has previously been reported to reduce conjunctival fibrosis in rabbits (Grisanti *et al.*, 2005). In addition, the use of calcium signalling channel blockers, such as nifedipine, are another potential mechanism for TCCT fibrosis reduction. Previous studies have demonstrated the use of nifedipine for fibrotic response reduction in tissues such as lung (Matta *et al*., 2015; Mukherjee *et al.*, 2015). However, no previous studies have tested the use of nifedipine for potential conjunctival fibrotic response reduction. It was therefore of interest to test these potential inhibitors on the established TCCT fibrosis model.

An alternative method to improve the outcome of glaucoma surgery, in addition to drug treatment optimisation, is with the use of medical devices such as the Xen Gel Stent for minimally invasive glaucoma surgery. The Xen Gel Stent, manufactured by Allergan, is a gelatin derived stent inserted into the subconjunctival space to create an alternative diffuse outflow pathway by which aqueous fluid can drain and thereby reduce IOP. One of the claimed benefits is that the stent is made from gelatin cross-linked with glutaraldehyde, hence, it is non-degradable, causes less foreign body reaction and can bend/conform in tissue to reduce the risk of erosion (Dervenis *et al.*, 2017). When hydrated the stent is claimed to be soft and tissue conforming, making it possible to manipulate the stent into the desired position. Similar to the trabeculectomy procedure, a subconjunctival bleb remains which is examined and monitored over time (Allergan, 2017). However, recent case studies highlighting problems with the Xen Gel Stent raise scepticism regarding its use (Fea *et al.*, 2015; Fernández-García *et al*., 2015; Ferreira *et al*, 2017). It may therefore be valuable to assess the stent within the established TCCT fibrosis model.

4.2 Aim

This study aimed to utilise the established 2D and 3D TCCT fibrosis models for investigation of fibrosis response reduction and glaucoma medical device assessment. The first objective was to assess the effect of intraoperative antimetabolite mitomycin C on TCCT fibroblast metabolism, followed by key growth factor inhibitors, decorin proteoglycan and L-type calcium signalling channel blocker nifedipine. In addition, the study aimed to undertake *in vitro* assessment of the Xen Gel Stent glaucoma medical device within the established TCCT fibrosis model.

4.3 Results

4.3.1 Effect of mitomycin C on metabolic function in the TCCT fibroblast model

Mitomycin C was initially tested on 3D cultured TCCT fibroblasts via topical application (10 µL droplet of 0.2 mg/mL mitomycin C solution) to mimic the clinical application process. The metabolic function, an indicator of proliferation for the fibroblasts, was assessed. As shown in Figure 4.1, 3D TCCT fibroblasts treated with mitomycin C had 31.6% less metabolic activity in comparison to the untreated control at day 3 (p= 0.043), 7.5% less at day 5 (not significant), 93.2% less at day 7 (p=0.003) and 93.3% less at day 14 (p= 0.002). As would be expected, TCCT fibroblasts had a decrease in metabolic activity following treatment with mitomycin C, observed at the day 3 time point. Whilst the treated fibroblasts appeared to have some increase in proliferation rate at the day 5 time point, cellular metabolism evidently did not fully recover and metabolism declined significantly in the long term by day 7 and 14.

Figure 4.1 The effect of mitomycin C on TCCT fibroblast metabolic function

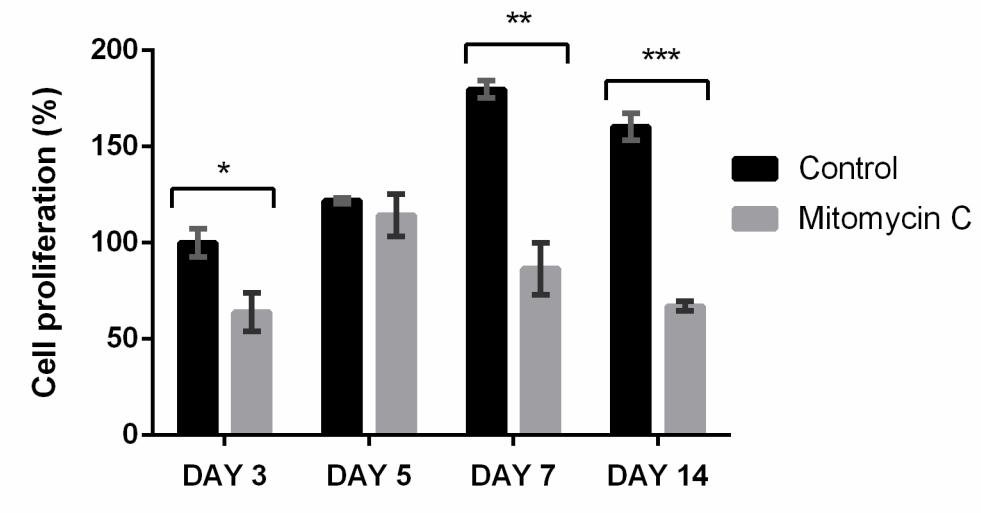

AlamarBlue® assay to assess the effect of topically applied mitomycin C (10 µL; one application at Day 1) on 3D TCCT fibroblast metabolic function. Data are expressed as mean ± SE (n=3). * indicates p <0.05, ** indicates p <0.01 and *** indicates p <0.005.

4.3.2 Assessment of growth factor inhibitors in the TCCT fibroblast model

4.3.2.1 Effect of TGF-β inhibitor on metabolic function in the TCCT model

For the investigation of potential alternative anti-fibrotic agents, TGF-β RI Kinase Inhibitor VI (10 μM) was tested on 3D TCCT fibroblasts cultured in medium containing 50% aqueous humour. The metabolic function, an indicator of proliferation for the fibroblasts, was assessed. As shown in Figure 4.2, TGF-β inhibitor significantly reduced the metabolic increase stimulated by 50% aqueous humour. Metabolic activity was 103.7% less at day 3 (p= 0.002), 201.7% less at day 5 (p= 0.004) and 152.5% less at day 7 (p=0.03), in comparison to fibroblasts treated with 50% aqueous humour without inhibitor.

Figure 4.2 The effect of TGF-β inhibitor on TCCT fibroblast metabolic function

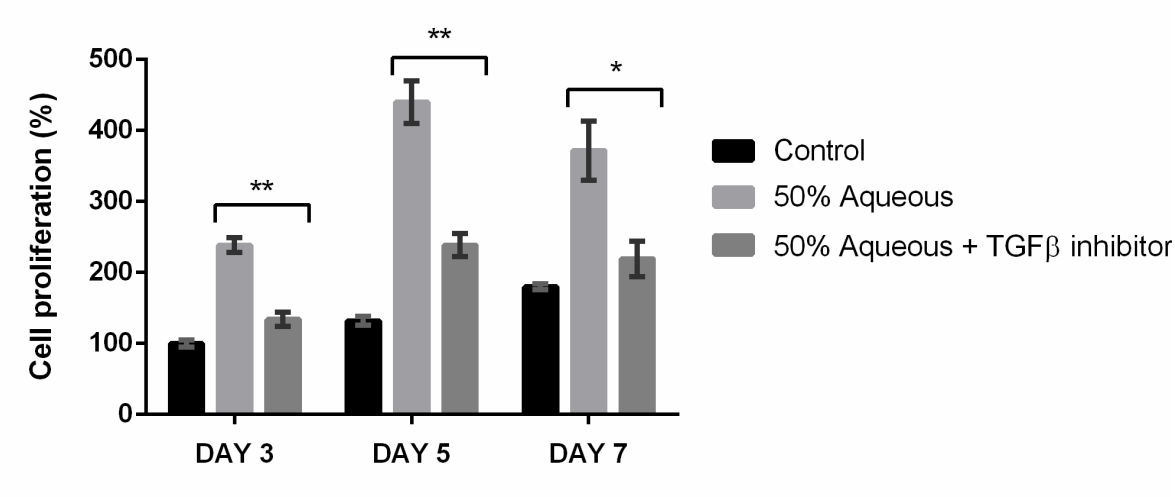

AlamarBlue® assay to assess the effect of TGF-β inhibitor (10 μM; application at Day 1, 3 and 5 via addition to culture medium) on the metabolic function of 3D TCCT fibroblasts cultured in medium containing 50% aqueous humour. Data are expressed as mean ± SE (n=3). * indicates p <0.05, ** indicates p <0.01.

4.3.2.2 Effect of TNF-α inhibitor on metabolic function in the TCCT model

TNF-α inhibitor (SPD304; 10 μM) was also tested on 3D TCCT fibroblasts cultured in medium containing 50% aqueous humour. The metabolic function, an indicator of

proliferation for the fibroblasts, was assessed. As shown in Figure 4.3, TNF-α inhibitor significantly reduced the metabolic increase stimulated by 50% aqueous humour, in comparison to 50% aqueous humour without inhibitor. Metabolic activity was 73.9% less at day 3 (p=0.002), 281.9% less at day 5 (p= 0.0007) and 201.1% less at day 7 (p=0.008).

Figure 4.3 The effect of TNF-α inhibitor on TCCT fibroblast metabolic function

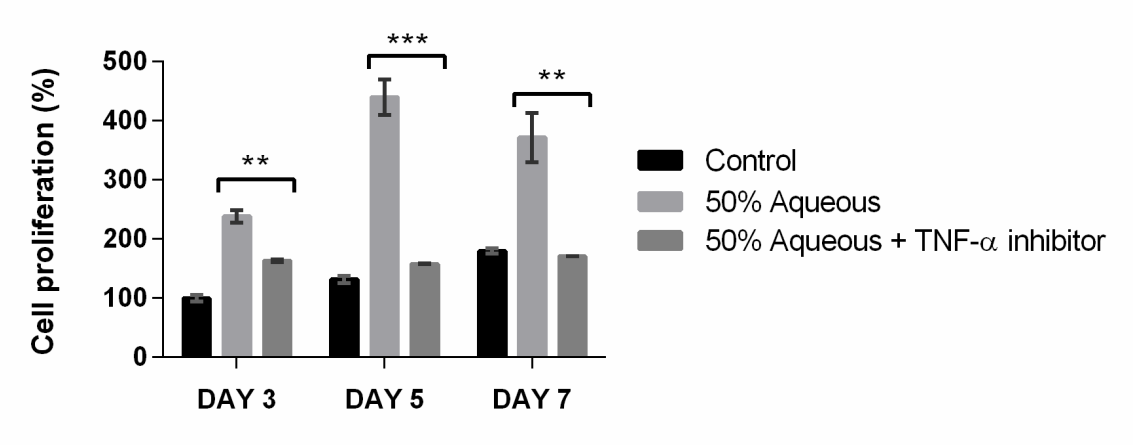

AlamarBlue® assay to assess the effect of TNF-α inhibitor (10 μM; application at Day 1, 3 and 5 via addition to culture medium) on the metabolic function of 3D TCCT fibroblasts cultured in medium containing 50% aqueous humour. Data are expressed as mean ± SE (n=3). * indicates p <0.05, ** indicates p <0.01 and *** indicates p <0.005.

4.3.2.3 Assessment of F-actin expression in response to growth factor inhibitors

Cellular morphology and F-actin expression also appeared to differ in the presence of 50% aqueous humour, with and without the presence of growth factor inhibitors, as shown in Figure 4.4. As observed in previous results (Figure 3.6), 3D TCCT samples cultured with 50% aqueous humour showed an evident increase in F-actin expression in comparison to the control group. This increase was evidently reduced with the addition of TGF-β and TNF-α inhibitor. Cellular morphology also appeared to change, with fibroblast shape being less defined and elongated with the addition of growth factor inhibitors.

Figure 4.4 Effect of growth factor inhibitors on fibroblast F-actin expression

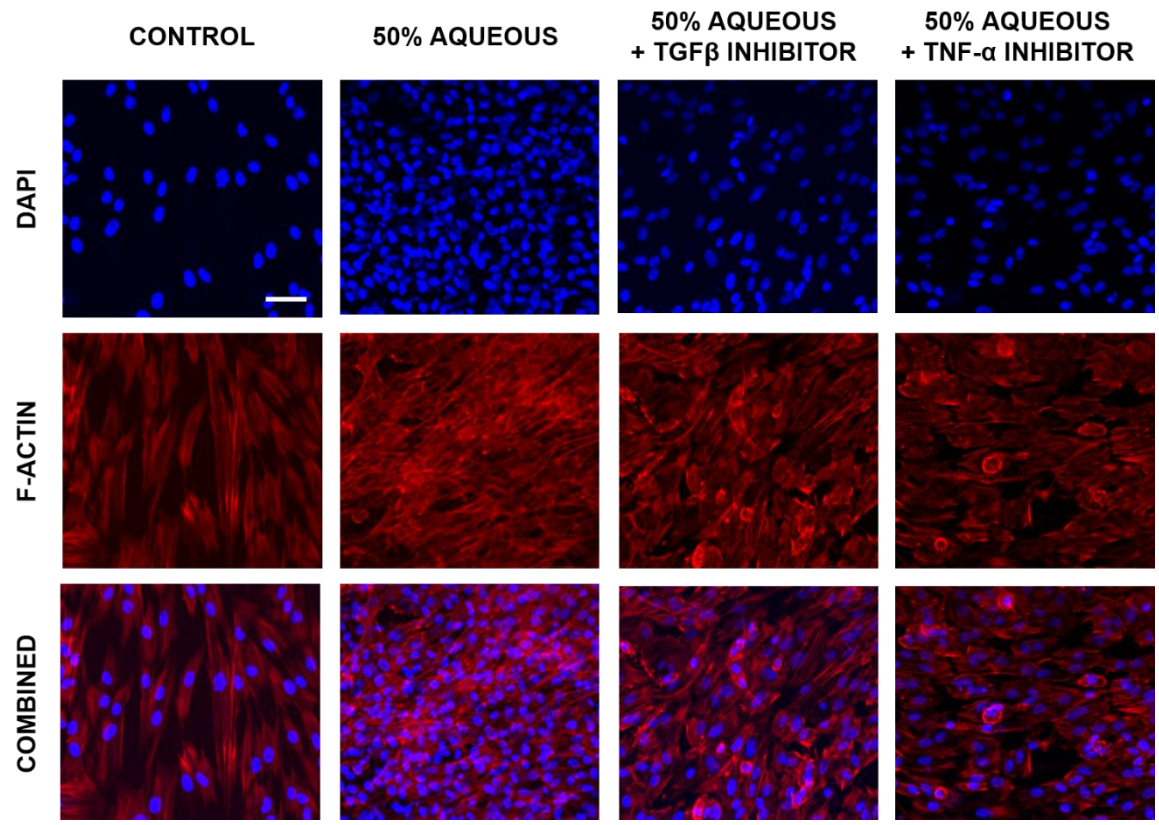

DAPI (blue) and F-actin (red) to indicate differences in cellular morphology and F-actin expression between 3D TCCT model fibroblasts cultured with 50% aqueous humour, with and without TGF-β and TNF-α growth factor inhibitors (n=3). Scale bar = 50 µm.

4.3.3 Assessment of decorin proteoglycan in the TCCT fibroblast model

4.3.3.1 Effect of decorin proteoglycan on metabolic function in 3D model

Low (0.2 µg/mL) and high (100 µg/mL) dosage decorin, a proteoglycan acknowledged in previous literature for its potential ability to modulate wound healing responses, was tested on 3D cultured TCCT fibroblasts with and without exposure to shear stress. As shown in Figure 4.5, decorin proteoglycan had an inhibitory effect on 3D fibroblast metabolic activity at 0.2 µg/mL dosage. For example, at day 5 metabolic activity appeared to decrease by 41.37% (p=0.02; without exposure to shear stress) and 53.1% (p= 0.001; with shear stress), with a similar trend observed across the other time points.

Figure 4.5 The effect of low decorin on 3D TCCT fibroblast metabolic function

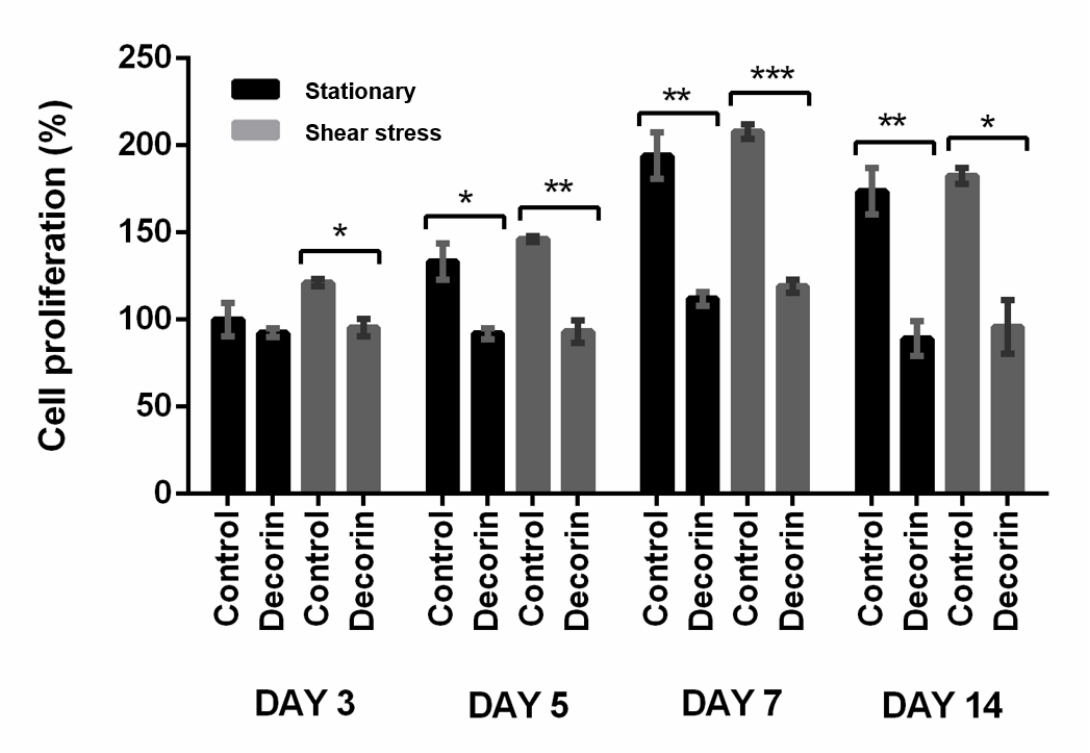

AlamarBlue® assay to assess the effect of low (0.2 µg/mL) dosage decorin on the metabolic function of 3D TCCT fibroblasts cultured with and without exposure to shear stress. Data are expressed as mean ± SE (n=3). * indicates p <0.05, ** indicates p <0.01 and *** indicates p <0.005.

As shown in Figure 4.6, decorin proteoglycan also had an inhibitory effect on 3D TCCT fibroblast metabolic activity at 100 µg/mL dosage. For example, at day 5 metabolic rate appeared to decrease by 45.5% (p=0.02; without exposure to shear stress) and 46.2% (p= 0.0005; with shear stress), with a similar trend observed across the other time points.

Figure 4.6 The effect of high decorin on 3D TCCT fibroblast metabolic function

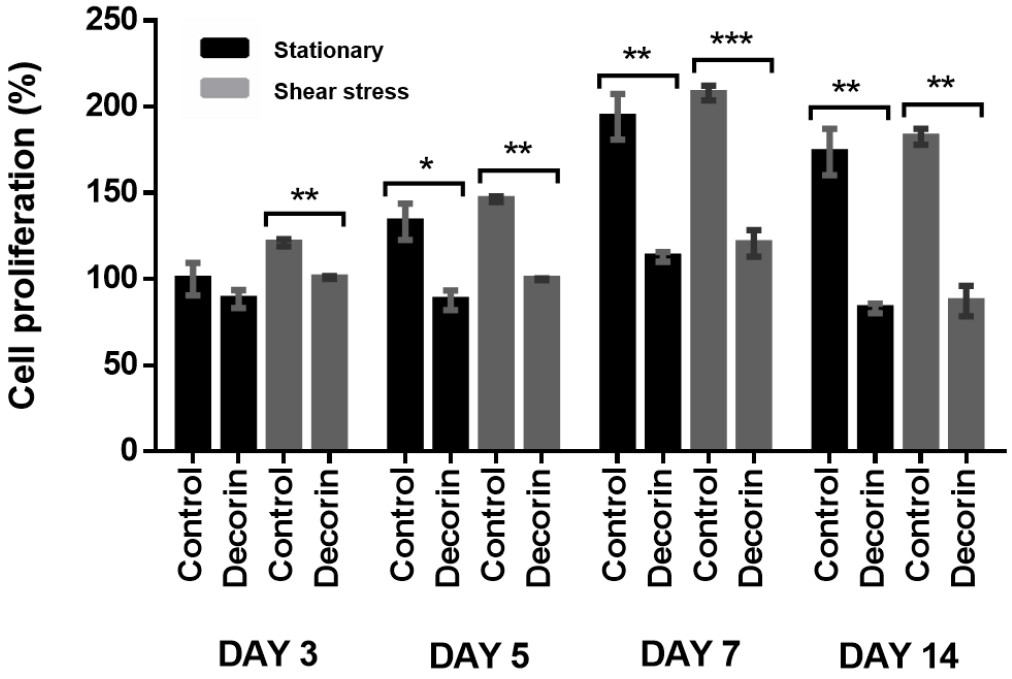

AlamarBlue® assay to assess the effect of high (100 µg/mL) dosage decorin on the metabolic function of 3D TCCT fibroblasts cultured with and without exposure to shear stress. Data are expressed as mean ± SE (n=3). * indicates p <0.05, ** indicates p <0.01 and *** indicates p <0.005.

4.3.3.3 Assessment of 3D TCCT neocollagen synthesis in response to decorin

Due to the known involvement of decorin proteoglycan in collagen synthesis, it was of interest to determine the neocollagen synthesis of TCCT fibroblasts treated with decorin. Azido-L-proline was added to the medium of experimental samples during culture and subsequently detected after incorporation into the neocollagen using Click-IT Alex Fluor 594 DIBO Alkyne stain. Figure 4.7 indicates the imaged neocollagen of 3D TCCT fibroblasts at day 14 of culture. Samples treated with decorin proteoglycan appeared to present more neocollagen than control samples. Furthermore, the quantity of labelled neocollagen appeared to be enhanced further with exposure to shear stress. Therefore, whilst decorin proteoglycan appeared to reduce the rate of fibroblast proliferation, it also appeared to increase the rate of neocollagen synthesis in TCCT.

Figure 4.7 The effect of decorin on 3D TCCT fibroblast neocollagen synthesis

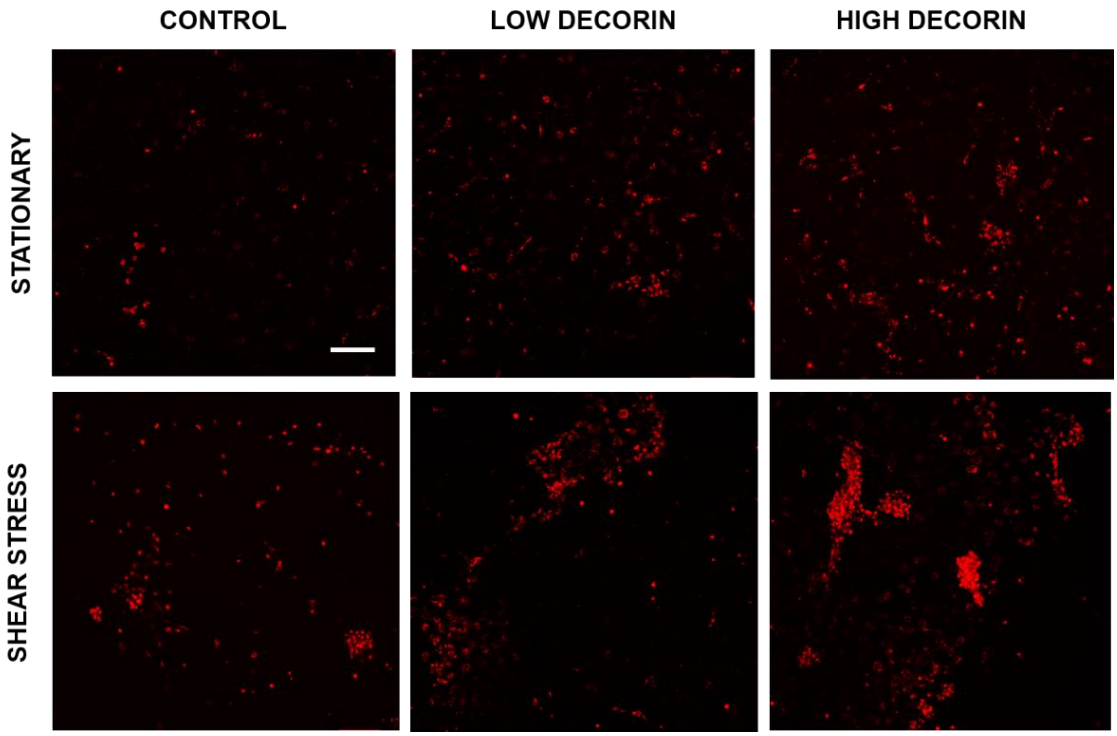

Imaging of neocollagen synthesis (red) monitored by Click-IT Alexa Fluor 594 DIBO Alkyne reaction with azido-L-proline, which was incorporated in the culture of 3D TCCT model samples treated with decorin proteoglycan under stationary and shear stress conditions (n=3). Scale bar = 150 μm.

4.3.4 Assessment of nifedipine on fibroblast calcium signalling in TCCT model

Another potential method acknowledged in previous literature to modulate fibrosis is the inhibition of calcium signalling (Matta *et al*., 2015; Mukherjee *et al.*, 2015). It was therefore of interest to assess the effect of growth factor and shear stress on TCCT fibroblast calcium signalling and test a known calcium channel blocker, nifedipine. As shown in Figure 4.8, exposure to TGF-β and shear stress appeared to increase TCCT fibroblast cytosolic calcium signalling. Furthermore, nifedipine appeared to modulate this response both individually and in combination with TGF-β and/or shear stress.

Figure 4.8 The effect of stimulators and nifedipine on TCCT calcium signalling

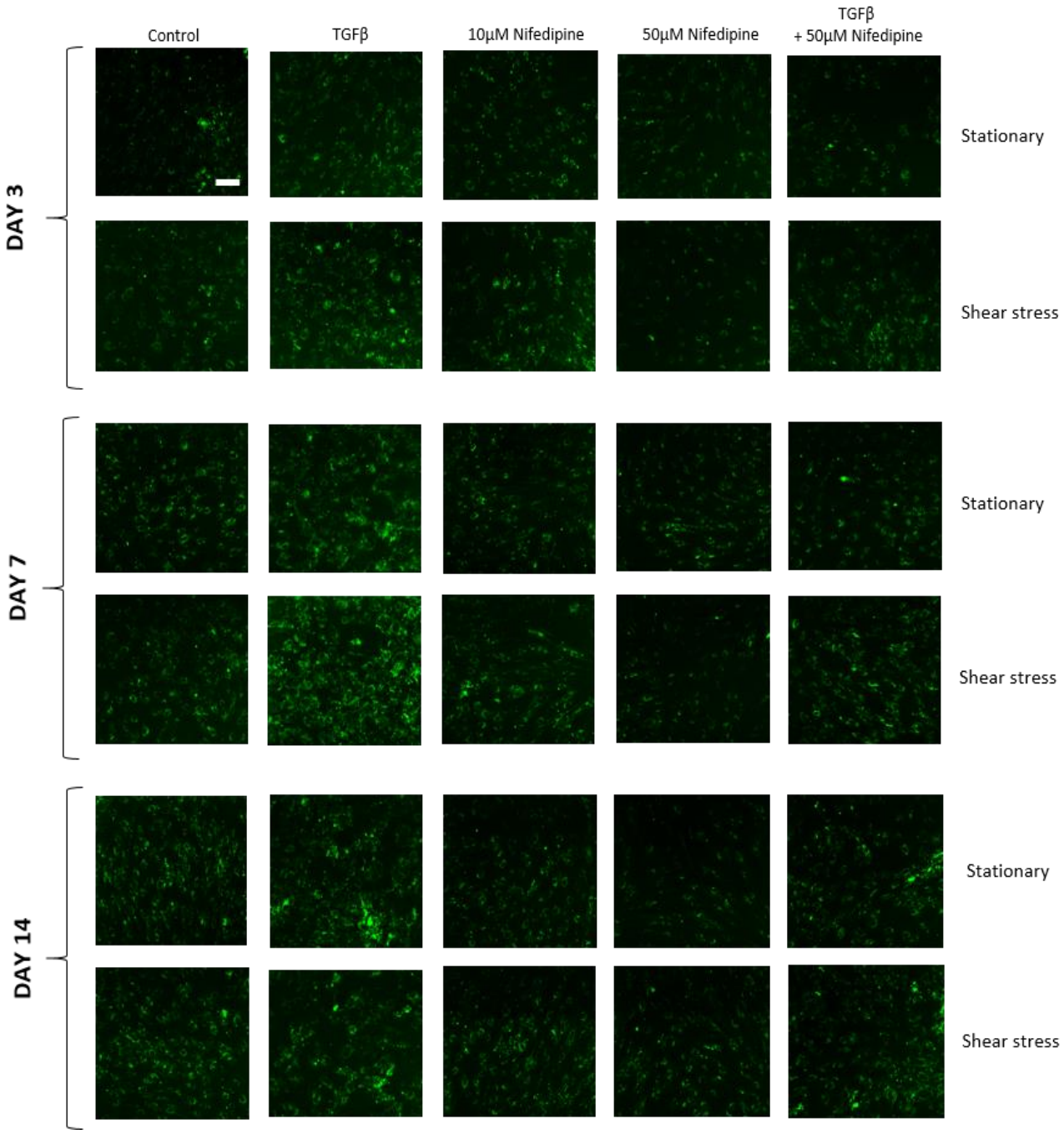

Images of 3D TCCT model Ca^{2+} signalling following treatment with TGF-β, nifedipine and TGF-β + nifedipine in combination, under stationary and shear stress conditions (n=3). TGF-β and/or nifedipine were administered every 2 days from Day 1, via addition to the culture medium. Cells were stimulated and labelled using Fluo-4 AM calcium indicator (green). Single images were taken at each time point. Scale bar = 150 μm.

Figure 4.9 presents the semi-quantified calcium signalling fluorescence intensity of 3D TCCT model fibroblasts at culture day 7, when the signalling was strongest. Similar to the images presented in Figure 4.8, exposure to TGF-β and shear stress appeared to increase TCCT fibroblast calcium signalling. Furthermore, nifedipine appeared to modulate this response. 50μM nifedipine appeared to significantly reduce calcium signalling of cultured fibroblasts (stationary) by approximately 32.9% (p= 0.024).

Figure 4.9 Semi-quantification of TCCT calcium signalling fluorescence intensity

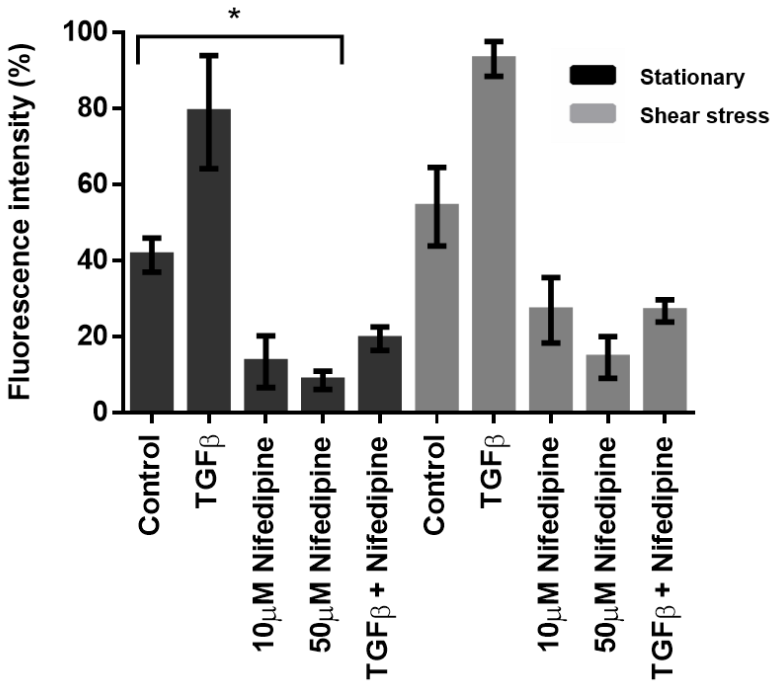

Semi-quantification of calcium signalling labelled using Fluo-4 AM calcium indicator on 3D TCCT samples treated with TGF-β, nifedipine and TGF-β + nifedipine in combination, under stationary and shear stress conditions (n=3). Images were semi-quantified using ImageJ software. Data are expressed as mean ± SE (n=3). * indicates p <0.05.

4.3.4.1 Effect of nifedipine on metabolic function in 2D TCCT model

Low (10μM), moderate (50μM) and high (100μM) dosage nifedipine was tested on 2D cultured TCCT fibroblasts with and without exposure to shear stress. Additionally, moderate dosage nifedipine was tested in combination with 20 ng/mL TGF-β growth factor

to assess whether its metabolic effect could be neutralised. As shown in Figure 4.10, nifedipine had some inhibitory effect on 2D TCCT fibroblast metabolic activity at 10µM dosage. Whilst no significant difference was observed at the day 3 time point, at day 5 metabolic rate appeared to decrease by 37.2% in comparison to control group (p=0.02) and 38.5% in comparison to shear stress control (p= 0.0004), with a similar pattern observed at the day 7 time point.

Figure 4.10 Effect of 10 µM nifedipine on 2D TCCT fibroblast metabolic function

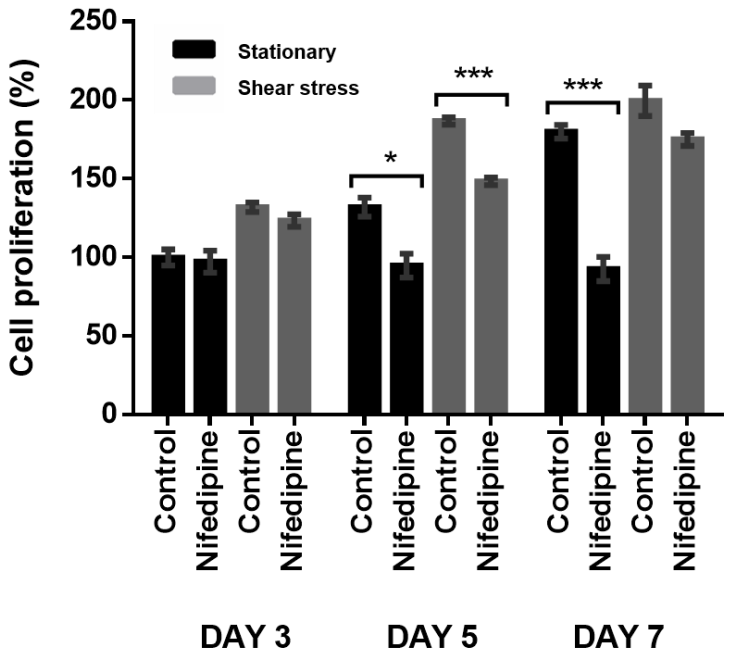

AlamarBlue® assay to assess the effect of 10 µM nifedipine on the metabolic function of 2D TCCT fibroblasts cultured with and without exposure to shear stress. Data are expressed as mean ± SE (n=3). * indicates p <0.05, ** indicates p <0.01 and *** indicates p <0.005.

As shown in Figure 4.11, nifedipine had a stronger inhibitory effect on 2D TCCT fibroblast metabolic activity at 50µM dosage. For example, at the day 3 time point metabolic rate decreased by 26.03% in comparison to control group (p=0.02) and 52.5% in comparison to shear stress control (p=0.0008). The decreased rate then remained constant for the day 5 and 7 time points.

Figure 4.11 Effect of 50 µM nifedipine on 2D TCCT fibroblast metabolic function

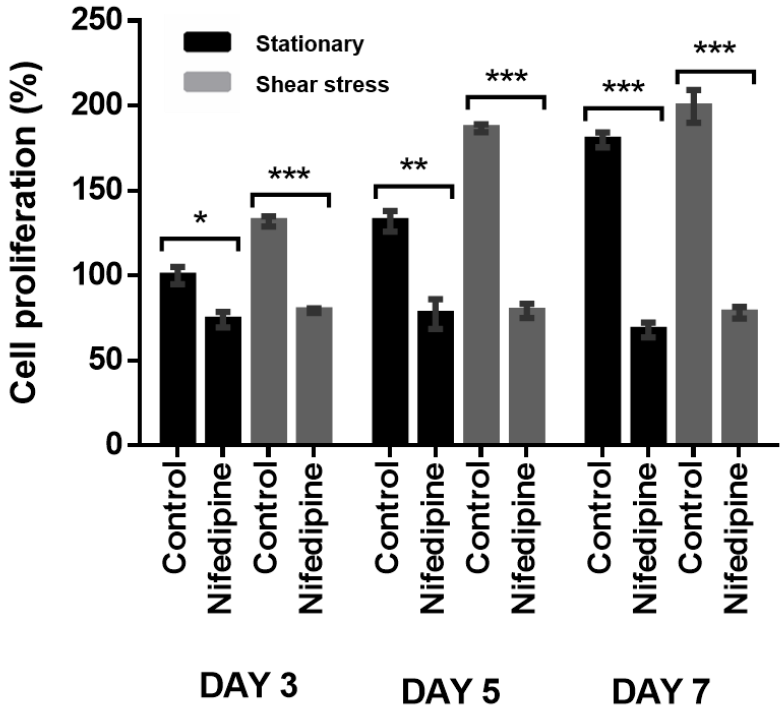

AlamarBlue® assay to assess the effect of 50 µM nifedipine on the metabolic function of 2D TCCT fibroblasts cultured with and without exposure to shear stress. Data are expressed as mean ± SE (n=3). * indicates p <0.05, ** indicates p <0.01 and *** indicates p <0.005.

As shown in Figure 4.12, nifedipine had an even stronger inhibitory effect on 2D TCCT fibroblast metabolic activity at 100µM dosage. For example, at the day 3 time point metabolic rate decreased by 44.2% in comparison to control group (p=0.001) and 76% in comparison to shear stress control (p=0.001). The decreased rate then remained constant for the day 5 and 7 time points.

Figure 4.12 Effect of 100 µM nifedipine on 2D TCCT fibroblast metabolic function

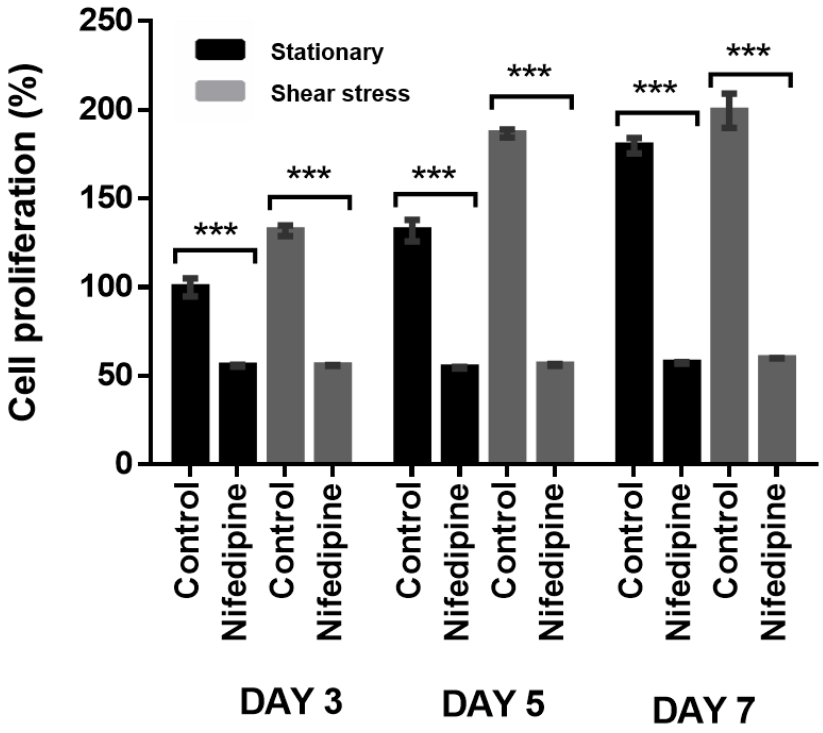

AlamarBlue® assay to assess the effect of 100 µM nifedipine on the metabolic function of 2D TCCT fibroblasts cultured with and without exposure to shear stress. Data are expressed as mean ± SE (n=3). * indicates p <0.05, ** indicates p <0.01 and *** indicates p <0.005.

As shown in Figure 4.13, 50µM nifedipine had a significant inhibitory effect on 2D TCCT fibroblasts treated with 20 ng/mL TGF-β. For example, at the day 3 time point metabolic rate decreased by 38% in comparison to TGF-β group (p= 0.002), counterbalancing the increase caused by TGF-β. The decreased rate then remained constant for the day 5 and 7 time points.

Figure 4.13 Effect of 50 µM nifedipine + TGF-β on 2D TCCT fibroblasts

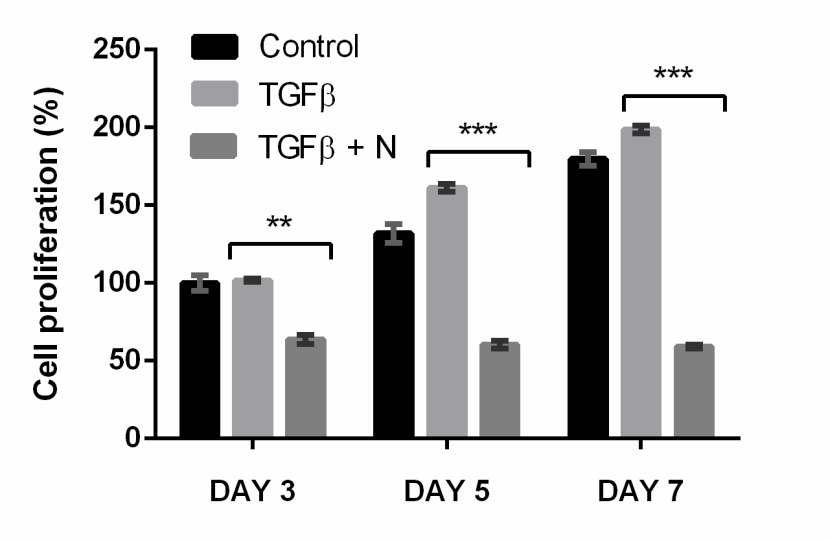

AlamarBlue® assay to assess the effect of 50 µM nifedipine on the metabolic function of 2D TCCT fibroblasts cultured in combination with 20 ng/mL TGF-β (D). Data are expressed as mean ± SE (n=3). * indicates p <0.05, ** indicates p <0.01 and *** indicates p <0.005.

4.3.4.2 Effect of nifedipine on metabolic function in 3D TCCT model

Low (10µM), moderate (50µM) and high (100µM) dosage nifedipine was tested on 3D cultured TCCT fibroblasts with and without exposure to shear stress. Additionally, moderate dosage nifedipine was tested in combination with 50 ng/mL TGF-β growth factor to assess whether its stimulatory effect could be neutralised. As shown in Figure 4.14, nifedipine had some inhibitory effect on 3D TCCT fibroblast metabolic activity at 10µM dosage. For example, at the day 3 time point metabolic rate decreased by 8% in comparison to the control group (p= 0.0001) and 12.9% in the shear stress group, with a similar trend observed at the day 5, 7 and 14 time points.

Figure 4.14 Effect of 10 µM nifedipine on 3D TCCT fibroblast metabolic function

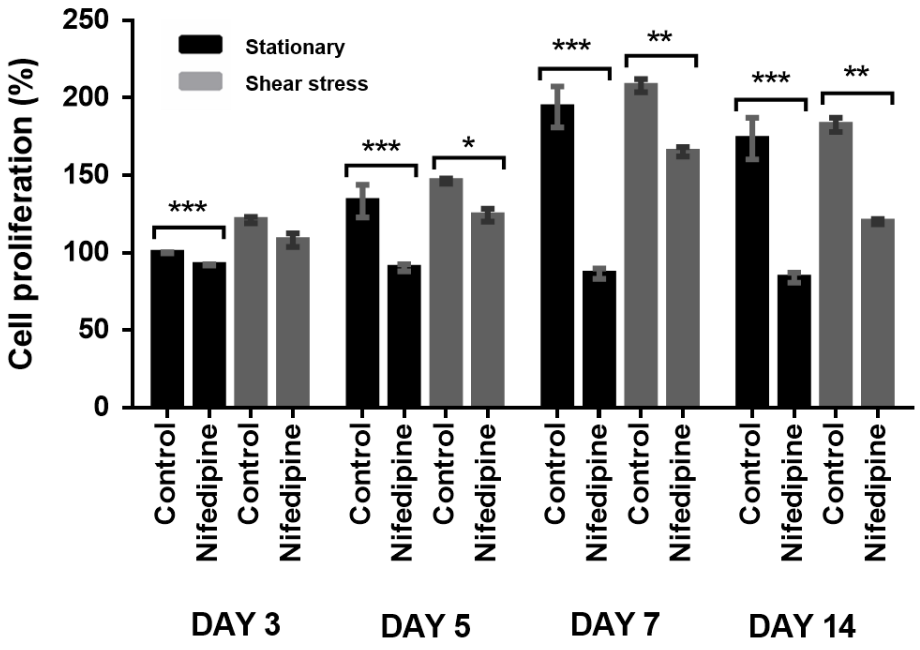

AlamarBlue® assay to assess the effect of 10 µM nifedipine on the metabolic function of 3D TCCT fibroblasts cultured with and without exposure to shear stress. Data are expressed as mean ± SE (n=3). * indicates p <0.05, ** indicates p <0.01 and *** indicates p <0.005.

As shown in Figure 4.15, nifedipine had a stronger inhibitory effect on 3D TCCT fibroblast metabolic activity at 50µM dosage. For example, at the day 3 time point metabolic rate decreased by 25.1% in comparison to control group (p=0.0002) and 45.1% in comparison to shear stress control (p=0.002). The decreased rate then remained constant for the day 5, 7 and 14 time points.

Figure 4.15 Effect of 50 µM nifedipine on 3D TCCT fibroblast metabolic function

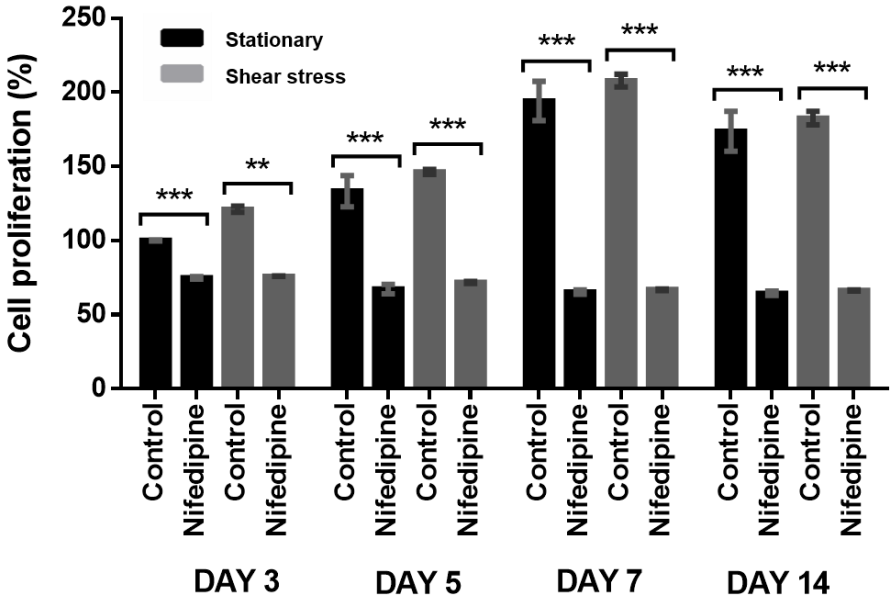

AlamarBlue® assay to assess the effect of 50 µM nifedipine on the metabolic function of 3D TCCT fibroblasts cultured with and without exposure to shear stress. Data are expressed as mean ± SE (n=3). * indicates p <0.05, ** indicates p <0.01 and *** indicates p <0.005.

As shown in Figure 4.16, nifedipine had an even stronger inhibitory effect on 3D TCCT fibroblast metabolic activity at 100µM dosage. For example, at the day 3 time point metabolic rate decreased by 38.4% in comparison to control group (p=0.0001) and 59.3% in comparison to shear stress control (p=0.001). The decreased rate then remained constant for the day 5, 7 and 14 time points.

Figure 4.16 Effect of 100 µM nifedipine on 3D TCCT fibroblast metabolic function

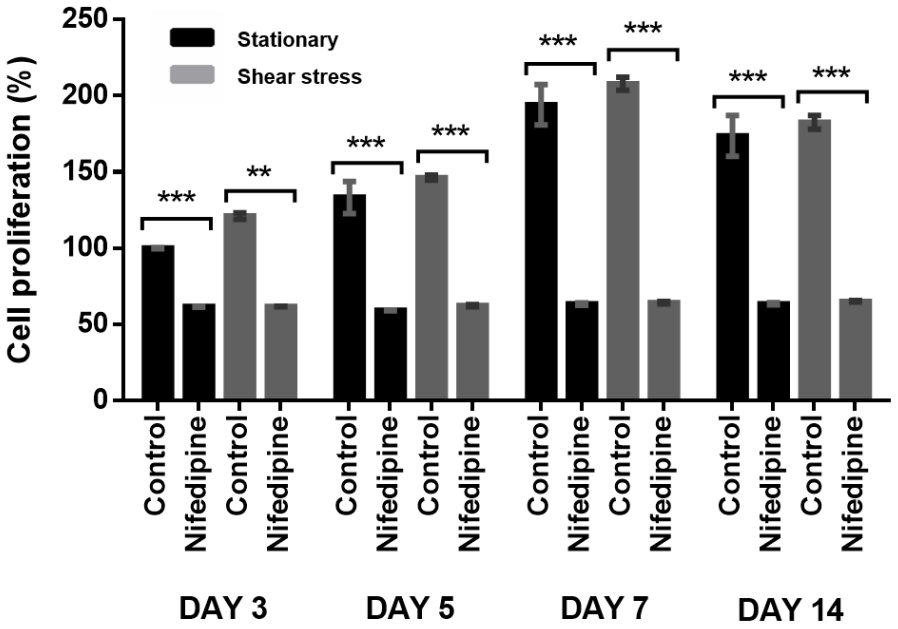

AlamarBlue® assay to assess the effect of 100 µM nifedipine on the metabolic function of 3D TCCT fibroblasts cultured with and without exposure to shear stress. Data are expressed as mean ± SE (n=3). * indicates p <0.05, ** indicates p <0.01 and *** indicates p <0.005.

As shown in Figure 4.17, 50µM nifedipine still had a significant inhibitory effect on 3D TCCT fibroblasts treated with 50 ng/mL TGF-β. For example, at the day 3 time point metabolic rate decreased by 42.6% in comparison to TGF-β group (p= 0.002), counterbalancing the 15.2% increase caused by TGF-β (p=0.047).

Figure 4.17 Effect of 50 µM nifedipine + TGF-β on 3D TCCT fibroblasts

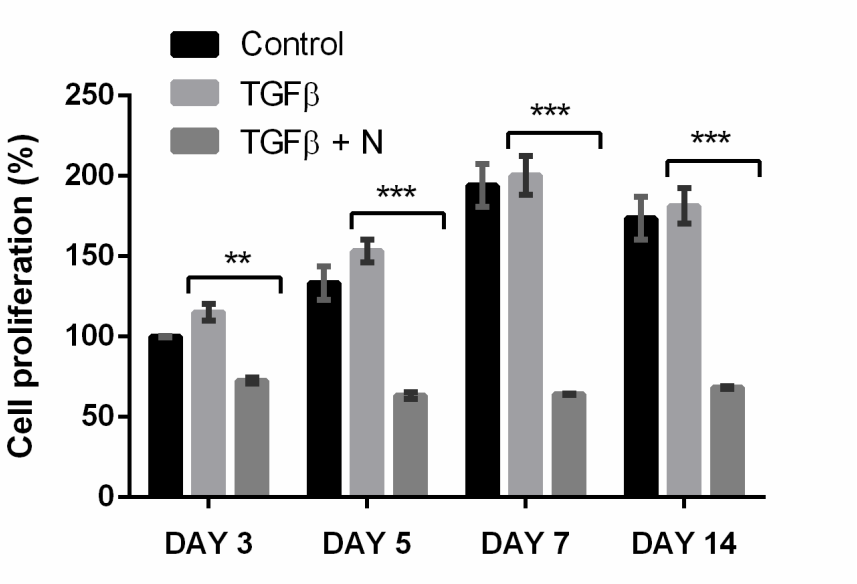

AlamarBlue® assay to assess the effect of 50 µM nifedipine on the metabolic function of 3D TCCT fibroblasts cultured in combination with 50 ng/mL TGF-β. Data are expressed as mean ± SE (n=3). * indicates p <0.05, ** indicates p <0.01 and *** indicates p <0.005.

4.3.5 *In vitro* assessment of Xen Gel Stent glaucoma medical device

Alternative methods which aim to improve the outcome of glaucoma filtration surgery include the use of medical devices, such as the Xen Gel Stent. Though the Xen Gel Stent is claimed to measure 6 mm in length with an internal diameter of 45 µm by the manufacturer, the differences in size and morphology before and after insertion remain unclear. It was therefore of interest to initially assess Xen Gel Stent size and morphology before and after hydration and following insertion into the 3D TCCT fibroblast model. As shown in Figure 4.18, before hydration the Xen Gel Stent measured to be approximately 4 mm in length with a diameter of 28.8 µm internally and 153.8 µm externally. Following submersion in sterile water, the stent size increased to 6 mm in length with a diameter of 43.3 µm internally and 211.5 µm externally, therefore expanding in width by approximately 150.3% internally and 137.5% externally.

Figure 4.18 Imaging of Xen Gel Stent medical device before and after hydration

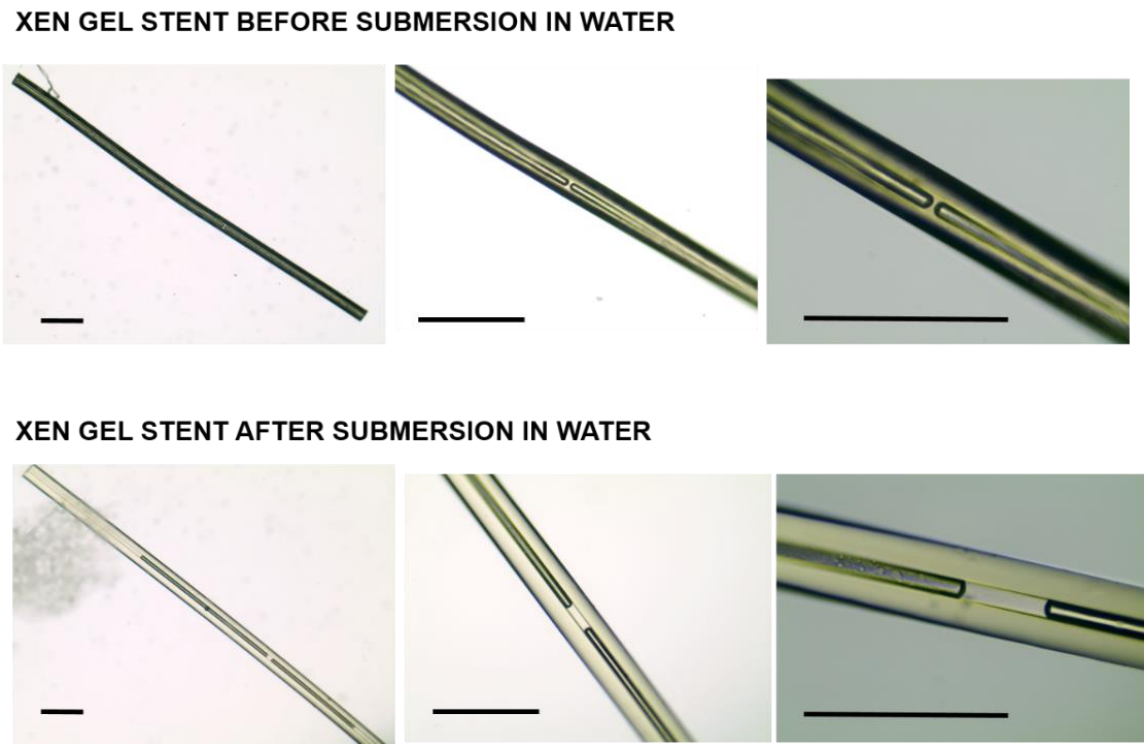

Xen Gel Stent medical device before and after submersion in water. Scale bar = 500 µm.

Xen Gel Stents were inserted into the 3D TCCT fibroblast model using the accompanying Xen Injector device. Despite practice beforehand, the stents were found to be very fragile and would become damaged during insertion. Though the manufacturer claims that hydration makes the device easier to manipulate, it was found to become too soft to push into the collagen hydrogel if hydrated. Furthermore, applying too much pressure with the Xen Injector needle would cause detrimental damage to the gel. It was therefore easier to insert the stents dry and allow hydration naturally once inside. However, even following this technique approximately one third of the stents available broke apart or became damaged during insertion. Figure 4.19 presents examples of a successfully inserted (intact) stent and a damaged one.

Figure 4.19 Xen Gel Stent medical device following insertion into 3D TCCT model

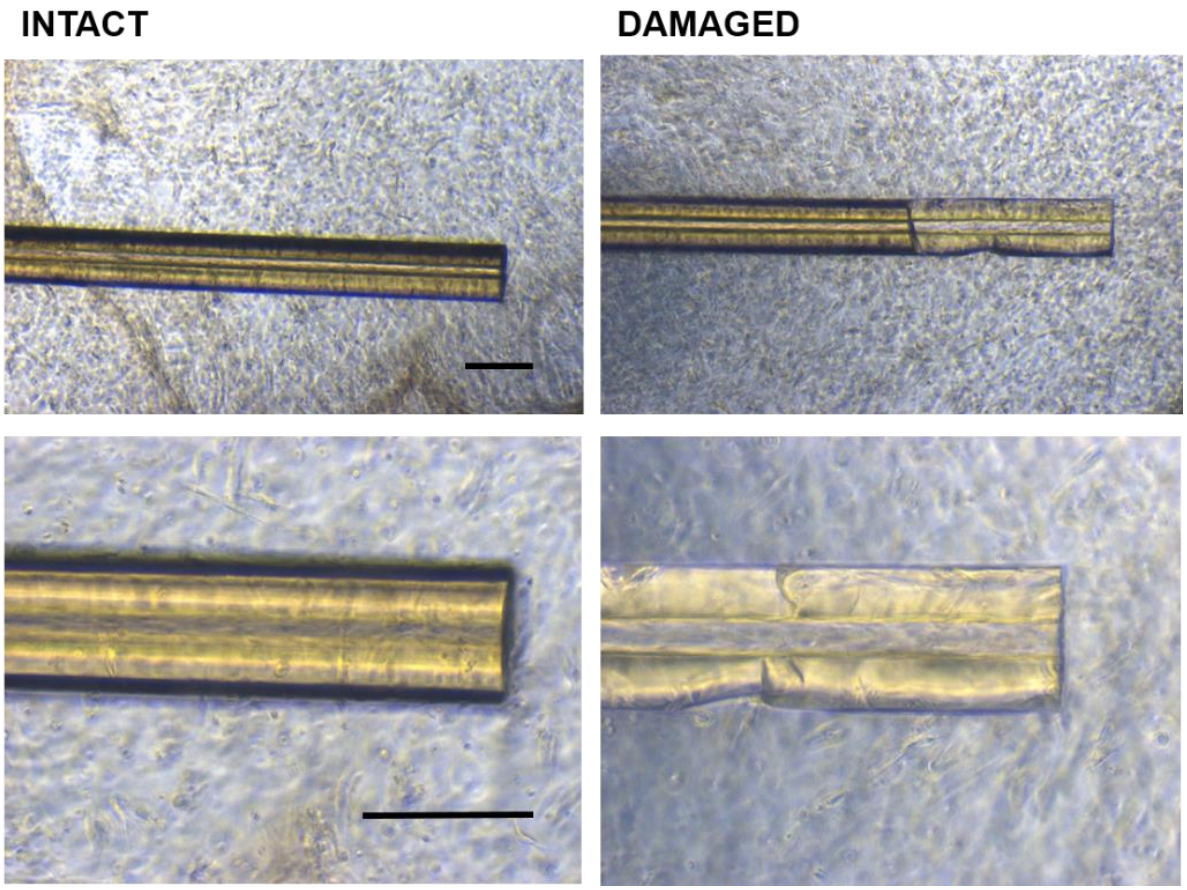

Examples of intact and damaged Xen Gel Stents immediately following insertion into the 3D TCCT fibroblast model. Scale bar = 500 µm.

Following insertion into the 3D TCCT fibroblast model the intact stents measured at approximately 5.9 mm in length with a diameter of 42.3 µm internally and 206.4 µm externally. In comparison to stent size before insertion, it therefore expanded by approximately 147% internally and 134.2% externally within the model. As shown in Figure 4.20, although difficult to image the fibroblast activity using light microscopy, Xen Gel Stent size and morphology appeared to remain consistent within the 3D model across the day 3, 7 and 14 time points with and without exposure to TGF-β.

Figure 4.20 Morphology of Xen Gel Stent maintained within 3D TCCT model over time

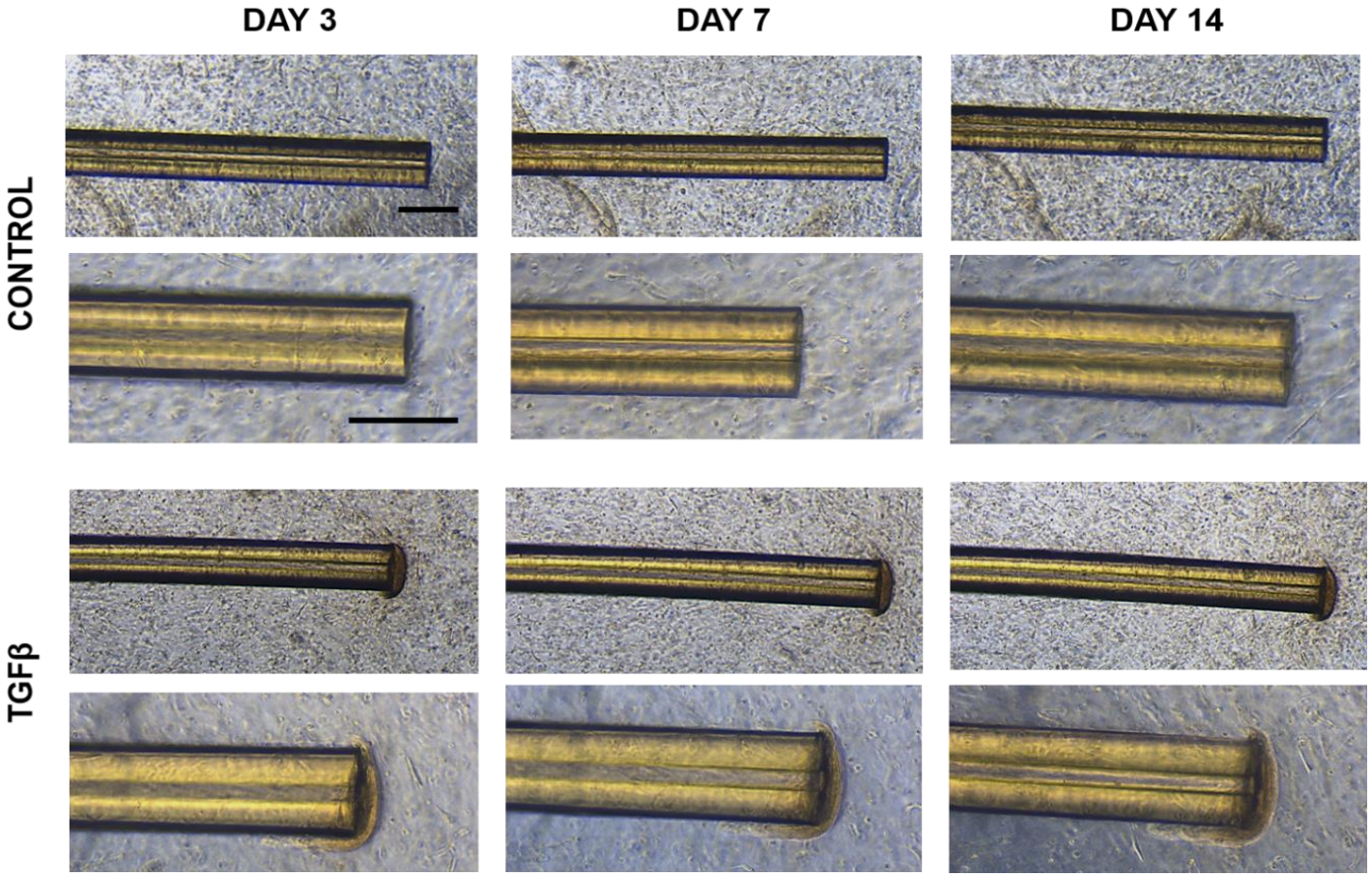

Xen Gel Stent following insertion into 3D TCCT fibroblast model over time, with and without exposure to TGF-β (n=2). Scale bar = 500 μm.

Whilst there is some deformation apparent at the Xen Gel Stent tip location between the control and TGF-β conditions in Figure 4.14, it is thought that this distortion occurred by chance during the insertion process.

4.3.5.2 Assessment of TCCT fibroblast activity surrounding Xen Gel Stent device

To assess fibroblast activity surrounding the Xen Gel Stent device in a potentially fibrotic environment, fibroblast location and neocollagen synthesis was monitored surrounding the device (n=2) whilst cultured within the 3D TCCT fibroblast model treated with TGF-β. Since fibroblasts remain viable for approximately 2 weeks within the TCCT model (see Figure 3.3, chapter 3), the stent was imaged at 1 and 2 weeks following insertion. As shown in Figure 4.21, numerous fibroblasts appear to surround the stent lumen at both time points. These were thought to have been pressed towards the lumen during stent insertion as the device was pushed through the collagen gel matrix and may have increased in number slightly with proliferation. Whilst the fluorescence intensity of the cell tracker dye had decreased by the day 14 time point, fibroblasts still appeared to surround the stent lumen. Interestingly, the Click-IT Alexa Fluor 594 dye used to react with azido-L-proline for the neocollagen labelling appeared to also bind strongly with the Xen Gel Stent device. Whilst this made visualisation of the neocollagen slightly more difficult, it was beneficial for imaging stent location whilst inside the model. Labelled neocollagen appeared to be minimal at day 7, but evidently increased surrounding the fibroblasts by day 14. However, it should be noted that these experiments were limited by low sample numbers (to be discussed further in section 4.4.4).

Figure 4.21 TCCT fibroblast activity surrounding Xen Gel Stent over time

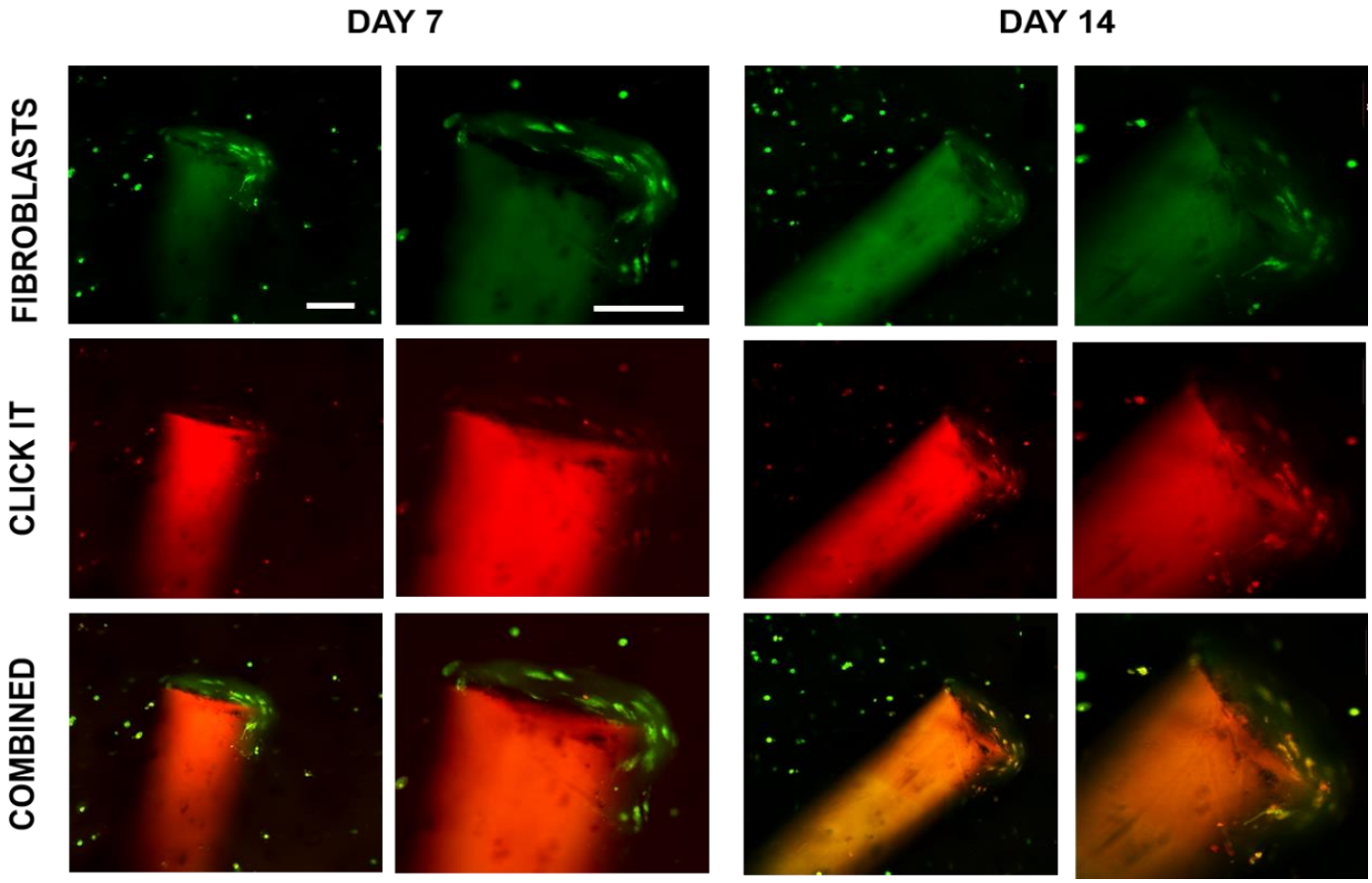

Imaging of TCCT fibroblast location (green) labelled by CFSE cell labelling dye and neocollagen synthesis (red) monitored by Click-IT Alexa Fluor 594 DIBO Alkyne reaction with azido-L-proline, which was incorporated into the culture of 3D TCCT model samples containing an inserted Xen Gel Stent medical device (n=2). Scale bar = 100 µm.

4.4 Discussion

Even with the use of anti-metabolic drugs intraoperatively, the 5-year failure rate of glaucoma surgery due to insufficient IOP control is 46.9% (Gedde *et al.*, 2012). Furthermore, the inhibitory mechanisms of currently used drugs are highly toxic and can lead to further complications. This study used the established 2D and 3D TCCT fibrosis models for investigation of fibrosis response reduction and glaucoma medical device assessment. Initially, the metabolic function of 3D cultured TCCT fibroblasts was tested following topical application of clinical dosage mitomycin C (Figure 4.1). As would be expected, TCCT fibroblast metabolic function declined by up to 93.3% by day 14. However, mitomycin C is known to reduce TCCT fibrosis via alkylation of DNA and subsequent inhibition of DNA synthesis; a highly toxic mechanism (Tomasz, 1995). There is therefore a high demand for more efficient anti-inflammatory agents which target key factors involved in the fibrosis process more specifically. Furthermore, reliable and reproducible biomimetic tissue models are required in order to assess these new agents and medical devices, for the improvement of trabeculectomy success rate post-operatively.

4.4.1 The effect of growth factor inhibitors on TCCT fibrosis

As previously discussed in Chapter 3, upregulated growth factors/cytokines such as TGF-β and TNF-α are believed to be key stimulators of scar tissue formation after glaucoma surgery (Khaw *et al.*, 1994, Grisanti *et al.*, 2005). The use of growth factor inhibitors for the potential reduction of TCCT fibrosis is therefore an interesting method to test on the established TCCT model. As presented, treatment with 10 µM TGF-β RI Kinase Inhibitor VI significantly reduced the metabolic rate of 3D TCCT fibroblasts cultured with 50% aqueous humour by up to 201.7% at day 5. Due to the limited availability of porcine aqueous humour, the day 14 time point was excluded from these experiments.

Furthermore, treatment with 10 µM SPD304 TNF-α inhibitor significantly reduced the metabolic rate of TCCT fibroblasts cultured with 50% aqueous humour by up to 281.9% at day 5. Treatment with both inhibitors also appeared to cause a decrease in F-actin expression within TCCT fibroblasts cultured with 50% aqueous humour, which further indicates the inhibitory response.

Primarily, these results further support data confirming the presence of TGF-β and TNF-α in aqueous humour. Additionally, it suggests that these growth factor inhibitors may have the potential to be used as alternative anti-inflammatory agents to Mitomycin C and 5-Fluorouracil. The commercially purchased TGF-β inhibitor used in this study is reported to inhibit the activity of ALK4 and ALK5 TGF-β receptors, with little to no reduced potency of other kinases. The commercially purchased TNF-α inhibitor is reported to inhibit TNFR1 receptor binding to TNF-α, by interfering with the protein-protein interactions on the contact surfaces of the trimeric TNF-α subunits (He *et al.*, 2005). They therefore target a specific inhibitory pathway, rather than disrupting the DNA synthesis of all cells. These inhibitors may therefore offer a more effective method for fibrotic response reduction, whilst also having a less toxic influence on the cells.

4.4.2 The effect of decorin proteoglycan on TCCT fibrosis

Decorin is a small, interstitial proteoglycan found in the ECM of various tissues, known to interact with several proteins involved with matrix assembly, cell adhesion, migration and proliferation (Chen and Birk, 2012). As shown in Figure 4.22, it regulates ECM assembly by binding to collagen fibrils, with its dermatan sulphate GAG chains extending into the interfibrillar space (Orgel *et al.*, 2009).

Figure 4.16 The association of decorin proteoglycan with collagen fibrils

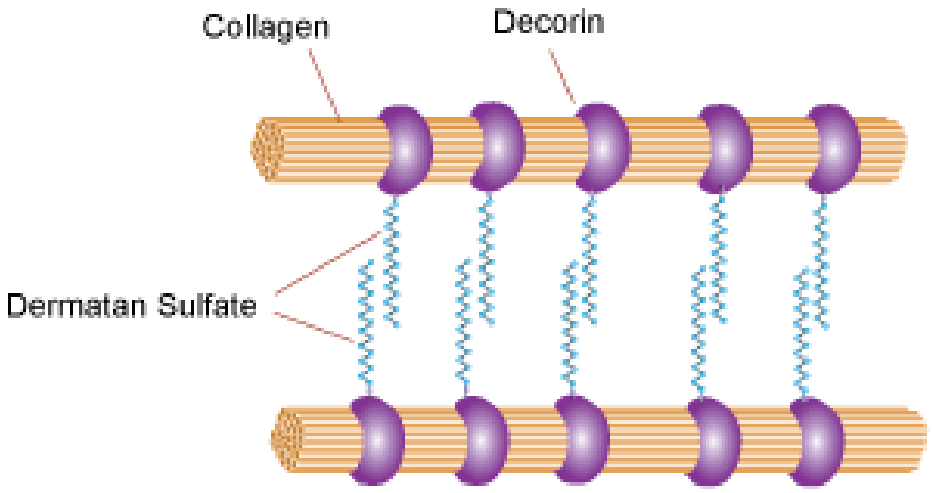

The binding of decorin proteoglycan with collagen fibrils. Source: Sigma-Aldrich, (2018).

Decorin is known to regulate wound healing and certain studies have found decorin deficient mice to exhibit slower scar tissue formation (Jarvelainen *et al.*, 2006). Biglycan is another associated proteoglycan which competes for the same fibril binding region as decorin, but with decorin having the higher affinity (Zhang *et al.*, 2009). Decorin is also recognised for its role in growth factor interaction, for example, it has the ability to bind to TGF-β and potentially neutralise its activity (Hildebrand *et al.*, 1994). Since it is naturally already present in tissue ECM, it may offer a less toxic and therefore safer method to control TCCT fibrosis. The experimental application of decorin has previously been reported to reduce conjunctival fibrosis in rabbits (Grisanti *et al.*, 2005).

Interestingly, decorin appeared to reduce the metabolic activity of 3D cultured TCCT fibroblasts, with and without exposure to shear stress in this study. Due to the known role of decorin in collagen matrix assembly, it was also of interest to determine the neocollagen synthesis of TCCT fibroblasts treated with decorin. As presented, decorin appeared to

stimulate an increase in TCCT fibroblast neocollagen synthesis, with a slightly greater effect exerted in combination with shear stress. Furthermore, the neocollagen morphology appeared to be aggregated and more structured. These results confirm the influence that decorin proteoglycan has on ECM synthesis, but may go against previous claims of its anti-fibrotic effect (Zhang *et al.*, 2018). Therefore, more research into the structural outcome of matrix assembly would be required in order to assess its suitability as an anti-fibrotic agent after glaucoma surgery. If decorin were to reduce scar tissue formation by promoting a more controlled and accurate matrix assembly, it may be beneficial as an anti-fibrotic agent. However, promotion of an uncontrolled and random matrix assembly would not be beneficial, since it may block or disrupt the drainage cavity created during a trabeculectomy.

4.4.3 The effect of nifedipine on TCCT fibrosis

Another potential inhibitory pathway is with the reduction of calcium signalling. Calcium signalling is an imperative secondary messenger regulating several cellular activities, such as secretion, proliferation, migration and neurotransmission. Although not all intracellular signalling mechanisms are clear, it is known that growth factors such as TGF-β exert part of their action in elevating cytosolic calcium, which triggers cellular responses such as proliferation (Clapham, 2007). Furthermore, it is known that shear stress induced mechanotransduction may also stimulate cytosolic calcium signalling (Ando and Yamamoto, 2013; Turczyńska *et al.*, 2013). As previously discussed in Chapter 3, a combination of both growth factor upregulation and shear stress induced mechanotransduction may synergistically stimulate excessive scar tissue formation after glaucoma surgery. It was therefore valuable to assess calcium signalling levels within the TCCT fibroblast model and test whether this could be inhibited. Nifedipine is an example

of an L-Type calcium signalling channel blocker, currently used in clinical practice to manage conditions such as high blood pressure, angina and premature labour. Recent studies have explored the potential use of nifedipine for fibrotic response reduction, to treat conditions such as pulmonary fibrosis. For example, by reducing the proliferation rate of lung fibroblasts (Matta *et al.*, 2015; Mukherjee *et al.*, 2015). Nifedipine was therefore an interesting inhibitor to test on the TCCT fibrosis model.

As presented in Figure 4.8, treatment with TGF-β growth factor potentially increased cytosolic calcium signalling in the TCCT model. Shear stress induced mechanotransduction may have also caused a slight increase in calcium signalling, though the imaged difference was subtle. Furthermore, treatment with nifedipine appeared to decrease cytosolic calcium signalling within TCCT fibroblasts, both individually and in combination with TGF-β and/or shear stress. However, these findings are limited by the fact that only single images were taken at each time point. In future work, it would be beneficial to take multiple images across a time-lapse in order to more accurately measure TCCT fibroblast cytosolic calcium signalling. Furthermore, determination of whether or not TCCT fibroblasts have L-Type calcium signalling channels is required.

In addition to cytosolic calcium imaging, TCCT metabolic function in response to nifedipine was also assessed using AlamarBlue® assay. As presented, 10 µM nifedipine significantly reduced the metabolic rate of 3D TCCT fibroblasts by 8% individually and 12.9% in combination with shear stress at the day 3 time point. Interestingly, the nifedipine + shear stress treated group appeared to follow a similar proliferation curve to the control group across the day 5, 7 and 14 time points. However, for the group treated with nifedipine only, the decreased level remained constant and metabolic activity did not

increase much further across the day 5, 7 and 14 time points. 10 µM nifedipine may therefore have limited metabolic function in the control group. Since shear stress exposure is believed to cause increased cytosolic calcium signalling and metabolic function in fibroblasts, 10 µM nifedipine probably reduced this metabolic activity, but may not have been a high enough dosage to halt metabolism completely in the shear stress treated group. A similar trend was observed in 2D TCCT fibroblasts treated with 10 µM Nifedipine.

To assess the dosage response further, 50 µM and 100 µM Nifedipine was also tested. As presented, 50 µM nifedipine significantly reduced the metabolic rate of 3D TCCT fibroblasts by 25.1% individually and 45.1% in combination with shear stress at the day 3 time point. Interestingly, both individually and in combination with shear stress the decreased level remained constant and metabolic activity did not increase much further across the day 5, 7 and 14 time points. Therefore, 50 µM nifedipine may have been a high enough dosage to limit metabolic activity, even in combination with shear stress. Furthermore, 50 µM nifedipine was also found to limit the metabolic rate in combination with TGF-β growth factor, with similar trends observed in the 2D cultures. As would be expected, 100 µM dosage nifedipine significantly reduced the metabolic rate of 3D TCCT fibroblasts even further, by 38.4% individually and 59.3% in combination with shear stress at the day 3 time point. Similar to 50 µM dosage, the decreased level remained constant in both groups and metabolic activity did not increase much further across the day 5, 7 and 14 time points. A similar trend was also observed in the 2D cultures.

In summary, whilst further experiments are required to more accurately determine TCCT cytosolic calcium signalling, AlamarBlue® assay data indicates that nifedipine could potentially be used as alternative anti-inflammatory agent to mitomycin C. Nifedipine is

already used commonly in clinical practice, is inexpensive and generally well tolerated. Though there are some listed side effects, nifedipine may have a less toxic influence on cells in comparison to the currently used anti-metabolites. Calcium channel blockers target a specific inhibitory pathway that is arguably less toxic to fibroblasts, in comparison to disruption of DNA synthesis. Nifedipine may therefore offer a more effective method for fibrotic response reduction in TCCT after trabeculectomy surgery.

4.4.4 Xen Gel Stent glaucoma medical device interaction with TCCT

Alternative methods which aim to improve the outcome of glaucoma surgery include the use of medical devices, for minimally invasive glaucoma surgery. The Xen Gel Stent, manufactured by Allergan, is a device inserted into the subconjunctival space to create an alternative diffuse outflow pathway by which aqueous fluid can drain and thereby reduce IOP. It is claimed to reduce the chance of inflammation and fibrotic response, since it is made from gelatin cross-linked with glutaraldehyde (Dervenis *et al.*, 2017). However, recent case studies have highlighted problems with the Xen Gel Stent, such as post-operative stent exposure (Fea *et al.*, 2015), blood clot formation inside the stent lumen (Ferreira *et al*., 2017) and bleb hypertrophy (Fernández-García *et al*., 2015). Aside from *ex vivo* testing of a similar medical device known as the iStent using human donor eyes (Bahler *et al.*, 2012), there has been little to no study of a minimally invasive glaucoma surgery device *in vitro.* It was therefore of interest to assess the Xen Gel Stent within the established *in vitro* TCCT fibrosis model.

Although the Xen Gel Stent is claimed by the manufacturer to measure 6 mm in length with an internal diameter of 45 µM, the differences in size and morphology before and

after insertion remain unclear. It was therefore of interest to initially assess Xen Gel Stent size before and after hydration and following insertion into the 3D TCCT fibroblast model. As shown, before hydration the Xen Gel Stent measured to be approximately 4 mm in length with a diameter of 28.8 µM internally and 153.8 µM externally. It can therefore be assumed that this would be the size of the Xen Gel Stent whilst pre-loaded in the Xen Injector device before insertion during glaucoma surgery. Interestingly, following hydration the Xen Gel Stent measured at 6 mm in length with a diameter of 43.3 µM internally and 211.5 µM externally. Though there may have been a margin of inaccuracy with the measurements, this suggests that the stent may have been up to 1.7 µM smaller in diameter than the manufacturer's claim. Whilst this difference is small, any slight variations in lumen diameter could make a difference in the long term success rate of treatment, especially if the lumen diameter was narrow enough to reduce fluidic outflow or increase the chance of blockage.

Although claimed by the manufacturer to be easier to manipulate whilst hydrated, Xen Gel Stents were inserted into the TCCT model whilst dry to increase rigidity and mimic their form whilst pre-loaded inside the Xen Injector device before insertion during glaucoma surgery. However, the Xen Gel Stents were found to be extremely fragile and highly prone to damage during insertion. Admittedly, the operator skill and environment during *in vitro* insertion had significant differences to the typical *in vivo* insertion during glaucoma surgery. However, this fragile nature of the Xen Gel Stent may still raise concern for *in vivo* usage. For example, there is a risk that the stent may break apart during insertion into the patients eye or once inside. The Xen Gel Stent is theoretically supposed to remain inside the patient's eye for several years. It is therefore questionable whether such a fragile device would maintain its integrity *in vivo* for this amount of time. Many previous studies

had small sample sizes and a short-term follow up of only 12 months (Sheybani *et al.*, 2015; Teus *et al.*, 2015; Pérez-Torregrosa *et al.*, 2016) . The long term success rate of the Xen Gel Stent is therefore unknown.

Once inserted into the 3D TCCT fibroblast model, the intact stents measured at approximately 5.9 mm in length with a diameter of 42.3 µM internally and 206.4 µM externally. Interestingly, this suggests that stents may only expand to their full size in pure water and may remain slightly smaller within a collagen matrix due to osmotic potential. In comparison, Xen Gel Stent diameter appeared to expand by 150.3% in pure water and 147% in collagen matrix; a 3.3% difference. Again, these slight variations in lumen diameter could make a difference in the long term success rate of treatment by reducing fluidic outflow or increasing the chance of blockage. As shown, although difficult to image the fibroblast activity using light microscopy in 3D, Xen Gel Stent morphology appeared to remain consistent within the TCCT model up to 2 weeks with and without exposure to TGF-β growth factor. Although it would have been beneficial to monitor the stent for longer, 2 weeks was found previously to be the optimum culture time for 3D cultured TCCT fibroblasts. To assess fibroblast activity surrounding the Xen Gel Stent device, fibroblast location and neocollagen synthesis surrounding the device was also monitored for up to 2 weeks, whilst treated with TGF-β to mimic the potentially fibrotic environment. As shown in Figure 4.14, numerous fibroblasts grew in close proximity to the Xen Gel Stent despite its claimed anti-inflammatory properties. Many fibroblasts were pushed towards the stent lumen during insertion, which may arguably occur by chance *in vivo* as the stent is pushed into the subconjunctival space. Labelled neocollagen also appeared to surround the fibroblasts by day 14. This evident fibroblast activity, particularly surrounding the stent lumen, could be another cause for concern relating to *in vivo* usage.

For example, the narrow Xen Gel Stent lumen may become blocked over time and lead to treatment failure. These findings may offer an explanation for the previous case study of a patient who had blood clot formation inside the stent lumen (Ferreira *et al*., 2017). Perhaps if blood platelets had accumulated in a similar way surrounding the stent lumen, it may have caused the blood clot formation.

However, it should be noted that due to the expense and limited availability of Xen Gel Stents, this study was limited by a very low sample number of only 7 stents, 2 of which were damaged during insertion into the TCCT model (Figure 4.19). This evidently limits the reliability and reproducibility of this data set. Furthermore, the operator skill and environment during *in vitro* insertion had significant differences to the typical *in vivo* insertion during glaucoma surgery. Since only one Xen Injector device was available, it was used multiple times for each insertion, despite recommendation from the manufacturer that the Xen Injector should only be used once to deliver a pre-loaded stent. A greater sample number would be required in future work in order to more accurately assess the Xen Gel Stent glaucoma medical device *in vitro*.

4.5 Conclusion

In summary, this study utilised the established 2D and 3D TCCT fibrosis models to investigate fibrosis response reduction methods and assess the Xen Gel Stent glaucoma medical device *in vitro* for the first time. Results indicate that the use of growth factor inhibitors and calcium signalling channel blockers, such as nifedipine, may both have potential to be used as alternative anti-inflammatory agents to mitomycin C and 5-Fluorouracil. The use of decorin proteoglycan may also be potentially beneficial in

controlling fibrotic response, but more research into the structural outcome of collagen matrix assembly would be required. Assessment of the Xen Gel Stent glaucoma medical device *in vitro* raises potential concerns for its use *in vivo*. Evident fibroblast activity surrounding the stent lumen following insertion within the 3D TCCT fibrosis model raises concerns about the possibility of stent lumen blockage. It may therefore be argued that fibrosis response reduction with drug treatment optimisation may be a safer and more promising method for the improvement of glaucoma surgery, in comparison to the use glaucoma medical devices. Despite low sample numbers, this study noticed the fragile nature of the Xen Gel Stent device and its evidently high chance of damage, particularly during insertion. These findings offer a useful insight for further study into the improvement of glaucoma surgery success rate. Furthermore, new reliable and convenient methods using the TCCT model for assessment of new glaucoma treatment agents and medical devices has been demonstrated.

Chapter 5

Development and application of an improved *in vitro* 3D organotypic retinal tissue model

5.1 Introduction

The retina is a complex, light-sensitive tissue layer on the inner surface of the eye, which functions to translate light stimuli into nerve impulses which travel to the brain via the optic nerve. Retinal tissue is made up of several neuronal layers consisting of at least eight different cell types including the photoreceptors (rods and cones), bipolar cells and ganglion cells (Livesey and Cepko, 2001). Typically, cell culture models only allow testing on singular cell types. Therefore, although the technique is more challenging, multicellular retinal tissue models with preserved cellular interactions are preferable for the study of retinal diseases, as these often affect more than one retinal cell type. Furthermore, *in vitro* tissue models are preferable in comparison to *in vivo* study using live animals, as the practice is more ethical and the tissue environment can be better controlled and manipulated (Kim and Takahashi, 1988).

Organotypic slice cultures allow *in vitro* growth of complex biological tissues, whilst still replicating a significant amount of normal physiology and function (Gähwiler *et al.*, 1997). Whereas acute slice preparations are often obtained from adult animals and used for experimentation on the same day that they are prepared, organotypic slice cultures can be preserved *in vitro* for several days or weeks (Wray, 1992). Previously developed organotypic retinal tissue culture systems include Johnson & Martin (2008) that cultured adult rat retinal explants. Although the retinal explants were viable for 17 days, there were some aspects of their methodology which could be optimised further. For example, the retina was peeled away from the adjacent tissue using a paintbrush, which is likely to have disrupted layers of the retinal tissue and caused disorganisation. Another study which was able to culture postnatal rat retina was Viktorov *et al*., (2004), which maintained the retinal tissue using roller-tube culturing. The roller-tube culture technique is advantageous in that

it maintains many organotypic features and thins the tissue substantially, allowing visualisation of individual cells throughout the cultured tissue. However, although some laminar structure of the retinal tissue was preserved using this technique, it was mainly only the ganglion cell layer and the model therefore did not preserve all physiological layers of the retinal tissue.

As the neuronal structure of the porcine retina is similar to that of the human retina (Guduric-Fuchs *et al.*, 2009), it is of interest to explore organotypic slice culture of the porcine retina. One of the most notable organotypic culture systems using adult porcine retinal explants was developed previously by Wang, *et al*., (2011), who were able to maintain full-thickness porcine retinal explants for at least seven days. One major advantage of their methodology is that the photoreceptor layer faces upwards, allowing an increased oxygen supply to photoreceptors and therefore overcoming some of the difficulties associated with culturing retinal tissue *in vitro*. However, aspects of their methodology could be optimised further. For example, the retinal explants were cultured on filter paper which may be a basic substrate for such a complex and fragile composition of tissue (Wang *et al.*, 2011). The *in vivo* retina makes contact with the vitreous humour; a hydrated, gel-like mass which consists almost entirely of water. Native vitreous is composed of 99% water, a network of collagen fibrils, hyaluronic acid and hyalocyte cells, as well as certain salts, sugar and ascorbic acid. The vitreous supports retinal metabolism by acting as a reservoir for substances such as oxygen, glucose and ascorbic acid, as well as a removal system for metabolic waste products (Kokavec *et al.*, 2016). A filter paper substrate is therefore not likely to mimic this highly complex environment required for the optimal preservation of full-thickness retinal explants. It would therefore be valuable to optimise previous methodologies further by culturing full-thickness retinal tissue explants

on a more highly hydrated and biocompatible substrate. As retinal tissue cultured *in vitro* is often in absence of the choroid, there are additional requirements for the culture substrate to compensate for this.

Research into tissue engineering strategies for the treatment of retinal diseases such as macular degeneration, glaucoma and retinitis pigmentosa have advanced significantly over recent years with promising results. However, challenges still remain with aspects such as; the delivery and integration of regenerative materials to the eye, overcoming the possibility of immune rejection and the guidance of axonal growth to establish useful connections (Ramsden *et al.,* 2013). Therefore, both clinical research and the field of regenerative medicine still require improved *in vitro* and *ex vivo* retinal models, for the study of retinal disease mechanisms and testing of neuroregenerative materials, whilst also reducing the requirement for live animal experiments. Additionally, the development of retinal injury models is particularly valuable, for assessment of stem cell therapies and the way they may interact and integrate with injured retinal tissue.

OCT is a non-invasive imaging technique capable of producing high resolution, cross sectional images of material such as biological tissue. It works by directing near-infrared light into samples and then, by measuring the intensity of the back reflected light, produces an image. As OCT penetrates samples more deeply than confocal imaging, but has a higher resolution than ultrasound imaging, it bridges the gap between these two imaging methods (Thorlabs, 2015). Since OCT enables cross-sectional assessment of live biological samples, without a requirement for staining or fixation, it could offer a valuable tool to monitor the viability and structural integrity of *in vitro* retinal tissues in response to

different culture environments, for a prolonged culture time. OCT for retinal model study has not been widely explored in previous work.

5.2 Aim

This study aimed to establish an improved, efficient and reproducible 3D organotypic retinal tissue system using porcine eyes, which better preserves all physiological layers of the retina with minimal cellular disorganisation. The first objective was to develop a reproducible and feasible dissection protocol to obtain the retinal explants and select a biomimetic vitreous-like hydrogel to support the retinal explants in culture. In addition, establishment of techniques to assess the function and viability of the retinal explants was required. The secondary objective was to then develop a consistent and reproducible injury in the retinal tissue model to mimic the damage of disease/trauma. Following exploration of retinal model injury techniques, the final objective then involved adding stem cells to the injured retinal model to observe their interaction with the tissue and injury site. For assessment of live retinal tissue viability and structural integrity during these experiments, the non-destructive imaging technique OCT was applied in order to monitor samples during culture without a requirement for staining or fixation. OCT was used to evaluate these outlined objectives, in addition to conventional destructive assessment techniques.

5.3 Results

5.3.1 Assessment of primary porcine posterior eye cup quality

Adult porcine eyes were obtained from a local abattoir for the purpose of isolating primary retinal explant cultures. Following removal of the anterior eye cup and vitreous humour (Chapter 2, Figure 2.4, B), posterior eye cup quality was assessed using OCT. As shown in Figure 5.1, the quality of neural retina lining the posterior eye cup varied considerably depending on the time collected after slaughter. If the abattoir provided eyes from a pig slaughtered within 1-2 days, the neural retina was often visibly wrinkled (Figure 5.1, A) and the layered structure disrupted/detached (Figure 5.1, B). However, if the abattoir provided eyes within approximately 2 hours of slaughter, the neural retina appeared visibly fresh (Figure 5.1, C) with the layered structure remaining distinct and intact against the posterior eye cup (Figure 5.1, D). It was therefore crucial to request that eyes be provided within 2 hours of slaughter and tissue explants obtained within this time frame had consistently better viability in all experiments. In addition, it was decided to obtain whole porcine heads from the abattoir and enucleate the eyes upon arrival at the laboratory (section 2.2.1.1). This decreased the time frame taken to obtain eyes and reduced the chance of deterioration during transportation.

Figure 5.1 OCT assessment of primary porcine posterior eye cup quality

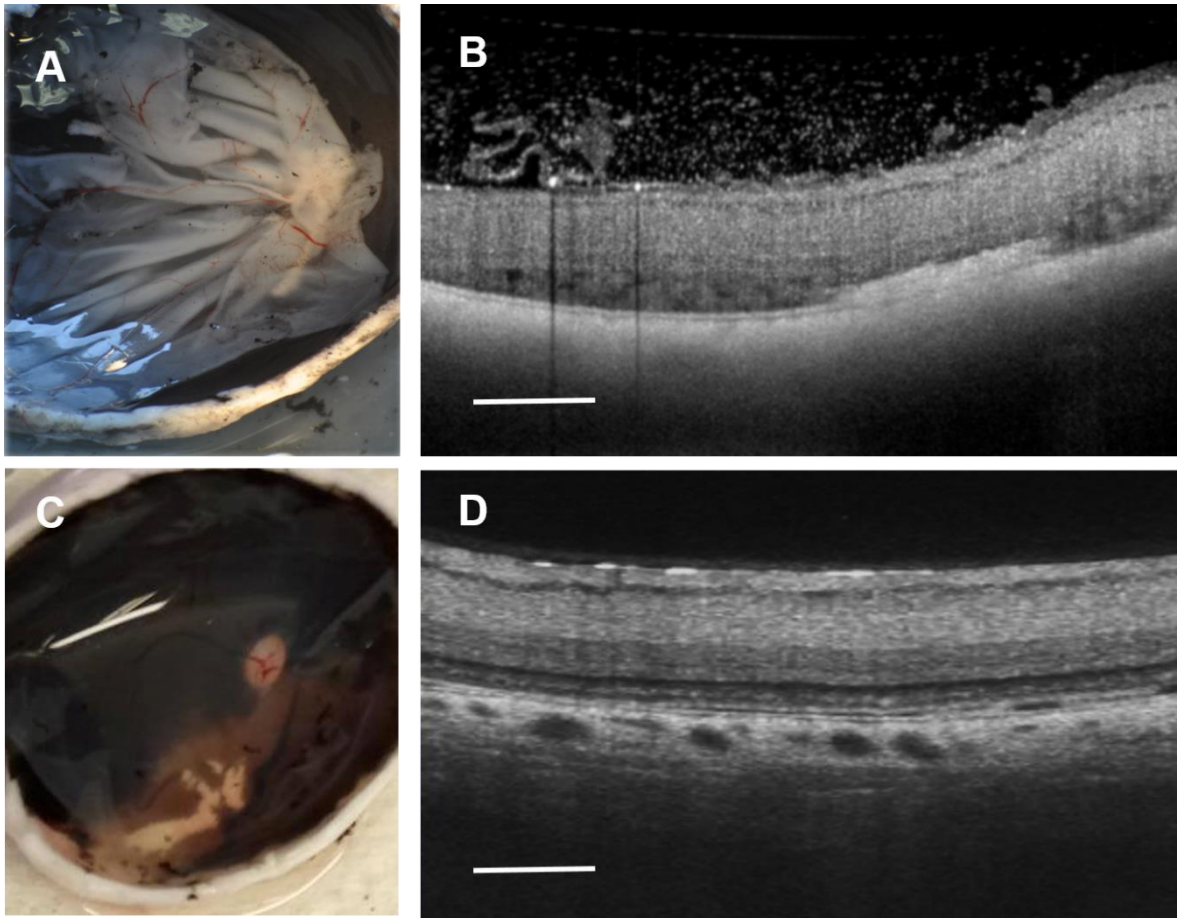

Representative photographs and OCT images of adult porcine posterior eye cups (n=3) following obtainment within 48 hours of slaughter (A, B) and 2 hours of slaughter (C, D). Scale bar = 500 µm.

5.3.2 Optimisation of *in vitro* 3D organotypic retinal tissue explant cultures

5.3.2.1 Optical coherence tomography assessment

3D organotypic retinal tissue explant cultures were obtained as previously described (section 2.2.1.9) and three culture substrates tested for the optimised culture of explants. To replicate the previous method of Wang, *et al*., (2011), explants were initially transferred to filter paper. To test the retinal tissue with a potentially more biocompatible culture substrate, explants were also transferred to 3 mg/mL collagen hydrogel (non- compressed)

as a comparison. The quality of cultured retinal explants (n=3) obtained within 48 hours and 2 hours of slaughter was initially compared for up to 4 days during culture on the two substrates (Figure 5.2). Similar to retina observed inside the posterior eye cup, the layered structure of isolated retinal explants was evidently more defined in samples isolated from eyes obtained within 2 hours of slaughter, in comparison to 48 hours. This further indicates the importance of obtaining the porcine eyes as fresh as possible, ideally within 2 hours of slaughter. In comparison of the two culture substrates at day 0, explants transferred onto collagen hydrogel maintained a distinct layered structure similar to retina observed inside the posterior eye cup, in comparison to explants transferred onto filter paper. However, over time the layered structure became less defined on both substrates. Samples adhered well to filter paper, but had an increasingly shrivelled morphology across the day 0, 2 and 4 time points. The tissue had a less shrivelled and more hydrated morphology on collagen hydrogel, but minimal adhesion with this substrate meant that samples either folded, moved around or detached completely during culture. This caused considerable disruption to the layered structure by the day 2 and 4 time points.

Figure 5.2 Assessment of retinal explant culture on filter paper and collagen hydrogel

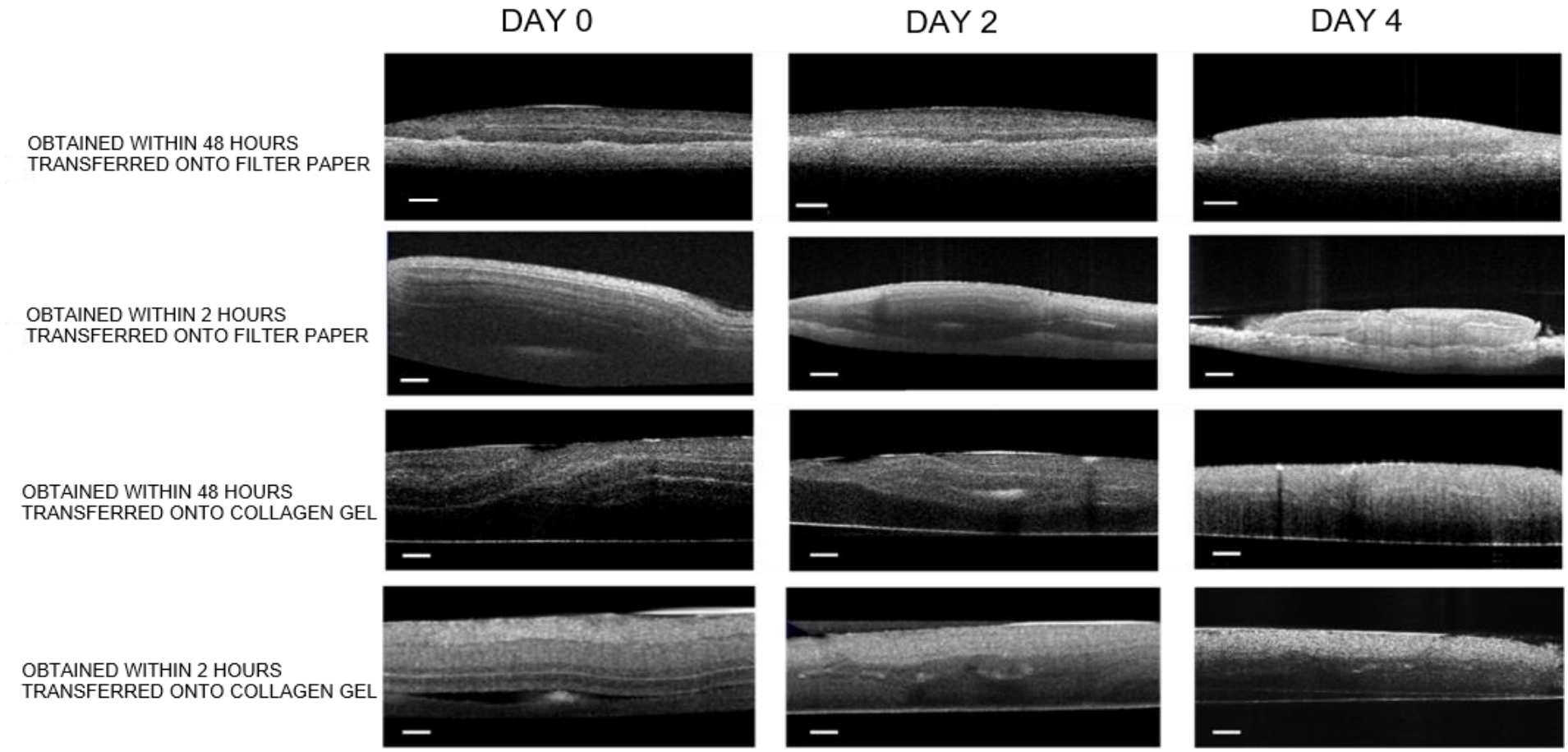

OCT assessment of organotypic retinal tissue explants (n=3) following obtainment within 48 hours and 2 hours of slaughter, cultured on filter paper and non-compressed collagen hydrogel for up to 4 days. Scale bar = 250 µm.

To improve sample adherence to the collagen gel substrate, compressed collagen hydrogel (section 2.2.1.8) was tested as a third substrate. As shown in Figure 5.3, isolated retinal explants had some improved adherence to the compressed collagen hydrogel. However, disruption of the retinal layers still occurred due to the upper layers of each sample floating in the surrounding culture medium. In an attempt to overcome this issue, culture insert use was also tested to provide an air-liquid interface. As presented, the use of culture inserts alone evidently did not preserve the retina's layered structure. However, the use of a compressed collagen substrate in combination with culture inserts greatly improved preservation of the retinal layers with minimal disorganisation.

Figure 5.3 Assessment of retinal tissue on compressed collagen and culture inserts

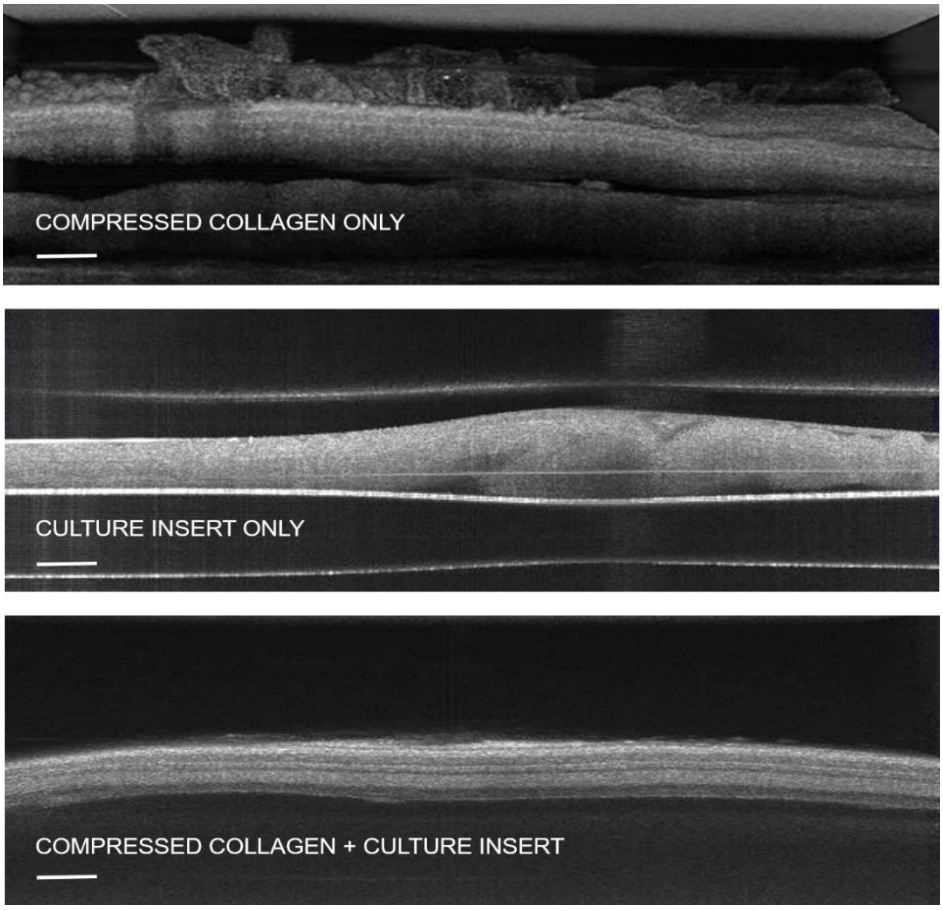

OCT assessment of fresh organotypic retinal tissue explants (n=3) following transfer onto compressed collagen, with and without the use of culture inserts. Scale bar = 500 µm.

As presented in Figure 5.4, there were approximately 1-2 retinal layers visible using OCT in samples transferred to culture inserts only, 2-3 layers visible in samples transferred to compressed collagen only and 4-5 layers visible in samples transferred to compressed collagen and a culture insert. The difference between groups was statistically significant (p= 0.0021).

Figure 5.4 Number of retinal layers visible on culture substrates using OCT

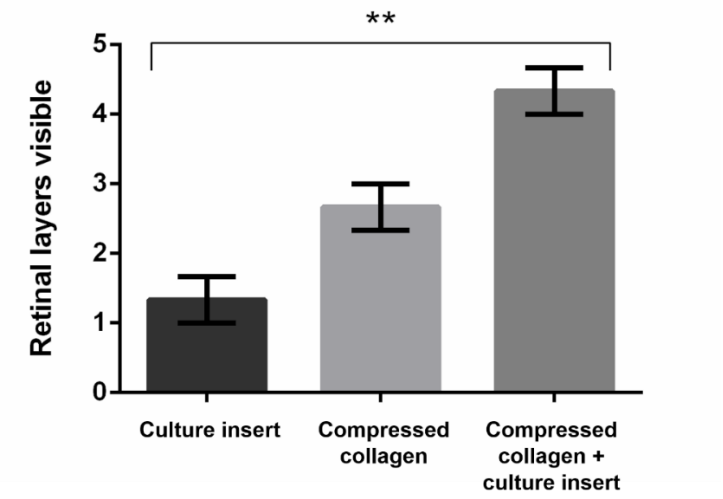

Semi-quantification of the number of retinal layers visible using OCT following transfer onto culture inserts, compressed collagen and in combination (n=3). Data are expressed as mean ± SE (n=3). * indicates p <0.05, ** indicates p <0.01.

As shown in Figure 5.5, the distinct layer regions visualised using OCT within cultured retinal explants are estimated to be the RPE + photoreceptor layers, nuclear + plexiform layers and ganglion + nerve fibre layers. The quality of retinal explants cultured on compressed collagen hydrogel and culture inserts (n=3) was assessed for up to 2 weeks of culture (Figure 5.3, B). Whilst samples still appeared to shrivel and distort slightly over time, the layered structure was reasonably visible with minimal distortion for up to 2 weeks. However, as the layers lost their stability over time, live retinal samples became more difficult to visualise using OCT.

Figure 5.5 Assessment of retinal explant culture on compressed collagen + inserts

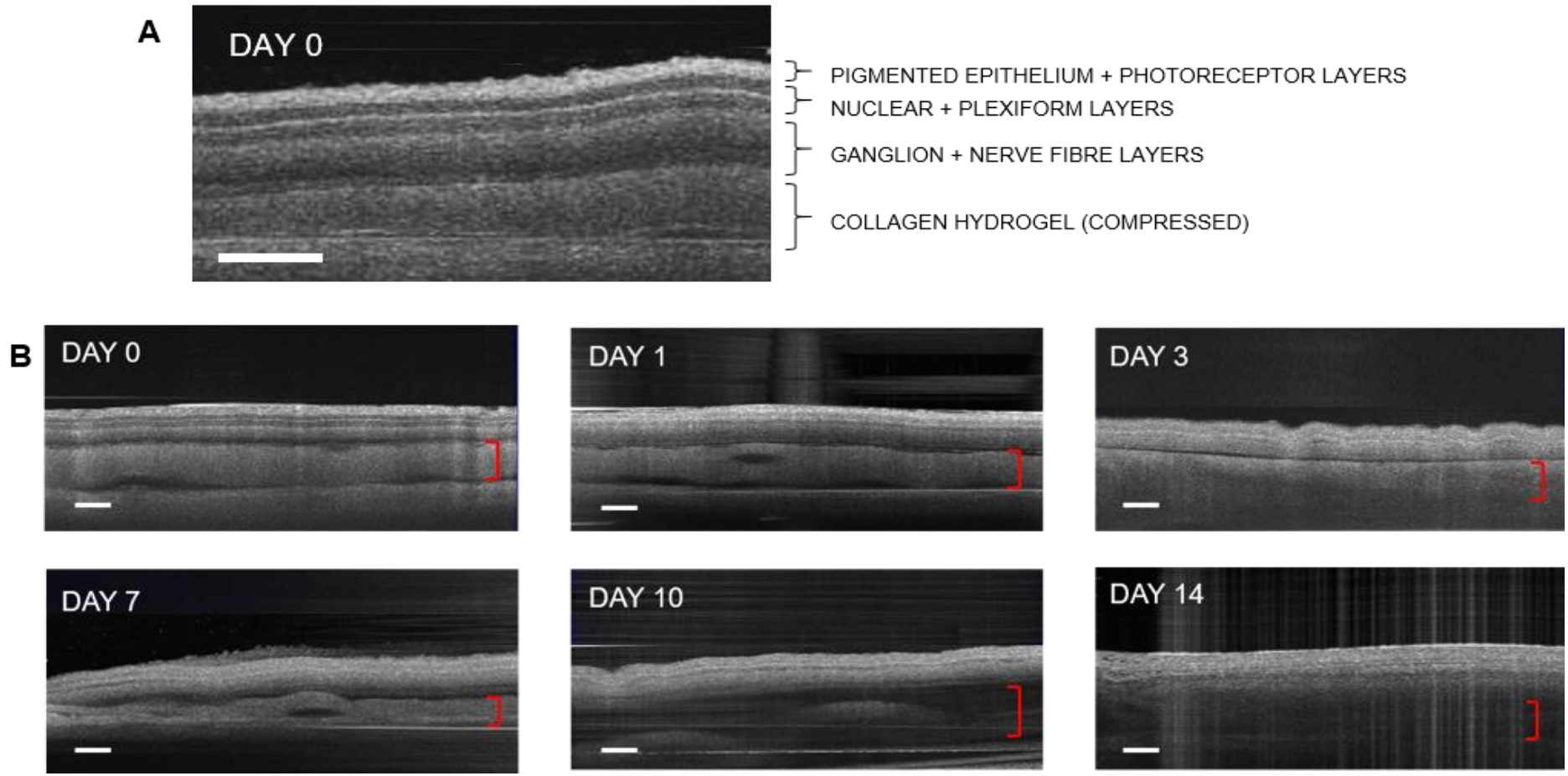

OCT assessment of organotypic retinal tissue explants (n=3) cultured on compressed collagen + culture inserts for up to 2 weeks. Red lines indicate the approximate regions of compressed collagen gel. Scale bar = 500 µm.

As presented in Figure 5.6, the number of retinal layer regions visible using OCT decreased significantly during the first 24 hours of culture, with approximately 4-5 layer regions visible at day 0 declining to approximately 2-3 visible layer regions at day 1 (p=0.024). The number of visible layer regions then gradually declined further beyond the day 1 time point, with approximately 1-2 layer regions visible by day 14 (p=0.003).

Figure 5.6 Number of retinal layers visible within cultured explants over time

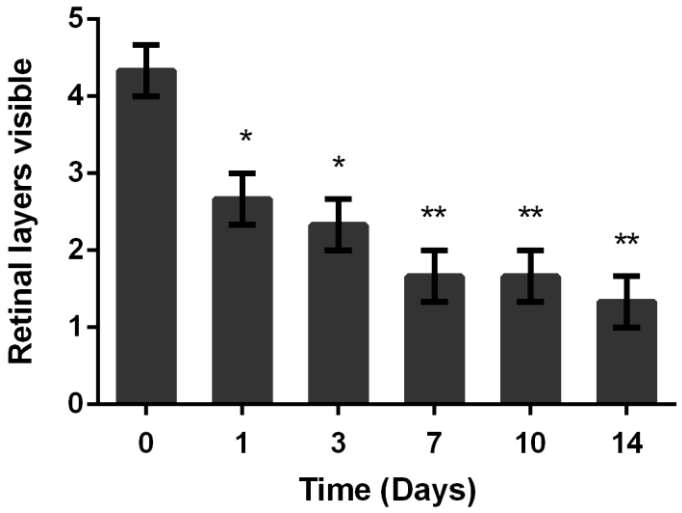

Semi-quantification of the number of retinal physiological layers visible using OCT during explant culture on compressed collagen + culture inserts over time (n=3). Data are expressed as mean ± SE (n=3). Statistical significance indicated in comparison to the day 0 group. * indicates p <0.05, ** indicates p <0.01.

5.3.2.2 Live/Dead tissue viability assessment

To cross validate the morphological assessment undertaken using OCT, Live/Dead tissue viability staining was carried out on retinal explants (n=3) cultured on compressed collagen hydrogel substrate at day 3, 5, 7, 10 and 14. As shown in Figure 5.7, tissue viability was maintained for up to 2 weeks, with small patches of dead tissue becoming evident at day 14. Interestingly the tissue morphology (as viewed from above) appeared to shrivel slightly over time in a similar way to the cross sectional morphology observed using OCT.

Figure 5.7 Tissue viability of retinal explants cultured on compressed collagen

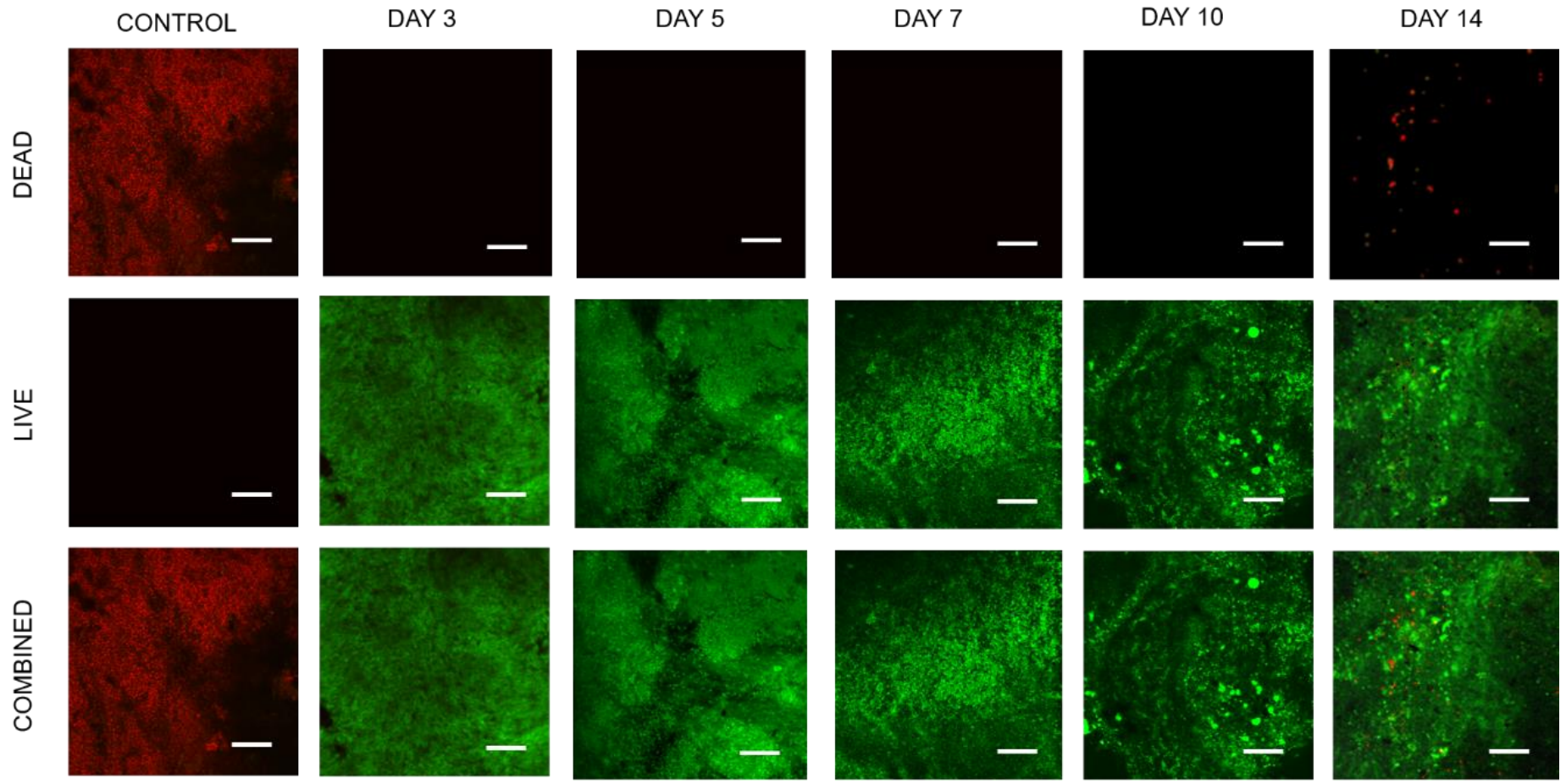

Live/Dead tissue viability staining of organotypic retinal explants (n=3) cultured on compressed collagen hydrogel up to 2 weeks. Negative control samples were obtained by immersion in 70% ethanol for 10 minutes before staining. Scale bar = 100 µm.

5.3.2.3 Histological assessment

Following fixation, histological assessment was also carried out on retinal explants after culture on compressed collagen hydrogels (n=3). This would enable further morphological assessment in addition to the cross sectional OCT assessment of live samples. As shown in Figure 5.8, histological assessment using haematoxylin & eosin staining confirms preservation of the retina's distinct layered structure with further clarity. Full thickness retina was evident and cultured samples had a similar structure to the non-cultured control sample of fresh retina. Approximately 6 distinct layer regions could be visualised at day 7 with histological assessment; an increase in detail from the 1-3 layer regions visualised with OCT. Whilst the cultured samples had some deterioration by the day 7 and 14 time points, the layered structure was evidently still present with the darker stained RPE + photoreceptor layers on top and the ganglion + nerve fibre layers at the bottom, where they would have made contact with the collagen hydrogel. Generally, the RPE + photoreceptor layers appeared to deteriorate less quickly in culture in comparison to the delicate ganglion + nerve fibre layers.

Figure 5.8 Histology of retinal explants cultured on compressed collagen

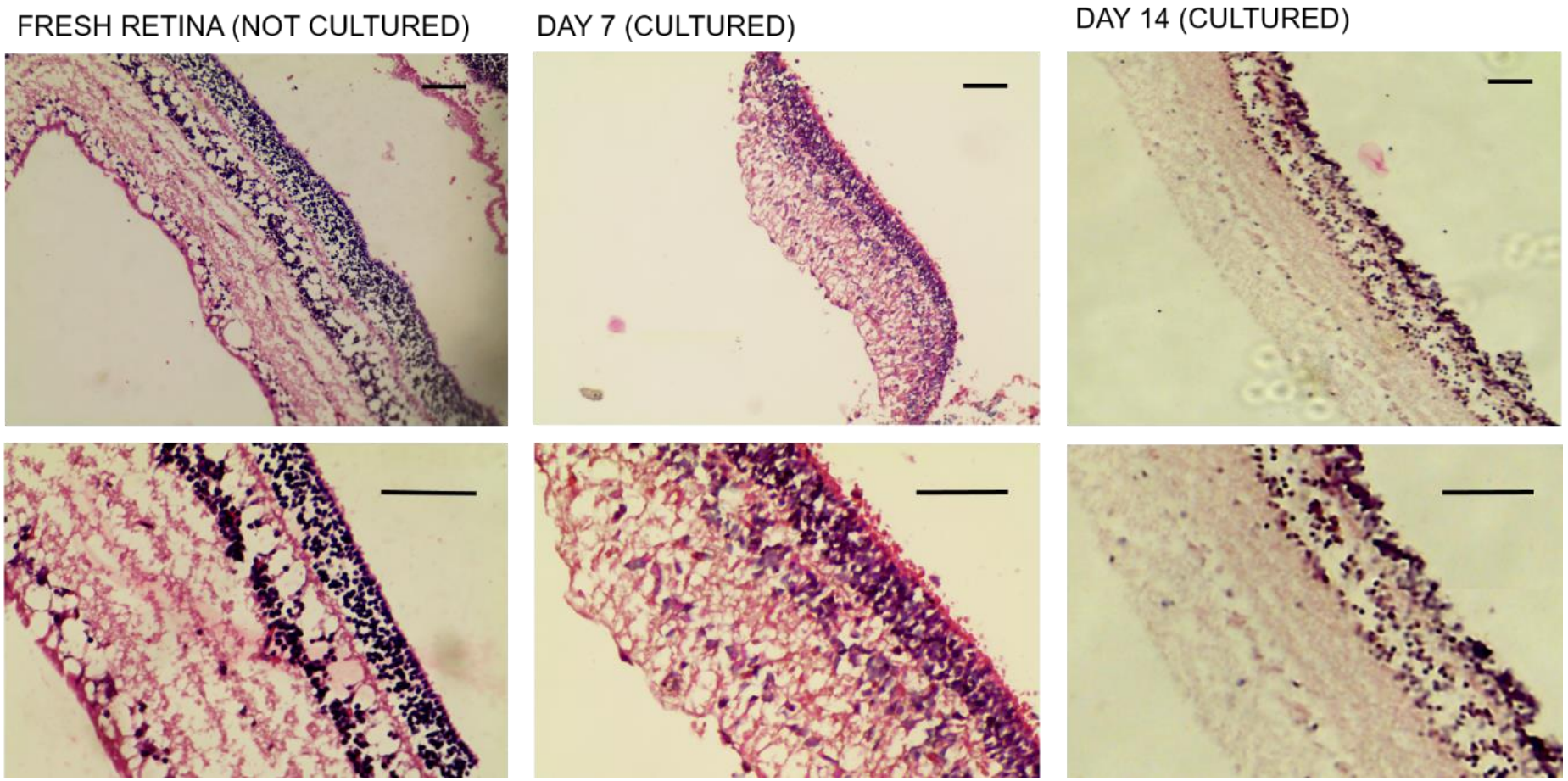

Histological assessment of organotypic retinal tissue explants (n=3) cultured on compressed collagen hydrogel at day 7 and 14. Scale bar = 100µm.

5.3.2.4 Retinal pigmented epithelium (RPE) characterisation

To confirm the presence and orientation of RPE in cultured organotypic retinal explants, immunostaining of the RPE layer was undertaken on histologically processed samples. As shown in Figure 5.9, the top layer of cultured porcine retina stained positively for RPE65 (using RPE65 mouse monoclonal primary antibody and goat anti-mouse TRITC secondary antibody; n=3), standing out more brightly in comparison to the non-specific background staining of other tissue layers. This indicates the presence of RPE in the cultured retinal explants and confirmed its orientation (facing upwards) during culture. Furthermore, RPE remained evident at the day 7 and 14 time points with minimal distortion.

Figure 5.9 Porcine retinal pigmented epithelium (RPE) characterisation

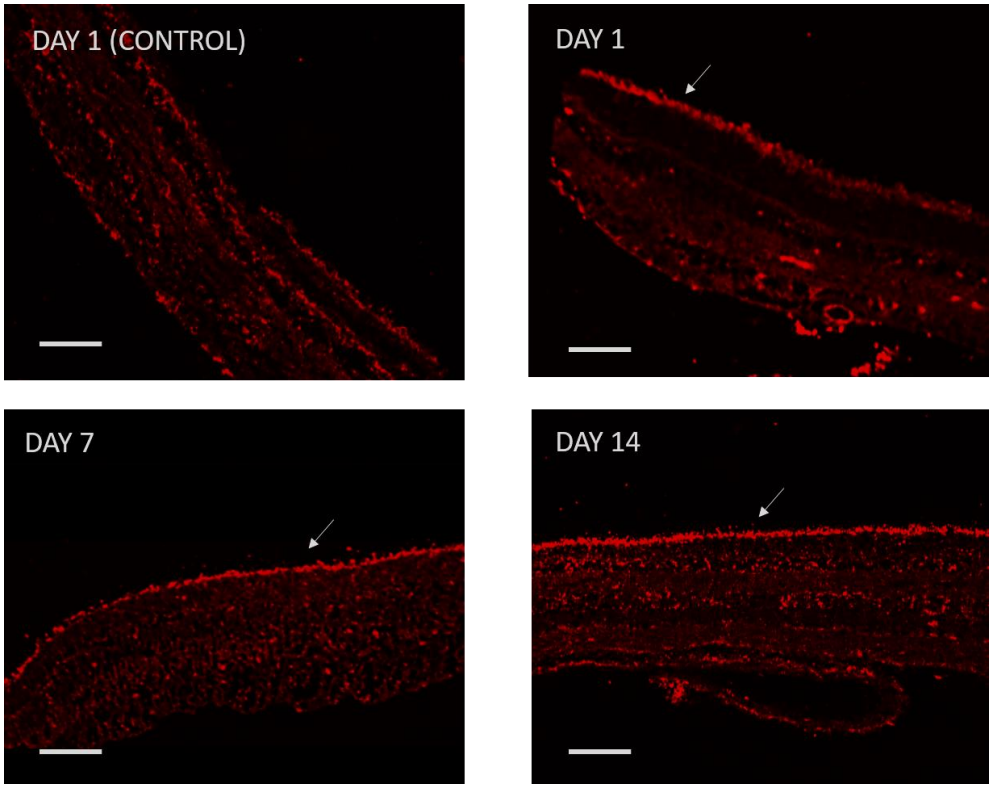

Cultured porcine retina (n=3) immunostained with RPE65 mouse monoclonal primary antibody and goat anti-mouse TRITC secondary antibody (red). Arrows (white) indicate RPE layer location. Negative control samples were stained with secondary antibody only (without primary antibody). Scale bar = 100 µm.

5.3.3 Investigation of retinal injury using mechanical and acetic acid lesioning

Once the *in vitro* 3D organotypic retinal tissue explant culture model had been established, it was then of interest to explore retinal model injury techniques to potentially mimic the damage of disease/trauma. The first and most basic method of injury explored was mechanical lesioning using a scalpel blade. However, due to the soft and fragile nature of retinal tissue it proved difficult to produce a partial lesion in the samples without 'dragging' the retinal tissue and disorganising the layered structure. The most efficient way to produce a mechanical lesion was to therefore make a full thickness cut through the retinal tissue and substrate, as shown in Figure 5.10. However, this lesion was evidently too large to mimic the subtle, 1-2 layer damage of most retinal diseases.

Figure 5.10 OCT assessment of retinal tissue subjected to mechanical lesioning

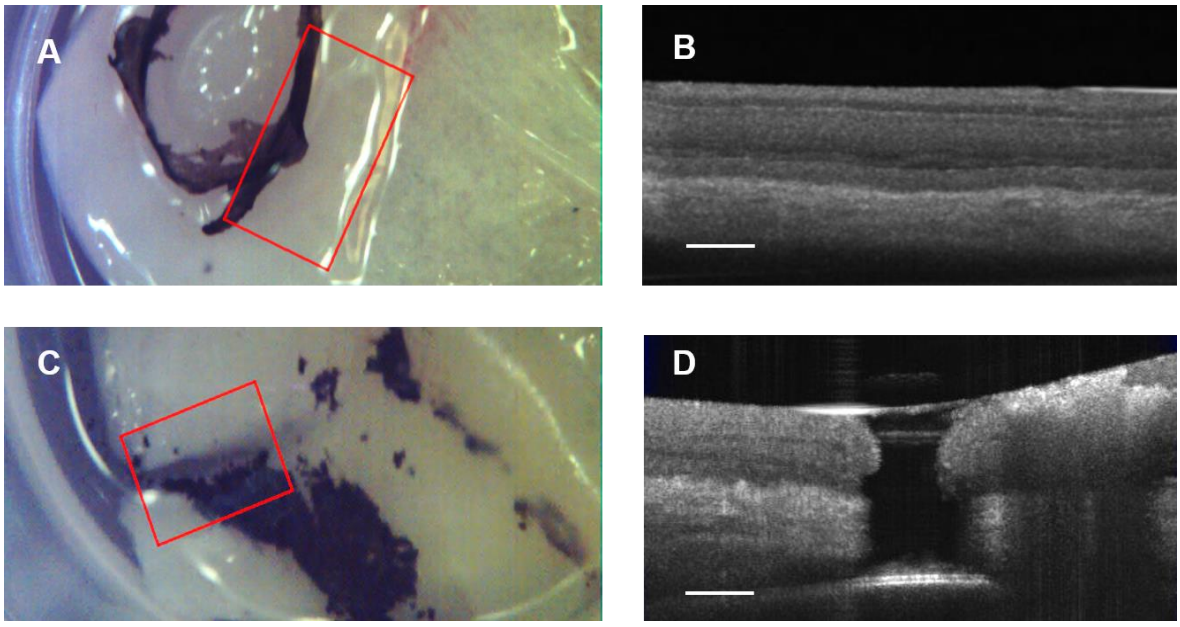

Photographs and OCT assessment of non-lesioned (A, B) and mechanically lesioned (C, D) organotypic retinal tissue explants (n=3). Highlighted areas (red) indicate the OCT imaging location. Scale bar = 500 µm.

An alternative injury method to mechanical lesioning was the possibility of chemical injury using 4% acetic acid. In order to apply the damage to a small area of the tissue, small filter paper pieces soaked in 4% acetic acid was placed on top of each sample for either 5 or 10 minutes. As shown in Figure 5.11, whilst the areas of damage did not pass through the full thickness of samples in the same way as mechanical lesioning, it still disrupted the retinal tissue layers considerably. Acid damage applied for 5 minutes was evidently less destructive, and could mimic disease damage more closely, in comparison to the widespread damage caused by 10 minute application. This method was an improvement from the mechanical lesioning, but the damage caused may still be too large to mimic the 1-2 layer damage of most retinal diseases.

Figure 5.11 OCT assessment of retinal tissue subjected to acetic acid injury

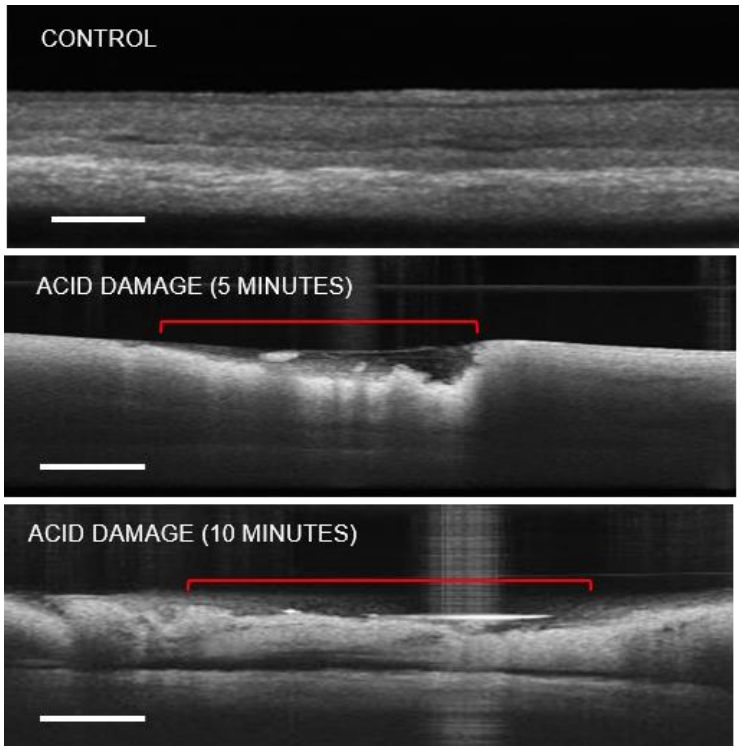

OCT assessment of non-lesioned (control) and chemically injured retinal tissue explants (n=3) following 5 and 10 minute application of 4% acetic acid. Red lines indicate the approximate regions of tissue damage. Scale bar = 500 µm.

To cross validate the assessment undertaken using OCT, Live/Dead tissue viability staining was carried out on injured retinal explants (n=3) following blade and acetic acid damage. As shown in Figure 5.12, both injury methods produced a distinct area of dead tissue on the retinal explant model samples, with the majority of surrounding tissue kept alive. It is thought that red fluorescence occurring in the surrounding substrate area was due to auto-fluorescence, caused by the collagen gel. Although the blade damage caused considerable disruption and movement to the retinal tissue, samples exposed to acetic acid damage remained in their circular biopsy shape, indicating less disruption to the surrounding tissue.

Figure 5.12 Retinal tissue viability following mechanical and acetic acid injury

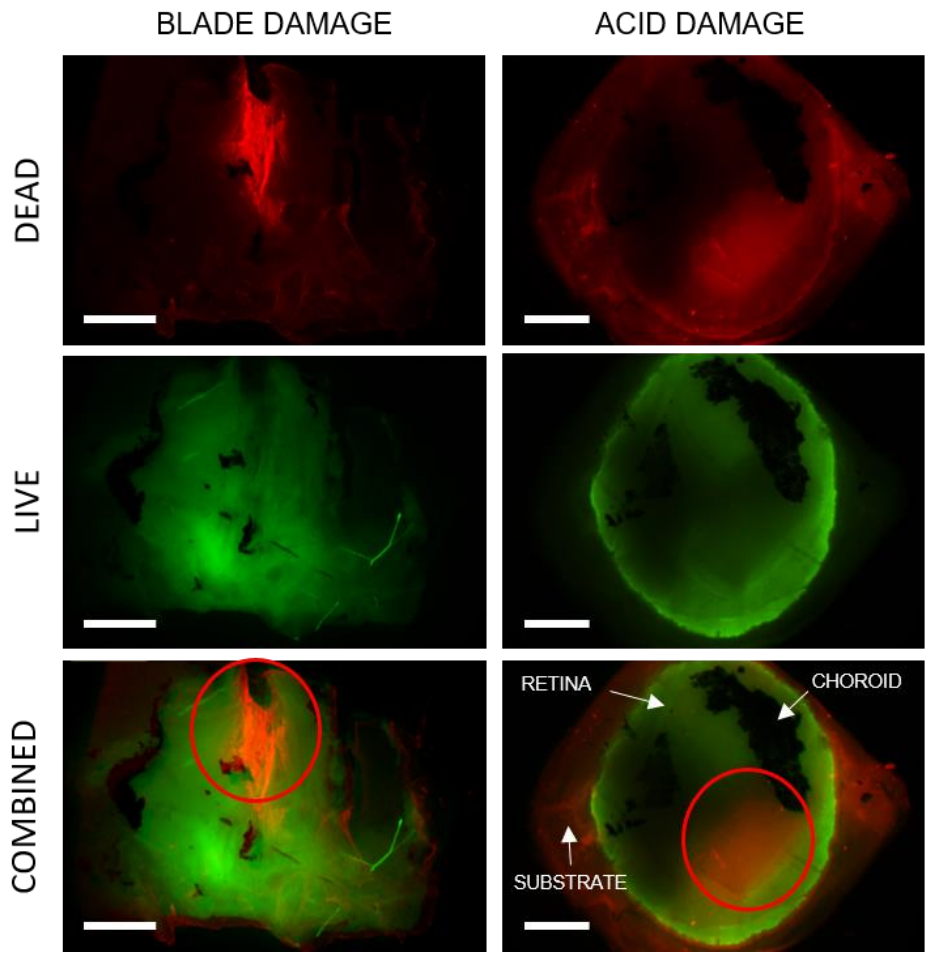

Live/Dead tissue viability staining of organotypic retinal explants (n=3) following mechanical and acetic acid injury. Red circles indicate the approximate regions of tissue damage. Scale bar = 2 mm.

5.3.4 Investigation of retinal injury using laser ablation

To explore a more subtle method of retinal model injury, laser ablation was tested as a third option. A summary of the lasers tested can be found in Chapter 2, Table 5. Laser ablation caused a very small level of structural injury, which was difficult to visualise accurately using cross-sectional OCT imaging. Furthermore, it was difficult to distinguish between areas of damage already present from the tissue isolation process and which areas were structurally damaged by the laser. Nevertheless, some potential areas of structural injury by laser ablation were imaged using OCT, as shown in Figure 5.13.

Figure 5.13 OCT assessment of retinal tissue model subjected to laser ablation

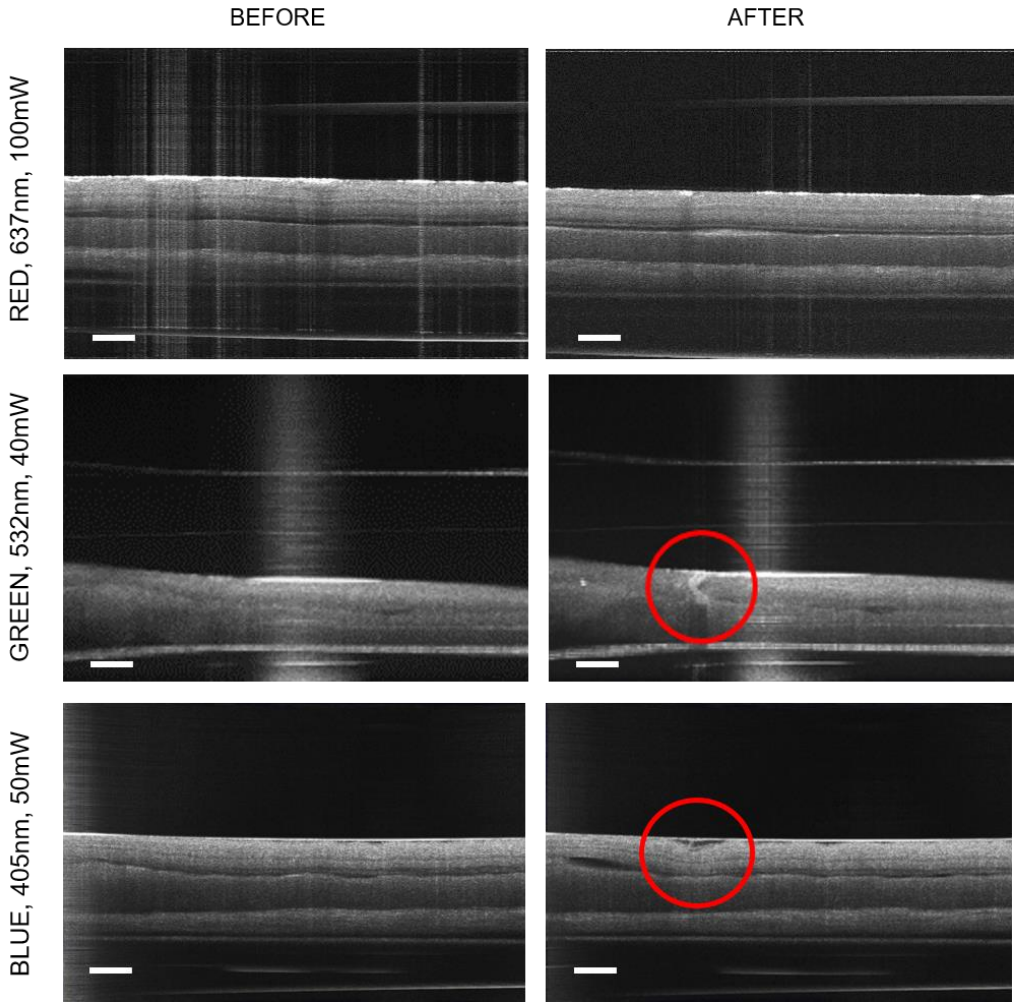

OCT assessment of organotypic retinal tissue explants (n=3) before and after laser ablation. Highlighted areas (red) indicate the possible site of injury. Scale bar = 500 µm.

Interestingly, no structural damage was visualised on samples following exposure to the Vortran red laser (637 nm wavelength and 100 mW power). However, some structural damage could be visualised on samples following exposure to the Vortran green laser (532 nm wavelength and 40 mW power). Whilst this damage would often differ in appearance, one of the clearest examples is presented in Figure 5.13. Since this example of damage occurred towards the edge of the retinal sample (where tissue is thinner) the retinal layers are less evident. However, there was clear evidence of ablation when comparing before and after images of the same sample location. Some structural damage could also be visualised on samples following exposure to the Fluoview 1200 confocal DAPI/blue laser (405 nm wavelength and 50 mW power) on maximum power. This damage also differed in appearance between samples, but one of the clearest examples is presented (Figure 5.13). Fortunately, this example of damage occurred close to the centre of the retinal sample, where the layered structure was more evident. There was again evidence of ablation when comparing before and after images of the same sample location. Blue laser damage usually produced a more widespread 'blistered' appearance, in comparison to the narrow injury caused by the green laser.

To cross validate the morphological assessment undertaken using OCT, Live/Dead tissue viability staining was carried out on retinal explants (n=3) following ablation by the green and blue lasers. As shown in Figure 5.14, a distinct 'crater' like ablation could be visualised on samples following exposure to the green (532nm, 40mW) laser, using confocal microscopy (10x and 20x magnification). When imaging was focused at the top of the lesion (focus 1) a distinct, circular ring of tissue damage can be visualised. When imaging was focused inside the lesion (focus 2) a clear patch of dead tissue was evident, surrounded by a combination of dead and live patches in the surrounding tissue.

Figure 5.14 Retinal tissue viability following green (532 nm, 40 mW) laser ablation

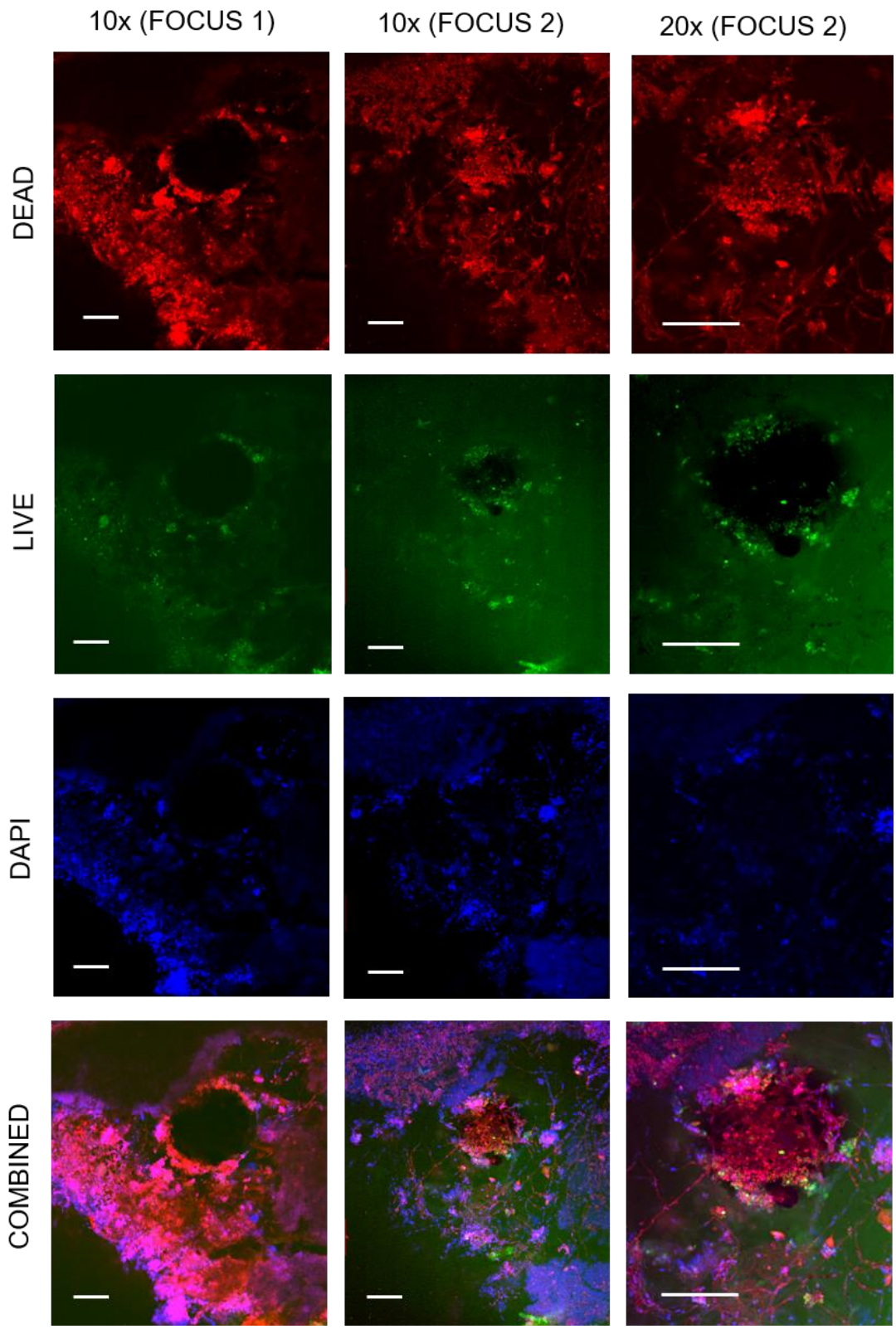

Live/Dead viability and DAPI staining of the retinal tissue explants (n=3) following Vortran green (532 nm wavelength, 40 mW power) laser ablation. Scale bar = 150 µm.

As shown in Figure 5.15, a distinct ‘blister’ like ablation could be visualised on samples following exposure to the DAPI/blue (405 nm, 50 mW) laser at maximum power, using confocal microscopy (4x and 10x magnification).

Figure 5.15 Retinal tissue viability following blue (405 nm, 50 mW) laser ablation

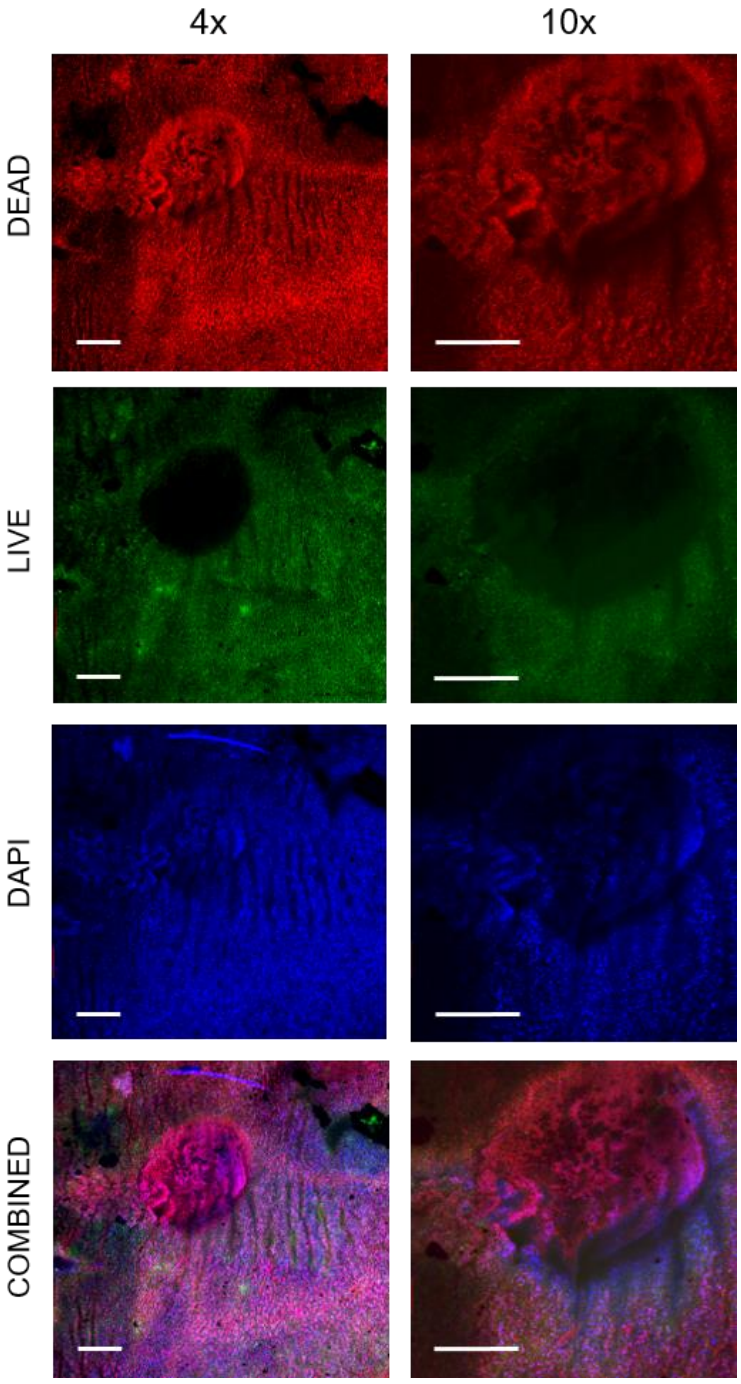

Live/Dead viability and DAPI staining of retinal tissue explants (n=3) following Fluoview confocal blue (405 nm wavelength, 50 mW power) laser ablation. Scale bar = 250 µm.

Damage caused by the blue laser ablation was found to have less depth and could be imaged at one focus point. Similar to the green laser ablation, a clear patch of dead tissue was evident, surrounded by a combination of both dead and live patches in the surrounding tissue. However, the injury site caused by the blue laser was considerably wider than injury caused by the green laser. The injury site measurement of samples exposed to the green laser ranged between approximately 330 - 413 µm wide, whereas the injury site of samples exposed to the blue laser ranged between approximately 500 - 857 µm wide. Whilst some samples exposed to the blue laser had a distinct circular shaped injury site (as presented), others had a less clear injury shape with a lighter, more widespread burn across the tissue surface. Despite these variations in tissue injury morphology, laser ablation generally produced a much smaller and more controlled site of damage in the retinal explants, in comparison to the mechanical and acetic acid injury techniques.

5.3.5 Assessment of mesenchymal stem cell interaction with retinal tissue

Following establishment of the retinal injury technique using laser ablation, the final objective was to add stem cells to the injured retinal model and observe their interaction with the tissue and injury site. Primary rMSCs were isolated from rat bone marrow for this purpose as previously described (Chapter 2, section 2.2.1.10).

5.3.5.1 Tri-lineage differentiation of primary rMSCs

To confirm the multipotency of isolated primary rMSCs a tri-lineage differentiation was firstly carried out for osteogenesis, adipogenesis and chondrogenesis. As shown in Figure 5.16, following 21 days of culture in tri-lineage differentiation medium the primary rMSCs

(n=3) stained positively with toluidine blue solution to indicate chondrogenesis, 2% alizarin red S to indicate osteogenesis and 0.5% oil red O to indicate adipogenesis.

Figure 5.16 Tri-lineage differentiation of primary rMSCs

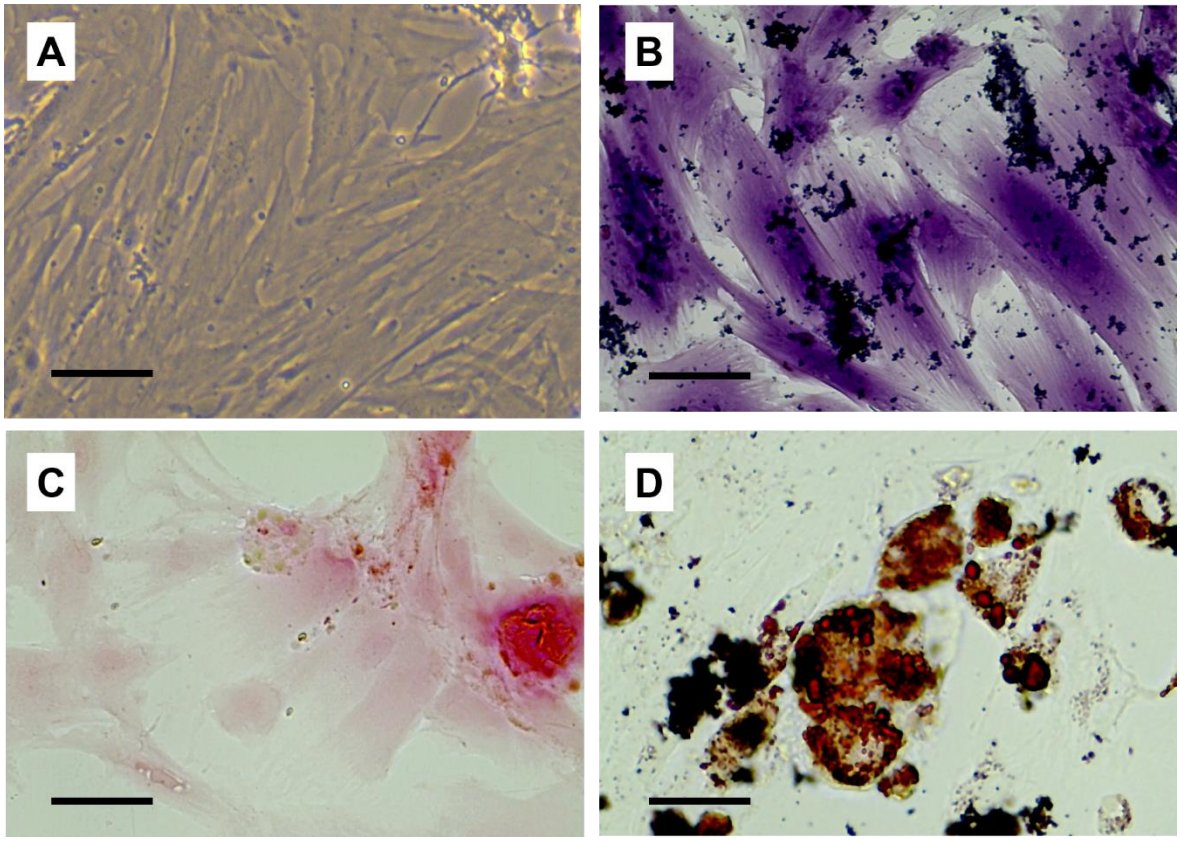

Primary rat bone marrow MSCs (n=3) cultured in control medium (A) and tri-lineage differentiation medium for chondrogenesis (B; stained with toluidine blue solution), osteogenesis (C; stained with 2% alizarin red S) and adipogenesis (D; stained with 0.5% oil red O). Scale bar = 150 µm.

5.3.5.2 Localised delivery and retention of rMSCs to injured retinal tissue

Following confirmation of multipotency, it was firstly decided to deliver rMSCs locally to the injury site of retinal explants damaged using the Vortran green laser. To optimise the accuracy of localised delivery, use of a 5µL Hamilton syringe was investigated. To test whether rMSCs would survive ejection through the narrow syringe needle, Live/Dead cell viability staining was carried out on rMSCs (n=3) following ejection. As shown in Figure

5.17, rMSCs survived ejection from the 5µL Hamilton syringe needle. Whilst an improved image quality would have been preferable, unfortunately the fluorescence and confocal microscopes were unavailable at the time of imaging and a dissecting fluorescence microscope was used for this.

Figure 5.17 rMSC viability following ejection from 5 µL Hamilton syringe needle

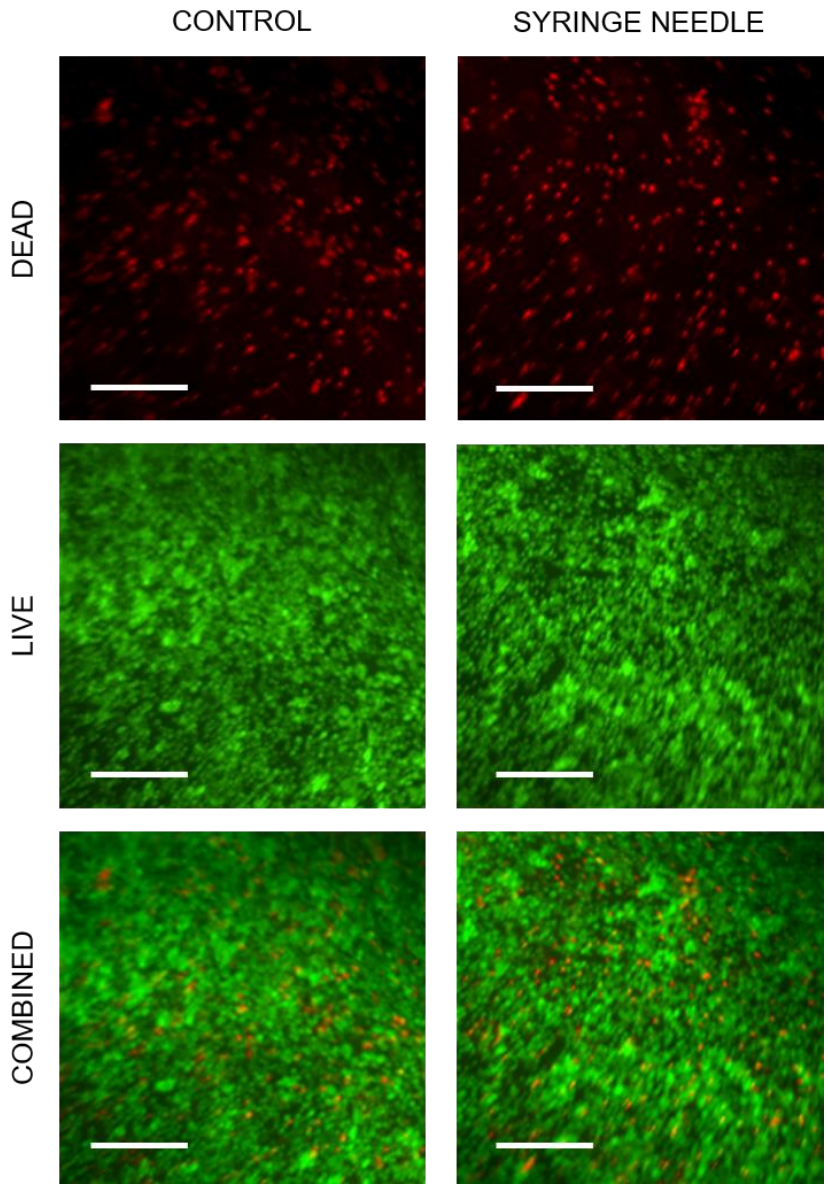

Live/Dead cellular viability staining of suspended rMSCs (n=3) under the control (not injected) condition and following ejection from the 5 µL Hamilton syringe needle. Scale bar = 500 µm.

Once rMSC viability with use of the 5 µL Hamilton syringe had been confirmed, rMSCs were locally delivered to the injury site of retinal explants damaged using the Vortran green laser. Accurate delivery proved very difficult, despite use of an acetate grid to help match the rMSC delivery location with the laser ablation site. After several attempts, localised delivery of rMSCs to the retinal injury site was achieved with some samples. Figure 5.18 presents the outcome of rMSC culture on injured retinal explants. As shown, rMSCs appeared to interact with the retinal injury site by day 3 of culture. Furthermore, the area surrounding rMSCs stained positively for RPE65 (using RPE65 mouse monoclonal primary antibody and goat anti-mouse TRITC secondary antibody; n=2), indicating a possible differentiation of some rMSCs into RPE.

Figure 5.18 rMSC interaction with retinal injury site following localised delivery

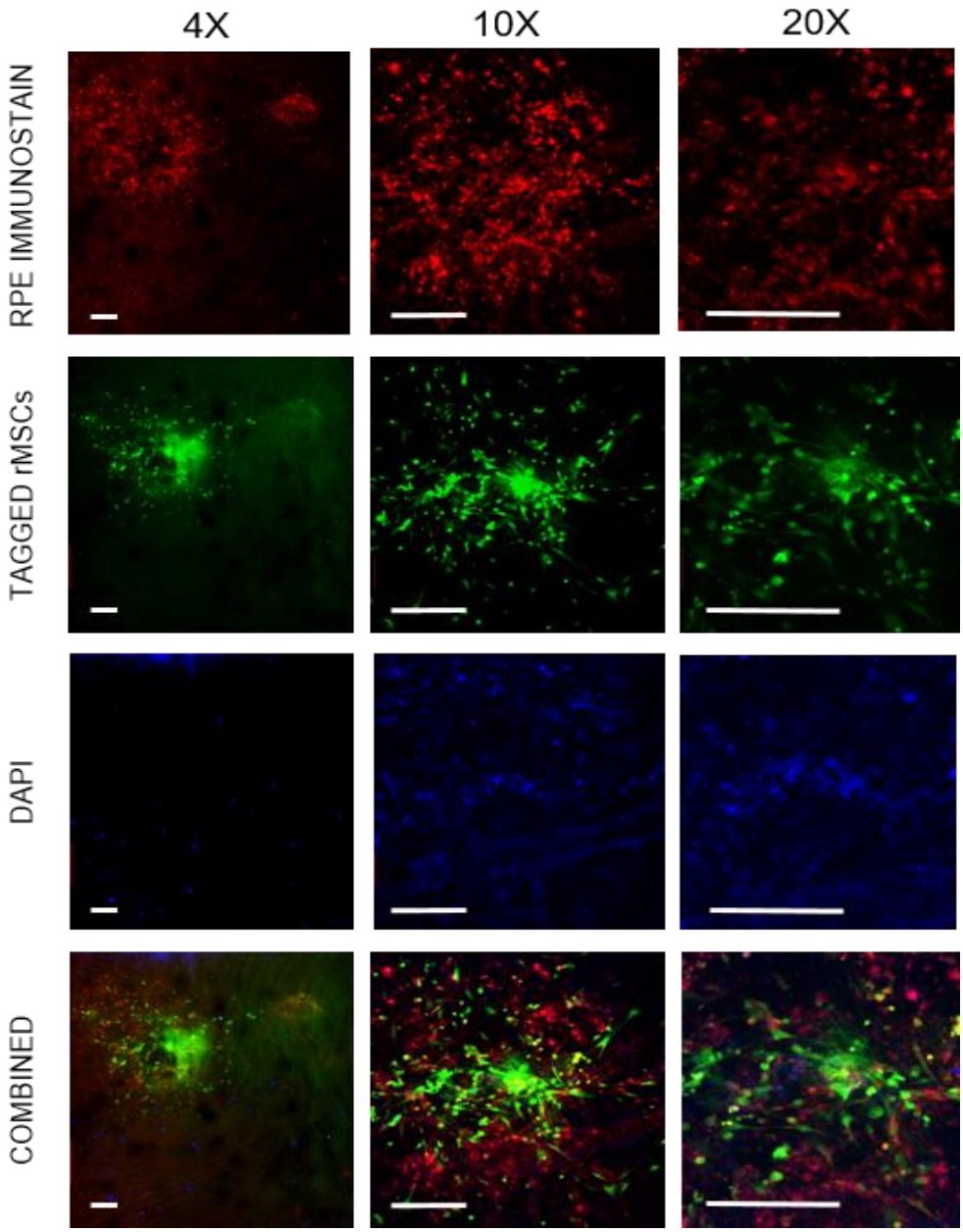

Retinal model injury site (n=2) immunostained with RPE65 mouse monoclonal primary antibody and goat anti-mouse TRITC secondary antibody (red) following localised delivery of rMSCs (green) labelled by CFSE cell labelling dye. Scale bar = 250 µm.

Due to the difficulty of accurate localised rMSC delivery to the small (approx 330 - 413 µm wide) retinal injury site produced by the Vortran green laser, it was decided to test rMSC delivery to injury produced by the Fluoview confocal blue laser (maximum power). Since the blue laser was found to produce a wider (approx 500 - 857 µm wide) injury site, a 20 µL cell culture pipette was used to deliver the rMSCs more widely across the retinal tissue sample. As well as compensating for the wider injury site, this also allowed for an opportunity to observe whether rMSCs may be drawn towards the injury site via chemoattractants. Expression of IL8, one of several chemokines associated with retinal damage, was assessed in addition to the tracking of rMSC location. As shown in Figure 5.19, injured retinal samples had evidently increased IL8 expression in comparison to control samples (n=3). Furthermore, rMSCs appeared to aggregate in the areas of increased IL8 expression. Due to the variability of injury shape between samples, it was difficult to accurately observe change between the day 3 and 7 time points. However, there was an evident ‘diagonal line’ distribution of rMSCs across the injured sample at day 3, which appeared to match the ‘diagonal’ distribution of IL8 expression. Additionally, there was an evident ‘horseshoe’ shaped distribution of rMSCs across the injured sample at day 7, which appeared to match the ‘horseshoe’ shaped distribution of IL8 expression in this example. In contrast, rMSCs appeared to be distributed evenly across control samples, with minimal aggregation observed in the absence of injury.

Figure 5.19 IL8 expression in retinal model following injury and rMSC delivery

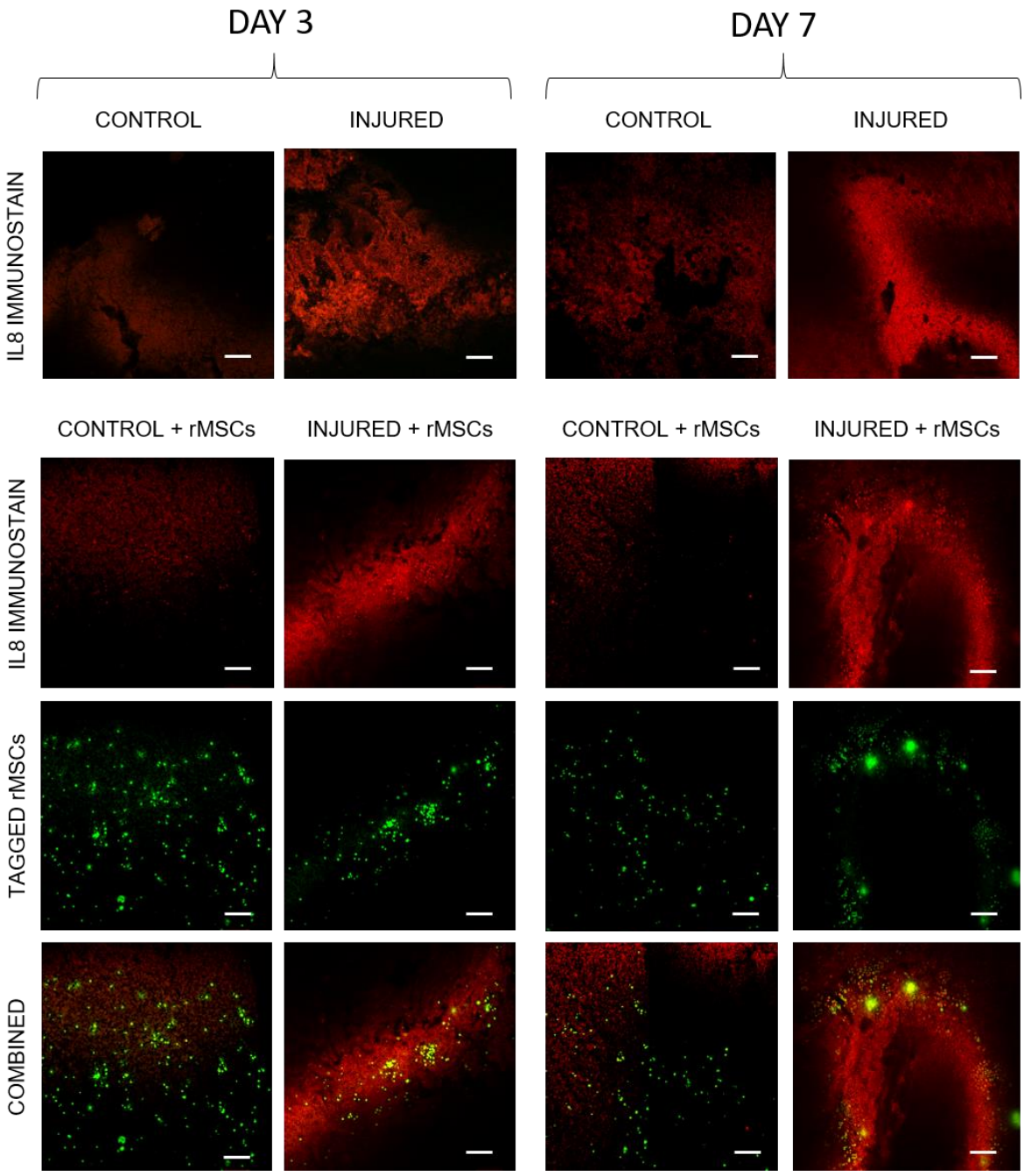

Immunostaining with IL8 mouse monoclonal primary antibody and goat anti-mouse TRITC secondary antibody (red) on retinal samples under control conditions (no damage) and following laser injury, with subsequent delivery of rMSCs (green) labelled by CFSE cell labelling dye. Scale bar = 150 µm.

The proportion of rMSCs which appeared to aggregate towards the laser injured area of retinal tissue was semi-quantified (Figure 5.20). As shown, there were significantly more

rMSCs aggregated towards the lasered area of samples in comparison to the control (non-lasered) area of retinal tissue samples at both the day 3 (p=0.018) and day 7 (p=0.02) time points. Whilst some increase of aggregation was observed at the day 7 time point in comparison to day 3, this difference was not significant.

Figure 5.20 Semi-quantified proportion of rMSCs aggregated towards laser injury

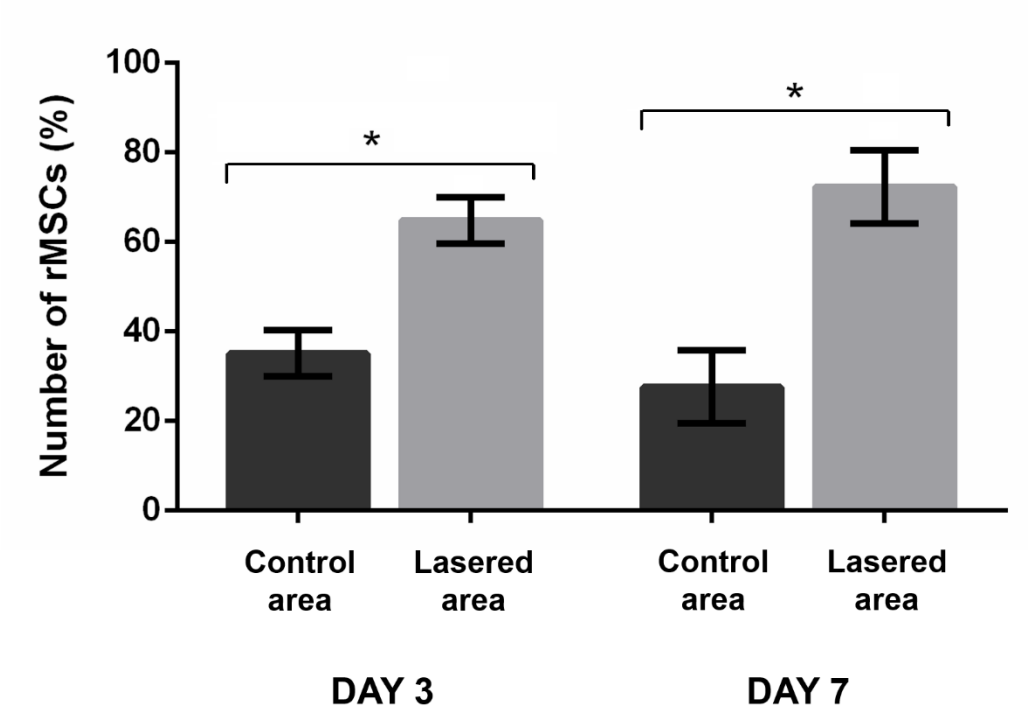

The semi-quantified proportion of rMSCs which appeared to aggregate towards the laser injured area of retinal tissue model samples (n=3). Data are expressed as mean ± SE (n=3). * indicates p <0.05.

In addition to chemokine and cellular location assessment, it was also of interest to try and characterise the rMSCs after culture on top of the retinal tissue model, to observe whether there was any potential differentiation into RPE. As shown in Figure 5.21, some rMSCs stained positively for RPE65 (using RPE65 mouse monoclonal primary antibody and goat anti-mouse TRITC secondary antibody; n=3). Similar to the previous experiment, it was

difficult to accurately observe change between the day 3 and 7 time points due to the variability of injury shape between samples. However, in both samples there was an evident ‘mosaic’ like pattern of non-differentiated rMSCs (green only) and rMSCs which may have differentiated into RPE (both green and red). Furthermore, the rMSCs had a rounded morphology more characteristic of native RPE in comparison to the first attempt presented in Figure 5.18. Therefore, injury created by the blue laser may damage the RPE in a small enough way to enable rMSC integration with this layer.

Figure 5.21 RPE expression in retinal injury model following rMSC delivery

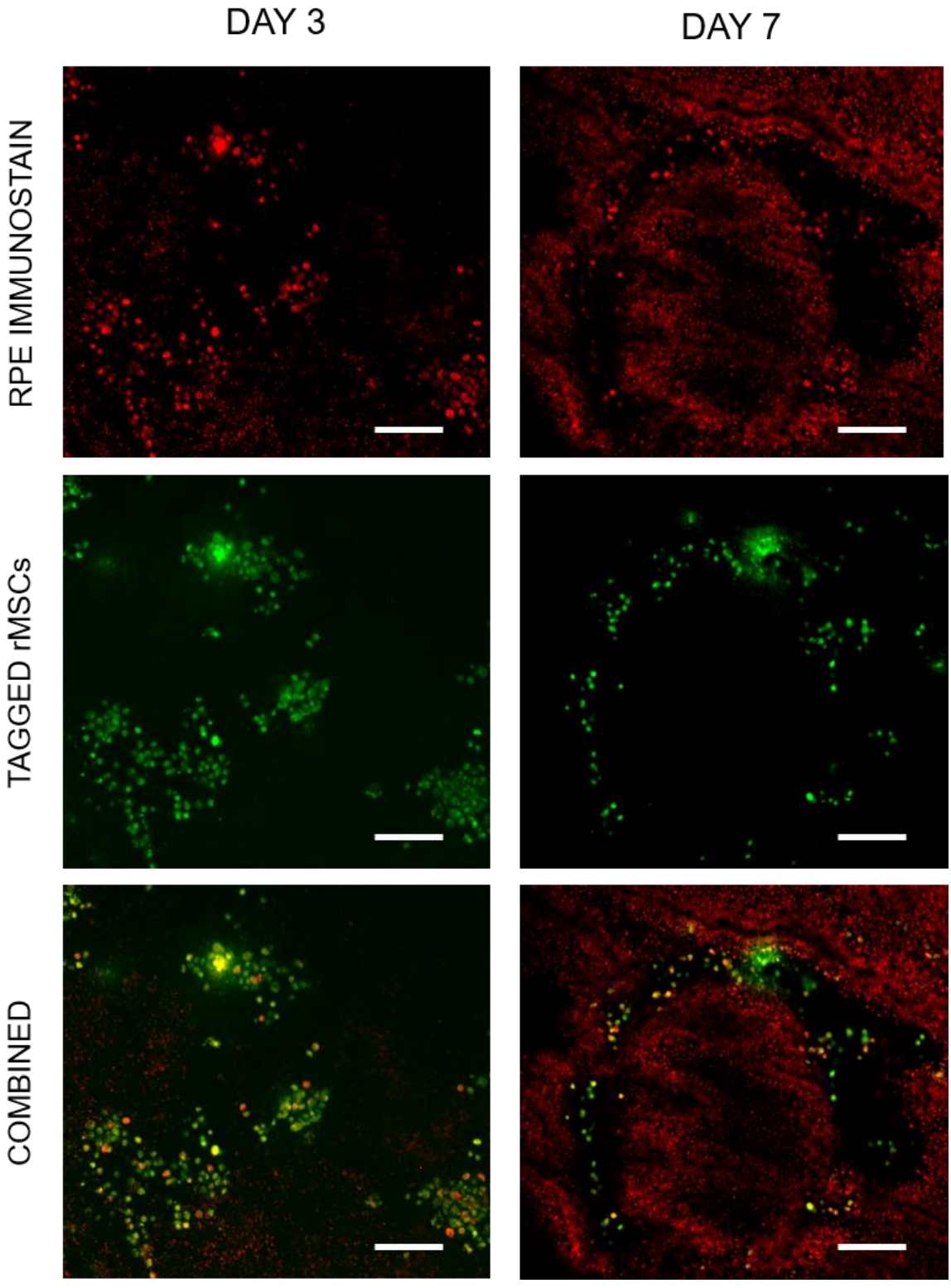

Retinal injury model (n=3) immunostained with RPE65 mouse monoclonal primary antibody and goat anti-mouse TRITC secondary antibody (red) following localised delivery of rMSCs (green) labelled by CFSE cell labelling dye. Scale bar = 100 µm.

5.4 Discussion

As the neuronal structure of the porcine retina is similar to that of the human retina (Guduric-Fuchs *et al.*, 2009), it is of interest to explore organotypic slice culture of the porcine retina. However, previous culture methodologies are arguably too basic to mimic the highly complex environment required for optimal preservation of retinal explants. Furthermore, previous isolation methodologies may disrupt the retina's distinct layered structure and cause disorganisation of the tissue. This study therefore aimed to establish an improved, efficient and reproducible 3D organotypic retinal tissue model using porcine eyes, which better preserves all intact layers of the retinal tissue with minimal distortion. Initially, an improved dissection protocol was developed to obtain the retinal explants and transfer them onto a more biocompatible substrate for culture. Once an improved culture method had been established, a secondary aim was to develop a consistent and reproducible injury in the retinal tissue to mimic the damage of disease/trauma. Finally, stem cells were to be added to the retinal injury model to observe their interaction with the tissue and injury site. Uniquely, OCT image modality was used to monitor structural alteration during the retinal tissue culture under various culture and injury conditions.

5.4.1 Optimised culture of 3D organotypic retinal explants

Due to the significant complexity of neural tissue in comparison to other tissues, biocompatible substrates (e.g. hydrogels) are highly valuable for neural tissue engineering. In particular, polymers which contain natural ECM components are known to provide enhanced biocompatibility to hydrogels because they provide structure and mechanical integrity to tissues, as well as support for cellular processes. Whilst certain synthetic polymers can mimic ECM components, a naturally occurring polymer such as collagen is likely to provide neural tissue with a more recognisable, physiologically relevant substrate

on which to reside (Aurand *et al.*, 2012). For this reason, type I collagen hydrogel was tested as a substrate for the culture of organotypic retinal tissue explants in this study. Initially, collagen hydrogel preserved the retina's layered structure relatively well in comparison to filter paper at day 0 of culture. However, a lack of adhesion between the soft retinal tissue and highly hydrated collagen hydrogel meant that samples either folded, moved around or detached completely beyond the first day of culture.

In an attempt to improve adhesion between the retinal tissue and collagen hydrogel, it was decided to test compressed collagen gel for the culture of organotypic retinal explants. Plastic collagen compression was first reported by Brown *et al.*, (2005). By removing the unbound water from collagen hydrogels, it can improve the mechanical properties of collagen gel, without a loss of biocompatibility or tissue viability. Compressed collagen gel was therefore an interesting substrate to test for retinal tissue culture. As predicted, the cultured retinal tissue explants had increased adhesion with the compressed collagen gel, which improved maintenance of the retinal tissue layers. In addition, 0.4 μm culture inserts were used to elevate samples above the culture medium and prevent retinal tissue detachment and movement due to floating. The air-liquid interface provided by culture inserts was also assumed to provide an extra benefit of improving oxygen supply to the photoreceptors, which are known to have a high energy demand (Narayan *et al.*, 2017).

During culture, the live retinal samples were monitored using a non-destructive imaging technique, OCT. OCT is capable of producing high resolution, cross sectional images of materials such as biological tissue. It works by directing near-infrared light into samples and then, by measuring the intensity of the back reflected light, an image is produced. OCT penetrates samples more deeply than confocal imaging, but has a higher resolution than

ultrasound imaging, therefore bridging the gap between these two methods. The commercially purchased OCT used in this study utilises a centre wavelength of 1300 nm, which provided approximately 3.5 mm imaging penetration in the retinal samples (Thorlabs, 2015). To maintain a sterile environment inside the culture plate, all live samples needed to remain covered by a lid during imaging. As the refractive index of a plastic culture plate lid caused image distortion, the plastic lid was exchanged for a manipulated lid with glass windows. Whilst this still caused a slight decrease in resolution during imaging, the layered structure and morphology of *in vitro* retinal model samples could be imaged successfully. OCT was a beneficial tool for this study since it allowed the assessment of live retinal samples at multiple time points, without a requirement for staining or fixation. During culture on compressed collagen gel and culture inserts, retinal samples had a gradual decrease in the number of retinal layers visible using OCT at each time point. However, there appeared to be minimal disorganisation of the retina's structure for up to 2 weeks.

To cross validate the morphological assessment undertaken using OCT, Live/Dead staining and histological assessment were also carried out to assess the viability of cultured 3D organotypic retinal explants on compressed collagen. Cultured retinal explants were viable for up to 2 weeks before small patches of dead tissue became evident at day 14. Additionally, the histological assessment confirmed preservation of the retina's distinct layered structure for up to 2 weeks, with increased detail. Therefore, whilst live retinal samples became more difficult to visualise using OCT over time due to a loss of stability in the tissue layers, preserved organisation of the layers could still be proven to an extent at day 14 using histological assessment. Furthermore, immunostaining indicated the presence of RPE in cultured organotypic retinal explants and confirmed its orientation (facing

upwards) during culture. These outcomes therefore offer an improvement in comparisons to previous work. For example, Johnson & Martin (2008) isolated rat retinal tissue using a paintbrush. Furthermore, Viktorov *et al*., (2004) preserved postnatal rat retina using roller-tube culturing. Both of these methods are likely to have disrupted the retina's fragile layered structure. Therefore, the isolation method of porcine retina developed in this study improves on these methods, by ensuring preservation of the retina's layered structure during isolation. Due to the high energy demand of photoreceptors and the associated RPE layer, the fact that these layers are maintained and face upwards during culture are another major advantage of the model developed in this study. This not only improves the oxygen supply to these layers, but also makes them more accessible for potential treatment testing and assessment.

The culture substrate used in this study can also be considered an improvement in comparison to previous methods. For example, Wang *et al.*, (2011) cultured porcine retina on filter paper, which is arguably a very basic substrate for neural tissue. Therefore, the biocompatible compressed collagen used in this study improves on this. Arguably, there are other biocompatible substrates mentioned in previous literature that could also be beneficial for *in vitro* retinal tissue culture. *In vivo* the retina makes contact with vitreous humour; a hydrated, gel-like mass composed of 99% water. The solid component of vitreous humour is thought to consist of a sparse network of collagen fibrils, hyaluronic acid and hyalocyte cells, as well as certain salts, sugar and ascorbic acid. The *in vivo* vitreous supports retinal metabolism by acting as a reservoir for substances such as oxygen, glucose and ascorbic acid, as well as a removal system for metabolic waste products (Kokavec *et al.*, 2016). Due to the highly supportive environment that vitreous humour provides for retinal tissue, substrates such as low polymeric content hydrogels

(Hayashi *et al.*, 2017) or hyaluronic acid based hydrogels (Januschowski *et al.*, 2019), may be other good alternatives for *in vitro* retinal tissue culture. However, due to the highly hydrated nature of vitreous-like hydrogels, these may be problematic for prolonged maintenance of the retina's layered structure *in vitro* without disorganisation. Testing of non-compressed collagen hydrogel in this study demonstrated this problem and highlighted the importance of mechanical strength and adhesion for long term culture. *In vivo*, the retina's structure is held in place by the vitreous humour in combination with IOP, which is challenging to mimic *in vitro*. Therefore, the adherence of retinal tissue to a compressed collagen hydrogel substrate was beneficial for providing the mechanical strength required to preserve the retina's layered structure in the absence of IOP, whilst still being highly biocompatible.

5.4.2 Assessment of retinal tissue model injury methods

Once the *in vitro* 3D organotypic retinal tissue culture model had been established, it was of interest to explore retinal injury techniques to potentially mimic the damage of disease. Retinal diseases such as macular degeneration and retinitis pigmentosa are typically characterised by the degeneration of photoreceptors and RPE layer, whilst untreated glaucoma can lead to the degeneration of ganglion cells (Hong *et al.*, 2005; Strauss, 2005; Hartong *et al*., 2006). Since the RPE and photoreceptor layers face upwards in the established culture model, it provides a convenient and valuable tissue explant to test potential injury methods which target these 1-2 layers. In previous work, retinal damage has been inflicted on animal models using methods such as inherited retinal degeneration (Samardzija *et al.*, 2010), blast induced trauma (Mammadova *et al.*, 2017), chemical lesioning (Paschalis *et al.*, 2017) and light induced damage (Grimm and Remé, 2012). *In vitro* retinal models have also been injured using techniques such as mechanical stress

(Farjood and Vargis, 2018) and light induced/laser lesioning (Denton *et al.*, 2010; Yu *et al.*, 2016). It was therefore of interest to test similar retinal injury methods on the developed *in vitro* retinal tissue model.

Initially, mechanical and acetic acid injury techniques were tested. However, these lesioning techniques were evidently too large to mimic the subtle, 1-2 layer damage of most retinal diseases. Furthermore, they caused considerable disruption and disorganisation of the surrounding retinal tissue layers. Nevertheless, both injury methods produced a distinct area of dead tissue on the retinal model samples, with the majority of surrounding tissue kept alive. Therefore, whilst the mechanical and acetic acid injury methods were probably unsuitable for mimicking retinal disease, these could be useful for research into traumatic injuries, such as retinal tear or chemical injury.

In an attempt to find a more subtle method of retinal injury, laser ablation was also tested. Interestingly, the green (532nm) laser tested was of the same wavelength as the frequency-doubled YAG green laser currently used in ophthalmology to create a capsulotomy to treat angle-closure glaucoma. Furthermore, the red (637nm) laser tested was of a similar wavelength to the Krypton red (647nm) laser currently used to coagulate choriocapillaries for treatment of the subretinal neovascular membrane (Abdulrahman and Marwan, 2019). As previously described, it proved difficult to image injury sites accurately using OCT and it was challenging to distinguish between areas of damage already present from the tissue isolation process and damage caused by the lasers. Nevertheless, some potential areas of structural injury could be identified using OCT after laser exposure. As presented, the Vortran red laser caused no structural damage visible using OCT. Whilst this laser had the highest power (100 mW) it also had the longest wavelength (637 nm), indicating that

wavelength may have more of an influence on retinal damage than power. Furthermore, since the *in vitro* retinal explants are cultured in the absence of a lens and other eye cup structures, all lasers would not have been focused on the retina in the same way as it would be *in vivo*. This may explain for any discrepancy in the results and could indicate why no cross sectional damage was observed after red laser ablation and on occasion with the other lasers. Even though no structural damage was produced using the red laser, it can be assumed that it must still have caused some functional damage.

Since diseases such as retinitis pigmentosa usually cause structural retinal damage visible using OCT *in vivo*, it was promising to observe potential structural damage using OCT on *in vitro* samples after green and blue laser ablation. Similar to *in vivo* case studies of laser damage (Dirani *et al*., 2013), the *in vitro* laser damage varied considerably in size and shape between samples. This may be explained by a difference in refractive index between retinal layers which can lead to light scattering (Yu *et al*., 2016). Furthermore, the transferred explants had an inconsistent surface topography and possible irregularity of the photoreceptor layer, which can lead to further light scattering (Yin *et al.*, 2003). Variability of retinal laser damage was observed in both live *in vitro* samples using OCT and fixed samples using confocal microscopy. The green laser was generally found to produce lesions approximately 330 - 413 µm wide. Although the green laser had a lower power (40 mW) than the red laser (100 mW), it had a shorter wavelength (532 nm) which may explain why it produced the structural damage visible using OCT which the red laser did not. Generally, longer light wavelengths are thought to penetrate more deeply into biological tissues and be less damaging in comparison to shorter wavelengths, due to an increased absorption into the tissue (Ash *et al.*, 2017). The blue/DAPI laser was found to produce more widespread lesions approximately 500 - 857 µm wide. The blue laser had a

short wavelength (405 nm) and higher power, estimated to be 50 mW based on information from the manufacturer. This higher power and shorter wavelength may therefore explain why the blue laser produced more widespread lesions in comparison to the green laser's more narrow lesions.

This reasoning may be further explained by photon energy, which can be calculated by multiplying Planck's constant by frequency. According to this equation, shorter light wavelengths generally exert more photon energy in comparison to longer light wavelengths (Meschede, 2008). Overall, this may explain why the red (637 nm) laser produced the least structural damage to retinal tissue, with an approximate photon energy of 3.12×10^{-19} joules. Additionally, this may explain why the blue (405 nm) laser, with an approximate photon energy of 4.90×10^{-19} joules, produced more widespread damage in comparison to the green (532 nm) laser, calculated to have an approximate photon energy of 3.73×10^{-19} joules. Since the blue laser had the greatest photon energy, it is likely that more photothermal damage was transferred onto the retinal tissue, therefore exerting more widespread damage (Youssef *et al*., 2011).

5.4.3 The interaction of mesenchymal stem cells with retinal tissue

Following establishment of the retinal laser injury technique, it was decided to add stem cells to samples injured by the green and blue lasers and assess their interaction with the tissue. As previously described, accurate localised delivery of rMSCs to the narrow injury site produced by the green laser proved difficult to achieve manually. This was despite use of a 5 µL Hamilton syringe needle and acetate grid to help guide the needle to the same location as the laser ablation. After several attempts, localised delivery of rMSCs to the

green laser injury site was achieved with some samples. rMSCs appeared to interact with the retinal injury site by day 3 of culture. However, due to the low success rate there were unfortunately not enough samples to observe interaction at an additional day 7 time point. Nevertheless, the experiment was an initial proof of efficacy and the delivery technique has the potential to be optimised in future work. For example, an automated laser ablation and stem cell delivery process would be highly valuable for improving precision and accuracy of the process.

As an alternative to localised delivery of rMSCs to the narrow retinal injury site produced by the green laser, it was decided to test widespread rMSC delivery to the wider injury site produced by the blue laser. In addition to alleviating the challenge of localised delivery, this experiment also allowed for an opportunity to observe whether rMSCs may be drawn towards the injury site via chemoattractants. The imaging of IL8 expression was another beneficial method to image retinal laser ablation, appearing as a light, widespread burn across the tissue surface. IL8 has been acknowledged in previous literature to increase in the vitreous fluid of several retinal diseases and has been detected after RPE injury during the wound healing response (Yang *et al.*, 2015; Yoshimura *et al.*, 2009). As presented, rMSCs appeared to aggregate towards areas of increased IL8 expression, in comparison to the control samples without injury. Therefore, it can be assumed that rMSCs may have been drawn towards this chemoattractant as would be expected. Furthermore, it was noticed that rMSCs usually aggregated around any areas of injury that were already naturally present on the control samples (Figure 5.22). Therefore, injury using the laser was not necessarily required to observe this effect. Arguably, the natural degradation of the cultured retinal samples themselves could be beneficial enough to study retinal disease damage, without the need for artificial damage to be created.

Figure 5.22 rMSC aggregation towards natural areas of damage on control sample

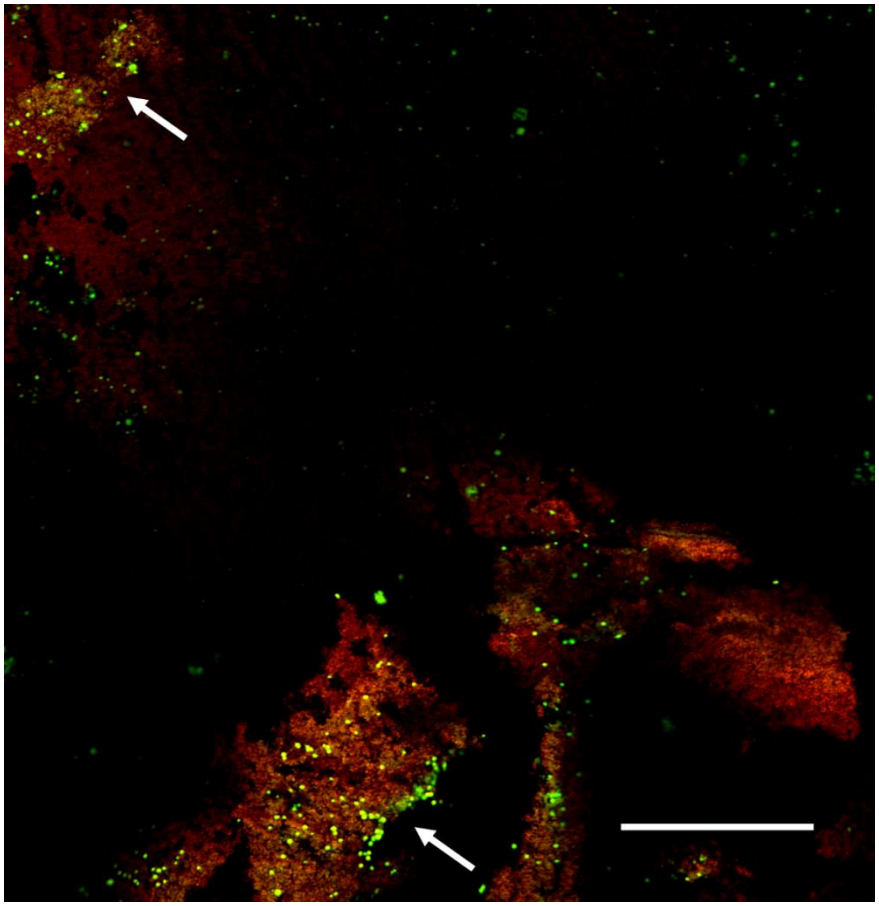

Control retinal tissue sample (n=2) immunostained with IL8 mouse monoclonal primary antibody and goat anti-mouse TRITC secondary antibody (red) with delivered rMSCs (green) labelled by CFSE cell labelling dye, at the day 3 time point. White arrows indicate rMSC aggregation towards the natural areas of damage. Scale bar = 500 µm.

In addition to IL8 expression and cellular location assessment, it was decided to characterise the rMSCs at day 3 and 7 of culture on the retinal injury model, to observe whether there was any differentiation of rMSCs into RPE. As shown in Figure 5.21, some rMSCs stained positively for RPE65. However, it was challenging to accurately observe change between the day 3 and 7 time points due to the variability of injury shape between samples. Nevertheless, in both sample groups there was an evident 'mosaic' like pattern of non-differentiated rMSCs and rMSCs which may have differentiated into RPE. The rMSCs also appear to have a rounded morphology more characteristic of native RPE. Therefore,

the less deep and more widespread injury created by the blue laser may damage the RPE specifically and in a small enough way to enable rMSC integration with this layer. For future work, it would be beneficial if a greater number of samples could be obtained per experiment, in order to more accurately observe these trends between sample groups. Additionally, it would be interesting to test whether more specialised stem cells such as induced pluripotent stem cells for retinal application (Kokkinaki *et al.*, 2011; Wright *et al.*, 2014) or retinal progenitor cells (Klassen *et al.*, 2004; Schmitt *et al.*, 2009; Luo *et al.*, 2014; ReNeuron, 2016) would show a greater amount of differentiation and interaction within this developed model.

5.5 Conclusion

To summarise, this study involved the development of a novel, improved *in vitro* 3D organotypic retinal tissue model using porcine eyes. For the first time, a compressed collagen gel substrate was found to be beneficial in providing the mechanical strength required to preserve the retina's layered structure *in vitro* and in the absence of IOP, whilst still being biocompatible. Furthermore, OCT was applied to *in vitro* retinal tissue culture for the first time and proved to be a beneficial tool for monitoring the live retinal explants during culture. OCT allowed assessment at multiple time points without a requirement for staining or fixation. Whilst an inevitable degree of tissue degradation occurred during retinal tissue culture on compressed collagen gel over time, an improved model which better preserves all retinal layers intact and with minimal distortion has been established. Furthermore, the model's orientation enables convenient access to the RPE and photoreceptor layers for further testing. In an attempt to mimic damage caused by retinal disease in the developed model, injury techniques involving mechanical lesioning, acetic acid lesioning and laser ablation were tested. Results confirm that whilst mechanical and

acetic acid lesioning may be beneficial for mimicking traumatic injuries, the laser ablation technique proved better for creating a small injury targeted at the RPE/photoreceptor tissue layers. Once an injury technique had been established, rMSCs were added to the retinal explants which were found to aggregate towards locations of retinal injury indicated by IL8 expression. Furthermore, some rMSCs had differentiated into RPE by day 3 and 7 of culture. These results present promising potential if more specialised stem cells, such as retinal progenitor cells, were to be tested in future work. In conclusion, this model may offer a useful tool for the study of retinal disease mechanisms and the testing of stem cell therapies and drug intervention to treat retinal disease, whilst also reducing the requirement for live animal experiments.

Chapter 6

Discussion

6.1 Summative discussion

Eye diseases such as glaucoma, macular degeneration and retinitis pigmentosa can, without treatment, lead to severe sight problems and blindness. Although there are some existing treatments for these ocular diseases, current treatments are often invasive, have a low long term success rate and cannot regenerate damaged eye tissue. The demand for more effective ocular disease treatments is therefore high. Tissue engineering approaches for ocular disease study and treatment have advanced significantly over recent years with promising results. However, challenges still remain with aspects such as; the fibrotic response after ocular surgery, the effective delivery of regenerative materials to the eye, the possibility of immune rejection and the guidance of replaced retinal neurons to establish functional connections (Ramsden *et al.*, 2013). Therefore, both clinical research and the field of regenerative medicine require reliable conjunctival and retinal models, for the investigation of ocular disease mechanisms and testing of treatments, whilst also reducing the requirement for live animal experiments. The establishment and application of conjunctival and retinal models undertaken in this thesis enabled eye disease study via two major angles; discovery of the main factors to control the conjunctival fibrosis response associated with glaucoma surgery and the development of an improved retinal model for ocular treatment testing.

6.1.1 The revealing of multiple factors and their synergistic effects on fibrotic response after glaucoma filtration surgery

During glaucoma filtration surgery (trabeculectomy) an opening is created into the sclera and sub-Tenon's capsule/conjunctival membrane to form a drainage cavity for aqueous humour fluid. However, fibrosis occurring in the TCCT after surgery can cause the created opening to heal up again and become blocked, reducing the treatment success rate to just

55% (Hong *et al.*, 2005). Due to an assumed increase in cytokine/growth factor expression triggered by the surgical wound (Cunliffe *et al.*, 1995; Schlunck *et al.*, 2016), in addition to the known presence of growth factors in aqueous humour (Jampel *et al.*, 1990; Huang *et al*., 2015), it is widely assumed that growth factors and cytokines play a significant role in this fibrotic response. Furthermore, it is known that the force of shear stress can trigger mechanotransduction and stimulate fibrosis in various bodily tissues (Iskratsch *et al*., 2014). With this knowledge, it can be assumed that the drainage of aqueous fluid via the new drainage pathway after trabeculectomy is likely to exert shear stress induced mechanotransduction on the TCCT wound. However, the quantifiable influence of shear stress induced mechanotransduction on TCCT fibrosis remains unclear. Furthermore, the synergistic effect of shear stress in combination with key growth factors/cytokines in aqueous humour on TCCT has not widely been explored. Therefore, these stimulators were tested on 2D and 3D conjunctival tissue models constructed through tissue engineering approaches using TCCT fibroblasts and epithelial cells in this study (Chapter 3). The static and stimulated dynamic culture models were applied, with the hypothesis that growth factors and shear stress would cause an increase in fibroblast metabolic activity both individually and in combination synergistically.

As previously described in chapter 3, initial establishment of the 2D TCCT fibroblast model was a useful starting point for this study, since it enabled direct assessment of the influence that growth factors and shear stress may have on TCCT fibroblasts, without a surrounding ECM. Subsequently, establishment of the 3D TCCT fibroblast model was valuable, to enable assessment of the additional influence that ECM may have on the fibroblasts and fibrotic response. It was thought that the 3D model would mimic native TCCT more closely, whilst still using a controlled, quantifiable method. Once established,

the TCCT models were exposed to key growth factors, cytokines and aqueous humour both individually and in combination with shear stress, applied using a see-saw motion rocker. As predicted, results found that each of these factors, both individually and in combination with shear stress, appeared to cause an increase in TCCT fibroblast metabolic activity and matrix production in the *in vitro* models.

Aqueous humour is a clear fluid present in the ocular anterior chamber *in vivo* with a range of functions including waste product removal, nutrient supply, the transport of neurotransmitters and stabilisation of eye structure (Goel *et al.*, 2010). Previous studies have quantified the presence of numerous different growth factors and cytokines in aqueous humour, which may explain the significant increase of TCCT fibroblast proliferation and matrix production stimulated by porcine aqueous humour in this study. ELISA quantification confirmed the presence of TNF-α and TGF-β in porcine aqueous humour in this study. In addition, quantities of cytokines such as hepatocyte growth factor (12.22 ng/mL) and glial cell-line derived neurotrophic factor (114.42 pg/mL) have previously been measured in human aqueous humour, in addition to TGF-β and TNF-α (Cvenkel *et al*., 2010). The quantity of TGF-β in human aqueous humour has also previously been reported to vary based on race and age, with healthy African American patients having an average of 165.69 pg/mL and Caucasian American patients having an average of 145.54 pg/mL TGF-β in their aqueous humour, which increased with age (Trivedi *et al.*, 2011). Though higher dosages of individual TGF-β and TNF-α growth factors were used in this study model, in comparison to the quantities found naturally in aqueous humour, aqueous humour still triggered a far higher metabolic rate on cultured TCCT fibroblasts. This confirms that there are likely to be many growth factors in aqueous humour with variable quantities, which in combination may synergistically cause the

significant increase in TCCT fibroblast metabolic activity observed in this study, outweighing the influence of TGF-β and TNF-α individually. Overall, it can be assumed that growth factors present in wounded TCCT and aqueous humour, in combination with the shear stress induced by aqueous fluid outflow, may synergistically trigger the fibrosis response in TCCT after glaucoma surgery.

Whilst 3D models using collagen are a widely explored technique for *in vitro* experiments (Lee *et al*., 2001; Giménez and Montero, 2011), this study adopted additional advanced techniques. The use of a see-saw motion rocker to apply shear stress to 3D collagen model constructs arguably had several advantages. For example, the method enabled a high throughput which was advantageous, allowing shear stress exposure to many samples at once for 1 hour per day during culture in 48 well plates. The method also had a low cost and was easy to establish. Due to the thickness of the 3D collagen model constructs, cells experienced heterogeneous shear stress. Arguably, the fibroblasts at the top of each collagen gel would have been exposed to more fluid shear stress than those at the bottom. However, since the 3D samples had a low collagen concentration (3 mg/mL) we can be confident that shear stress would have passed through sample pores, previously estimated to measure between 2.2 – 1.1 µm in 1 - 4 mg/mL collagen hydrogels (Miron-Mendoza *et al*., 2010). Furthermore, it could be argued that this phenomenon mimics the *in vivo* environment more realistically. Fibroblasts located closer to the fluid flow in TCCT after trabeculectomy surgery would have exposure to shear stress stimulus, whereas fibroblasts located more deeply inside the tissue would not. The fluid shear stress generated in the 3D model is calculated following a protocol previously described in Zhou et al., (2010), to be approximately 0.065 Pa, based on fluid viscosity (10^{-3} Pa s), a maximum 7° flip angle, 1.6 mm fluid depth, 11 mm well length and 12 second cycle (5 rpm). The significant increase

of metabolic rate observed in the see-saw motion treated groups, in comparison to control groups, clearly indicated the influence shear stress had on TCCT fibroblast activity. This finding supports conclusions made in previous literature that shear stress induced mechanotransduction can increase fibroblast activity. In addition, this finding contributes to the knowledge that shear stress induced mechanotransduction occurring in TCCT after glaucoma surgery may synergistically enhance the fibrotic effect of growth factors.

In addition to metabolic activity, the subsequent formation of neocollagen by fibroblasts is another feature of the fibrosis believed to lead to excessive accumulation of ECM and scar tissue. To determine the influence that growth factors and shear stress may have on the collagen synthesis of TCCT fibroblasts, a novel non-destructive neocollagen monitoring technique was applied. Azido-L-proline was added to the culture medium of experimental 3D samples and subsequently imaged after incorporation into neocollagen through the Click-IT Alex Fluor 594 DIBO Alkyne reaction with the azido-L-proline (Bardsley *et al.*, 2017). This technique has not applied to eye tissue study previously. Results found that cytokines TGF-β, TNF-α and VEGF, plus 50% aqueous humour, all appeared to stimulate an increase in TCCT fibroblast neocollagen synthesis in comparison to the control, with 50% aqueous humour having the greatest effect. Exposure to shear stress also appeared to trigger a subtle increase in neocollagen synthesis. These findings therefore confirm the influence that cytokines and shear stress are likely to have on TCCT ECM synthesis, in addition to an increase in fibroblast metabolic function. Additionally, neocollagen fluorescent labelling was an advantageous technique for determining the fibrotic response of TCCT fibroblasts over a prolonged culture time period.

Additional experiments in Chapter 3 involved seeding conjunctival epithelial cells on top of the 3D TCCT fibroblast model. Results from these experiments indicated that key growth factors and shear stress may also enhance the fibrotic effect on TCCT with an epithelial layer. However, previous studies on healthy skin and ocular surface epithelium would not support this finding, since TGF-β is thought to inhibit the effect of epidermal growth factor. Therefore, whilst the elevated TGF-β levels triggered by ocular surface disease can promote the proliferation of fibroblasts, it may also arguably inhibit the proliferation of epithelial cells (Zheng *et al.*, 2010; Law *et al.*, 2016; Utsunomiya *et al.*, 2016). Nevertheless, these findings may be characteristic of what would be expected for injured epithelium. Since conjunctival epithelial cells were seeded on top of the 3D TCCT model gel using a cell culture pipette, any unevenly distributed areas, plus the edges of each gel, would have been 'incomplete' and therefore potentially mimicking injured epithelium. According to Izumi et al., (2005), a healthy/complete corneal epithelial cell layer protects and suppresses any abnormal proliferation and differentiation of fibroblasts via regulation of TGF-β and basic fibroblast growth factor (bFGF) signalling. However, when epithelial layers are injured or disrupted they are thought to release various growth factors triggering events such as fibroblast proliferation, migration and differentiation into myofibroblasts (Kunihiko *et al.*, 2002; He *et al.*, 2017; Richardson, 2017). The increase in metabolic activity observed in the 3D TCCT fibroblast-epithelium co-culture model may therefore be explained by the fact that the model mimicked the activity of injured epithelial cells and therefore further promoted fibroblast metabolic rate.

To summarise, the key results described in chapter 3 confirm that a combination of both the cytokines present in aqueous humour, as well as the shear stress induced by aqueous fluid outflow, may synergistically stimulate the fibrosis response in TCCT after trabeculectomy surgery. Furthermore, the established 3D TCCT fibroblast-epithelium co-

culture model potentially mimics injured conjunctival epithelium, which may further stimulate the fibrotic response.

6.1.2 Effective tissue models to assess the improvement of glaucoma treatment

Current anti-metabolic drugs used in an attempt to reduce the fibrotic response after glaucoma surgery include Mitomycin C and 5-Fluorouracil. These mitigate TCCT fibrosis to an extent by triggering apoptosis of fibroblasts via disruption of DNA synthesis (Tomasz, 1995). However, even with their use the 5-year failure rate of glaucoma surgery due to insufficient IOP control is 46.9% (Gedde *et al.*, 2012). Furthermore, their inhibitory mechanism is highly toxic and can lead to additional complications such as sub-conjunctival bleb thinning and leakage, cytotoxicity and damage to other tissues such as the cornea (Wolner *et al.*, 1991; Stamper *et al*., 1992). These issues have also led to an increased interest in the use of medical devices, such as the Xen Gel Stent, to improve the efficiency of glaucoma filtration surgery and reduce the detrimental effect of fibrosis. In light of these ideas, a selection of potential alternative inhibitors were tested on the 2D and 3D TCCT models established in chapter 3, in an attempt to find safer and more efficient anti-inflammatory agents. It was hypothesised that these would lead to a decrease in fibroblast metabolic activity within the model. Furthermore, *in vitro* assessment of the Xen Gel Stent medical device was undertaken using the TCCT fibroblast model. It is evident that 3D TCCT models were convenient and effective for the assessments.

As described in chapter 4, TGF-β and TNF-α growth factor inhibitors, Decorin proteoglycan and calcium signalling channel blocker Nifedipine were each individually tested on the established TCCT models via addition to the cell culture medium. Findings indicated that both growth factor inhibitors and Nifedipine caused a decrease in fibroblast

metabolic rate, making them potential alternatives to current anti-inflammatory agents. Decorin proteoglycan also appeared to cause a decrease in 3D cultured TCCT fibroblasts. However, due to an apparent increase in ECM synthesis, more research into the structural outcome of collagen matrix assembly would be required to draw an accurate conclusion.

Whilst TCCT fibroblast activity in response to inhibitors was evident in the quantitative and qualitative data, this work had some benefits and limitations to be acknowledged. For example, it is challenging to know whether cellular activity *in vitro* would be the same as *in vivo*, due to the lack of surrounding tissue structures. Furthermore, it is difficult to know whether mechanisms such as growth factor and calcium signalling inhibition would cause other undesirable side effects if used clinically. Nifedipine is currently used clinically as a drug treatment for high blood pressure. Therefore, there would be a chance that Nifedipine could adversely cause a change in ocular blood pressure if used clinically for this alternative anti-fibrotic purpose. Consequently, the requirement for *in vivo* testing would be inevitable for future work. Nevertheless, *in vitro* studies such as this one are a good starting point in the discovery of new treatment options and a decrease in fibroblast activity was clear, particularly in response to growth factor inhibitors and Nifedipine. These findings support the conclusions made in previous literature that calcium signalling channel blocking can cause a decrease in fibrotic activity (Matta *et al.*, 2015; Mukherjee *et al.*, 2015). In addition, these findings contribute to the knowledge that inhibitors and/or calcium signalling channel blocking could potentially be used to reduce the fibrotic effect of TCCT fibroblasts after glaucoma surgery.

The Xen Gel Stent medical device was inserted into 3D TCCT fibroblast model samples using the accompanying Xen Injector. Once inserted into the 3D *in vitro* model, TCCT

fibroblast activity, location and neocollagen synthesis surrounding the device was monitored for up to 2 weeks of culture, whilst treated with TGF-β to mimic the potentially fibrotic environment. During this time, numerous fibroblasts appeared to grow in close proximity to the Xen Gel Stent device and several appeared to have been pushed towards the stent lumen during insertion. Furthermore, labelled neocollagen appeared to surround the fibroblasts by day 14. This evident fibroblast activity, particularly surrounding the stent lumen, therefore raises another cause for concern relating to *in vivo* usage. For example, the narrow Xen Gel Stent lumen may become blocked over time and lead to treatment failure in patients.

Overall, assessment of the Xen Gel Stent glaucoma medical device *in vitro* raised concerns for its use *in vivo*, evident fibrotic activity surrounding the stent lumen *in vitro*. Most previous clinical studies by the manufacturer have only followed patients for up to 12 months, meaning little is known about any long term complications associated with the Xen Gel Stent. Furthermore, aside from some *ex vivo* testing of a similar medical device known as the iStent using human donor eyes (Bahler *et al.*, 2012), there has previously been little to no study of MIGS devices *in vitro*, making these findings an interesting contribution to the field.

Due to the expense and limited availability of Xen Gel Stents, this study had a very low sample number of only 7 stents, 2 of which were damaged during insertion into the TCCT model. Furthermore, the operator skill and environment during *in vitro* insertion had significant differences to the typical *in vivo* insertion during glaucoma surgery. Since only one Xen Injector device was available, it was used multiple times for each insertion, despite recommendation from the manufacturer that the Xen Injector should only be used once to deliver a pre-loaded stent. Whilst a greater sample number would be required to

accurately determine fibroblast activity surrounding the Xen Gel Stent lumen, the fragile nature of the Xen Gel Stent was clear and arguably still raises concern for *in vivo* usage. Therefore, the device should perhaps be made using a stronger material in order to reduce the chance of breakage during insertion and *in vivo*. In consideration of other medical stents (e.g. vascular stents), a metallic material such as Nitinol may offer a better alternative, which is strong, flexible and biocompatible (Kapoor, 2017). Interestingly, a MIGS device made from Nitinol named 'Hydrus' was recently approved by the Food & Drug Administration (FDA, 2018), which may offer a better alternative in comparison to the Xen Gel Stent.

6.1.3 Improvement of retinal disease study and treatment

In cases where glaucoma treatment is not undertaken, is undertaken too late, or fails, an increased IOP can eventually lead to retinal tissue damage, causing vision loss. Furthermore, eye diseases such as macular degeneration and retinitis pigmentosa can also cause retinal tissue damage and subsequent vision loss. To investigate these ocular disease mechanisms, plus explore potential drug, neuroregenerative and cell therapy treatment options, complex and reliable retinal models are required. As the neuronal structure of the porcine retina is similar to that of the human retina (Guduric-Fuchs *et al.*, 2009), it is of interest to explore organotypic slice culture of the porcine retina. However, previous culture methodologies are arguably too basic to recreate the highly complex environment required for optimal preservation of retinal explants. Furthermore, previous methodologies may disrupt the retina's distinct layered structure and cause disorganisation of the tissue. In consideration of these previous limitations, this study tested organotypic retinal tissue culture using a biocompatible, collagen hydrogel substrate (Chapter 5). It was hypothesised that collagen hydrogel would provide retinal tissue with a more biologically relevant

material on which to reside and aid in better preservation of the retina's layered structure. Once an improved culture method for retinal explants was established, a retinal injury technique was then optimised with the retinal explants and stem cells subsequently injected to the injury to observe their interaction with the damaged tissue. Thus, this study provided an improved platform to study retinal disease and potential treatments.

As previously described in chapter 5, full thickness retinal tissue samples were isolated from porcine eyes and maintained *in vitro*, with the aim of preserving the retina's layered anatomical structure. In an attempt to improve adhesion between the retinal tissue and collagen hydrogel, it was decided to test compressed collagen gel for the culture of organotypic retinal explants. Plastic collagen compression was first reported by Brown *et al.*, (2005). By removing the unbound water from collagen hydrogels, it can improve the mechanical properties of collagen gel, without a loss of biocompatibility or tissue viability. Findings from OCT imaging confirmed that, whilst an inevitable degree of retinal tissue degradation occurred during culture on a compressed collagen gel substrate over time, an improved model which better preserves all retinal layers intact and with minimal distortion has been established. These findings contribute to the current literature by building on previous work such as Wang *et al.*, (2011) and demonstrating the pros and cons of compressed collagen hydrogel as a substrate for retinal tissue. Arguably, other substrates which mimic the vitreous humour more closely, such as low polymeric content hydrogels (Hayashi *et al.*, 2017) or hyaluronic acid based hydrogels (Januschowski *et al.*, 2019), may offer better alternatives. However, due to the highly hydrated nature of vitreous-like hydrogels, these may be problematic for prolonged maintenance of the retina's layered structure *in vitro* without disorganisation. Testing of non-compressed collagen hydrogel in this study therefore demonstrated this problem and highlighted the importance of

mechanical strength and adhesion for long term culture. *In vivo*, the retina's structure is held in place by the vitreous humour in combination with IOP, which is challenging to mimic *in vitro*. Therefore, the adherence of retinal tissue to a compressed collagen hydrogel substrate offered mechanical strength to the model, important for maintaining the retina's layered structure in the absence of IOP and the choroid tissue.

In an attempt to mimic damage caused by retinal disease in the developed model, injury techniques involving mechanical lesioning, acetic acid lesioning and laser ablation were tested on the established retinal model. Findings confirmed that, whilst mechanical and acetic acid lesioning may be beneficial for mimicking traumatic injuries, the laser ablation technique proved better for creating a small injury targeted to the RPE/photoreceptor tissue layers. Similar to *in vivo* case studies of laser damage (Dirani *et al*., 2013), the *in vitro* laser damage varied considerably in size and shape between samples, which may be explained by a difference in refractive index between retinal layers leading to light scattering (Yu *et al*., 2016). Despite this, generally the green laser (532 nm, 40 mW) was found to produce narrow lesions approximately 330 - 413 µm wide. Meanwhile, the blue/DAPI laser (405 nm, 50 mW) was found to produce more widespread lesions approximately 500 - 857 µm wide. It proved difficult to image the small injury sites accurately using OCT, since it was challenging to distinguish between areas of damage already present from the tissue isolation process and damage caused by the lasers. Nevertheless, some potential areas of structural injury could be visualised after laser exposure using OCT, plus in more detail using confocal microscopy. Following laser injury, added stem cells were found to aggregate towards the locations of retinal injury indicated by IL8 expression. Furthermore, some rMSCs had differentiated into RPE by day 3 and 7 of culture.

6.1.4 Advantage of using non-destructive imaging modalities

In addition to the requirement for improved *in vitro* modelling, clinical research and the field of regenerative medicine also require the continued improvement of *in vitro* monitoring techniques, enabling visualisation of treatment interactions with cells and tissue in a prolonged treatment period without terminating the samples. Therefore, this study also aimed to apply reliable and convenient non-destructive imaging techniques to assess cellular responses towards treatment and to evaluate the associated mechanisms. To monitor TCCT samples, a non-destructive neocollagen monitoring technique was applied. Azido-L-proline was added to the culture medium of experimental samples and subsequently imaged after incorporation into neocollagen through the Click-IT Alex Fluor 594 DIBO Alkyne reaction with the azido-L-proline (Bardsley *et al*., 2017). This technique was an advantageous tool for monitoring fibrotic response *in vitro*, since it allowed imaging of ECM synthesis at multiple time points throughout experiments, without the need to terminate samples for fixation. Furthermore, the technique was applied to effectively image fibrotic response surrounding the Xen Gel Stent medical device, which could easily be replicated to assess fibrosis surrounding other medical devices *in vitro.*

To monitor the *in vitro* retinal tissue samples during culture, OCT imaging was applied. OCT is a non-invasive imaging technique capable of producing high resolution, cross sectional images of materials such as biological tissue. It works by directing near-infrared light into samples and then, by measuring the intensity of the back reflected light, an image is produced. Since OCT penetrates samples more deeply than confocal imaging, but has a higher resolution than ultrasound imaging, it therefore bridges the gap between these two methods. The commercially purchased OCT used in this study utilises a centre wavelength of 1300 nm, providing approximately 3.5 mm imaging penetration in the retinal samples

(Thorlabs, 2015). Furthermore, the lateral resolution of the OCT used was 13 µm and had an axial resolution of 5.5 µm in air. OCT was a beneficial tool for *in vitro* retinal tissue modelling since it allowed the assessment of live retinal samples at multiple time points, without a requirement for staining or fixation. The retina's layered structure was observed effectively throughout experiments and could be visualised in a similar way to previous *in vivo* retinal tissue studies.

6.2 Overall conclusion

In summary, the establishment and use of tissue engineered conjunctival and retinal models, plus the application of non-destructive *in vitro* imaging techniques, outlined in this thesis has revealed some interesting findings. Consistently, 2D and 3D TCCT models have been established to investigate the factors influencing fibrotic response after trabeculectomy surgery. In addition to cellular metabolic assessment, a new non-destructive assay using added azido-L-proline to quantify neocollagen synthesis in response to these factors, was applied for up to 14 days of culture. Key results found that 3D TCCT fibroblast metabolic activity, actin expression and neocollagen synthesis increased by up to 60% by day 7 of culture with the addition of TGF-β, VEGF, TNF-α (50 ng/mL) or 50% aqueous humour. Furthermore, shear stress-induced mechanotransduction was found to promote metabolic activity across experimental conditions, with shear stress in combination with aqueous humour triggering the strongest fibrotic response, followed by TGF-β, TNF-α and VEGF. Shear stress therefore appeared to enhance the influence of growth factors and further promoted fibrotic response within the TCCT model.

Following characterisation of how TCCT fibroblasts synergistically respond to cytokines and shear stress in chapter 3, the established TCCT models were then utilised to evaluate potential glaucoma treatment efficacy and assess the Xen Gel Stent glaucoma medical device *in vitro*. Key growth factor inhibitors, calcium signalling channel blocker Nifedipine and Decorin proteoglycan were each tested. Furthermore, the Xen Gel Stent glaucoma medical device was tested *in vitro* using the 3D TCCT model. Key results found that TCCT fibroblast activity decreased by up to 281.9% by day 3 of culture with the addition of TNF-α and TGF-β inhibitors (10μM) or Nifedipine (100 μM). Furthermore, fibroblast activity surrounding the stent lumen was evident when implanting the Xen Gel Stent glaucoma medical device into the 3D TCCT tissue model, offering a convenient method to assess new glaucoma treatment devices.

Following study of how glaucoma treatment methods could be improved in this chapter 4, the potential preservation and regeneration of damaged retinal tissue was assessed in the establishment of a 3D *in vitro* organotypic retinal tissue model in chapter 5. A compressed collagen gel substrate was found to be beneficial in providing the biochemical and mechanical strength appropriate to preserve retinal tissue *in vitro* and in the absence of IOP, whilst still being biocompatible. The substrate preserved all layers of porcine retinal tissue intact and with minimal distortion for 14 days culture. Furthermore, OCT was demonstrated as a powerful tool for monitoring the integrity of the live retinal explants during culture. Following establishment of a laser injury method for the retinal tissue, added stem cells were found to aggregate towards the location of retinal injury, with some differentiation into RPE evident by day 3 and 7 of culture. These results convey promising potential if more specialised stem cells were to be tested in future work.

Overall, the conjunctival and retinal models, plus non-destructive imaging techniques developed and applied in this thesis, offer useful tools for the study of ocular disease mechanisms and testing of potential drug/device interventions and stem cell therapies to treat eye disease. The ongoing use and development of *in vitro* and *ex vivo* conjunctival and retinal models in future work will continue to be beneficial in future research for the investigation of ocular disease mechanisms and treatment testing, whilst also reducing the requirement for live animal experiments.

6.3 Future perspectives

In relation to the TCCT model establishment, though challenging, it would be interesting to establish a model using human TCCT samples, which would enable study to be as relevant to humans as possible. Furthermore, it may be useful to try and isolate conjunctival epithelial layer cells using a better technique for 3D TCCT fibroblast-epithelium co-culture model establishment. Since epithelial cells in this study were isolated using a 'scraping' method, some fibroblasts may have been mixed with the cultured epithelial cells from underneath tissue, which could have influenced results. Though scraping methods have been used successfully in previous literature (Wei *et al.*, 1993; Cook *et al.*, 1998), the use of better tools (e.g. Jeweler's forceps) and a more specialised dissection protocol to peel away the epithelium might have improved this method (Geggel and Gipson, 1984; Niiya *et al.*, 1997).

In light of the potential for growth factor inhibitors and calcium signalling channel blockers (e.g. Nifedipine) to be used as alternative anti-inflammatory agents after glaucoma surgery, further *in vitro* and *in vivo* studies are ultimately required in order to determine the safety and efficacy of these suggested alternative treatment methods. In

future work, it would be beneficial to take multiple images across a time-lapse in order to more accurately measure TCCT fibroblast cytosolic calcium signalling. Additionally, determination of whether or not TCCT fibroblasts have L-Type calcium signalling channels is required. Furthermore, since the commercially purchased decorin used in chapter 4 was derived from bovine articular cartilage, it may not have interacted with the porcine TCCT fibroblasts in the same way as native porcine TCCT decorin, which may explain for any unusual results observed. Therefore, a source of porcine derived decorin would be beneficial for any further testing with decorin proteoglycan.

In consideration of MIGS device use, future *in vitro* studies of the Xen Gel Stent would need a greater sample number in order to draw more accurate conclusions. In addition, more long term patient studies are arguably required in order to determine the long term effect of the Xen Gel Stent *in vivo*. Most previous clinical studies by the manufacturer have only followed patients for up to 12 months, meaning little is known about any long term complications associated with the Xen Gel Stent. Moreover, MIGS devices which use a stronger material may offer better alternatives in comparison to the fragile Xen Gel Stent. In consideration of other medical stents (e.g. vascular stents), a metallic material such as Nitinol (used in the 'Hydrus' MIGS device) may offer a better alternative, which is strong, flexible and biocompatible (Kapoor, 2017; FDA, 2018). In addition, future research into possible preventative treatment options for glaucoma would be beneficial. For example, a treatment option to stop trabecular meshwork blockage in the first place might be more beneficial than trying to open a drainage pathway once it has already become blocked.

Finally, in consideration of the *in vitro* retinal injury model establishment, some study limitations can be acknowledged in relation to the injury method testing. Evidently, all

three injury methods did not realistically mimic damage caused by retinal diseases and instead more closely replicated damage caused traumatic, chemical and laser injuries. Whilst these injury methods may still be useful, more realistic methods to mimic the damage caused by retinal diseases would be beneficial in future work. Suggested strategies could be found by observing how retinal disease damage occurs naturally. For example, a method of applying mechanical pressure to the model could be used to mimic damage caused by glaucoma. Furthermore, a method to inhibit function of the rhodopsin gene could more realistically mimic damage caused by retinitis pigmentosa. More realistic injury methods such as these would not only aid in a better understanding of retinal disease mechanisms, but would also allow for more realistic testing of retinal repair methods.

References

Abdulrahman, F. A. Marwan, A. A. (2019) Lasers (surgery). Available at: https://eyewiki.aao.org/Lasers_(surgery) (Accessed: 7 September 2019).

Allergan (2017) For the surgical treatment of refractory glaucoma | XEN®. Available at: https://hcp.xengelstent.com/about-xen (Accessed: 8 March 2019).

Alovisi, C. et al. (2017) 'Vitreous Substitutes: Old and New Materials in Vitreoretinal Surgery', *Journal of Ophthalmology*, 2017, pp. 1–6.

Amin, K. (2012) 'The role of mast cells in allergic inflammation', *Respiratory Medicine*, 106(1), pp. 9–14.

Ando, J. Yamamoto, K. (2013) 'Flow detection and calcium signalling in vascular endothelial cells', *Cardiovascular Research*, 99(2), pp. 260–268.

Ash, C. et al. (2017) 'Effect of wavelength and beam width on penetration in light-tissue interaction using computational methods', *Lasers in Medical Science*, 32(8), pp. 1909–1918.

Aurand, E. R. et al. (2012) 'Building Biocompatible Hydrogels for Tissue Engineering of the Brain and Spinal Cord', *Journal of Functional Biomaterials*, 3(4), pp. 839–863.

Bahler, C. K. et al. (2012) 'Second-generation Trabecular Meshwork Bypass Stent (iStent inject) Increases Outflow Facility in Cultured Human Anterior Segments', *American Journal of Ophthalmology*, 153(6), pp. 1206–1213.

Bardsley, K. Yang, Y. Haj, A. J. El. (2017) 'Fluorescent Labeling of Collagen Production by Cells for Noninvasive Imaging of Extracellular Matrix Deposition', *Tissue Engineering. Part C, Methods*, 23(4), pp. 228–236.

Binder, S. et al. (2007) 'Transplantation of the RPE in AMD', *Progress in Retinal and Eye Research*, 26(5), pp. 516–554.

Bongso, A. Fong, C. Y. Gauthaman, K. (2008) ‘Taking stem cells to the clinic: Major challenges’, *Journal of Cellular Biochemistry*, 105(6), pp. 1352–1360.

Brown, B. R. A. et al. (2005) ‘Ultrarapid Engineering of Biomimetic Materials and Tissues: Fabrication of Nano- and Microstructures by Plastic Compression’, *Advanced Functional Materials*, 15(11), pp. 1762-1770.

Brown, C. T. et al. (1994) ‘Age-related changes of scleral hydration and sulfated glycosaminoglycans’, *Mechanisms of Ageing and Development*, 77(2), pp. 97–107.

Caplan, A. I. (1991) ‘Mesenchymal stem cells’, *Journal of Orthopaedic Research*, 9(5), pp. 641–50.

Cavet, M. E. et al. (2013) ‘Anti-allergic effects of mapracorat, a novel selective glucocorticoid receptor agonist, in human conjunctival fibroblasts and epithelial cells’, *Molecular vision*, 19, pp. 1515-1525.

Chen, S. Birk, D. E. (2012) ‘Focus on Molecules: Decorin’, *Experimental Eye Research*, 92(6), pp. 444–445.

Chouhan, G. et al. (2019) ‘A self-healing hydrogel eye drop for the sustained delivery of decorin to prevent corneal scarring’, *Biomaterials*, 210, pp. 41–50.

Clapham, D. E. (2007) ‘Calcium Signaling’, *Cell*, 131(6), pp. 1047–1058.

Colthurst, M. J. et al. (2000) ‘Biomaterials used in the posterior segment of the eye’, *Biomaterials*, 21(7), pp. 649–665.

Cook, E. B. et al. (1998) ‘Isolation of human conjunctival mast cells and epithelial cells: tumor necrosis factor-alpha from mast cells affects intercellular adhesion molecule 1 expression on epithelial cells’, *Investigative Ophthalmology & Visual Science*, 39(2), pp. 336–343.

Coulson-Thomas, V. J. et al. (2015) ‘Loss of Corneal Epithelial Heparan Sulfate Leads to Corneal Degeneration and Impaired Wound Healing’, *Investigative Ophthalmology & Visual Science,* 56(5), pp. 3004-3014.

da Cruz, L. et al. (2018) ‘Phase 1 clinical study of an embryonic stem cell–derived retinal pigment epithelium patch in age-related macular degeneration’, *Nature Biotechnology,* 36(4), pp. 328–337.

Cunliffe, I. A. et al. (1995) ‘Effect of TNF, IL-1, and IL-6 on the proliferation of human Tenon’s capsule fibroblasts in tissue culture’, *The British Journal of Ophthalmology,* 79(6), pp. 590–595.

Cvenkel, B. Kopitar, A. N. Ihan, A. (2010) ‘Inflammatory Molecules in Aqueous Humour and on Ocular Surface and Glaucoma Surgery Outcome’, *Mediators of Inflammation,* 2010, pp. 1-7.

Dan, L. Chua, C. Leong, K. (2010) ‘Fibroblast Response to Interstitial Flow: A State-of-the-Art Review’, *Biotechnology and Bioengineering*, 107(1), pp. 1–10.

Denton, M. L. et al. (2010) ‘In vitro retinal model reveals a sharp transition between laser damage mechanisms’, *Journal of Biomedical Optics,* 15(3), pp. 1-3.

Dervenis, N. et al. (2017) ‘Dislocation of a previously successful XEN glaucoma implant into the anterior chamber: a case report’, *BMC Ophthalmology,* 17(1), pp. 148-150.

Dirani, A. Chelala, E. Fadlallah, A. (2013) ‘Bilateral macular injury from a green laser pointer’, *Clinical Ophthalmology*, 7, pp. 2127–2130.

Edmondson, R. et al. (2014) ‘Three-Dimensional Cell Culture Systems and Their Applications in Drug Discovery and Cell-Based Biosensors’, *Assay and Drug Development Technologies,* 12(4), pp. 207–218.

Falavarjani, K. G. Nguyen, Q. D. (2013) ‘Adverse events and complications associated with intravitreal injection of anti-VEGF agents: a review of literature’, *Eye*, 27(7), pp. 787–94.

Farjood, F. Vargis, E. (2018) ‘Novel devices for studying acute and chronic mechanical stress in retinal pigment epithelial cells’, *Lab on a Chip*, 18(22), pp. 3413–3424.

FDA (2018) Recently-Approved Devices - Hydrus® Microstent - P170034. Available at: https://www.fda.gov/medical-devices/recently-approved-devices/hydrusr-microstent-p170034 (Accessed: 26 March 2019).

Fea, A. et al. (2015) ‘Managing Drawbacks in Unconventional Successful Glaucoma Surgery: A Case Report of Stent Exposure’, *Case Reports in Ophthalmological Medicine*, 2015, pp. 1-4.

Fernández-García, A. Romero, C. Garzón, N. (2015) ‘“Dry Lake” technique for the treatment of hypertrophic bleb following XEN® Gel Stent placement’, *Archivos de la Sociedad Española de Oftalmología*, 90(11), pp. 536-538.

Ferreira, N. P. Pinto, L. A. Marques-Neves, C. (2017) ‘XEN Gel Stent Internal Ostium Occlusion: Ab-Interno Revision’, *Journal of Glaucoma*, 26(4), pp. 150-152.

Frantz, C. et al. (2010) ‘The extracellular matrix at a glance’, *Journal of Cell Science*, 123(24), pp. 4195–4200.

Franz Marie, O. et al. (2009) ‘Predictors for failure of primary trabeculectomy’, *Philippine Journal of Ophthalmology*, 34(1), pp. 8–14.

Gabelt, B. T. Kaufman, P. L. (2005) ‘Changes in aqueous humor dynamics with age and glaucoma’, *Progress in Retinal and Eye Research*, 24(5), pp. 612–637.

Gabriele, M. L. et al. (2010) ‘Three dimensional optical coherence tomography imaging: Advantages and advances’, *Progress in Retinal and Eye Research*, 29(6), pp. 556–579.

Gähwiler, B. H. et al. (1997) ‘Organotypic slice cultures: a technique has come of age’, *Trends in Neurosciences*, 20(10), pp. 471–477.

Gao, Q. et al. (2008) ‘A new strategy to replace the natural vitreous by a novel capsular artificial vitreous body with pressure-control valve’, *Eye*, 22(3), pp. 461–8.

Garcia-Posadas, L. et al. (2017) ‘An engineered human conjunctival-like tissue to study ocular surface inflammatory diseases’, *PLOS One*, 12(3), pp. 1–17.

Gedde, S. J. et al. (2012) ‘Treatment outcomes in the tube versus trabeculectomy (TVT) study after five years of follow-up’, *American Journal of Ophthalmology*, 153(5), pp. 789-803.

Geggel, H. S. Gipson, I. K. (1984) ‘Removal of Viable Sheets of Conjunctival Epithelium with Dispase II’, *Investigative Ophthalmology & Visual Science*, 26(1), pp. 55-22.

Gill, K. P. et al. (2016) ‘Enriched retinal ganglion cells derived from human embryonic stem cells’, *Scientific Reports*, 6(1), pp. 1-11.

Giménez, B. Montero, M. P. (2011) ‘Functional and bioactive properties of collagen and gelatin from alternative sources: A review’, *Food hydrocolloids*, 25(8), pp. 1813–1827.

Gir, P. et al. (2012) ‘Human adipose stem cells: current clinical applications’, *Plastic and reconstructive surgery*, 129(6), pp. 1277–1290.

Goel, M. et al. (2010) ‘Aqueous Humor Dynamics: A Review’, *The Open Ophthalmology Journal*, 4, pp. 52–59.

Grimm, C. Remé, C. E. (2012) ‘Light Damage as a Model of Retinal Degeneration’, *Methods in Molecular Biology*, 935, pp. 87–97.

Grisanti, S. et al. (2005) ‘Decorin modulates wound healing in experimental glaucoma filtration surgery: a pilot study’, *Investigative Ophthalmology & Visual Science*, 46(1), pp. 191–196.

Groneberg, D. A. et al. (2003) ‘Animal models of allergic and inflammatory conjunctivitis’, *Allergy*, 58(11), pp. 1101–1113.

Guduric-Fuchs, J. et al. (2009) ‘Immunohistochemical study of pig retinal development’, *Molecular vision*, 15, pp. 1915–1928.

Haddad-Mashadrizeh, A. et al. (2013) ‘Human adipose-derived mesenchymal stem cells can survive and integrate into the adult rat eye following xenotransplantation’, *Xenotransplantation*, 20(3), pp. 165–76.

Hartong, D. T. Berson, E. L. Dryja, T. P. (2006) ‘Retinitis pigmentosa’, *The Lancet*, 368(9549), pp. 1795–1809.

Harvey, A. R. et al. (2006) ‘Gene therapy and transplantation in CNS repair: the visual system’, *Progress in retinal and eye research*, 25(5), pp. 449–489.

Hayashi, K. et al. (2017) ‘Fast-forming hydrogel with ultralow polymeric content as an artificial vitreous body’, *Nature Biomedical Engineering*, 1(3), p. 44.

He, J. et al. (2017) ‘Modeling alveolar injury using microfluidic co-cultures for monitoring bleomycin-induced epithelial/fibroblastic cross-talk disorder’, *Royal Society of Chemistry Advances*, 7(68), pp. 42738–42749.

He, M. et al. (2018) ‘Artificial polymeric scaffolds as extracellular matrix substitutes for autologous conjunctival goblet cell expansion’, *Investigative Ophthalmology & Visual Science*, 57(14), pp. 6134–6146.

He, M. M. et al. (2005) ‘Small-Molecule Inhibition of TNF-alpha’, *Science*, 310(5750), pp. 1022–1025.

Heijl, A. (2014) ‘Glaucoma treatment: by the highest level of evidence’, *The Lancet*, 385(9975), pp. 1264–1267.

Hildebrand, A. et al. (1994) ‘Interaction of the small interstitial proteoglycans biglycan, decorin and fibromodulin with transforming growth factor beta’, *The Biochemical Journal*, 302(2), pp. 527–34.

Hill, L. J. et al. (2015) ‘Decorin reduces intraocular pressure and retinal ganglion cell loss in rodents through fibrolysis of the scarred trabecular meshwork’, *Investigative Opthalmology & Visual Science*, 56(6), pp. 3743-3757.

Hill, L. J. et al. (2018) ‘Sustained release of decorin to the surface of the eye enables scarless corneal regeneration’, *npg Regenerative Medicine*, 3(1), pp. 1-23.

Hong, C. H. et al. (2005) ‘Glaucoma drainage devices: a systematic literature review and current controversies’, *Survey of Ophthalmology*, 50(1), pp. 48–60.

Huang, W. et al. (2014) ‘Inflammation-related cytokines of aqueous humor in acute primary angle-closure eyes’, *Investigative Ophthalmology & Visual Science*, 55(2), pp. 1088–1094.

Huang, W. Gao, X. Chen, S. (2015) ‘Vascular Endothelial Growth Factor is Increased in Aqueous Humor of Acute Primary Angle-Closure Eyes’, *Journal of Glaucoma*, 25(7), pp. 647-651.

Idriss, H. T. Naismith, J. H. (2000) ‘TNFα and the TNF receptor superfamily: Structure-function relationship(s)’, Microscopy Research and Technique, 50(3), pp. 184–195.

Iskratsch, T. Wolfenson, H. Sheetz, M. P. (2014) ‘Appreciating force and shape — the rise of mechanotransduction in cell biology’, *Nature Publishing Group*, 15(12), pp. 825–833.

Izumi, K. et al. (2005) ‘Corneal epithelial cells are essential for prevention of myodifferentiation of corneal fibroblasts in a coculture system’, *Investigative Ophthalmology & Visual Science*, 46(13), pp. 2155–2155.

Jaalouk, D. E. Lammerding, J. (2009) ‘Mechanotransduction gone awry’, *Nature Reviews. Molecular Cell Biology*, 10(1), pp. 63-73.

Jampel, H. D. et al. (1990) ‘Transforming growth factor-β in human aqueous humor’, *Current Eye Research*, 9(10), pp. 963-969.

Jampel, H. D. et al. (2005) ‘Perioperative Complications of Trabeculectomy in the Collaborative Initial Glaucoma Treatment Study (CIGTS)’, *American Journal of Ophthalmology*, 140(1), pp. 16–22.

Januschowski, K. et al. (2019) ‘Ex vivo biophysical characterization of a hydrogel-based artificial vitreous substitute’, *PLOS One*, 14(1), pp. 1-12.

Jarvelainen, H. et al. (2006) ‘A role for decorin in cutaneous wound healing and angiogenesis’, *Wound Repair and Regeneration*, 14(4), pp. 443–452.

Johnson, T. V. Martin, K. R. (2008) ‘Development and characterization of an adult retinal explant organotypic tissue culture system as an in vitro intraocular stem cell transplantation model’, *Investigative Ophthalmology and Visual Science*, 49(8), pp. 3503–3512.

Joosten, E. (2012) ‘Biodegradable biomatrices and bridging the injured spinal cord: the corticospinal tract as a proof of principle’, *Cell and Tissue Research*, 349(1), pp. 375–95.

Kador, K. Goldberg, J. (2013) ‘Scaffolds and stem cells: delivery of cell transplants for retinal degenerations’, *Expert Review Ophthalmology*, 7(5), pp. 459–470.

Kaneko, M. Takaku, I. Katsura, N. (1986) ‘Glycosaminoglycans in pterygium tissues and normal conjunctiva’, *Japanese Journal of Ophthalmology*, 30(2), pp. 165-173.

Kang, Y. G. et al. (2014) ‘Effects of Flow-Induced Shear Stress on Limbal Epithelial Stem Cell Growth and Enrichment’, *PLOS One*, 9(3), pp. 1-7.

Kapoor, D. (2017) ‘Nitinol for Medical Applications: A Brief Introduction to the Properties and Processing of Nickel Titanium Shape Memory Alloys and their Use in Stents’, *Johnson Matthey Technology Review*, 61(1), pp. 66–76.

Khaw, P. T. et al. (1994) ‘Activation and suppression of fibroblast function’, *Eye*, 8(2), pp. 188–95.

Kim, S. U. Takahashi, H. (1988) ‘Tissue culture study of adult human retina neurons’, *Investigative Ophthalmology & Visual Science*, 29(9), pp. 1372–1379.

Klassen, H. J. et al. (2004) ‘Multipotent retinal progenitors express developmental markers, differentiate into retinal neurons, and preserve light-mediated behavior’, Investigative Ophthalmology and Visual Science, 45(11), pp. 4167–4173.

Klassen, H. Sakaguchi, D. S. Young, M. J. (2004) ‘Stem cells and retinal repair’, *Progress in Retinal and Eye Research*, 23(2), pp. 149–81.

Kobuch, K. et al. (2008) ‘Maintenance of adult porcine retina and retinal pigment epithelium in perfusion culture: Characterisation of an organotypic in vitro model’, *Experimental Eye Research*, 86(4), pp. 661–668.

Kohen, L. et al. (1997) ‘Mechanisms of graft rejection in the transplantation of retinal pigment epithelial cells’, *Ophthalmic Research*, 29(5), pp. 298–304.

Kokavec, J. et al. (2016) ‘Biochemical analysis of the living human vitreous’, *Clinical & Experimental Ophthalmology*, 44(7), pp. 597-609.

Kokkinaki, M. Sahibzada, N. Golestaneh, N. (2011) ‘Human induced pluripotent stem-derived retinal pigment epithelium (RPE) cells exhibit ion transport, membrane potential, polarized vascular endothelial growth factor secretion, and gene expression pattern similar to native RPE’, *Stem Cells*, 29(5), pp. 825–835.

Kolb, H. Fernandez, E. Nelson, R. (2010) ‘The Organization of the Retina and Visual System’, *Webvision*, pp. 1-5.

Kolb, M. et al. (2001) ‘Proteoglycans decorin and biglycan differentially modulate TGF-beta-mediated fibrotic responses in the lung’, *American Journal of Physiology. Lung cellular and molecular physiology*, 280(6), pp. 1327–1334.

Kummer, M. P. et al. (2007) ‘Artificial vitreous humor for in vitro experiments’, *Annual International Conference of the IEEE Engineering in Medicine and Biology - Proceedings*.

Kunihiko, N. et al. (2002) ‘Injured corneal epithelial cells promote myodifferentiation of corneal fibroblasts’, *Investigative Ophthalmology & Visual Science*, 43(8), pp. 2603–2608.

Lamba, D. A. Gust, J. Reh, T. A. (2009) ‘Transplantation of human embryonic stem cell-derived photoreceptors restores some visual function in Crx-deficient mice’, *Cell Stem Cell*, 4(1), pp. 73–9.

Law, J. X. et al. (2016) ‘A comparative study of skin cell activities in collagen and fibrin constructs’, *Medical Engineering & Physics*, 38(9), 854-861.

Lawley, E. Baranov, P. Young, M. (2015) ‘Hybrid vitronectin-mimicking polycaprolactone scaffolds for human retinal progenitor cell differentiation and transplantation’, *Journal of Biomaterials Applications*, 29(6), pp. 894-902.

Lee, C. H. Singla, A. Lee, Y. (2001) ‘Biomedical applications of collagen’, *International Journal of Pharmaceutics*, 221, pp. 1–22.

Lee, S. J. et al. (2015) ‘Intraperitoneal administration of adipose tissue derived stem cells rescue Retinal degeneration in mouse model’, *Investigative Ophthalmology & Visual Science*, 56(7), pp. 1842-1852.

Liu, Z. et al. (2014) ‘Enhancement of retinal pigment epithelial culture characteristics and subretinal space tolerance of scaffolds with 200 nm fiber topography’, *Biomaterials*, 35(9), pp. 2837–2850.

Livesey, F. J. Cepko, C. L. (2001) ‘Vertebrate neural cell-fate determination: lessons from the retina’, *Nature reviews. Neuroscience*, 2(2), pp. 109–118.

Lu, A. Q. Barnstable, C. J. (2018) ‘Generation of Photoreceptor Precursors from Mouse Embryonic Stem Cells’, *Stem Cell Reviews and Reports*, 14(2), pp. 247–261.

Lu, Q. et al. (2017) ‘An in vitro model for the ocular surface and tear film system’, *Scientific Reports*, 7(1), pp. 1–11.

Luo, J. et al. (2014) ‘Human retinal progenitor cell transplantation preserves vision’, *Journal of Biological Chemistry*, 289(10), pp. 6362–6371.

Machalińska, A. et al. (2013) ‘Long-term neuroprotective effects of NT-4-engineered mesenchymal stem cells injected intravitreally in a mouse model of acute retinal injury’, *Investigative Ophthalmology & Visual Science*, 54(13), pp. 8292–8305.

Mammadova, N. et al. (2017) ‘Lasting Retinal Injury in a Mouse Model of Blast-Induced Trauma’, *The American Journal of Pathology*, 187(7), pp. 1459–1472.

Massagué, J. (2000) ‘How cells read TGF-beta signals’, *Nature Reviews. Molecular Cell Biology*, 1(3), pp. 169-178.

Matta, C. Zakany, R. Mobasheri, A. (2015) ‘Voltage-dependent calcium channels in chondrocytes: roles in health and disease’, *Current Rheumatology Reports*, 17(7), pp. 1–26.

Mehat, M. S. et al. (2018) ‘Transplantation of Human Embryonic Stem Cell-Derived Retinal Pigment Epithelial Cells in Macular Degeneration’, *Ophthalmology*, 125(11), pp. 1765–1775.

Meschede, D. (2008) Optics, Light and Lasers: The Practical Approach to Modern Aspects of Photonics and Laser Physics: Second Edition, Wiley (US). pp. 1-5.

Miron-Mendoza, M. Seemann, J. Grinnell, F. (2010) ‘The differential regulation of cell motile activity through matrix stiffness and porosity in three dimensional collagen matrices’, *Biomaterials*, 31(25), pp. 6425-6435.

Molladavoodi, S. et al. (2017) ‘Corneal epithelial cells exposed to shear stress show altered cytoskeleton and migratory behaviour’, *PLOS One*, 12(6), pp. 1–16.

Moorfields Eye Hospital (2017) Acute angle-closure glaucoma | Moorfields Eye Hospital NHS Foundation Trust. Available at: https://www.moorfields.nhs.uk/content/acute-angle-closure-glaucoma (Accessed: 6 March 2019).

Mukherjee, S. et al. (2015) ‘Disruption of calcium signaling in fibroblasts and attenuation of bleomycin-induced fibrosis by nifedipine, *American Journal of Respiratory Cell and Molecular Biology*, 53(4), pp. 450–458.

Mutti, D. (2003) ‘Optics of the Human Eye’, *Optometry and Vision Science*. 1(1), pp. 1-5.

Narayan, D. S. et al. (2017) ‘Glucose metabolism in mammalian photoreceptor inner and outer segments’, *Clinical and Experimental Ophthalmology*, 45(7), pp. 730-741.

National Centre for the Replacement Refinement & Reduction of animals in research (NC3Rs) (2016) Challenge 23: Retinal 3D | CrackIT. Available at: https://crackit.org.uk/challenge-23-retinal-3d (Accessed: 8 March 2019).

Neeley, W. L. et al. (2008) 'A microfabricated scaffold for retinal progenitor cell grafting', *Biomaterials*, 29(4), pp. 418–426.

Ng, C. P. Hinz, B. Swartz, M. A. (2005) 'Interstitial fluid flow induces myofibroblast differentiation and collagen alignment in vitro', *Journal of Cell Science*, 118(20), pp. 4731–4739.

Nguyen, D. Q. et al. (2012) 'A Model to Measure Fluid Outflow in Rabbit Capsules Post Glaucoma Implant Surgery', *Investigative Ophthalmology & Visual Science*, 53(11), pp. 6914–6919.

NICE (2019) Glaucoma. Available at: https://cks.nice.org.uk/glaucoma (Accessed: 7 September 2019).

Niiya, A. et al. (1997) 'Collagen gel-embedding culture of conjunctival epithelial cells', *Graefe's Archive for Clinical and Experimental Ophthalmology*, 235(1), pp. 32–40.

Orgel, J. P. et al. (2009) 'Decorin core protein (decoron) shape complements collagen fibril surface structure and mediates its binding', *PLOS One*, 4(9), pp. 1-10.

Park, C. Y. et al. (2017) 'Details of the collagen and elastin architecture in the human limbal conjunctiva, Tenon's capsule and sclera revealed by two-photon excited fluorescence microscopy', *Investigative Ophthalmology & Visual Science*, 57(13), pp. 5602-5610.

Paschalis, E. I. et al. (2017) 'Mechanisms of Retinal Damage after Ocular Alkali Burns', *The American Journal of Pathology*, 187(6), pp. 1327–1342.

Pei, B. et al. (2017) ‘Fiber-reinforced scaffolds in soft tissue engineering’, *Regenerative Biomaterials*, 4(4), pp. 257–268.

Pera, M. F. Reubinoff, B. Trounson, A. (2000) ‘Human embryonic stem cells’, *Journal of Cell Science*, 113(1), pp. 5–10.

Pérez-Torregrosa, V. T. et al. (2016) ‘Combined phacoemulsification and XEN45 surgery from a temporal approach and 2 incisions’, *Archivos de la Sociedad Española de Oftalmología*, 91(9), pp. 415–421.

Przekora, A. Zarnowski, T. Ginalska, G. (2017) ‘A simple and effective protocol for fast isolation of human Tenon’s fibroblasts from a single trabeculectomy biopsy – a comparison of cell behaviour in different culture media’. *Cellular & Molecular Biology Letters*, 22(5), pp. 1–16.

Puwanun, S. et al. (2018) ‘A simple rocker-induced mechanical stimulus upregulates mineralization by human osteoprogenitor cells in fibrous scaffolds’, *Journal of Tissue Engineering & Regenerative Medicine*, 12(2), pp. 370-381.

Quigley, H. A. (2011) ‘Glaucoma’, *The Lancet*, 377(9774), pp. 1367–77.

Ramsden, C. M. et al. (2013) ‘Stem cells in retinal regeneration: past, present and future’, *Development*, 140(12), pp. 2576–85.

Read, S. A. et al. (2016) ‘Anterior eye tissue morphology: Scleral and conjunctival thickness in children and young adults’, *Scientific Reports*, 20(6), pp. 1–10.

Redenti, S. et al. (2009) ‘Engineering retinal progenitor cell and scrollable poly(glycerol-sebacate) composites for expansion and subretinal transplantation’, *Biomaterials*, 30(20), pp. 3405–3414.

ReNeuron (2016) Phase I/II clinical trial in retinitis pigmentosa - ReNeuron. Available at: http://www.reneuron.com/clinical-trials/phase-iii-clinical-trial-in-retinitis-pigmentosa/ (Accessed: 31 March 2016).

Reynolds, J. Lamba, D. (2014) 'Human embryonic stem cell applications for retinal degenerations', *Experimental eye research*, 123, pp. 151–160.

Richardson, J. (2017) 'Application of a human primary epithelial-fibroblast co-culture system to study fibrosis'. Available at: http://eprints.nottingham.ac.uk/46427/ (Accessed: 22 April 2019).

Riolobos, L. et al. (2013) 'HLA engineering of human pluripotent stem cells', *Molecular therapy: The journal of the American Society of Gene Therapy*, 21(6), pp. 1232–1241.

ReNeuron (2016) First Patient Treated in RP Clinical Trial | ReNeuron Group plc. Available at: http://www.reneuron.com/first-patient-treated-in-rp-clinical-trial/ (Accessed: 10 April 2016).

Robinton, D. A. Daley, G. Q. (2012) 'The promise of induced pluripotent stem cells in research and therapy', *Nature*, 481(7381), pp. 295–305.

Saeidnia, S. Manayi, A. Abdollahi, M. (2015) 'From in vitro experiments to in vivo and clinical studies; pros and cons', *Current Drug Discovery Technologies*, 12(4), pp. 218-224.

Samardzija, M. et al. (2010) 'Animal Models for Retinal Diseases', *Animal models for Retinal Degeneration*. New York: The Humana Press Inc, pp. 51–79.

Schlunck, G. et al. (2016) 'Conjunctival fibrosis following filtering glaucoma surgery', *Experimental Eye Research*, 142, pp. 76–82.

Schmitt, S. et al. (2009) 'Molecular characterization of human retinal progenitor cells', Investigative Ophthalmology & Visual Science, 50(12), pp. 5901–5908.

Schramm, C. et al. (2012) ‘The cross-linked biopolymer hyaluronic acid as an artificial vitreous substitute’, *Investigative Ophthalmology & Visual Science*, 53(2), pp. 613–621.

Schwartz, S. D. et al. (2012) ‘Embryonic stem cell trials for macular degeneration: a preliminary report’, *The Lancet*, 379(9817), pp. 713–720.

Sernagor, E. Eglen, S. J. Wong, R. O. (2001) ‘Development of retinal ganglion cell structure and function’, *Progress in Retinal and Eye Research*, 20(2), pp. 139–174.

Shafaie, S. et al. (2016) ‘In Vitro Cell Models for Ophthalmic Drug Development Applications’, *Bioresearch*, 5(1), pp. 94–108.

Sherwood, M. B. et al. (1987) ‘Cysts of Tenon’s Capsule Following Filtration Surgery: Medical Management’, *Archives of Ophthalmology*, 105(11), pp. 1517–1521.

Sheybani, A. et al. (2015) ‘Phacoemulsification combined with a new ab interno gel stent to treat open-angle glaucoma: pilot study’, *Journal of Cataract & Refractive Surgery*, 41(9), pp. 1905–1909.

Shibuya, M. (2011) ‘Vascular endothelial growth factor (VEGF) and its receptor (VEGFR) signaling in angiogenesis: a crucial target for anti- and pro-angiogenic therapies’, *Genes & Cancer*, 2(12), pp. 1097–1105.

Silber, P. C. et al. (2015) ‘Conjunctival epithelial cells cultivated ex vivo from patients with total limbal stem cell deficiency’, *European Journal of Ophthalmology*, 25(1), pp. 60–64.

Simon, M. Green, H. (1985) ‘Enzymatic cross-linking of involucrin and other proteins by keratinocyte particulates in vitro’, *Cell*, 40(3), pp. 677–683.

Song, S. et al. (2013) ‘Collaborative effects of electric field and fluid shear stress on fibroblast migration’, *Lab on a Chip*, 13(8), pp. 1602-1611.

Stamper, R. L. McMenemy, M. G. Lieberman, M. F. (1992) ‘Hypotonous maculopathy after trabeculectomy with subconjunctival 5-fluorouracil’, *American Journal of Ophthalmology*, 114(5), pp. 544–553.

Stefánsson, E. et al. (1988) ‘Refractive changes from use of silicone oil in vitreous surgery’, *Retina*, 8(1), pp. 20–23.

Stern, J. Radosevich, M. Temple, S. (2010) Stem Cell Retinal Replacement Therapy. Available at: http://worldstemcellsummit.com/files/2009_report/WSCRs2.pdf. (Accessed: 7 September 2019).

Stone, E. M. (2007) ‘Macular degeneration’, *Annual Review of Medicine*, 58, pp. 477-490.

Strauss, O. (2005) ‘The retinal pigment epithelium in visual function’, *Physiological Reviews*, 85(3), pp. 845–881.

Suzuki, R. et al. (2002) ‘Long-term follow-up of initially successful trabeculectomy with 5-fluorouracil injections’, *Ophthalmology*, 109(10), pp. 1921–1924.

Teotia, P. Mir, Q. Ahmad, I. (2015) ‘Chemically defined and retinal conditioned medium-based directed differentiation of embryonic stem and induced pluripotent stem cells into retinal ganglion cells’, *Investigative Ophthalmology & Visual Science*, 56(7), p. 3606.

Teus, M. et al. (2015) ‘12 month results from a minimally invasive, 45μm lumen ab-interno gelatin stent in combination with a preoperative MMC in open angle glaucoma with and without concurrent cataract surgery: a multicenter prospective study conducted in Spain’, *XXXIII Congress of the ESCRS: Glaucoma II proceedings*

The Niche (2015) Landmark IPSC clinical study on hold due to genomic issue. Available at: http://www.ipscell.com/2015/07/firstipscstop/ (Accessed: 7 May 2016).

ThermoFisher Scientific (2014) Collagen I, Rat Tail. Available at: https://www.thermofisher.com/document-connect/document-connect.html?url=https%3A%2F%2Fassets.thermofisher.com%2FTFS-Assets%2FLSG%2Fmanuals%2FCollagen_I_rat_tail_PI.pdf&title=Q29sbGFnZW4gSSwgUmF0IFRhaWw= (Accessed: 4 April 2019).

Thorlabs (2015) OCT Systems Tutorial. Available at: https://www.thorlabs.com/newgrouppage9.cfm?objectgroup_id=10763 (Accessed: 1 May 2019).

Tomasz, M. (1995) 'Mitomycin C: small, fast and deadly (but very selective)', *Chemistry & Biology*, 2(9), pp. 575-579.

Toris, C. (2013) Glaucoma Today - Uveoscleral Outflow. Available at: http://glaucomatoday.com/2013/10/uveoscleral-outflow/ (Accessed: 17 April 2019).

Tovell, V. E. et al. (2011) 'Advancing the Treatment of Conjunctival Scarring: a novel ex vivo model', *Archives of Ophthalmology*, 129(5), pp. 619-627.

Tripathi, R. C. et al. (1992) 'Quantitative and qualitative analyses of transferrin in aqueous humor from patients with primary and secondary glaucoma', *Investigative Ophthalmology & Visual Science*, 33(10), pp. 2866–2873.

Trivedi, R. H. et al. (2011) 'Influence of Race and Age on Aqueous Humor Levels of Transforming Growth Factor-Beta 2 in Glaucomatous and Nonglaucomatous Eyes', *Journal of Ocular Pharmacology and Therapeutics*, 27(5), pp. 477–480.

Tucker, R. P. et al. (2014) 'See-saw rocking: an in vitro model for mechanotransduction research', *Journal of the Royal Society Interface*, 11(97), pp. 1-9.

Turczyńska, K. M. et al. (2013) ‘Regulation of vascular smooth muscle mechanotransduction by microRNAs and L-type calcium channels’, *Communitive & Integrative Biology*, 6(1), pp. 1–4.

Uesugi, K. et al. (2017) ‘A Self-Assembling Peptide Gel as a Vitreous Substitute: A Rabbit Study’, *Investigative Ophthalmology & Visual Science*, 58(10), pp. 4068-4075.

Utsunomiya, T. et al. (2016) ‘Transforming Growth Factor-β Signaling Cascade Induced by Mechanical Stimulation of Fluid Shear Stress in Cultured Corneal Epithelial Cells’, *Investigative Ophthalmology & Visual Science*, 57(14), pp. 6382-6388.

Vadillo-Ortega, F. et al. (1989) ‘A latent collagenase in human aqueous humor’, *Investigative Ophthalmology & Visual Science*, 30(2), pp. 332–335.

Vayl, A., Gomaa, A. and Rajashekhar, G. (2014) ‘Adipose stromal cells attenuate p38 MAPK in retinal ischemia-reperfusion injury’, *Investigative Ophthalmology & Visual Science*, 55(13), 55, pp. 4005-4006.

Venugopalan, P. et al. (2016) ‘Transplanted neurons integrate into adult retinas and respond to light’, *Nature Communications*, 7, pp. 10472-10482.

Viktorov, I. V. et al. (2004) ‘Roller organotypic cultures of postnatal rat retina’, *Bulletin of Experimental Biology and Medicine*, 137(4), pp. 419–422.

Wang, J. et al. (2011) ‘Organotypic culture of full-thickness adult porcine retina’, *Journal of visualized experiments: JoVE*, 49, p. 2655.

Wei, Z. et al. (1993) ‘In vitro growth and differentiation of rabbit bulbar, fornix, and palpebral conjunctival epithelia. Implications on conjunctival epithelial transdifferentiation and stem cells’, *Investigative Ophthalmology & Visual Science*, 34(5), pp. 1814–1828.

World Health Organisation (WHO) (2015) ‘WHO | Priority eye diseases’. Available at: http://www.who.int/blindness/causes/priority/en/index6.html (Accessed: 28 September 2015).

Wolner, B. et al. (1991) ‘Late bleb-related endophthalmitis after trabeculectomy with adjunctive 5-fluorouracil’, *Ophthalmology*, 98(7), pp. 1053–1060.

Wray, S. (1992) ‘Organotypic slice explant roller-tube cultures’, *Practical Cell Culture Techniques*, 23(1), pp. 201–239.

Wright, L. S. et al. (2014) ‘Induced pluripotent stem cells as custom therapeutics for retinal repair: progress and rationale’, *Experimental Eye Research*, 123, pp. 161–172.

Xu, W. Xu, G. X. (2011) ‘Mesenchymal stem cells for retinal diseases’, *International Journal of Ophthalmology*, 4(4), pp. 413–421.

Yang, I. et al. (2015) ‘Involvement of Intracellular Calcium Mobilization in IL-8 Activation in Human Retinal Pigment Epithelial Cells’, *Investigative Ophthalmology & Visual Science*, 56(2), pp. 761-769.

Yang, Z. et al. (2010) ‘Amelioration of diabetic retinopathy by engrafted human adipose-derived mesenchymal stem cells in streptozotocin diabetic rats’, *Graefe’s Archive for Clinical and Experimental Ophthalmology*, 248(10), pp. 1415–1422.

Yao, J. et al. (2015) ‘Enhanced differentiation and delivery of mouse retinal progenitor cells using a micropatterned biodegradable thin-film polycaprolactone scaffold’, *Tissue Engineering Part A*, 21(7), pp. 1247–1260.

Yao, Q. et al. (2017) ‘Electrospun collagen / poly(L-lactic acid-co-ε-caprolactone) scaffolds for conjunctival tissue engineering’, *Experimental and Therapeutic Medicine*, 14(5), pp. 4141–4147.

Yin, S. et al. (2003) ‘Light Scatter Causes the Grayness of Detached Retinas’, *Archives of Ophthalmology*, 121(7), pp. 1002-1008.

Yoshimura, T. et al. (2009) ‘Comprehensive Analysis of Inflammatory Immune Mediators in Vitreoretinal Diseases’, *PLoS ONE*, 4(12), pp. 1-9.

Youssef, P. N. Sheibani, N. Albert, D. (2011) ‘Retinal light toxicity’, *Eye*, 25(1), pp. 1–14.

Yu, B. Shao, H. Su, C. et al. (2016) ‘Exosomes derived from MSCs ameliorate retinal laser injury partially by inhibition of MCP-1’, *Scientific Reports*, 6, pp. 1-12.

Zhang, G. et al. (2009) ‘Genetic Evidence for the Coordinated Regulation of Collagen Fibrillogenesis in the Cornea by Decorin and Biglycan’, *The Journal of Biological Chemistry*, 284(13), pp. 8888–8897.

Zhang, W. et al. (2018) ‘Decorin is a pivotal effector in the extracellular matrix and tumour microenvironment’, *Oncotarget*, 9(4), pp. 5480–5491.

Zheng, X. et al. (2010) ‘Evaluation of the Transforming Growth Factor β Activity in Normal and Dry Eye Human Tears by CCL-185 Cell Bioassay’, *Cornea*, 29(9), pp. 1048–1054.

Zhou, X. et al. (2010) ‘Quantifying fluid shear stress in a rocking culture dish’, *Journal of Biomechanics*, 43(8), pp. 1598–1602.